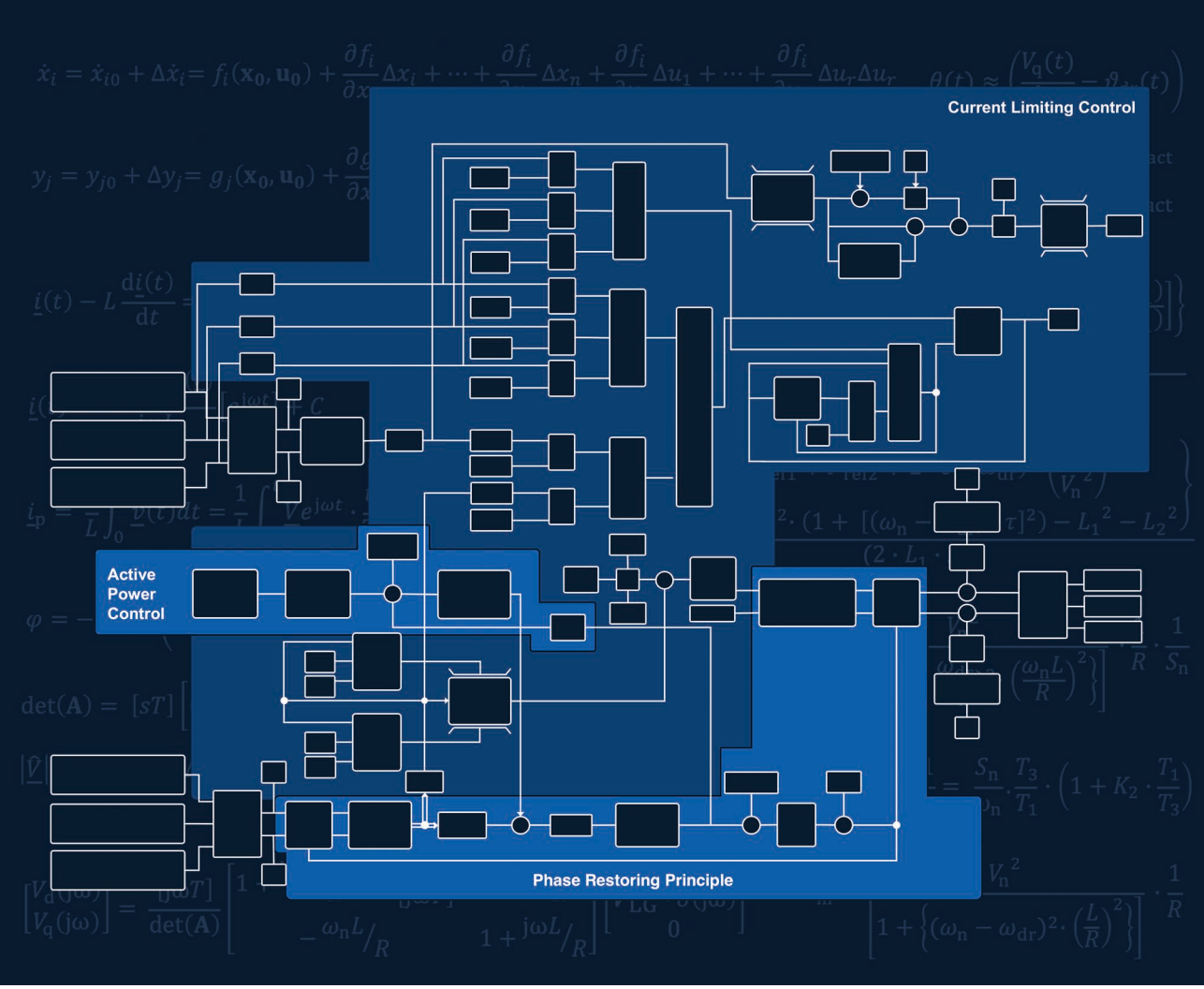

FAU Forschungen, Reihe B, Medizin, Naturwissenschaft, Technik 47

Ananya Kuri

A Grid-Forming Control Concept from Power System Perspective

FAU University Press

Ananya Kuri

A Grid-Forming Control Concept from Power System Perspective

FAU Forschungen, Reihe B
Medizin, Naturwissenschaft, Technik
Band 47

Herausgeber der Reihe:
Wissenschaftlicher Beirat der FAU University Press

Ananya Kuri

A Grid-Forming Control Concept from Power System Perspective

Erlangen
FAU University Press
2025

Bibliografische Information der Deutschen Nationalbibliothek:
Die Deutsche Nationalbibliothek verzeichnet diese Publikation in der Deutschen Nationalbibliografie; detaillierte bibliografische Daten sind im Internet über http://dnb.d-nb.de abrufbar.

Kontakt: Ananya Kuri, Friedrich-Alexander-Universität Erlangen-Nürnberg (ROR https://ror.org/00f7hpc57), ORCID: 0000-0002-8731-7208

Bitte zitieren als
Kuri, Ananya. 2025. *A Grid-Forming Control Concept from Power System Perspective.* FAU Forschungen, Reihe B, Medizin, Naturwissenschaft, Technik Band 47. Erlangen: FAU University Press. DOI: 10.25593/978-3-96147-823-1.

Der vollständige Inhalt des Buchs ist als PDF über OPEN FAU
der Friedrich-Alexander-Universität Erlangen-Nürnberg abrufbar:
https://open.fau.de/home

Verlag und Auslieferung:
FAU University Press, Universitätsstraße 4, 91054 Erlangen

Druck: docupoint GmbH

ISBN: 978-3-96147-822-4 (Druckausgabe)
eISBN: 978-3-96147-823-1 (Online-Ausgabe)
ISSN: 2198-8102
DOI: 10.25593/978-3-96147-823-1

A Grid-Forming Control Concept from Power System Perspective

Ein netzbildendes Regelungskonzept aus Sicht des elektrischen Energiesystems

Der Technischen Fakultät
der Friedrich-Alexander-Universität
Erlangen-Nürnberg

zur
Erlangung des Doktorgrades Dr.-Ing.

vorgelegt von

Ananya Kuri
aus Shillong, Indien

Als Dissertation genehmigt
von der Technischen Fakultät
der Friedrich-Alexander-Universität Erlangen-Nürnberg

Tag der mündlichen Prüfung:	07.02.2025
Gutachter/in:	Univ.-Prof. Dr.-Ing. Matthias Luther Univ.-Prof. Dr.-Ing. Dirk Westermann

Table of Contents

Acknowledgement

I am grateful to my doctoral supervisor and mentor, Univ.-Prof. Dr.-Ing. Matthias Luther, for the opportunity to work in his research group at the Institute of Electrical Energy Systems. His wise words went beyond technical topics and ingenious ideas. I will always treasure the precious advice and encouragement for my future career and personal life.

I am thankful to Univ.-Prof. Dr.-Ing. Dirk Westermann for reviewing my PhD thesis and to the other members of the examination committee, especially Univ.-Prof. Dr.-Ing. Johann Jäger, Univ.-Prof. Dr. Christoph Pflaum. It was a great pleasure and an honour for me to discuss my work with them. I also want to thank Univ.-Prof. Dr.-Ing. Thomas Dürbaum for his engaging discussions.

I am grateful to Dr. Rainer Zurowski, my advisor and guide. He tirelessly supported me during my research, even before I began my PhD. His encouragement and perspective have made this PhD possible, and I am indebted to him.

I want to express my deep gratitude and special appreciation to Dr.-Ing. Gert Mehlmann for his unwavering support, discussions, and advice. His willingness to engage in discussions, review my work, and patiently provide input has greatly enriched my work.

I am also thankful to my colleagues at the Institute of Electrical Energy Systems, especially Ilya Burlakin, Johannis Porst, Alexander Raab, Julian Richter, Michael Richter, Christian Scheibe and Timo Wagner, with whom I shared numerous moments of my time at FAU and continue to do so.

I would also like to thank Dr. Dirk Audring and Siemens PTI for supporting me and allowing me to pursue my PhD in parallel to working at Siemens PTI. The work cooperation and understanding were unparalleled.

My heartfelt gratitude must also go to my family, especially my late father, Nikhil Kuri, mother, Mita Kuri, father-in-law, Ajay Jasani, and husband, Devashish Jasani, without whom I would have never achieved this goal. Thank you for always being by my side, encouraging me, and convincing me not to give up, especially during the most challenging moments of this journey. Thank you for making it possible to realize my dream.

Erlangen, February 2025

Ananya Kuri

Kurzfassung

Die weltweit in elektrischen Energieversorgungssystemen zunehmende Anzahl von Umrichter-basierten Komponenten erhöht deren Bedeutung hinsichtlich der Bereitstellung von Systemdienstleistungen (SDL). Zur Aufrechterhaltung der Netzstabilität und Versorgungszuverlässigkeit müssen Umrichter-basierte Betriebsmittel zukünftig einige der bisher von Synchronmaschinen (SM) erbrachten SDL übernehmen. Die überwiegende Mehrheit der gegenwärtig installierten Umrichter verfügt über eine netzfolgende Regelung. Jedoch erfordert die Vision eines zu 100 % auf erneuerbaren Energien (EE) basierenden Systems die Fähigkeit, die Netzspannung und somit die Netzfrequenz ausschließlich mit Umrichtern zu bilden. Infolgedessen haben aktuelle Entwicklungen zu netzbildenden Regelungskonzepten geführt, um die Schnelligkeit und Flexibilität von leistungselektronischen Komponenten mit den stabilisierenden Eigenschaften von SM zu kombinieren. Um diesen Herausforderungen zukünftiger Energieversorgungssysteme zu begegnen, wurde im Rahmen dieser Dissertation eine neuartige netzbildende Umrichterregelung entwickelt, implementiert und validiert.

Insbesondere für Microgrids mit einem hohen Anteil an EE haben sich netzbildende Umrichter als praktikable Lösung zur Sicherung der Stabilität erwiesen. Das Grundverständnis für das Systemverhalten von großflächigen Energieversorgungssystemen mit netzbildenden Umrichtern befindet sich allerdings noch im Anfangsstadium. Dennoch haben weltweit Netzbetreiber und Verbände mit den Definitionen von Anforderungen an netzbildende Anlagen begonnen. Das Hauptaugenmerk liegt auf der schnellen Anpassung des Systemverhaltens, um die Regelungsstabilität aufrechtzuerhalten, die Wirk- und Blindleistung zu regeln sowie die Netzsynchronisation und Kompatibilität mit anderen Betriebsmitteln zu gewährleisten.

Um eine unterbrechungsfreie Unterstützung durch netzbildende Komponenten zu garantieren, müssen in allen Netzsituationen die Betriebsgrenzen der Umrichter eingehalten werden. Insbesondere die begrenzte Stromtragfähigkeit der Leistungshalbleiter ist hierbei eine maßgebende Kenngröße. Infolgedessen muss das Konzept eine Strombegrenzung beinhalten, die sowohl einen Beitrag zum Fehlerstrom als auch zur Aufrechterhaltung der Netzspannung leistet. Zusätzlich sind präzise Definitionen zur Bereitstellung von Systemdienstleistungen netzbildender Umrichter notwendig. Aufgrund der Freiheitsgrade beim Regelungsdesign ist es sinnvoll, die Perspektive von den Betriebsmitteln auf das Netz zu übertragen und die Regelungsanforderung aus Sicht der Netzstabilität zu definieren.

Im Rahmen der vorliegenden Arbeit werden Stabilitätsaspekte untersucht, die aus der Zunahme von Umrichter-basierten Betriebsmitteln resultieren und daraus ein neues Regelungskonzept für netzbildende Umrichter abgeleitet. Die Entwicklung der Regelung erfolgt in drei Phasen:

Zunächst wird das neue „Phase Restoring Principle“ (PRP) Regelungskonzept vorgestellt, dass die wesentliche Phasen-Frequenz Kohärenz in ausgedehnten Netzen gewährleistet. Dieses Konzept verzichtet auf eine Phasensynchronisation zugunsten einer neuartigen Winkeltransformation zur Bildung der Netzfrequenz. Hierbei kehrt die Netzfrequenz trotz fehlender überlagerter Regelung stets auf den Nominalwert zurück. Somit entspricht das Verhalten einem physikalischen Netzäquivalent mit einer hohen Trägheit, vergleichbar mit einer idealen Spannungsquelle. Außerdem ist die Reglerantwort frei von Schwingungen, wirkt dämpfend und erreicht auf direktem Wege stabile Arbeitspunkte. Somit wird das, beispielsweise von National Grid (UK) vorgeschlagene, Kriterium des „Limited-Vector-Shift“ berücksichtigt. Bei der Entwicklung der netzbildenden Regelung stellt das PRP die unterste Ebene in der Reglerhierarchie dar, auf der die überlagerten, langsameren Regler aufbauen. Diese Reglerhierarchie priorisiert Störungsverhalten vor Führungsverhalten.

Die stationären Arbeitspunkte des Systems werden mithilfe eines analytischen Ansatzes hergeleitet. Die Forderung von Existenz und Eindeutigkeit zulässiger Arbeitspunkte bedingen eine Einschränkung der Systemparameterbereiche. Die generalisierte Beschreibung des Kleinsignalverhaltens wird durch Linearisierung ermittelt. Unabhängig von Netzparametern und -topologie wird anschließend die globale Stabilität (einschließlich Netz und Regelung) analytisch bewiesen.

In der zweiten Phase wird das Konzept durch eine optimierte Wirkleistungsregelung erweitert, um den Verbundbetrieb mit anderen Erzeugungsanlagen bei beliebigem Wirkleistungseinsatz zu ermöglichen.

Unter Berücksichtigung der Kompensation der transienten Gleichstrom-komponente wird in der dritten Phase eine Strombegrenzung implementiert, die auf innovativen Regelungsansätzen wie Anti-Windup-Methoden basiert. Die netzbildenden Eigenschaften bleiben dennoch erhalten und es wird ein robustes Regelverhalten bei schwerwiegenden Fehlern erreicht.

Anschließend wird das Regelungskonzept und dessen drei Entwicklungsstufen in einem realistischen ohmsch-induktiven Testsystem sowohl analytisch als auch mithilfe numerischer Simulationen untersucht. Nach Erweiterung der PRP-Regelung kann für die betrachteten Fehlerszenarien ein robustes Reglerverhalten nachgewiesen werden. Darüber hinaus wird das PRP-Konzept mit etablierten netzbildenden Umrichtertopologien, Synchronmaschinen und idealen

Spannungsquellen verglichen. Hierbei werden das Regelungsverhalten und die Randbedingungen der Modellierung in verschiedenen Domänen (RMS, EMT) untersucht. Zusätzlich wird die Funktionsfähigkeit mithilfe eines Echtzeitsimulators im Rahmen eines Power-Hardware-in-the-Loop Prüfstandes demonstriert.

Die durchgeführten Untersuchungen belegen die Leistungsfähigkeit des PRP-Konzepts. Hierbei konnte die globale Stabilität unter Verwendung geeigneter Parameter nachgewiesen werden. Außerdem genügt das Reglerverhalten den Anforderungen zur Bereitstellung von Systemdienstleistungen und gewährt zusätzlich die Kompatibilität zu anderen Betriebsmitteln. Die gesamte Reglerstruktur besitzt Vorzüge gegenüber bestehenden netzbildenden Regelungen. Das im Rahmen der Arbeit entwickelte Konzept ist systemtechnisch ausgereift und eignet sich für den großflächigen praktischen Einsatz von netzbildenden Umrichtern in bestehenden und zukünftigen elektrischen Energieversorgungssystemen.

Abstract

The rising number of inverter-based resources (IBRs) deployed in power systems worldwide has led to redefining their roles with evolved service requirements. In the future, to maintain grid stability and reliability, IBRs will need to deliver some of the services synchronous machines still provide. Currently, almost all installed IBRs are grid-following, essentially following the system frequency and offering only a subset of benefits. However, envisioning a 100 % converter-operated system requires the ability of IBRs to participate in creating the grid voltage and, hence, the grid frequency. Thus, recent developments have led to Grid-Forming (GFM) controls, which combine power electronic equipment's speed and flexibility with synchronous machines' stabilizing characteristics. To tackle future power system challenges, a novel GFM converter control is conceptualized, implemented and validated as part of this dissertation.

GFM is well-established, particularly for microgrids and a necessary enabler for high integration of IBR-interfaced renewable resources with enhanced capability for stability. Understanding its impact on bulk power system is still in the early stages, but regulatory bodies have begun to define various tiers of requirements. The primary emphasis is on rapidly adjusting to system changes to maintain control stability, regulate active and reactive power, synchronize with the grid, and ensure compatibility with devices in the power system. Furthermore, to ensure uninterrupted support from the GFM resource during severe disturbances, it is required to characterize the converter operation during the current limiting mode. This mode is typically defined by a converter's hardware capability and the ability to transition in and out of this restricted range. Thus, the GFM control should achieve current magnitude limitation with fault current contribution, have recovery capability to protect the semiconductor devices and sustain the grid.

Additionally, the technological transition necessitates new definitions of system demands and services, concise explanations of main characteristics, and utilization of services offered by GFM in bulk power systems. Due to the flexibility in design offered by these IBR controls, it is prudent to change perspective from inverter requirements to evolving system needs to derive GFM capabilities.

In a broader context, GFM assures global stability of a power system. The objective of this thesis is to propose a control strategy for GFM converters

from a power system perspective that attains global stability. The control strategy is developed in three phases.

In Phase 1, a new concept called the 'Phase Restoring Principle' (PRP) is introduced, which preserves the essential phase-frequency relationship of voltage in extended power systems. PRP generates a nominal frequency via a novel angular transformation, ensuring exclusively phase-frequency stability. The power system frequency always returns to its nominal value with minimal order dynamics and no additional master control. Therefore, it presents a physical equivalence of an unlimited source and is analogous to an ideal slack. Further, the response is free of non-beneficial swing dynamics and attains the new operating point directly displaying the limited Vector Shift criteria proposed, for example, by National Grid (UK). PRP is the fundamental building block in developing the GFM control with slower control dynamics built over it. This concept prioritizes response to disturbances over response to setpoint changes from the control hierarchy.

The steady-state operating point, uniqueness, and boundary conditions of the system are derived analytically, as mandated by the *'Existence Theorem'*. The requirement of existence and uniqueness imposes a restriction on one parameter ratio of the overall system model. The generalized small-signal solution of the control principle is deduced and evidenced based on the linearization method. The proof of global stability of PRP is displayed based on the necessary boundary conditions and small-signal criteria indicating stable control behavior independent of variations in network parameters and topology (e.g., strong or weak grid).

Further, Phase 2 development addresses the need for steady-state active power limitation and relaxes the constant frequency response of PRP, though dynamic current overshoots are inherent. The Phase 1 control is enhanced with optimized active power control (APC). This allows the scheme to cooperate with other sources considering arbitrary active power dispatch via setpoints.

Finally, Phase 3 considers current limitation by adequate control of voltage magnitude. A current limiting control based on the voltage limiter concept with innovative usage of anti-windup methods is supplemented. The algorithm helps preserve the GFM properties while maintaining voltage source behavior and provides the best possible control response under severe faults.

The complete control concept and its three distinctive development stages are numerically investigated in a realistic ohmic-inductive test bench, and

power system stability is analyzed under various network configurations. Simulation results for each phase are presented to support the mathematical hypothesis and visualize the controller's response. The control scheme is extensively tested to ensure robustness under normal operating ranges, severe faults, and weak grid scenarios without other active sources (i.e., Short Circuit Ratio of zero). PRP responses are also compared with typical voltage sources and known GFM schemes. Investigation in both electromagnetic transients (EMT) and root mean square (RMS) simulation domains are conducted. The control scheme is further demonstrated and validated on a real-time simulator in a laboratory environment by adopting Power-Hardware-in-the-Loop test benches.

The above investigations reinforce the control performance, enabling interoperability with other converter controls and fulfilling ancillary service requirements. The complete control scheme retains global stability under a viable choice of parameters. The comprehensive development of the PRP control scheme reveals its capabilities and advantages against existing GFM schemes. The developed scheme is mature and viable for transfer to GFM field applications.

1 Introduction

This section presents the background and the motivation behind the work. A primer is first provided, discussing the necessity for investigating new converter control strategies enabling high-penetration of power electronics (PE). The essential grounds include technological leap, cost incurred due to inaction, impacts of high inverter-based resource (IBR) penetration, and the challenges arising due to the high share of renewables. Lastly, the outline of the thesis is reported, including the research proposal, the structure of the thesis and the publications related to the different sections.

1.1 Motivation for new converter strategies

The power system is undergoing unprecedented changes resulting in a shift in the power generation and transmission from the classical synchronous generator to IBR and DC-based transmission. Some of the services formerly provided by synchronous machines (SM), especially those inherent to rotating inertia and its accompanying frequency and voltage control mechanisms, are reduced or no longer available. Thus, the power system is transformed to low inertia and, hence, a weak grid. To tackle the challenges associated with the retirements of SMs, power system requirements previously served by SM will be reliant on IBRs with new and advanced functionalities.

Existing IBRs are primarily wind turbines, solar photovoltaic (PV) arrays, and batteries operating with state-of-the-art control concepts called Grid-Following (GFL), offering some benefits. The fundamental GFL IBR design assumption relies on a sufficient number of SMs in the grid to provide a relatively strong and stable voltage and frequency signal, which GFL IBRs can 'follow'. However, as grid strength declines, the power system is susceptible to transient voltage instability, impacting system dynamics and causing converter instability in the GFL IBRs. Thus, the power system stability and reliability will be significantly challenged by system development and operation in this future decarbonized grid. [1, 2]

The limitedly abled GFL controls need to be replaced by new advanced converter controls capable of supporting the grid voltage and frequency, thereby maintaining system stability. Additionally, envisioning a 100 % renewable-based system or a converter-operated system requires the ability of IBRs to become the primary support for stable grids. This lays the foundation of the concept of Grid-Forming (GFM) IBRs. GFM converters

have been widely researched. Several installed projects of GFM functions have successfully been tested and deployed in microgrids and are under commissioning in larger grids. A general understanding of GFM controls and their impact on bulk power system (BPS) performance is still in the early stages. Nonetheless, the technology shows significant promise [3–5].

1.1.1 Technological leap

Power systems around the globe are on the brink of making this technological leap. Analysis and findings of system conditions with high IBR proliferation show the benefits of GFM controls, and various equipment vendors have commercially available products that can provide GFM capability. While GFM converters still need to be examined and adjusted to specific system conditions (similar to GFL), they are expected to be advantageous compared to the GFL schemes. GFM converters play a critical role in contributing to the stability and reliability of the BPS under high IBR conditions ($> 75\ \% - 80\ \%$) [1, 6].

However, today, system operators (SOs), planners, asset owners, and manufacturers need assistance deploying advanced IBR controls. Procuring or mandating services from IBRs to serve system needs without thoroughly understanding their capabilities can be challenging. Hence, it may lead to operational constraints. Simultaneously, manufacturers are unable to incentivize the deployment of new advanced IBR controls due to a lack of precise technical specifications to serve system requirements. These challenges result in creating economic and deployment constraints. It is imperative that researchers, original equipment manufacturers (OEMs), SOs, and policymakers work jointly to develop requirements, norms, technologies, and commissioning mechanisms for this advanced technology that reflect evolving grid reliability needs. Identifying practical capabilities of equipment to address the conditions effectively is crucial. Thus, placing system requirements foremost, rather than equipment constraints, in defining the GFM capabilities is essential [5, 7, 8].

1.1.2 The cost of inaction

Failure to break from the conundrum of requirement and deployment may have far-reaching negative consequences, hindering the ability to meet energy transition targets and thus increasing the costs. The cost of inaction may be very high. Countries like Australia, Ireland, and the United Kingdom (UK) envision a 100 % renewable power system by 2025 [9], while the European Union target to achieve carbon neutrality by 2050 [10]. This

is feasible by solely depending on renewable energy as an electricity source, typically IBRs. Such a system would be volatile and operate on high instantaneous levels, ensuring system stability through sufficient GFM assets. IBR interconnection worldwide comprises hundreds of gigawatts (GW) with a high share of battery storage. With precise requirements and planning, a significant proportion of these battery storage resources could be equipped with GFM functionality today, avoiding the costs of installing much larger grid-supporting devices or additional grid reinforcements. A prime example of the preceding scenario is the project named '*Netzbooster*' (Grid Booster). It is a 250 MW battery-based GFM energy storage system supplied by Fluence Energy Inc. to the German Transmission System Operator (TSO) TransnetBW GmbH [11]. In contrast, customers will incur additional costs implementing GFL with additional reliability measures in the absence of precise requirements and market incentives [7].

1.1.3 Impact of high inverter-based resource penetration with system overviews

The power industry is learning from small and medium island systems with high penetrations of IBRs or GFM pilot projects. Based on these networks, challenges can be determined which aid in design strategies for large systems representing most of the world's power consumption. Stability risks manifesting in four types of power systems with high IBR penetration Broadly, the prime stability risks under high IBR share include frequency, voltage, angular and control stability [1]. The reasons are discussed for the four types of power system below and in depth in Section 2.4.

***Small Islands*:** Small permanent island system such as Hawaii is rapidly approaching a 100 % IBR proliferation level. As these islanded systems need to maintain stable operation without assistance and aid from neighboring grids, the key stability issues encountered include frequency sensitivity due to low inertia, leading to large Rate of Change of Frequency (RoCoF). Voltage instability due to voltage events, control-driven issues, and protection coordination are the prime challenges. Recent GFM-based battery development projects have shown promise, but unexpected behaviors are foreseen due to a lack of knowledge [1, 12, 13].

***Medium Islands**:* Medium island systems are in the GW range. As an example, Ireland includes very high wind generation shares with two HVDC interconnectors and has achieved 75 % IBR penetration. These medium-sized island systems experience voltage-induced frequency dips

due to wider-area low-voltage propagation during faults. Thus, causing more pressing frequency-related issues than voltage stability [14].

Large Islands: For large island systems in several GW range, stability concerns depend on the size of the largest contingency relative to the system size, geographic dispersion of IBRs, and distance between IBR generation and load centers. In tightly integrated large island systems such as Great Britain, inertia limits are implemented, and fast frequency response (FFR) is introduced due to frequency stability-related risks. In Texas (for political reasons, Texas operates its power grid as an island), mainland Australia, and remote parts of Great Britain, IBR generating units are located far from load centers. Hence, voltage stability and low system-strength concerns, result in weak interconnection in these IBR-dominated regions. Weak interconnections may split into several electrical islands, increasing complexity, and furthering the stability issues. Specific solutions have been implemented in these large islanded systems, including minimum inertia, introducing FFR products, GFL based IBR tuning, etc. However, better understanding and utilizing GFM devices' capabilities is paramount [1, 15, 16].

***Geographically interconnected systems*:** Large-scale power systems, such as the entire Continental Europe synchronous area, the Eastern and Western Interconnections in North America, and the national grid in China, are generally resilient. These systems are not expected to operate with 100 % IBR in the near future. However, issues pertaining to high IBR share may create challenges, especially in weaker and more localized grids leading to voltage and control stability issues.

One potential issue is the possibility of system separation or split scenarios dividing the interconnected grid during peak loadings. A prime incident was witnessed on 08 January 2021 at 14:05 Central European Time (CET). The Continental Synchronous Area in Europe was separated into two frequency areas (northwest and southeast areas) due to the tripping of several transmission network elements [17]. This results in power imbalances for each subsystem after the separation, resulting in rapid frequency excursions. Without effective countermeasures, frequency limits would be exceeded causing loss of generating units and, finally, leading to a system blackout. This is an increasing concern in Continental Europe under high cross-border trade and IBR penetration, and necessary precautions via GFM IBRs supplemented by FFR are underway. Another challenge for systems with heavily loaded transmission corridors is maintaining steady-state and dynamic voltage stability. The German TSOs

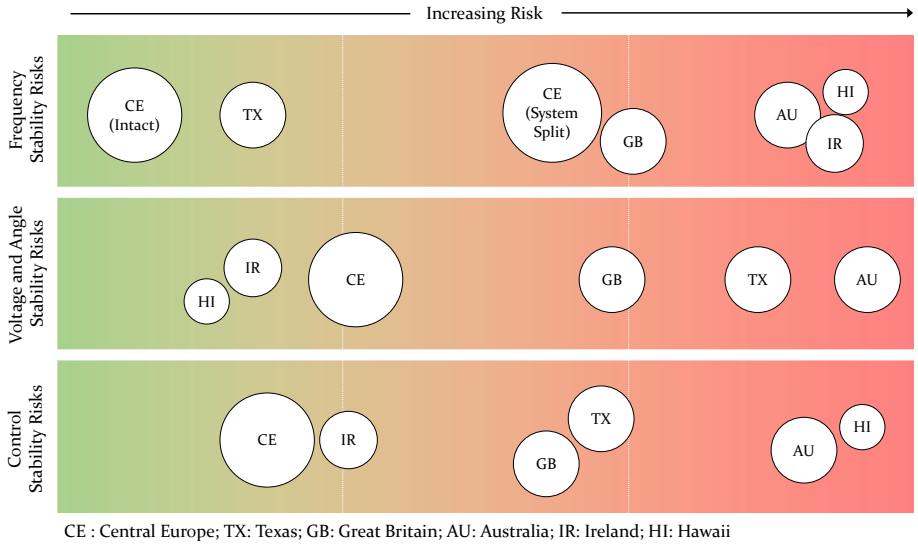

Figure 1.1: Stability risks identified in various power systems were published in November 2021 in article [1] (Figure is modified and adapted from [1]).

have identified solutions to this issue that may include Static Synchronous Compensators (STATCOMs), High Voltage Direct Current (HVDC) links, and GFM-capable technologies that can provide sufficient energy buffers during and after significant disturbances [1, 2, 18, 19].

Figure 1.1 provides an overview of the stability risks for the six exemplary power systems mentioned above in a qualitative manner. Here, the color denotes **red** as high risk, **yellow** as medium risk, and **green** as risk-free.

1.1.4 Arising issues to meet the future needs

On the rationale mentioned above, some of the issues which need addressing for a high share of IBRs are listed below [2, 7, 20–22]:

- **Methods and Depth of Modelling**: This comprises of an accurate representation of power electronic converters, their controls, limitations, and procedures of stability assessments in both time and frequency domain.
- **Control Stability**: This includes control interaction with the rest of the system (sub - and super - synchronous controller interaction) and the different control strategies pertaining to GFL and GFM.
- **Power System Stability**: It relates to a more holistic system concept of stability, studying impacts on all levels and time-scales,

including angle separation, frequency and voltage issues, frequency response, and increased RoCoF. Grid interconnection studies assist in understanding the stability issues related to IBRs connected to the grid, causing voltage fluctuations, frequency instability, and grid imbalances.

- **Power System Operation and Control**: The transition to IBR impacts system- and device-level operation and control. The requirements for the operation of future low-inertia grids need to be understood and considered.
- **Protection**: Protection coordination and sufficient short circuit current may also be challenging in future power systems unless addressed with modern and new protection philosophies.

1.2 Research proposal

Two main targets constitute the backbone of this thesis: firstly, discussing the concepts, definitions, and requirements for the deployment and understanding of GFM for a bulk power system. Secondly, a novel GFM control scheme developed from a power system perspective and its proof of concept.

Target I: Holistic GFM requirements in bulk power system

This target involves understanding the problem statement, outlining the requirements, and analyzing the potential of GFM converters in stabilizing a system with high penetration of IBR generation. As this technology is at its inception, precise requirements have yet to be uncovered. In designing services to meet needs, the flexibility of the converter can be exploited to a significant level. It is possible to create services based on the wide latitude of the converter's functionality and meet system obligations more effectively rather than mimicking the services offered by SMs or reusing known converter control concepts. Recognizing that there is no one-to-one mapping between service and needs is essential and is addressed by this work. Therefore, the aim is to achieve power system stability and rethink the design and services offered by the GFM for a bulk power system.

Given the centrality of equipment performance during disturbances, a core element of today's system planning and operation relies on accurate system studies using advanced power system modelling and simulation techniques. Modelling is a mathematical solution of a physical system, including an inevitable numerical error. Therefore, developing insights into the present institutional reality of modelling and analyzing system

dynamics is accented in the thesis's goal. In the evolution to systems with high levels of IBRs, with a complex mix of GFL and GFM IBR, there is an increasing need for electromagnetic transient (EMT) analysis in addition to phasor domain analysis to aid in design and evaluation of power systems. This work further highlights the structural limitations of phasor domain modelling and exemplifies its impairing stability analysis under high shares of IBRs. The potential issues related to implementing a GFM control algorithm are discussed, and a possible solution is proposed providing an overview of the advantages and challenges of this technology.

Target II: A proposal of a Grid-Forming control scheme

The second objective of this thesis is to develop a GFM control scheme that caters to the requirements and quality parameters outlined by Target I. The control development is carried out in three distinct phases, where each subsequent phase builds on the previous phase:

- **Phase 1** (PRP) focuses on development of the fundamental and novel building block called 'Phase Restoring Principle' (PRP).
- **Phase 2** (PRP + APC) supplements PRP with enhanced active power control for power dispatch capability.
- **Phase 3** (PRP + APC + CL) lastly, synthesizes a current limiting control compatible with the second phase.

The above notation is used to reference control development throughout the thesis. Obtaining a stable response from the cascaded control structure inherently prioritizes the response to disturbances over setpoint adaptations, an essential requirement highlighted in Target I for the GFM to stabilize the power system.

To ensure robustness and validity, every phase of development is mathematically analyzed and simulatively verified in both online and offline environments. The *'Existence Theorem'* is employed to assist in establishing the necessary and sufficient conditions for obtaining a stable operating point. According to the phenomena of interest, attaining small-signal stability between the GFM control scheme and power system interactions is among the goals of this thesis. Achieving global stability through the PRP scheme is a significant objective. This is performed by considering sufficient parametric conditions for operating points' existence and applying linearized theory for closed-loop small-signal analysis to prove PRP's stability independent of the variation of network parameters and loading. The investigations are focused on the boundary between root

mean square (RMS) and EMT domain, demonstrating similar results in positive sequence EMT. The positive sequence system of EMT domain (termed as averaged) is calculated by a moving average filter (i.e., sliding window discrete Fourier transform over one cycle) and matches the RMS results under nominal frequency condition in the network. Thus, accounting for the modelling details and analysis.

Thus, the two targets above encapsulate the issues of control stability, methods and depth of modelling, and analysis of IBRs. Control stability is one of the essential building blocks on which system stability and load dispatch rely.

1.3 Structure of the thesis

***Chapter 1*:** This chapter introduces the future power system trends and the research topic's motivation. It also provides an overview of the research proposal, thesis structure, and related publications.

***Chapter 2*:** This chapter outlines the foundational concepts and theory required for comprehending further chapters. State-of-the-art control principles and current limiting methodologies of GFM converters are discussed with the aim of a classification. The latest developments in the grid code and aspects of GFM control requirements are presented based on the power system perspective. Further, the modelling aspects of converters are derived considering the influence of time step on EMT and phasor domains numerical simulation, discretization of control, and digital simulation of analog systems.

***Chapter 3*:** The novel control scheme based on 'Phase Restoring Principle', fulfilling key system needs, outlined in Chapter 2, is introduced. The chapter is subdivided into sections based on the development phases of the PRP control, including a description and its corresponding analytical derivations. Sufficient existence, uniqueness, global stability, and boundedness conditions met by appropriate choice of network parameters are evidenced. The small-signal stability of the linearized closed-loop transfer function under the restriction of realistic large loads corresponding to small phase conditions is evidenced. Further, the general small-signal solution in the frequency domain with no load constraints is derived. The control extension with active power loops for arbitrary power dispatches is derived. The safety constraints of the power converter by augmenting a new current limiting control compatible with PRP is described.

***Chapter 4*:** This chapter provides simulative evidence of the analytical deductions obtained in Chapter 3. The simulations are performed with PSS®NETOMAC for the development of stability analysis under single and double converter topologies and loadings. Small-signal stability corroborating the analytical investigations is simulatively visualized. A plethora of simulation cases is conducted to describe the control's robustness under challenging network conditions such as weak grid and islanded scenario, low Short Circuit Ratio (SCR = 0), three-phase bolted faults, and small as well as large disturbances.

***Chapter 5*:** Unique characterization of the PRP control and performance with current control is presented and discussed in this chapter. The scheme is compared against voltage sources and other well-known GFM schemes. PRP at the functional level is contrasted against Phase-Locked Loop (PLL), whose destabilizing effects are described. The inertial response of PRP is illustrated and correlated to a slack or ideal machine. The fulfillment of most of the reported grid code requirements or desired features is related to PRP's attributes.

Chapter 6: This chapter presents a real-time demonstration of the PRP control scheme on a multi-converter test bench including Control- and Power-Hardware-in-the-Loop. The interaction of PRP control with real hardware and another GFM control scheme is validated.

Chapter 7: This section concludes the thesis by providing an outlook on possible future research topics.

The publications related to this thesis are reported in the Appendix and are assigned to the different chapters as given in Table A 7.

1.3.1 Preface adopted in this thesis

PRP is an offspring of the idea to map the phasor of RMS to the phasor in dq representation – averaged – in EMT domain viable in case of constant frequency condition. Therefore, at first, the mathematics described in this work is in the continuous or frequency domain (Laplace). However, the simulation model considers both RMS and EMT domain with discrete controller modelling especially in context with current limitation aspects.

Before evaluating the working principles of PRP, the novel building block, and its extensions applied to form the Phase 3 (PRP+APC+CL) GFM control, the following notions are adopted in this work:

- The benchmarked network model consists of an ohmic-inductive system reflecting the characteristic of the majority of power systems around the fundamental frequency.
- Under disturbance converters and machines are inductive in nature from a small-signal sense. Therefore, emphasis on the inductive characteristic of converters is placed.
- The control system operation is examined to achieve power-frequency stability under regular operating conditions.
- The investigation originated from investigations at the boundary between EMT and RMS domains. The RMS domain is understood to reflect positive sequence system quantities.
- The active sign convention is adopted as such generating unit has positive power flow, whereas loads have negative power flow.
- Circuit diagrams follow the passive sign convention with English voltage source orientation (conventional current flow).
- PRP assumes free energy exchange between AC and DC power systems (e.g., a battery or a capacitor bank).

2 Converter control requirements and modelling for renewable dominated networks

This chapter provides the foundation for understanding the technology of Grid-Following (GFL) and Grid-Forming (GFM) converters. The fundamental system needs must be met to maintain reliability and stability by comprehending the evolving power system's advanced modelling and simulation techniques. Section 2.1 discusses the classification of converter control based on system strength and their relevance in the bulk power system to achieve stability. The main distinguishing characteristic of GFM is its control scheme. Hence, this section scrutinizes and contrasts the state-of-the-art and upcoming schemes. The impact on stability and methodologies of current limitations on GFM are also presented as an integral part of converter control in Section 2.2. Recommended definitions, present-day grid codes, global experiences in formulating requirements, and characterization of GFM IBRs of some countries, are presented in Section 2.3. Additionally, an introduction to the concept of stability of a dynamic system with its implication under high IBR in the power system is discussed. An overview of the techniques adopted in evaluating the stability of GFM control for further chapters is supplied. Lastly, a general formulation of modelling and simulation of discrete control systems to thoroughly study grid stability in a high IBR-based future is discussed in Section 2.5. Simulation tools also need to evolve as the generation mix continues toward higher shares of control-driven IBRs (both GFL and GFM). While phasor domain simulations remain at the center of stability assessment, the increasing need to supplement models and studies with electromagnetic transient domain is also discussed. Section 2.6 summarizes the complete chapter. Terminology notations are available in Abbreviations & Symbols. Certain chapter sections are published in articles and conferences, such as J3, C1, C2, C3, C4, C5 and C13, cited in Table A 7.

2.1 Classification of converters based on control strategy

Two network limiting cases need to be addressed when designing the different control schemes for IBRs. The first is a strong power system better served by GFL, and the second is a weak grid scenario suited for GFM. Figure 2.1 (a) and (b) show typical GFL and GFM converter representations, respectively. There is no universally agreed definition of the industry's

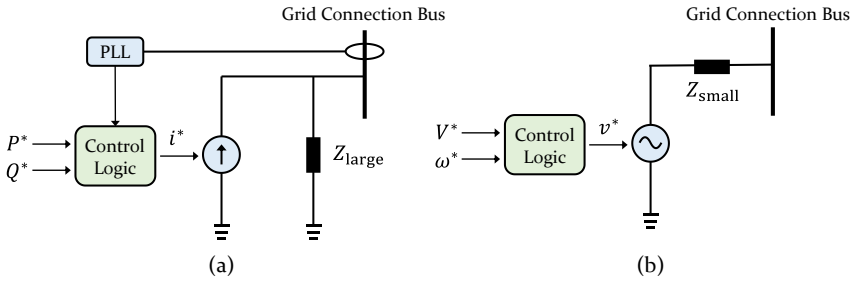

Figure 2.1: Simplified converter representation (a) Grid-Following (GFL); (b) Grid-Forming (GFM) (adapted from [5]).

recently coined terminologies of GFL and GFM. According to [7], the topology of a GFL converter unit may be approximated to a controlled current source with a high parallel impedance. In contrast, a GFM converter is represented via a voltage source with low series impedance.

In a strong power system, both active and reactive power controls are developed, which indirectly control frequency and voltage. This design is favorable for the state-of-the-art current control installed in the power system. The new term for this type of control is the GFL converter [21]. Current-controlled converters regulate the current injection into the power system based on the terminal voltage measurement and prioritize given power setpoints. Due to the setpoint approach, these converters inject power independent of voltage or frequency deviations at the terminal.

In case of a weak grid where voltage and frequency controls are developed, active and reactive power are at their limits and influenced indirectly. This serves as an advantageous design for voltage control. With increasing proliferation of IBRs, the future power system is transforming into a weak grid; hence, voltage control design, or GFM, is considered a future solution [23]. GFM converters consist of control approaches allowing the converter to directly control the terminal voltage and form the grid voltage purely by converters considering necessary reserve and storage [5, 24–27].

2.1.1 Grid-Following and associated issues

The present-day grid-connected converters worldwide are operated and controlled based on the mature technology called GFL. A GFL converter is designed to measure and follow the grid voltages and inject current to provide appropriate power; hence, known as GFL. Figure 2.2 presents an exemplary control structure. The active and reactive power injected by the GFL converter unit into the grid is regulated by controlling active and

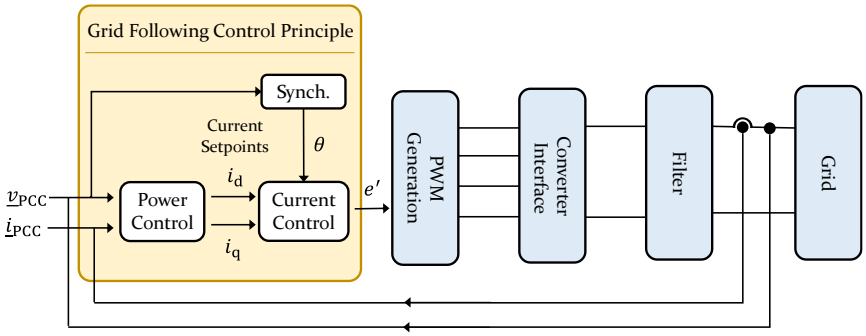

Figure 2.2: Exemplary control structure of a GFL converter (adapted from [28]).

reactive currents. The converter may entail additional outer loops to modify active and reactive current setpoints to regulate grid frequency and voltage at the Point of Common Coupling (PCC). The current setpoints are calculated with respect to the phasor at the fundamental frequency of the grid voltage. The injected currents are controlled to have a specific phase displacement to the grid voltage at the PCC. Therefore, a dedicated synchronization unit is necessary to estimate the magnitude and phase of the grid voltage. The commonly adopted solution uses a PLL or advanced and robust modifications of a PLL. PLL is an essential element for the GFL technology and is widely used for synchronization and tracking the system voltage waveform, typically at the PCC. When analyzing weak grid scenarios, the synchronization unit's dynamic response and the fast inner control loop need to be considered, as the converter dynamics affect the voltage at the PCC. This is due to the volatile voltage vector's magnitude and angle, and the voltage waveform may deviate from its balanced sinusoidal shape. Hence, synchronization is challenging and may not be precisely performed, leading to control instability. Thus, this fast-acting synchronizing function may lead to detrimental effects in weak grid scenarios and has been studied at length in various works [5, 24–27].

Therefore, the present-day control design based on PLL does not support or stabilize the power system but essentially emulates a current source. Furthermore, this control scheme is unable to deliver fast energy injection and is hence devoid of inertial response under disturbance. GFL based IBRs require a minimum system strength (SCR > 1 %) for stable operation and cannot be an initial black start resource. Both system strength and SCR are defined for reference in Appendix A1. Thus, it cannot operate a power system with 100 % GFL-based IBR penetration, and research community has perused the concept of GFM as an alternate robust IBR controller [5, 24–27].

2.1.2 Grid-Forming and its prospects

The concept of GFM converter technology has materialized to serve future power system needs by offering the speed and flexibility of PE equipment combined with the stabilizing characteristics of SMs. A typical control structure of a GFM converter, is described in Figure 2.3. A GFM control creates its internal reference based on the power flow of the converter instead of using the grid voltage to generate its reference for the control scheme. A GFM control scheme may operate without a PLL for synchronizing to the grid. Thus, a GFM converter operates analogous to a SM but is not identical to a machine [5, 24–27].

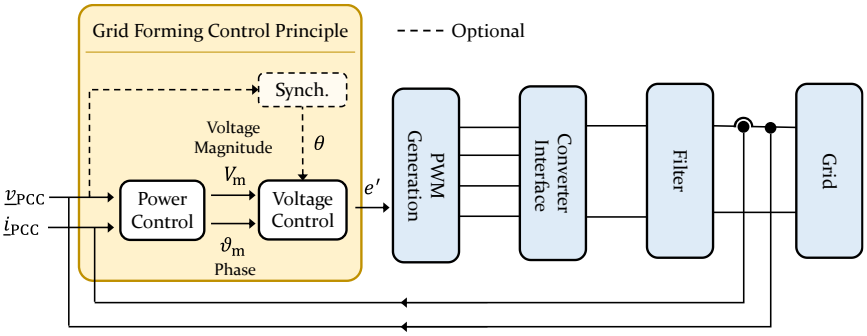

Figure 2.3: Exemplary control structure of a GFM converter (adapted from [28]).

Prevalent approaches for attaining stability in future grids imitate the machine's swing equation in PE converters and are termed 'Virtual Synchronous Machine' (VSM). VSM control is currently the most commonly used in GFM IBR pilots, primarily due to its similarity to SM behavior [7]. Other approaches include emulating droop-based and inertia characteristics of SM with GFM converters dependent on energy storage elements. Droop-based and its variants are another popular control scheme. Another emerging GFM control is the virtual oscillatory control, a decentralized control based on emulating dynamics of coupled nonlinear oscillators or 'Liénard-type oscillators' and machine matching control, combining aspects of primary and inner current control. The Siemens New Grid Access (NGA) technology for large offshore wind power plants implemented the GFM technology with a frequency-locked loop (FLL) for a robust solution. Recent GFM schemes have recognized PLL's drawbacks and considered direct power control variants based on instantaneous power theory as a possible concept but yet to be implemented. The key distinction of these schemes lies in their active power control loops and synchronization technique [1, 7, 21, 29–33].

Table 2.1 presents the fundamental differences between GFL and GFM converter and control schemes [27, 31, 33, 34]. The following sections provides an overview into some of the popular GFM methodologies.

Table 2.1: Duality of GFL and GFM converters [27, 31, 33, 34].

Attributes	GFL	GFM
External performance	Current source	Voltage source
Type of applicable grid	Strong	Weak or island operation
Black-start capability	No	Yes
Standalone operation	No, dependent on other resources and provides only grid support	Yes
Dynamic performance	Control IBR current magnitude and phase angle	Control IBR terminal voltage magnitude and angle or frequency
Synchronization mechanism	PLL or equivalent is mandatory	PLL or equivalent is optional
Functional behavior	Lack of inertial response	Fast energy injection in the inertial timeframe

2.1.2.1 Droop control

The Droop control concept is based on a reactance-dominated transmission system frequency and voltage droop characteristics. The control structures regulate the active and reactive power by simulating traditional SMs' P/f and Q/V droop characteristics. It is widely used to enable load sharing in distributed generation (DG) networks with parallel connected converters due to an easy implementation. It does not rely on communication links between the converters. It is the most straightforward implementation of a machine's equation, disregarding the smoothing time constant. It is one of the most widely used methods of GFM control and is used in nearly all experimentally implemented microgrids [35]. The governing droop equations are derived using the expression for the transmitted apparent power over a transmission line and are given in (2.1) and (2.2) where, ω is angular frequency and V stands for voltage. The measured active and reactive power are denoted with P_{meas} and Q_{meas}, while k_{p} and k_{q} are frequency and voltage droop coefficients respectively. The quantities P_{ref}, Q_{ref}, ω_{ref} and V_{ref} indicate reference values. Figure 2.4 illustrates a basic method to acquire phase synchronization [32, 36].

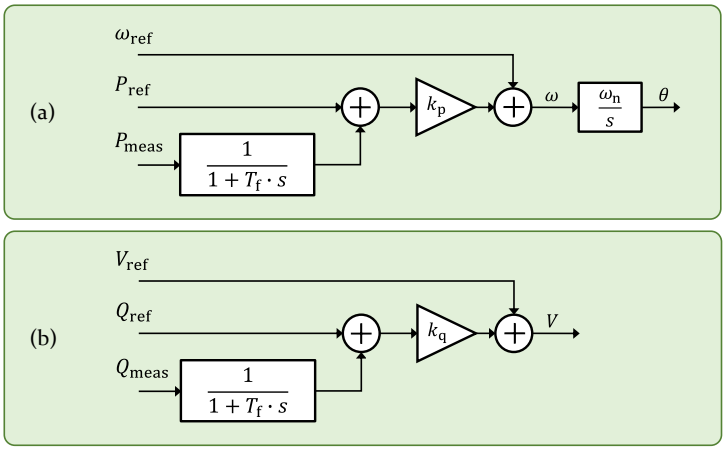

Figure 2.4: General control scheme for the droop-based control (a) active power loop; (b) reactive power loop (adapted and modified from [36]).

$$\omega = \omega_{ref} - k_p(P_{meas} - P_{ref}) \tag{2.1}$$

$$V = V_{ref} - k_q(Q_{meas} - Q_{ref}) \tag{2.2}$$

This control structure obtains θ through frequency estimation based on active power output, thereby disregarding a PLL in its control structure and providing an inertial response similar to SMs. The block diagram in Figure 2.4 shows that the measured active and reactive power is passed through the low-pass filter to discard the measurement noises and stabilize the control loops. However, higher values of the droop coefficients result in better power-sharing with degraded voltage regulation. This scheme has a slow transient response and is unable to handle smooth load sharing between parallel-connected converters in the case of nonlinear loads [32, 34, 37–39].

2.1.2.2 Virtual Synchronous Machine (VSM) control

The 'Virtual Synchronous Machine' (VSM), also known as VISMA, was initially introduced by Beck and Hesse in 2007 [37, 40]. The approach is based on emulating the machine swing dynamics, which yields the inertial response and creates a voltage phase angle as a reference. Thus, this concept does not require a PLL to be synchronized with the grid. Multiple control algorithms have been proposed, which primarily differ in the depth of emulation, amount of additional current, and voltage control and may include a PLL for enhanced stabilization. However, they all include some form of the swing equation. The second-order swing equation emulation

can be approximated to represent a VSM. The inertial dynamics of a VSM is described below in the Laplace domain:

$$T_{\mathrm{a}} \cdot s \cdot \omega_{\mathrm{VSM}} \approx P_{\mathrm{ref}} - P_{\mathrm{e}} - k_{\mathrm{d}}(\omega_{\mathrm{VSM}} - \omega_{\mathrm{ref}}) \tag{2.3}$$

where, $(T_{\mathrm{a}} = 2H)$ is the mechanical time constant representing rotor inertia, ω_{ref} is rotational grid frequency, ω_{VSM} is the rotating speed of VSM, P_{ref} and P_{e} represent the reference active power and electrical power output, respectively, and an additional damping coefficient k_{d} is defined. The resulting control structure is depicted in Figure 2.5. VSM is currently the most commonly used control scheme in GFM IBR pilot projects primarily due to its resemblance to the synchronous machine [7].

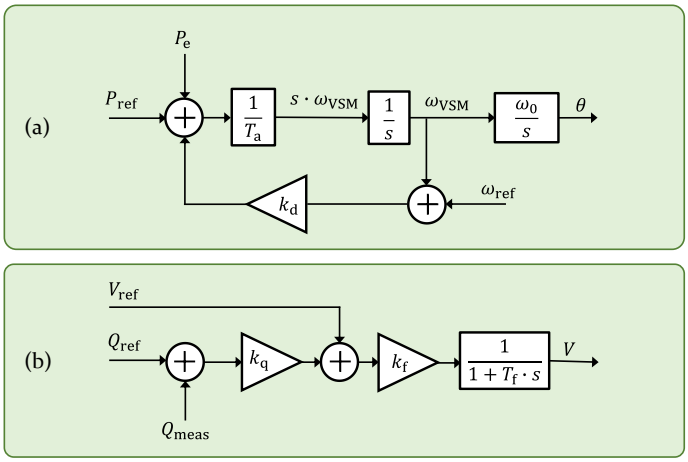

Figure 2.5: General control scheme for the Virtual Synchronous Machine (VSM) control (a) Active power loop; (b) Reactive power loop (adapted and modified from [37]).

A comparison between Droop control and VSM control performed in [37], revealed striking similarities. An equivalence between the two control strategies is derived in [37]. The VSM control features better damping, lower overshoot, and better frequency stability due to larger inertia compared to Droop control which is of interest in low inertia systems such as microgrids. However, due to the swing dynamics the output active power of VSM is more oscillatory creating challenges in coordination of VSMs, SMs and other GFM based control schemes [32, 34, 37–39]. Additionally, it is anticipated that this 'machine-like' behavior could result into oscillations between devices, mimicking electromechanical instabilities [1].

2.1.2.3 Other upcoming control concepts

A few recent concepts are described below with illustrations in Figure 2.6.

Siemens New Grid Access (NGA) (2015) was one of the early GFM control approach developed by Siemens AG for the New Grid Access (NGA) project, which utilizes offshore AC to HVDC conversion by diode rectifiers and a high-performance voltage source converter (VSC) located onshore. This GFM control strategy was robust and based on advanced approaches with FLL implementation. As depicted in the vector diagram (Figure 2.6 (a)), two dynamically coupled control quantities act on the phase:

- $\vartheta(f)$ is the contribution of the frequency controller to the total angle of the converter output voltage, and
- $\vartheta(P)$ contributes to the active power controller providing an operating point to the total angle.

The NGA project helped develop some key insights into the weak grids and evolving power system. It was established that conventional current control would not support the ability to operate the wind turbine generators (WTGs) with diode rectifiers due to the inherent discontinuous change in the mode of operation and being connected to weak grids. The standard synchronization method utilizes a PLL or FLL, where an FLL is a more robust solution [41]. A key insight gained was frequency detection had to be the fastest and a weak coupling existed between reactive power and frequency, hinting at the impedance characteristic of the power system. It generated frequency and stable operation. Though NGA considered a ring bus configuration, it was not investigated for an extended power system with varying parameters and topology [21, 42–44].

Virtual Oscillator Control (VOC) (2019) is a control concept proposed to output voltage phasors by simulating the dynamic properties of limit cycle oscillators, such as dead-zone oscillators and Van der Pol oscillators. It is a sinusoidal time-domain implementation that uses only the output current of the converter as input and can respond to instantaneous current changes without voltage measurement, power calculation, or power filters. A pictorial representation is shown in Figure 2.6 (b). Based on phasor representation, VOC controls cause the IBR to act as a nonlinear oscillator with a dead zone. It has been successfully applied to several microgrid networks [7, 29, 34, 38, 39].

Matching control (2020) mimics the behavior of a synchronous machine by emulating the back-end DC side of a converter, where the current flow

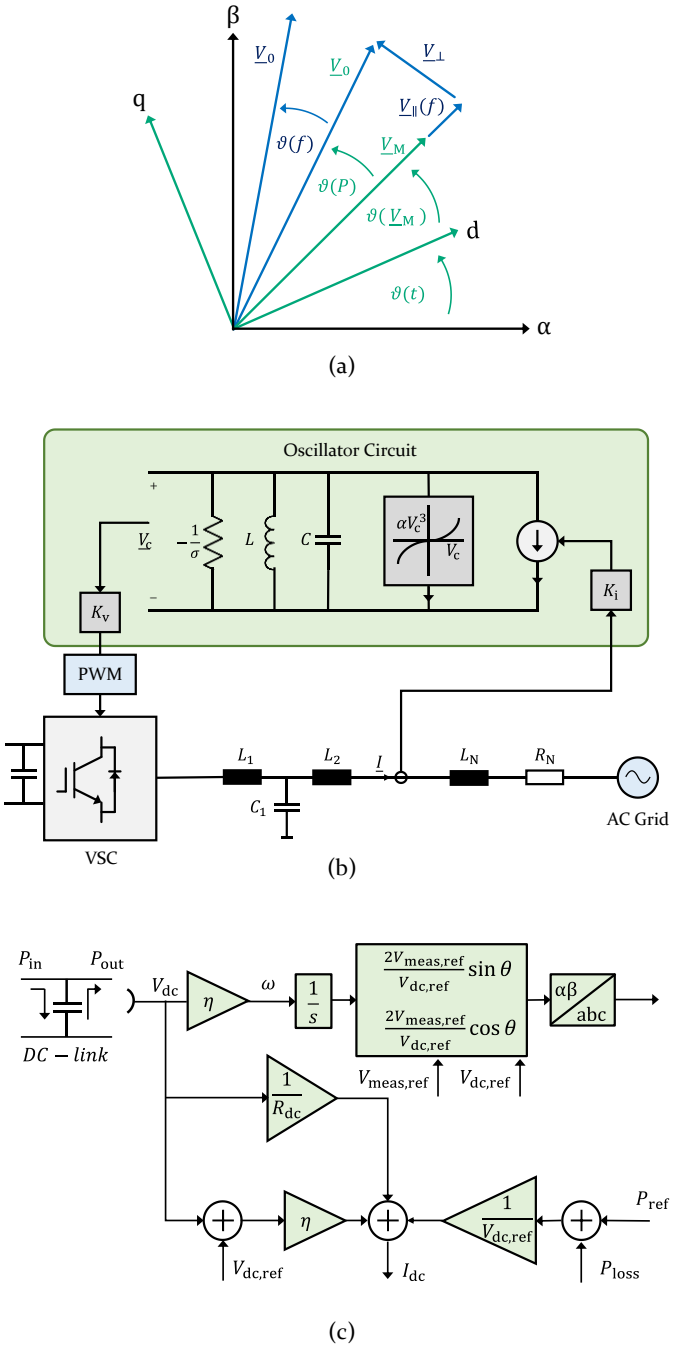

Figure 2.6: Upcoming GFM concepts – (a) Siemens New Grid Access (NGA) [43]; (b) Virtual Oscillator Control (VOC) [34]; (c) Matching control [45]

through the DC bus is controlled by using the energy transfer relationships between capacitor and inductor elements. It is an emerging control technique that aims at creating a coupling between the frequency and active power balance by achieving a crucial coupling between the DC-side voltage and the AC-side frequency. It is a very new concept under development and shown in Figure 2.6 (c) [7, 29, 34, 38, 39, 45].

The above discussed GFM controls operate with the underlying principle of an operating point's existence without focusing on generating a constant frequency and achieving global stability [29]. The existing concepts are realized from a controlled source perspective and not based on power system dynamics. Hence, a gap exists to address the GFM control requirements to obtain a stable operation starting from a system needs perspective [7]. This opens a large window of research, development of control concepts, and converter requirements to be established for GFM.

2.2 Current limiting control concepts for Grid-Forming under symmetrical disturbances

The GFM control concepts are required to operate during normal and disturbance conditions. The converter's short-circuit capability is a fundamental distinction between a GFM converter and a synchronous machine during faults. During an overcurrent event, a synchronous machine provides the maximum current available from the alternator. During the first six cycles following the event, the generator is limited by sub-transient reactance ($x_d'' \geq 0.12\ \text{per} - \text{unit}$ for a 50 Hz system) and excitation generated from the voltage regulator [46, 47].

The GFM control concepts describe the behavioral response, which needs to be overlayered with hardware constraints to create a meaningful and pragmatic reaction. The GFM converters modelled as voltage sources result in their output currents being dependent on external system conditions. In case of a large disturbance, such as voltage drops or phase jumps at the PCC [16], a SM usually injects fault currents or overcurrent, generally in the range of 3–7 per-unit (pu) [46, 48, 49]. In contrast, present-day semiconductor-based converter-interfaced sources are typically limited by their trip levels at approximately 1.2–2 pu overcurrent at its nominal rating due to economic considerations. [48, 50–53]. Hence, unlike SMs, which can tolerate overcurrent for a particular duration, the converter has a rigid current limit to avoid overcurrent damage and thus prevent maintaining the voltage profile in regular operation [50]. To successfully ride through the disturbances, appropriate current limiting methodologies are required

to be implemented in the GFM schemes, satisfying the following requirements [50, 54–57]:

- Current magnitude limitation: The phase current magnitude of the GFM converter should be below the maximum allowable limit to protect the power semiconductor devices and avoid disconnection.
- Fault current contribution: The GFM converter is required to supply active and reactive currents to support the network during disturbances.
- Fault recovery capability: The GFM converter should be capable of restoring to normal operation once the fault is cleared.

Figure 2.7 shows a basic circuit model of a grid-tied GFM converter with internal voltage $\underline{v}_e = E e^{j\theta}$, instantaneous measured PCC voltages ($\underline{v}_{PCC}$), an inductive coupling reactance X_C and an inductive transformer reactance X_T (disregarding resistive part). Using *Kirchhoff's law*, the phase current magnitude (I) is calculated as displayed in (2.4) in pu and $\underline{i}$ denotes independent phase output current [50] .

$$I = |\underline{i}| = \frac{|\underline{v}_e - \underline{v}_{PCC}|}{|X_C + X_T|} \tag{2.4}$$

Due to a disturbance event, the current I may exceed its allowed threshold of the GFM converter. The literature reports various current limiting control methods for GFM converters to meet the above requirements under large disturbances. The broad classifications are namely current limiter, virtual impedance, and voltage limiter. A brief discussion is as follows:

Current limiter: The current limiter method aims to switch the control structure to a GFL structure during the fault, resulting in a current source behavior of the converter during overcurrent conditions. Thereby, the procedure facilitates the regulation of the output current vector angle to

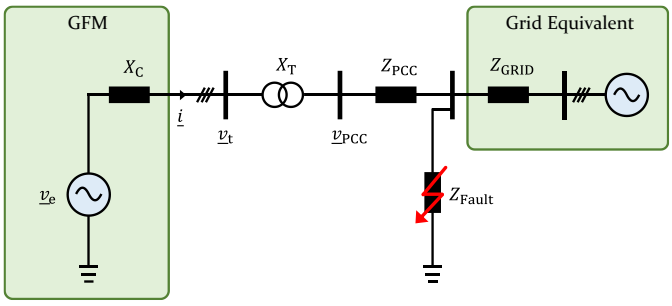

Figure 2.7: Simplified circuit of GFM converter under fault (based on [50]).

meet the fault current contribution requirement. GFM control restricts the phase current magnitude within the maximum allowed value through the closed-loop current control [58–60].

Three variants of current limiters are commonly utilized for GFM converters: the instantaneous limiter, the magnitude limiter, and the priority-based limiter. All these three current limiters achieve satisfactory current magnitude (I) limitations under severe disturbances, however, resulting in temporary transient overcurrent caused by the current control loop dynamics. In addition to the current magnitude limitation, these limiter strategies generally have difficulties meeting the fault current contribution objective required by grid codes. Thus, the GFM converter control switches the control structure to the GFL mode during the fault [54, 61, 62]. This solution requires a backup PLL for the synchronization, resulting in small-signal or transient instability issues under weak grid conditions [41, 55, 63]. The converter's robust GFM properties are lost due to the switching to a GFL structure during faults making it less attractive. An alternative solution has been discussed in [55, 64, 65] that bypasses switching of the synchronization methods to adjust the active and reactive power references based on grid codes, which are further tracked by power control loops to achieve fault current contribution goal [66]. This scheme may fail to recover due to windup of voltage controllers [50, 55, 67].

Virtual impedance: Virtual impedance has been suggested for numerous applications, such as damping, mitigating the impact of unequal or resistive line impedances, and current limitations. Compared to the previous limitation method, this technique maintains the voltage source behavior of the GFM converter to some extent during severe faults. Virtual impedance is used to increase the inverter's output impedance during transients and thereby limit the current. Considering Figure 2.7, a virtual impedance (R_v and X_v) is added to the voltage reference generated by outer-loop control, when the phase current magnitude (I) exceeds a given threshold. The GFM control adjusts the phase current magnitude by increasing the total impedance ($|X_\mathrm{C} + X_\mathrm{T}|$), including coupling with filter impedance and transformer impedance, based on virtual impedance or admittance methods [68–71]. The virtual impedance method requires a derivative controller to achieve a virtual inductor. In contrast, the virtual admittance technique represents a more practical approach for modifying the output impedance without performing the derivative of measured currents [71].

The virtual impedance method directly modifies the voltage reference, while the virtual admittance method with a fast-tracking current control

loop achieves good current limitation performance in case of severe faults. The method includes a high dependence on control parameter selection. Thus, a proper design of the X/R ratio is thus needed to meet the fault current contribution requirement. It has been demonstrated that the converter unit's power control and sharing performance are highly improved with the appropriate design and implementation of the virtual impedance control. However, this method may introduce current distortions and adversely affect the system's stability and dynamics if poorly designed or implemented [50, 55, 69, 70, 72]. The virtual impedance structure on the current limitation largely relies on the fault location and the selected virtual impedance, which may limit its usefulness in practice as the maximum converter current is desired to be utilized during any fault condition. Hence, the virtual impedance concept may cause problems in parallel operation [55, 73].

Voltage limiter: Similar to the virtual impedance methods, voltage limiters can maintain the voltage source behavior of the GFM converter to a certain degree under severe disturbances, allowing for automatic fault recovery. GFM control regulates the phase current magnitude (I) by reducing the voltage difference between the internal voltage reference and its terminal via voltage limiters [62, 74, 75]. It aims to reduce the voltage difference below the threshold defined by the product of equivalent output impedance (X_C) and maximum allowed current magnitude. As a result, the voltage reference generated by the outer-loop control is modified to realize the current magnitude limitation. This method is advocated in the UK grid code [16], since it does not mandate an adaptive virtual impedance which may destabilize the system under certain network conditions. Considering Figure 2.7, the implementation of the voltage limiter is usually achieved by regulating voltage magnitude (E) and phase angle (θ) generated by the outer-loop control. This type of voltage limiter, similar to the previous methods, is implemented without the converter output current's magnitude and angle information. However, additional information on phase angle θ_t and magnitude V_t, which are a part of the three-phase terminal voltage $\underline{v}_t$, is required as implemented in [74, 75]. Another variant of the voltage limiter is directly designed in the abc-frame, limiting each phase current based on the calculated voltage limits as in [76] and [77]. In [67], a voltage limiter method is proposed and a procedure for selecting the limitation value corresponding to the current limit value under different grid states and grid code requirements.

A detailed comparison of the three concepts has been documented in [50] and the key findings of each scheme is displayed in Table 2.2.

Table 2.2: Comparison of performance of different current limiting control methods under symmetrical disturbances (adapted from [50]).

	Current limitation performance	**Fault current controllability**	**Fault recovery capability**
Current limiter	• Effective under steady-state • Temporary overcurrent in transients exists	• Switch to PLL-based GFL and adjust current references • Adjust power references	• May fail to recover due to the windup of voltage controllers
Virtual impedance	• Compromise between current limitation and stability • Temporary overcurrent in transients exists	• Dependent on virtual impedance and electrical network parameters • Adjust power references	• Restoration under normal operation automatically achieved
Voltage limiter	• Effective under steady-state • Temporary overcurrent in transient exists	• Depend on the voltage limiter and electrical network parameters	• Restoration under normal operation automatically achieved

2.3 System needs and grid code requirements for Grid-Forming converters

In a system where most or all resources are converter based, there is an opportunity to rethink the grid services designed to support system stability and reliability. Predominantly, IBRs include switched passive circuit intrinsic behavior, and their overall performance is dictated by the control systems. Hence, there is a degree of freedom in the design of the IBR's control systems, considering hardware limitations. GFM converter technology is gaining momentum and speedy deployment because of its superior performance during system disturbances. The key attributes, benefits, and risks of this new converter technology need to be determined to achieve precise implementation and integration to provide reliability to the bulk power system [7, 21, 78–80].

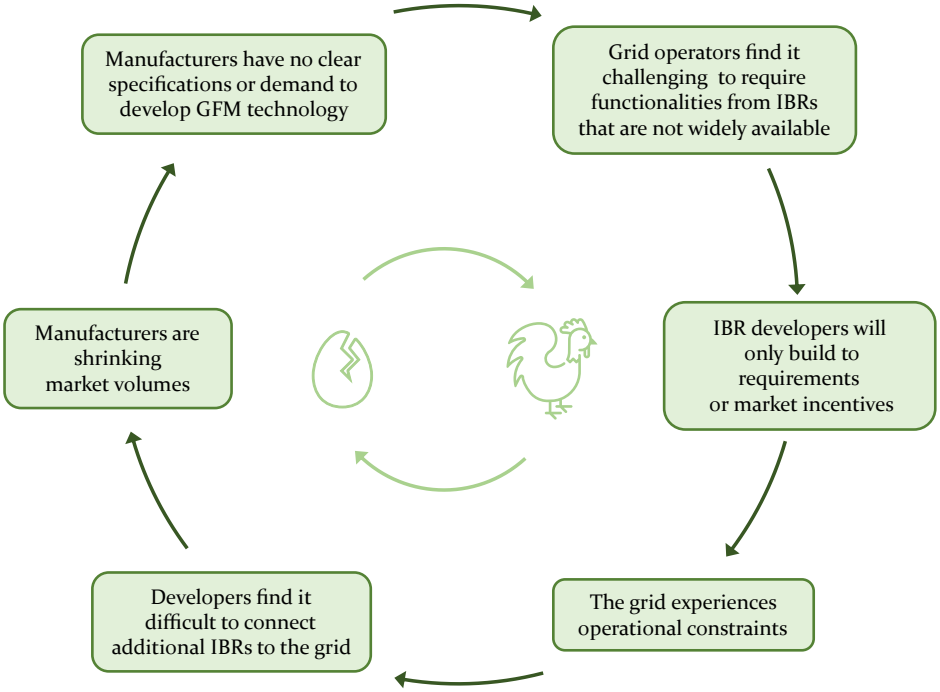

Figure 2.8: The circular problem of requirements and deployment of advanced IBR controls (adapted from [7]).

System operators, planners, equipment owners, and manufacturers face a chicken-and-egg analogy for deploying this new advanced IBR control. Defining the chronological order of the requirement for a capability or the capability itself for GFM necessitates assistance in making an informed decision. Figure 2.8 provides a pictorial illustration of the analogy.

The 'High Share of Inverter-Based Generation Task Force 2022' in their report addresses this issue [7]. It discusses the transition's main challenges, argues for the need of new definitions of system demands and services, provides concise explanations about the main characteristics of GFM converters and discusses ways to utilize the unique services offered by them. It further emphasizes 'breaking the cycle, starting from a system needs perspective', implying that the definition of the GFM capability and its requirements are based on the perspective of the evolving system obligations. Thus, fortifying the preceding sentences.

The system needs may be categorized under three main requirements as follows [1, 7, 80]:

1. Stability and Power Quality include four key aspects:
    - Synchronization and angle stability: All generation sources need to be synchronized and maintain synchronism during faults.
    - Frequency regulation: System frequency should be maintained close to the nominal value and must be limited and corrected following an event.
    - Voltage regulation: Voltage magnitude must be held close to nominal, and recovery from adverse events need to be mitigated to maintain desired voltage quality.
    - Damping: Oscillatory modes need to be positively damped and settled.
2. Continuity of Service and Safety describes the following:
    - Protection: Faulty network equipment and resources must be detected and selectively isolated safely and promptly.
    - Restoration: System service must be restored after a partial or system-wide loss of service.
3. Resource Adequacy comprises of:
    - Capacity: Sufficient capacity needs to be installed and made available to serve immediate demands and ensure the security of supply.
    - Energy: Adequate energy must always be available to serve demands continuously.

Based on the points mentioned above, some system operators have begun defining specific requirements of GFM in their network codes, mapping the presented key aspects. Great Britain and Australia are the forerunners in modifying grid codes to add requirements for GFM IBRs and HVDC systems, ensuring numerous options for increasing system strength for stable and reliable operation with high penetration of IBRs [31]. In comparison, discussions in Germany focus on the fast reaction of IBR aiding in system frequency regulation and inclusion of renewable energy sources (RES) in the grid restoration process after a black-out or system split scenario [7, 21]. The GFM-based IBR expected functions, capabilities, impacts, and specification requirements for grid code to the future high IBR penetration grid based on regional activities are summarized next.

2.3.1 Great Britain

Great Britain's transmission system operator, National Grid Electricity System Operator (NGESO), has been very proactive in defining the GFM requirements and capabilities for its integration into the power system. NGESO has listed the expected non-mandatory performance requirements for GFM capability and launched a series of competitive tenders to procure new system services needed with the changing generation mix in the power system. As a first step toward developing technical requirements for GFM technology, NGESO published a proposed grid code change GC0137 to the NGESO Grid Code. GC0137 identified several critical features of GFM capability that form the basis for a GFM IBR providing the same performance as that traditionally provided by synchronous machines in terms of supporting the grid during disturbances. It also addresses this upcoming technology's simulation compliance, models, and testing requirements. Some of the essential requirements of GFM IBRs as of August 2021 are listed below [16] :

- Limit the RoCoF after sudden loss of generation or load
- Inject instantaneous active power at the time of a fault as a result of corresponding phase change
- Inject instantaneous fault current at the time of a fault as a result of corresponding voltage change
- Contribute to the damping of power oscillations
- Limit Vector Shift
- Contribute to synchronizing torque
- Contribute to maintaining an improved voltage profile during disturbed conditions (a fundamental prerequisite for fault ride-through for all resources)

The intent was to keep the grid code requirements at a higher level while continually updating the best practice guide as more operational experience is gained with GFM technology onset. Key definitions of 'Grid-Forming Capability', 'RoCoF Response Power', 'Phase Jump Active Power', 'Damping Active Power', 'Control Based', and 'Control Based Real Droop Power' are available in [16], while '*Vector Shift*' (VS) is referenced in [81]. Additionally, prior to the commissioning of the GFM facility, a dynamic RMS and an EMT model providing a true and accurate reflection of the facility's grid gorming capability needs to be submitted to NGESO, as a part

of the grid code requirement. A recently coined terminology called phasor-domain transient (PDT as per [14]) is the recommend synonym for RMS domain. Greater details regarding models and tool domain requirements are covered in sub-section 2.5 [14, 16, 30, 82–84].

2.3.2 ENTSO-E and German activities

To define GFM capabilities for IBRs, a joint effort among the various European stakeholders resulted in the technical report by European Network of Transmission System Operators or ENTSO-E titled 'High Penetration of Power Electronic Interfaced Power Sources and the Potential Contribution of Grid-Forming Converters' (*ENTSO-E, 2020*). The report elaborates on the potential contribution of GFM converters to enable a secure power system operation with IBR-dominated generation. The report highlights the following seven system obligations with a high proliferation of IBRs:

- Creating or forming the system voltage
- System fault level (short-circuit power)
- Contributing to system inertia (limited by energy storage capacity and available power rating of the IBRs)
- System survival to enable the effective operation of low-frequency demand disconnection for rare system splits
- Sink for harmonics and inter-harmonics in system voltage
- Sink for unbalance in system voltage
- Preventing adverse control system interactions

The technical report by ENTSO-E suggestions at the advanced capabilities of IBRs, ensuring stable response under normal, disturbed, and emergency states with 100 % Converter Operated Power System (COPS). It also outlines several issues concerning this new technology and its implementation with follow-up work [7, 21, 85–87].

The German VDE|FNN guideline: 'Grid forming behaviour of HVDC systems and DC-connected PPMs' [88], the supplement to standard *VDE-AR-N-413*, presents technical details for dynamic frequency-active power performance and voltage control of GFM-based IBRs. It is a national-level implementation of the European network code [89]. It outlines verification test criteria adapted specifically for GFM voltage source converter with modular multilevel converter (VSC-MMC) HVDC technology. The

guideline defines system-level requirements, emphasizing on system split scenarios, maximum permissible RoCoF, minimum inertia conditions, and fault scenarios, ensuring controller robustness and stability. Lastly, the guideline outlines verification and test scenarios to validate the overall performance of GFM IBRs. Both European and German grid codes resonate similar requirements at this stage [7, 21, 88, 90].

Additionally a British-German joint work of the two research projects namely '*Battery-VSM*' and '*VerbundnetzStabil*', recently concluded and the recommended GFM findings, similar to VDE|FNN guidelines and are accessible at [91]. An important outcome was the four recommended criteria as requirements of GFM-based IBR listed below [82, 90, 92–96]:

1. **Voltage Source Properties**: Demonstrate stable operation in grid-tie mode, load sharing with other sources.
2. **Power Quality**: Passive, damped response of voltage harmonics and asymmetries.
3. **Inertial Response**: An instantaneous short-term transfer of active power during the dynamic frequency changes in the system with damping influences.
4. **Overload and Grid Faults**: Contribute to system demands in case of overload and grid fault where the converter's physical current and power limits exceed.

2.3.3 Australia

Australia is one of the leading countries in deploying or proposing the connection of several GFM battery energy storage systems in various parts of the Australian National Electricity Market (NEM). These range from 30 MW to 600 MW. With the growing number of grid-scale batteries committed or proposed in Australia, it forms an excellent opportunity to deploy GFM capabilities in the upcoming grid expansion and transition with little or no synchronous generation [97, 98]. In the process, GFM capabilities are demonstrated and tested. A close working approach with stakeholders is adopted. Thus, with its regulatory bodies, the Australian Energy Market Operator (AEMO) has a broader classification of requirements, including IBR connection in weak grids with stable operation, providing system security, island operation, and black start.

Additionally, due to the very high penetration of IBR in weak grid scenarios, AEMO has been using wide-area EMT simulation models for several years. New generation connection applications, which are almost exclusively

GFM-based IBRs, AEMO plans to employ wide-area EMT models to the same extent as phasor domain models (RMS) and form a part of the grid code requirement [7, 14, 15, 99, 100].

2.3.4 Hawaii

The Hawaiian Electric Company (HECO) plans by 2023 with new project goals, a very high share of distributed energy resources, and a significant reduction of the operation of synchronous machines. To prepare for the future, HECO requested GFM functionality from all of the proposed projects that included battery storage system. High-level performance requirements were proposed stating that the GFM IBRs shall be capable of operating and supporting system operation under normal and emergency conditions without depending on synchronous machines. Hence, it implies voltage source operation during normal and transient conditions within the physical limits of the converter and the ability to synchronize with other sources or operate autonomously if a grid reference is unavailable [101]. In addition to these high-level requirements, a detailed set of tests was provided, which were to be applied to the prospective source models and ensure the desired GFM performance. HECO had performed full planning studies in RMS and EMT for their entire island-wide networks, anticipating 100 % renewable penetration scenarios by 2023. The studies presented concrete recommendations on operation and controls to improve grid reliability and evaluated GFM control technology in battery applications as a measure to mitigate weak grid issues. These high-level GFM requirements, supplemented with early studies, indicated an appropriate starting point for other system operators and policymakers to assist in specifying GFM capability under their jurisdictions where none currently exists. Thus, ensuring stability to the future grid at high levels of IBRs [7, 13, 14].

2.3.5 North American Electric Reliability Corporation

The North American Electric Reliability Corporation (NERC) is an international regulatory authority established to evaluate the reliability of the bulk power system in North America. With the recent Texas crisis (February,2021) [102] and the continued growth and penetration of IBR across North America, NERC has issued a new report highlighting the key attributes, benefits, and risks of various converter controls to support the implementation of the GFM technology. At present, there is no standard universally agreed definition of the industry's recently coined terminologies of GFM or GFL. The recently published white paper from

NERC recommends the following definition for GFM Control for bulk power system:

'Connected Inverter-Based Resources are controls with the primary objective of maintaining an internal voltage phasor that is constant or nearly constant in the sub-transient to transient time frame. This allows the IBR to immediately respond to changes in the external system and maintain IBR control stability during challenging network conditions. The voltage phasor must be controlled to maintain synchronism with other devices in the grid and must also regulate active and reactive power appropriately to support the grid' [31].

Thus, the GFM converter is expected to immediately respond to disturbances in external power system and maintain control stability. The regulation of active and reactive power to support the grid is deemed a secondary task, implying prioritizing response to a disturbance event over setpoint changes.

This white paper compares known GFM and GFL IBR capabilities, performance characteristics, and advantages. Also, it provides suggestions for entities across North America to consider investigating and analyzing GFM technology to support bulk power system (BPS) reliability and resilience with increasing IBR penetration levels. According to NERC, GFM control is recommended to provide robust dynamic support to the grid and support but not limited to the following features [31]:

- Operation in low system strength condition
- Grid frequency and voltage stabilization
- Small-signal stability damping to maintain power system stability
- Re-synchronization capability to restore and reconnect to the grid
- Fault ride-through for large grid disturbance events with adequate fault current contribution as required by protection systems (within hardware limits)
- System restoration and black-start capability

Utilities are advised to carefully review NERC's advice regarding converter-based technology and its recommendations. Working groups and committees are set up to provide guidelines to enhance understanding, integrate GFM technology and perform better interconnection studies. A key concern in analyzing this technology requires accurate resource

modelling; thus, tooling or simulation domain has significance. Two critical working groups (WGs) reports, namely:

- Reliability Guideline: Recommended Approach to Interconnection Studies for BPS Connected Inverter-Based Resources (Q4, 2022)
- Reliability Guideline: Electromagnetic Transient Modeling and Simulations (Q1, 2023),

try to shed light on improving the study process for bulk power system connected IBRs, and considering EMT modelling and simulations with increasing penetrations and growing system complexity of performing sufficient studies to ensure bulk power system reliability [103].

Although the phasor domain has been prevalent in conducting stability and planning studies, concerns regarding the fundamental limitations (covered in greater detail in Section 2.5) in their ability and accuracy compared to EMT domain model have been discussed, and is recommended by various WGs. The topic of user-defined models over generic ones is also a scope of ongoing NERC and international activities [2, 7, 21, 22, 31, 104–107].

Of all the requirements mentioned under system needs, stability is of utmost importance from the system needs hierarchy. The factors listed are related and sub-aspects of voltage and frequency stability (magnitude and phase). GFM-based IBRs are controlled voltage sources; therefore, the overall performance depends on the built-in control system strategy [78–80]. To fulfill system needs stability is required to be ascertained via analysis considering accurate and realistic models.

2.4 Methods of stability analysis

The power system is a large, hybrid (discrete-continuous) and dynamical system, which includes several kinds of nonlinear elements. Its stability analysis can be performed as of any dynamic system. Attaining stability is the fundamental objective from system requirement perspective with high IBR share (Section 2.3). Analysis of GFM controls in a realistic power system environment needs to be performed and comprehended. The transient stability is a typical example that originated in the power of swing equation, a sine function of rotor angle [108, 109]. Additionally, all converter controls are highly nonlinear which interact with the power system.

Various methods exist for investigating the stability of dynamic systems driven by different objectives and techniques. Prevalent linear, nonlinear, and mathematical methodologies have been adopted for stability

assessment in this work for performing stability analysis of GFM converters. Nonlinear methods consider the power system's full dynamics, including the effects of nonlinear elements and complex interactions between system components, and provide a more accurate representation of power system behavior than linear methods. However, linear approaches for stability analysis are preferred in both power systems and the PE community due to simplified analysis and well-defined stability criteria.

Further, mathematical or simulative models represent a system's behavior over time in system dynamics, and a set of differential or difference equations can describe these models. The stability analysis of the power system may also be performed by evaluating the solution to the differential equations that describe the system's behavior [108–110]. However, first, the general definition of a dynamic system's stability needs to be discussed, followed by an understanding of power system stability and, finally the analysis procedure to evaluate power system stability.

2.4.1 Concept and definition of stability

The solutions of differential or difference equations may describe the stability of a dynamical system, and the most prevalent stability solutions exist near the equilibrium point [111]. This mathematical concept of stability of a dynamic system is often associated with Lyapunov's stability, who laid the foundation of this theory and is conceptually explained as follows.
Lyapunov's stability: It states that the stability of a system signifies that the system trajectory is kept arbitrarily close to the origin by starting sufficiently close to it. Thus, the origin is defined as stable or in equilibrium if the solution is maintained within an arbitrarily defined stability radius; as such, it develops within the radius and remains close to the origin thereafter ($t \rightarrow \infty$) [112].

In many engineering applications, Lyapunov stability is not applicable; hence few extended requirements catering to it are explained below.

Asymptotic stability*:* Asymptotic stability implies that the solutions developed are close enough and not only remain close but eventually converge to equilibrium. The region of stability is called *domain of attraction* of the equilibrium point [112].

An equilibrium point that is Lyapunov stable but not asymptotically stable is called *marginally stable* [112]. Figure 2.9 provides a pictorial view of the stability concepts introduced above.

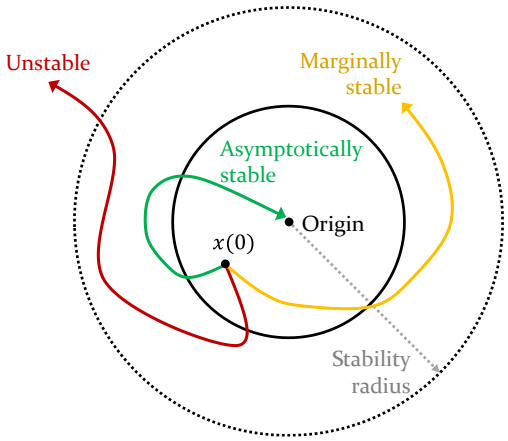

Figure 2.9: Illustration of the interpretation of Lyapunov 's stability (based on [111, 112]).

Additionally, from an engineering applications perspective, it may not be sufficient to know that a system will converge to the equilibrium point after infinite time. There is a need to estimate how fast the system trajectory approaches origin or equilibrium. The concept of exponential stability also known as globally asymptotically stability is hence explained [112].

Exponential stability: An equilibrium point is exponentially stable if the state vector converges to the origin faster than an exponential function. The rate at which it converges is called the *rate of exponential* convergence. The definition of exponential convergence provides an explicit bound on the state at any time. Please note that exponential stability implies asymptotic stability. But asymptotic stability does not guarantee exponential stability [112].

The above definitions to characterize the local behavior of systems and local properties inform little on the system characteristic when the initial state is away from the equilibrium, as in case of nonlinear system. Therefore, global concepts are required.

Globally asymptotically stable: If the solution of an exponentially stable system converges to the origin faster than an exponential function and if asymptotic (or exponential) stability holds for any initial states, the equilibrium point is said to be asymptotically stable in the large. It is also called globally asymptotically (or exponential) stable [112].

Linear time-invariant systems are either asymptotically stable, marginally stable, or unstable. Furthermore, linear asymptotic stability is always global and exponential, while linear instability always implies exponential blow-

up. These refined notions of stability are introduced in this sub-section for a better interpretation of power system and control stability [112].

One of the basic requirements of designing both linear and nonlinear control systems is stability. The stability analysis of a nonlinear system is complicated and Lyapunov functions are commonly involved. When evaluated along the dynamical system's motions, the Lyapunov functions decrease monotonically with increasing time and tend to zero as $t \rightarrow \infty$ as defined above. Such functions are called monotonic Lyapunov functions and serves as a criterion for global asymptotic stability in discrete-time system [113–116].

Global asymptotic stability or global stability is an essential concept in the design and analysis of control and power systems, as it measures the system's ability to remain stable and perform its intended function over a wide range of operating conditions. A globally stable control implies stable control operation under all operating conditions, independent of the variation of network parameters. Achieving global stability in control and power systems is paramount for ensuring the safe and reliable operation of the system. Definitions and detailed explanations of the presented stability concepts are available in [112].

2.4.2 Power system stability

The formal definition of power system stability from [79] is provided below, aligned with the massive system transformation due to integration of IBRs.

'*Power system stability is the ability of an electric power system, for a given initial operating condition, to regain a state of operating equilibrium after being subjected to a physical disturbance, with most system variables bounded so that practically the entire system remains intact*' [79].

The definition above deems a system stable subsequent to a perturbation, attains a new state of operational equilibrium, or reverts to its original operating condition. It discusses the system behavior under a disturbance without discriminating between a synchronous machine or an IBR. This formulation is consistent with the previously expounded definition of asymptotic stability as per Lyapunov.

However, the power system stability analysis is highly complex as a typical modern system comprises various devices with distinctive dynamic characteristics and time-constants, and maintaining stability is challenging. Endeavors have been undertaken to categorize stability into suitable categories based on their specific events. Historically, the power

system was machine-dominated, and its typical stability phenomenon was categorized into three classes. Due to the increased IBR proliferation in the power system, two new stability classes have been recently added by the '***IEEE Power System Dynamic Performance Committee***' in their technical report on stability [79]. An overview of the classification is displayed in Figure 2.10. The revised classification is discussed with a greater emphasis on the challenges related to frequency, voltage, angular stability, and converter-driven stability since novel and existing stability phenomena are manifesting with high-IBR shares [79, 117].

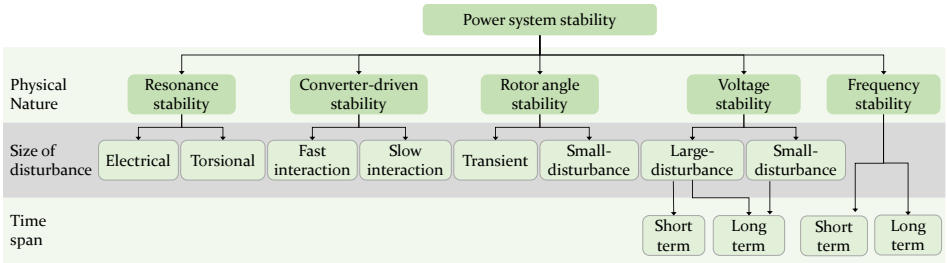

Figure 2.10: Classification of power system stability (adapted from [79]).

Rotor Angle stability or Angle stability*:* Rotor angle stability represents the ability of SMs in an interconnected power system to maintain synchronism during regular operation and regains synchronism after a small or large disturbance [1]. This can be further categorized into small-disturbance rotor angle stability and transient or large-disturbance rotor angle stability.

Small-disturbance rotor angle stability, or small-signal, refers to the ability of the system to maintain synchronism in response to small disturbances, such as fluctuations in load and generation. In contrast, transient or large-disturbance rotor angle stability is the system's ability to recover synchronism after experiencing significant disturbances, such as major faults or sudden changes in system conditions [47, 79, 117].

The phenomenon of angular stability undergoes modifications with the increase in IBR penetration, especially with 100 % COPS. The large-signal rotor angle stability has conventionally been considered the measure of SMs' ability to maintain synchronism during grid faults. This concept stems from the rotor and stator magnetic fields' angular displacement and the corresponding accelerating or decelerating torque. During grid faults, the mismatch between mechanical power input and reduced electrical power output generates accelerating energy in SM, which governs the fault-

clearing dynamics. A duality exists between voltage stability limits, represented by power–voltage curves, and angle limits, as described in [1]. The IBR GFM control determines the phase angle based on active current injection and voltage control, which may be adjusted to maximize the fault power contribution, subject to converter limits. In the context of IBR, voltage and angle stability becomes predominantly dependent on IBR control and post-disturbance grid characteristics. The IBR controls generally exhibit greater stability with a lower angular swing. However, during periods of high grid stress, such as high-power transfers and large network impedance during contingencies, the network angle swing must be carefully managed (minimize phase jump) to prevent system dynamic instability. Further, in IBR-dominated systems, damping small-signal oscillations is another aspect of angular stability that requires attention. [1, 80]

***Voltage Stability*:** It refers to the ability of a power system to maintain steady voltages at all network buses after being subjected to a disturbance from a given initial operating point. Based on the time frame of interest voltage stability is categorized as short term and long term [79].

With the increasing adoption of IBRs and the subsequent reduction of system strength, maintaining voltage and angular stability across the grid has become a new concern. This is due to the varying number of online voltage regulators with high gains, differences in IBR responses, and potential interactions between IBRs and other dynamic devices. For example, supposing the system strength at a point of interconnection is low. In such a scenario, the critical voltage at the nose of the power-voltage curve may fall within the normal operating voltage range, thereby masking a voltage condition that exceeds the reliable operating point and leading to a collapse. Contingencies such as line trips can lead to more stressed system conditions. Under fault conditions, IBRs' fault ride-through mode can result in the rapid increase of reactive power and the reduction of active power to assist voltage recovery. However, during no-fault contingency conditions, improper IBR response, such as too-aggressive active power recovery, could cause a cascading high- or low-voltage collapse in bulk power system where IBRs are concentrated in remote pockets far from load centers [1, 47, 79, 117].

Frequency Stability: It is the ability of a power system to maintain a steady frequency following a severe system perturbation causing a significant imbalance between generation and load [79].

In a bulk power system with SM, the initial RoCoF is arrested by the inertial response after a contingency. The governor performs primary control and stabilizes the system, restoring the frequency to its nominal value. However, with the displacement of SMs by GFL IBRs resources, their inertial response may also be displaced, resulting in a higher RoCoF after an event, leading to the exceedance of frequency limits and triggering protection devices, further worsening the situation. The state-of-the-art IBRs can provide superior frequency control with a faster response speed compared to SMs. However, overly aggressive controls may lead to frequency oscillations and other types of instability in low-inertia systems due to adverse system interactions. Therefore, requiring system operators to review and revise frequency response continuously needs in terms of performance and reserve amounts, especially with changing bulk power system characteristics. Additionally, the largest generation or load contingency size is essential for frequency stability since it is about the power balance and the stability limit of the interconnecting lines. New common modes of failure may be introduced with high shares of IBRs, affecting several IBRs simultaneously, leading to voltage-induced frequency dips in geographically compact systems, such as Ireland. Such events need to be understood and studied to determine appropriate mitigation measures. While in large interconnected systems, a synchronous area split is of grave concern as it may be challenging to maintain frequency stability in independent subsystems [1, 23, 79, 117].

***Resonance Stability*:** The term resonance stability encompasses the phenomenon of sub-synchronous resonance (SSR), which may manifest in two distinct forms as resonance between series compensation and the mechanical torsional frequencies of the turbine-generator shaft, and a resonance between series compensation and the electrical characteristics of the generator. The former condition involves a resonance between the electrical network with series compensation and the mechanical modes of torsional oscillations on the turbine-generator shaft. In contrast, the latter is purely an electrical resonance referred to as the Induction Generator Effect. Resonance stability mainly includes torsional interactions of mechanical components of the conventional turbine generator with either series compensated lines or power systems. Sub-synchronous oscillations may also arise due to the interaction of fast-acting control devices, such as HVDC, Static Var Compensators (SVCs), static synchronous compensators (STATCOM), and power system stabilizers (PSS) with the torsional mechanical modes of nearby turbine-generators. They are treated as resonance stability [79, 117].

However, the PE converters with fast control loops designed with different bandwidths interact with the grid impedance. The resultant frequency-coupling dynamics may lead to harmonic instability phenomena from the sub-synchronous frequencies to multiple kilohertz and are treated as converter-driven stability (discussed below) [118].

***Converter-Driven Stability*:** The behavior of IBRs differs from conventional SMs due to the predominant use of voltage source converter (VSC) technology for grid interface. IBRs rely on fast response control loops, PLL algorithms and inner-current control loops, which operate on a wide range of timescales. This can result in cross-coupling with the electromechanical dynamics of machines and electromagnetic transients of the network, causing unstable power system oscillations over a broad frequency range. Classification is based on slow and fast interactions to differentiate the frequencies of observed phenomena. Slow-Interaction Converter-Driven Stability typically shows low frequencies of less than 10 Hz, while Fast-Interaction Converter-Driven Stability displays relatively high frequencies ranging from tens to hundreds of Hz, possibly even up to several kHz.

Fast-Interaction Converter-Driven Stability relates to the instabilities that affect power systems and is driven by fast dynamic interactions between the control systems of PE-based systems and fast-response components of the power system such as the transmission network, SM, or other PE-based devices. This instability can arise in various ways, such as high-frequency oscillations caused by interactions between the fast inner-current loops of IBR and passive system components, known as harmonic instability. These instabilities have high frequency ranges and can cause system-wide stability problems. Whereas Slow-Interaction Converter-Driven Stability refers to the instability affecting the power system caused by slow dynamic interactions between the control systems of PE-based devices and the electromechanical dynamics of SM and machine controllers. This instability may cause system-wide disturbances comparable to voltage instability, as both can result from maximum power transfer between the converter and a weak system. However, voltage instability is typically caused by loads, whereas converter-driven instability is associated with the control systems of PE converters [79, 117].

The proliferation of IBRs has led to increasingly complex and hierarchical control layers. These controls are responsible for managing a range of attributes, including active and reactive current and power, voltage, phase angle, mechanical torque and speed, and others. However, coordinating

and interoperating these control layers to maintain stability is becoming more challenging, particularly in low-system-strength conditions. In such situations, the controls of GFL converters that rely on continuous voltage measurements may become unstable due to inaccurate voltage measurements resulting from current injection. This instability can be addressed by gradually varying the voltage using slower controls such as GFM. GFM has the ability to tackle instability and weak grids associated interactions, as discussed in Section 2.1.2. Control interactions between IBRs and other converter-based devices may also lead to reactive power deficiencies, oscillations, and instabilities, if not coordinated via a communications scheme or voltage droop function. As the penetration of IBR increase and the system load characteristics change, new aspects of instability may arise. Therefore, frequent and systematic analyses are needed to ensure the robust performance of all components across various system conditions [1, 79].

Further in-depth details on the classification are available in [47, 79, 117].

2.4.3 Stability assessment

Several approaches to studying the stability of a power system are based on the transfer function, state-space modelling, and small-signal analysis based on the linearization around an operating point, eigenvalue analysis, nonlinear methods, and impedance-based methodologies exist [119]. Known mathematical methods which can be applied for stability analysis of power system have been compared in [25]. This work utilizes the linear differentiation equations explained as *'Existence Theorem'*, and small signal analysis performed via linearization approach with solutions created by numerical method for assessing stability solutions. The theory related to the implemented procedures is presented.

2.4.3.1 Existence Theorem

In the theory of linear differential equations, a global *'Existence Theorem'* can be proved regarding the solution space. It is a mathematical concept related to system dynamics in analyzing its behavior. Mathematical models representing a power system's dynamic behavior are constructed to perform analysis and interpret stability. These are a set of differential or difference equations and, thus, establishes the existence of solutions for a mathematical model of the power system.

The *'Existence Theorem'* for initial value problems of ordinary differential equations indicates that under given conditions in a linear or nonlinear

system, at least a unique solution is determined. It is often used in mathematics and control theory to prove the existence of solutions [120, 121]. A detailed understanding of the theorem and it's proof is available in [108, 121] for review.

In power system analysis, this theorem is often used in stability analysis, involving studying the behavior of a power system following a small or large disturbance [122]. It determines whether a solution to the differential equations that describe the system's behavior exists and is unique within a certain time interval after the disturbance. It serves as the prerequisite for the global stability of these mathematical or simulative models, providing the necessary conditions and establishing a solution trajectory that satisfies specific requirements, such as initial or boundary conditions. Additional stability analysis is required to establish global stability [121, 122].

2.4.3.2 Small signal analysis

Small-signal stability allows the prediction of the behavior of the power system after small disturbances that may not result in significant changes in the system's operating conditions. The resultant system response equations can be linearized as the disturbance is small. Several methods for analyzing nonlinear systems have yet to be devised with a consensus on a standard approach. Frequency analysis is a fundamental concept in evaluating small-signal stability in dynamic systems. The frequency response is defined as the steady-state response of a system to a sinusoidal input signal, allowing for the computation of the system's response in a range of frequencies. This technique is mainly used with closed-loop linear time-invariant systems to determine both absolute and relative stability metrics. Although it is typically applicable to linear control systems, frequency analysis can be extended to nonlinear control systems through the *linearization* of the control model [123].

***Linearization*:** The term *linearization* in control and power systems is commonly used to refer to an arbitrarily small change with respect to an operating point. The *linearization method* is well-known and one of the most widely used analytical method concerned with the local stability of a nonlinear system. It formalizes the assertion (linearization theorem) that a nonlinear system should behave similarly to its linearized approximation for small-range motions. Since all physical systems are inherently nonlinear, the *linearization* method serves as the fundamental justification for using linear control techniques in practice. It displays that a stable design by linear control guarantees the stability of the original physical system locally. The deduction about the local stability of a nonlinear system

is performed around an operating equilibrium point based on the stability properties of its linear approximation. A short description of this technique to determine the stability is described below. Equations below represents a nonlinear system:

$$\dot{\mathbf{x}} = \mathbf{f}(\mathbf{x}, \mathbf{u}) \tag{2.5}$$

$$\mathbf{y} = \mathbf{g}(\mathbf{x}, \mathbf{u}) \tag{2.6}$$

where, **x** is the state vector, **u** is the unit vector, **y** the output vector and **f** and **g** both are vectors of nonlinear functions. By adding a small perturbation indicated by Δ to the state-space vector **x** and the input vector **u** the linearized system described below is obtained:

$$\mathbf{x} = \mathbf{x_0} + \Delta\mathbf{x} \qquad\qquad \mathbf{u} = \mathbf{u_0} + \Delta\mathbf{u} \tag{2.7}$$

By applying Taylor's series expansion around the operating point $(\mathbf{x_0}; \mathbf{u_0})$, the nonlinear functions can be approximated by the following equations:

$$\begin{aligned} \dot{x}_i = \dot{x}_{i0} + \Delta\dot{x}_i = f_i(\mathbf{x_0}, \mathbf{u_0}) + \frac{\partial f_i}{\partial x_i}\Delta x_i + \cdots + \frac{\partial f_i}{\partial x_n}\Delta x_n + \frac{\partial f_i}{\partial u_i}\Delta u_1 \\ + \cdots + \frac{\partial f_i}{\partial u_n}\Delta u_r \end{aligned} \tag{2.8}$$

$$\begin{aligned} y_j = y_{j0} + \Delta y_j = g_j(\mathbf{x_0}, \mathbf{u_0}) + \frac{\partial g_i}{\partial x_i}\Delta x_i + \cdots + \frac{\partial g_i}{\partial x_n}\Delta x_n \\ + \frac{\partial g_i}{\partial u_i}\Delta u_1 + \cdots + \frac{\partial g_i}{\partial u_n}\Delta u_r \end{aligned} \tag{2.9}$$

with $i = 1,2,\ldots,n$ and $j = 1,2,\ldots,m$. The linearized system assumes the form given by:

$$\Delta\dot{\mathbf{x}} = \mathbf{A}\Delta\mathbf{x} + \mathbf{B}\Delta\mathbf{u} \tag{2.10}$$

$$\Delta\mathbf{y} = \mathbf{C}\Delta\mathbf{x} + \mathbf{D}\Delta\mathbf{u} \tag{2.11}$$

The above are partial derivative matrices evaluated at the equilibrium point about a small perturbation to be analyzed. **A** represents the system matrix of size $n \times n$, **B** is the system input matrix of size $n \times r$, **C** is the system output matrix of size $m \times n$, and **D** is the feedforward matrix of dimension $m \times r$. The matrix **A** is the so-called Jacobian matrix, and the association between the linearized system and the original nonlinear system is stated by the linearization theorem given in [47, 108, 112]. The stability of the

Jacobian matrix needs to be ascertained as either strictly stable, unstable, or marginally stable. The proof of the theorem is available in [124].

Evaluating the transfer function of the Jacobian matrix in frequency domain by replacing s with $j\omega$ (j is the imaginary unit and ω is the frequency of interest) assists in evaluating a system's small-signal behavior. The magnitude and phase information gained from the transfer function at the frequency of interest helps to comprehend system stability [123, 125].

Any real system is nonlinear, assuming a nonlinear system linear under small development ranges, strongly depending on the magnitude of the nonlinearities affecting the system. Small-signal stability represents a necessary condition, and the theorem is true by continuity, implying that the deductions from a linear system can be extrapolated to a nonlinear one. It is worth mentioning that the *linearization* theorem is recognized as the theoretical justification of linear control theory [112].

Numerical Simulation: Numerical simulation in MATLAB-Simulink® is applied in this work for illustrations to support the theoretical justifications obtained by the *linearization* method and evaluating the transfer functions. MATLAB's ode23tb solver is used in this work as it represents the robust Runge-Kutta with trapezoidal method for numerical analysis.

The appropriateness of numerical integration methods is highly dependent on the features of the simulated system and its purpose [126]. Solving a large nonlinear set of differential-algebraic equations assists in analyzing various timescale phenomena. The principal attributes of a numerical simulation approach consist of numerical stability, accuracy, and efficiency. The numerical simulation allows assessment of various network configurations and controllers (discrete, nonlinear, unbalanced) but requires additional effort for implementing disturbances and interpreting small-signal results, as observed in this work.

2.5 Modelling aspects of converter technologies

Defining and deploying new system services requires detailed engineering and planning studies, as mentioned in Section 2.3. Phasor-domain or RMS models satisfactorily represent the traditional study of slow dynamics of machine-based systems. However, this is not valid for converter-dominated systems since the smallest time constants are in the range of and below the electromagnetic propagation times in extended power systems ($>$ 300 km) [127]. These small time-constants result in smaller simulation time steps. Additionally, stability studies conducted in RMS domain are phasor models

based on the assumption that power transfer occurs at constant or mono-frequency. Studies determine the fidelity of IBR models and ensure reliability, stability, and risks under all relevant grid conditions. Therefore, RMS is insufficient for viable, dynamic analysis of converter-dominated power systems (> 75 %) [1, 6]. The application of EMT tools for a broader range of studies is becoming indispensable.

Additionally, as hinted in Section 2.3, AEMO, NERC, NGESO, and various other grid operators have expressed the need to consider both EMT and phasor domain models (RMS) for interconnection-wide area stability studies [14]. The following paragraphs highlight factors that assert appreciable differences when considering IBR modelling in both EMT and RMS domains, thus enhancing modelling grasp. After all, simulation is a mathematical solution of a physical system and includes an inevitable numerical error. Modelers need to be better aware of the inadequacies of converter modelling in the phasor domain, as mentioned in [109]. The subsequent sections below describe the boundary of RMS analysis and its influence on converter-dominated power systems. Emphasis is placed on understanding the influence of the time constants instead of addressing the computational challenges [22, 107, 127]. The CIGRE Technical Report C4.56 has recently substituted the word 'RMS' simulation domain models as PDT (phasor-domain transient) for better expression[14]. However, this work will use the terminology RMS due to familiarity.

Converters are inherently discrete systems controlled by digital signal processing (DSP) units, with closed-loop feedback over the continuous power system. The numerical solution is a discrete simulation of a combination of continuous (power system) and discrete (converter DSP) systems [128]. The idealization inherent to RMS studies disregards the contributions of all power system electromagnetic transients. In a continuous system, this general proceeding is validated via the dominant eigenvalues of the corresponding system matrix related to the particular solution of the systems' state-space representation. The machines, loads, and disturbances contribute to the system dynamics. However, this approach needs to be revised when power system transients are composed of a sequence of step responses, as is in converter modelling. The discrepancy stems from the sample and hold (S&H) element, which demonstrates two key features, firstly the sampling of signal and transitioning from the continuous to discrete and, secondly, it contributes to the dead-time created by the time required for code processing of the digital signal (DSP) [110, 128]. The slow converter control may be represented in the phasor domain. However, the fast dynamics and

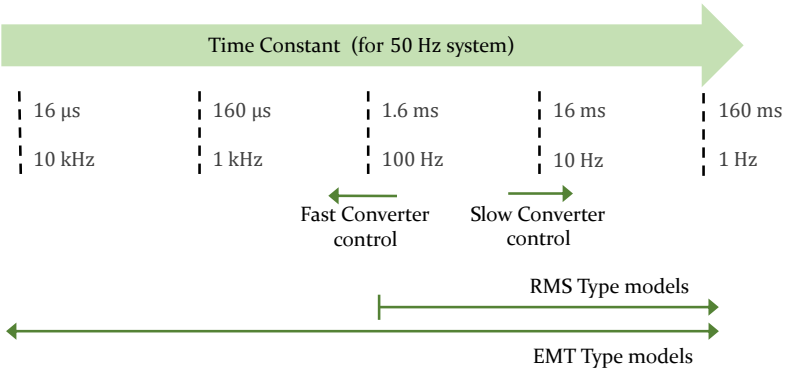

Figure 2.11: Frequency and time domain of different converter associated phenomena (adapted from [129]).

controls at higher frequencies lead to appreciable differences between the respective phasor domain and EMT models considering closed-loop with passive network elements. Therefore, due to the small-time constants ($\leq$ 1 cycle) and the constant frequency assumption in RMS studies no longer provides tenable results for converter-dominated power systems [127]. Figure 2.11 displays the converter harmonics phenomena's time and frequency ranges [129]. This figure indicates that the dominant frequency of power system harmonic phenomena can range from a few hertz to several kilohertz, often associated with pulse width modulation (PWM) in converters. It displays the possible demarcation for using EMT and RMS/Phasor domain system models.

Founded on the context of the boundary of RMS analysis for converter-dominated power systems, three key issues can be identified:

1. **Time step induced issues** in numerical solution of a mathematical model
2. **Dynamics interaction** of a continuous system with a discrete system
3. **Digital simulation of an analog system**

2.5.1 Time step induced issues

Power systems are commonly expressed as a set of algebraic differential equations and are approximately solved through time-domain simulations. The solution of any nth-order differential equation is derived as the summation of homogeneous ($\underline{i}_h$) and particular ($\underline{i}_p$) solutions described by:

$$\underline{i}(t) = \underline{i}_h + \underline{i}_p \qquad (2.12)$$

The $\underline{i}_{\mathrm{h}}$ under a given initial condition ($t(0)$) represents the transient natural response of the system, which decays over time, tending to zero as time approaches infinity ($t \to \infty$). The $\underline{i}_{\mathrm{p}}$ represents the system's steady-state or long-term response. Over time, as transients decay, the steady-state solution persists. The homogeneous equation has exactly one solution determined by the initial condition, while the particular solution depends on the input signal [120, 127].

The differential network equations are numerically solved at each integration step in either an EMT or an RMS simulation domain, where EMT simulation comprises the complete general solution represented by (2.12) The RMS simulation (without additional frequency-dependent manipulation to passive network components) evaluates the long-term particular solution, and short-term electromagnetic transients are disregarded, which are strongly influenced by the time step. While RMS results are typically displayed on a fixed time step frame, the time constant of the homogeneous solution is ignored. Please note that the term 'RMS or PDT' in simulation is equivalent to $\underline{i}_{\mathrm{p}}$ in analytical solutions, and the term 'transient' is equivalent to $\underline{i}_{\mathrm{h}}$ and is used interchangeably in this work [127].

In modern numerical simulations, SMs and converters are typically present in a power system. Although, SMs form a part of power system but do not constitute the transmission system. As a result, it is not necessarily valid to assume that the transmission system is in quasi-stationary or steady-state conditions, as is often done in RMS studies. In the following sections, a mathematical model of a basic network is derived to gain a deeper understanding of the overall solution. The impact of the particular solution on the general solution is examined to understand the deficiencies and make an informed decision for considering simulation domains for converter-based system models. Further insights and details on a novel parameter called '*Transient Voltage Difference*' (ΔV_{CTR}) is presented. This index highlights the importance of simulation time step, its influence on numerical errors inherent to converter or VSC system modelling in RMS domain and its possible application. Details are available in [127].

2.5.1.1 Mathematical model

The analysis of a minimal inductive circuit with a three phase AC voltage source, as depicted in Figure 2.12 is considered. The impedance of the circuit is represented by the complex quantity, $\underline{Z} = \mathrm{j}X$ where j is the imaginary unit and X denotes the reactance. The voltage source is represented using space vector, given by $\underline{v}(t) = \left|\underline{\hat{V}}\right| \mathrm{e}^{\mathrm{j}arg(\underline{\hat{V}})} \cdot \mathrm{e}^{\mathrm{j}\omega t}$, where $\underline{\hat{V}}$

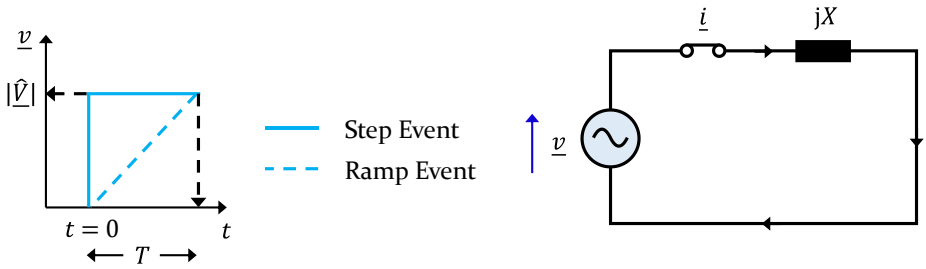

Figure 2.12: Inductive circuit (losses neglected) considered for analytical solution.

is the phasor voltage with magnitude $\hat{V}$ as peak value [130]. The losses are initially assumed to be negligible for the purposes of this analysis. The voltage and resultant current in the circuit are denoted by $\underline{v}(t)$ and $\underline{i}(t)$ respectively, in a complex time domain. The differential equation in (2.13) describes the circuit's response, with $\underline{i}(t)$ as the current through inductor.

$$\underline{i}(t) - L\frac{\mathrm{d}\underline{i}(t)}{\mathrm{d}t} = 0 \tag{2.13}$$

Utilizing (2.12), the general solution for the circuit which consists of the homogeneous solution ($\underline{i}_{\mathrm{h}}$), and the particular solution ($\underline{i}_{\mathrm{p}}$), is denoted by:

$$\underline{i}(t) = \frac{|\underline{\hat{V}}|e^{\mathrm{j}arg(\underline{\hat{V}})}}{\mathrm{j}\omega L}\left[e^{\mathrm{j}\omega t}\right] + C \tag{2.14}$$

$$\underline{i}_{\mathrm{h}} = C \tag{2.15}$$

$$\underline{i}_{\mathrm{p}} = \frac{|\underline{\hat{V}}|e^{\mathrm{j}arg(\underline{\hat{V}})}}{\mathrm{j}\omega L}\left[e^{\mathrm{j}\omega t}\right] \tag{2.16}$$

where, the constant 'C' is dependent on the initial conditions and can be obtained by applying $\underline{i}(t) = \underline{i}(0) = 0$ at $t = 0$. Solving for 'C' and substituting the initial conditions in the complete solution (2.14), solution (2.17) is achieved, where 'C' is given by the following expression:

$$\underline{i}(t) = \frac{|\underline{\hat{V}}|e^{\mathrm{j}arg(\underline{\hat{V}})}}{\mathrm{j}\omega L}\left[e^{\mathrm{j}\omega t} - 1\right] \tag{2.17}$$

$$C = -\frac{|\underline{\hat{V}}|e^{\mathrm{j}arg(\underline{\hat{V}})}}{\mathrm{j}\omega L}[1] \tag{2.18}$$

As known in RMS calculation, the $\underline{i}_{\mathrm{h}}$ or transient solution is typically ignored, while the full solution is considered in electromechanical transient

(EMT) calculation. To evaluate the potential error that may be introduced by neglecting the homogeneous solution for small time cycles, a ramp event is considered as a disturbance, as shown in Figure 2.12. The response of the circuit to this disturbance, denoted by $r(t)$, allows us to examine the general relationship between rise time and the range defined by:

$$r(t) = tu(t) = \begin{cases} t & t \geq 0 \quad (2.19) \\ 0 & t < 0 \quad (2.20) \end{cases}$$

A step function denoted by $u(t)$ represents the limiting case of a ramp with zero rise time. The equations are formulated as causal systems in inverse Laplace domain ($L^{-1}\{F(s)\} = f(t)$).
The magnitude of the periodic input voltage is ramped up over a specified time period. This ramp event is superimposed on the voltage source $\underline{v}(t)$, with a duration of 'T', resulting in a modified input voltage source given by:

$$\underline{v}(t) = \begin{cases} \underline{\hat{V}} e^{j\omega t} \cdot \dfrac{t}{T} & T > t > 0 \quad (2.21) \\ 0 & t < 0 \quad (2.22) \\ \underline{\hat{V}} e^{j\omega t} & t > T \quad (2.23) \end{cases}$$

Equation (2.23) represents the voltage source after the ramp event, which is identical to the initial input voltage or a unit function. This rise time 'T' is related to the simulation time step (a discrete signal) 'Ts',where $T = nTs$ (where n is multiplier) and determines the slope of the ramp in seconds. [110, 128]

Given that the network conditions remain unchanged, it follows that the solution, $\underline{i}_h$ is identical to that presented in (2.15). This is because precisely one homogeneous solution exists for the specified initial conditions. However, the solution for $\underline{i}_p$ depends on the input signal, and in this case, a ramp event has been applied. To determine the value of $\underline{i}_p$, initial conditions are assessed and solved for $\underline{i}_p$ by the following equation:

$$\underline{i}_p = \frac{1}{L}\int_0^t \underline{v}(t)dt = \frac{1}{L}\int_0^t \underline{\hat{V}} e^{j\omega t} \cdot \frac{t}{T} dt \quad (2.24)$$

The particular solution $\underline{i}_p$ during ramping interval T is given by:

$$\underline{i}_{\mathrm{p}} = \frac{\underline{\hat{V}}}{TL(\mathrm{j}\omega)}\left(e^{\mathrm{j}\omega t}t - \frac{e^{j\omega t}}{\mathrm{j}\omega} + \frac{1}{\mathrm{j}\omega}\right) \tag{2.25}$$

By applying the initial conditions at $t = 0$, and solving (2.25), $\underline{i}_{\mathrm{p}}(0) = 0$ is obtained. This implies that $\underline{i}_{\mathrm{h}}(0) = C = 0 = \underline{i}_{\mathrm{h}}$. Consequently, the total solution $\underline{i}(t)$, taking into account the initial conditions, is deduced using the following equations:

$$\underline{i}(t) = \underline{i}_{\mathrm{h}} + \underline{i}_{\mathrm{p}} = 0 + \underline{i}_{\mathrm{p}} = \underline{i}_{\mathrm{p}} \tag{2.26}$$

$$\underline{i}(t) = \frac{\underline{\hat{V}}}{TL(\mathrm{j}\omega)}\left(e^{\mathrm{j}\omega t}t - \frac{e^{\mathrm{j}\omega t}}{\mathrm{j}\omega} + \frac{1}{\mathrm{j}\omega}\right) \tag{2.27}$$

To determine the value of $\underline{i}(t)$, at the boundary conditions and limits, hereby the following conditions are considered at $t = T$, where 'T' is a constant and of finite value. Equation (2.28) and (2.29) describe the left and right limits and conditions as an outcome.

$$\underline{i}(t) = \begin{cases} \dfrac{\underline{\hat{V}}}{TL(\mathrm{j}\omega)}\left(e^{\mathrm{j}\omega t}t - \dfrac{e^{\mathrm{j}\omega t}}{\mathrm{j}\omega} + \dfrac{1}{\mathrm{j}\omega}\right) & t \leq T \quad (2.28) \\ \dfrac{\underline{\hat{V}}e^{\mathrm{j}\omega t}}{(\mathrm{j}\omega)L} + C_{\mathrm{R}} & t > T \quad (2.29) \end{cases}$$

where, 'C_{R}' is the new variable, whose value needs to be determined. By equating (2.28) and (2.29), 'C_{R}' is evaluated and yields the following:

$$C_{\mathrm{R}} = \frac{\underline{\hat{V}}\left(1 - e^{\mathrm{j}\omega T}\right)}{(\mathrm{j}\omega)^2 LT} \tag{2.30}$$

According to the calculations presented above, the current response to the input signal $\underline{v}(t)$ is given by:

$$\underline{i}(t) = \begin{cases} \dfrac{\underline{\hat{V}}}{\mathrm{j}\omega LT}\left(e^{\mathrm{j}\omega t}\cdot t - \dfrac{e^{\mathrm{j}\omega t}}{\mathrm{j}\omega} + \dfrac{1}{\mathrm{j}\omega}\right) & T > t > 0 \quad (2.31) \\ 0 & t < 0 \quad (2.32) \\ \dfrac{\underline{\hat{V}}e^{\mathrm{j}\omega t}}{(\mathrm{j}\omega)L} + \dfrac{\underline{\hat{V}}\left(1 - e^{\mathrm{j}\omega T}\right)}{(\mathrm{j}\omega)^2 LT} & t > T \quad (2.33) \end{cases}$$

The current response described above in (2.31), (2.32) and (2.33).is the total solution that comprises both the $\underline{i}_{\mathrm{h}}$ and $\underline{i}_{\mathrm{p}}$ solutions. This can be considered the EMT solution. It is necessary to discard the $\underline{i}_{\mathrm{h}}$ or transient solution to obtain only the $\underline{i}_{\mathrm{p}}$ or RMS solution. The discarded value can be quantified as the '*Transient Voltage Difference* (ΔV_{CTR})'.

2.5.1.2 Transient Voltage Difference (ΔV_{CTR}) equation

The homogenous solution part of the current response can be fully compensated by superposition of the novel quantity '*Transient Voltage Difference* (ΔV_{CTR})' onto the source voltage, thus recreating the RMS solution [127]. This parameter annihilates the transient or homogeneous part ($\underline{i}_{\mathrm{h}}$) of the current response in the EMT solution. Hence, the EMT current response in *dq* frame matches the RMS current response. Utilizing the network solution in (2.13) and substituting the current responses from (2.31) to (2.33), ΔV_{CTR} is calculated as:

$$\Delta V_{\mathrm{CTR}} = \begin{cases} -\dfrac{\underline{\hat{V}} e^{\mathrm{j}\omega t} t}{T} & T > t > 0 \quad (2.34) \\ 0 & t < 0 \quad (2.35) \\ 0 & t > T \quad (2.36) \end{cases}$$

Equations (2.34) to (2.36) describes this parameter as causal function definition in Laplace domain under different boundary conditions of $t = T$. The ΔV_{CTR} is active during the transient phase to compensate the homogenous solution of the current, i.e., the part not proportional to the driving voltage. From (2.34), it is deducible that ΔV_{CTR} is inversely proportional to time period or simulation time step '$Ts = T$' and dependent on frequency. Thus, implying smaller time step lead to larger compensations or inaccuracies in models in RMS domain to match EMT results. ΔV_{CTR} helps estimates the transient response or can be superimposed on the source to obtain immediate steady-state responses. Further details and usage of ΔV_{CTR} is available in [127]. The following sub-section provides simulative evidence of the mathematical analogies and assists in developing a better understanding of simulation domains.

2.5.1.3 Numerical solution of a mathematical model

Simulation is a numerical solution of differential equations, which can be comprehended as a discrete approximation of a continuous system [110, 128]. Modelling involves building these mathematical equivalents and

performing numerical simulations. This section presents visual evidence of the concepts and details discussed in Section 2.5.1.1 to illustrate the difference in responses to a step event in EMT and RMS simulations. A basic circuit as a closed-loop system is simulated in PSS®NETOMAC. A negligible damping resistance is added to the circuit in Figure 2.12 to obtain Figure 2.13. The simulation output quantities are based in per-unit system.

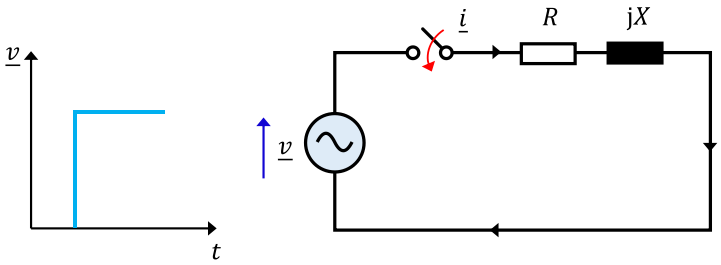

Figure 2.13: Inductive circuit with losses considered for numerical simulation.

A voltage step magnitude of 1 pu is considered. Step responses are the worst-case scenarios that result in the largest transients in simulation. Additionally, a step represents the limit of a steep ramp, and the integral of a step is a ramp. Thus, with numerical simulations of converters, the reaction to a disturbance is a sequence of step responses, predicting the response of the network and involved elements. The network is simulated in both the RMS and EMT domains to compare the results using the same time step. The step event, which is analogous to a disturbance, is applied at 15 msec, and the current response due to the voltage increase is evaluated. The resulting time traces are displayed in Figure 2.14. The initial conditions for the simulation include a voltage of 0 pu and a current of 0 pu.

The step response in the voltage source of the circuit, shown in Figure 2.14 (b) results in a 1 pu RMS current as in Figure 2.14 (a). RMS domain accounts for the steady-state or the particular solution ($\underline{i}_p$) response after the transients have decayed as obtained in dq frame. The particular solution is highlighted (**black box**) and marked as steady-state solution in the general solution (Figure 2.14 (c)). When considering $\underline{i}_p$ in the general solution of Figure 2.14 (c) and disregarding the rotational part, the result is transformed from abc → αβ → dq coordinate system corresponding to the magnitude in the RMS domain or the steady-state response as described in Figure 2.14 (a). For the general solution current response, a damping resistance of value $R = 1.E - 2$ pu was employed to decay the transients in EMT domain to attain $\underline{i}_p$ and thus RMS simulation result within 1 sec.

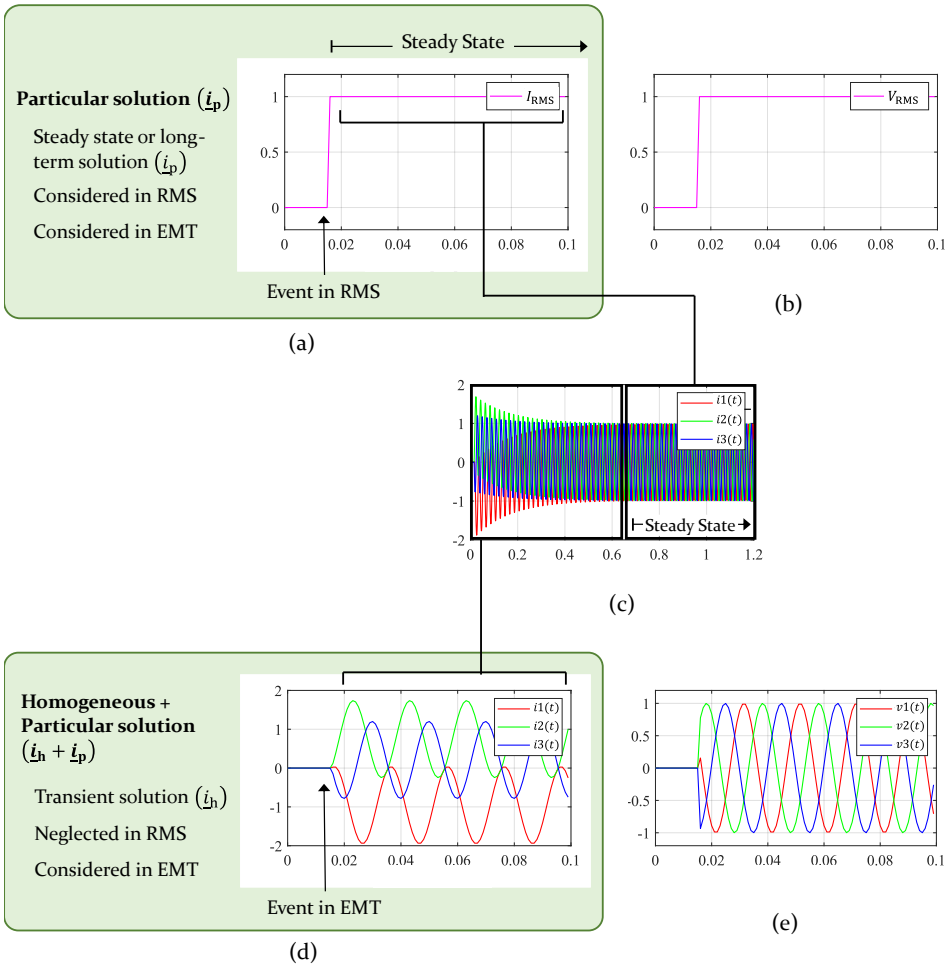

Figure 2.14:
(a) Magnitude of current response due to voltage step in RMS domain;
(b) Magnitude of voltage step response in RMS domain;
(c) General current solution due to step response with a damping resistor (R) highlighting steady-state and transient responses. It illustrates the complete solution of a numerical simulation;
(d) Current response due to voltage step in EMT domain;
(e) Voltage step event in EMT domain [127].

In converter-dominated systems, it is necessary to investigate fast current loops with smaller time constants and their interaction with transients. A power system is typically characterized by an ohmic-inductive network with a low resistive component, making the inductive component dominant. Thus, the time required for transients to decay is relatively high. The damping due to regular loads is not relevant in this context. Using RMS

domain to represent IBRs under the assumption of steady-state conditions will result in an inadequate power system representation, rendering the analysis results unreliable. It is essential to consider models that can accurately capture the system's behavior during transient periods.

The showcase network in Figure 2.13 in EMT domain displays the voltage and current responses portrayed in Figure 2.14 (e) and Figure 2.14 (d), respectively. The 1 pu step increase in voltage results in current magnitude responses that are higher than 1 pu compared to the RMS domain plot (Figure 2.14 (a)). This is due to the superimposed contribution of transients as highlighted in the general solution displayed in Figure 2.14 (c). The steady-state response is reached based on the network damping ($^{L}/_{R}$) ratio and is not a step event as displayed by RMS. The EMT plots display the first cycles of complete network solution. [127]

The impact of the particular solution ($\underline{i}_{\mathrm{p}}$) on the general solution is examined and displayed to understand the deficiencies and make an informed decision for stability analysis and controller time constants while considering simulating converter-based models.

2.5.2 Dynamics interaction

The well-established 5th order (dq) model or even reduced order models due to the inherent large time constants of machines depict reasonable accuracy while maintaining a larger time step in the simulation. Therefore, synchronous machine model representation fits into the approach of continuous system response.

A simple first-order example has been calculated to illustrate the main distinction and to determine and explain the boundary conditions which need to be considered for continuous and discrete systems. Stability issues depending on the choice of gain for comparing continuous vs. discreet systems are discussed below. A first-order closed-loop model given by a proportional controller with a gain of K_{R} is examined. Here, current as input, voltage as output and an inductive path 'L' as a continuous system in Figure A 1 is considered. The system is calculated considering the standard equation for an inductor and a resistor representing a proportional controller. The solution of the system is expressed by:

$$\underline{i}(t) = \underline{i}_0 \mathrm{e}^{-\frac{K_{\mathrm{R}} t}{L}} \tag{2.37}$$

where $\underline{i}_0$ is a constant obtained when applying initial conditions.

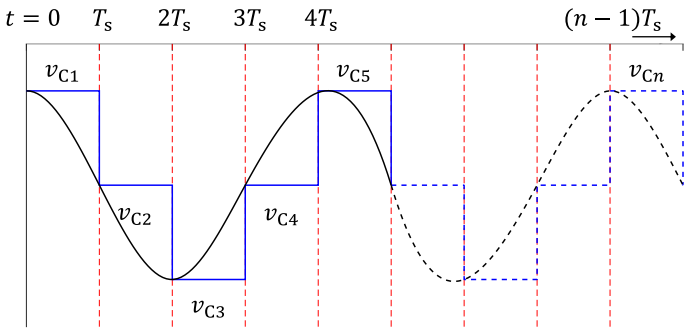

Figure 2.15: Sample and hold applied to continuous system. (**Black** - continuous signal, Blue – S&H signal with jumps at each sampling time and $\boldsymbol{v_{Cn}}$ – arbitrary voltage input).

Solution (2.37) is globally stable for all values for the network modelled as a continuous system with positive gain values. Hence, the simple continuous system with an instantaneous feedback loop is independent and stable for all choices of positive gain values, i.e., $K_R \geq 0$.

The same system is discretized via a sample and hold (S&H) of input current to investigate a discrete system, deemed as a digital simulation of a continuous system. An exemplary response of continuous and discrete signal is displayed in Figure 2.15. The output voltage solution is given by:

$$\underline{i}(nT_S) = \underline{i}_0 \left(1 - \frac{K_R T_S}{L}\right)^n \tag{2.38}$$

where, $\underline{i}_0$ is the initial value of current from load flow, T_S is the sampling period and n is the number of samples. The intermediate steps along with circuit diagram for complete solution of (2.38) is given in Appendix A2.

Now, unlike the continuous system, which is globally stable, determining stability in a discrete system, limits needs to be imposed as given in (2.39). On simplification the following boundary conditions are obtained as:

$$\left|1 - \frac{K_R T_S}{L}\right| < 1 \tag{2.39}$$

$$0 \leq \frac{K_R T_S}{L} \leq 2 \tag{2.40}$$

By evaluating the boundary conditions, two distinguishing boundary limits on the gain are obtained and provided in (2.41). Let $T_S = 1$ and $L = 1$, results in $K_R = 2$. The possible gain values are described as:

$$0 \leq K_R \leq 2 \tag{2.41}$$

Thus, (2.40) determine the conditions under which a discrete system is stable. The interesting point is that the continuous system is stable for all positive gain values $K_R \geq 0$. In contrast, for a sampled or discrete system, stability imposes a constraint on the possible values for the gain i.e.,(2.41). Furthermore, the dynamics differs in case of high gains. The dynamics of continuous and sampled systems get numerically close together when the condition $\frac{K_R T_S}{L} \ll 1$ is fulfilled, with gain values in (2.41). Additionally, the dynamics of the discrete system change from monotonic decay with $\frac{K_R T_S}{L} < 1$, to damped oscillation with $1 < \frac{K_R T_S}{L} < 2$. Thus, hinting at the *global stability* criteria of discrete systems.

Therefore, form the above it is inferred that although gains may be chosen as high as possible (Laplace or *s* domain) to obtain fast dynamics in the case of an overall continuous system, the gains may not give a stable outcome in discrete simulation. Global stability under all parameter conditions may be true in case of a particular continuous system but not always valid in case of the same discrete system. Hence, to determine and explain the boundary conditions, care must be taken between continuous and discrete systems to obtain global stability under all parameter conditions.

In this work, the mathematical deductions are in continuous domain (Laplace) since a true similarity is achieved with RMS domain simulation or at steady-state $\underline{i}_p$ However, the control simulated in the EMT domain is discrete, as stated in the Preamble (Section 1.3.1), abiding by the bounds.

2.5.3 Digital simulation of an analog system

Power systems correspond to analog systems. The numerical solution of the continuous power system equations is called a simulation. It can be interpreted as a discrete system such that the input values of the discrete system are equal to the sampled values of the continuous system. When a system can process all the sampled inputs to get continuous outputs, such a system is called an – ideal – digital simulator [110]. The equations beneath express ideal discrete input and output signals as:

$$f[n] = f[nT] \qquad g[n] = g[nT] \qquad (2.42)$$

where, $f[n]$ is the input signal and $g[n]$ is the output signal. [110]

The above relations in (2.42) are in reality untrue since a discrete simulator does not have an infinite number of samples but instead has a finite number of samples [110, 131], and the values of $f[t]$ and $g[t]$ will not

necessarily coincide. To satisfy the simulation conditions, the band-limited input signal must be considered.

Hence, a discrete simulator of an analogous system considers the following:

- Limited sampled impulse response values of the analogous system
- The discrete simulator is specified in terms of a unit circle.

The above leads to the simulation of an analogous system with sampled inputs. A discrete simulator is a realizable computer system that should be rational and causal. However, an arbitrary simulation task is not necessarily rational, thus leading to an approximation of a discrete-time domain or frequency domain error [110]. Therefore, only band-limited data or signals principally allow accurate simulation of continuous systems.

2.5.4 Discussion on modelling aspects

The purpose of a simulation is to solve mathematical models numerically, but if the errors encountered are too large, the validity of the simulation is compromised. It is essential to accurately represent converter control models when investigating power systems with IBRs. The simulation time step plays a significant role in the numerical errors inherent in converter modelling. Smaller control time constants require a smaller simulation time step. The responses of the fast closed-loop signals are not appropriately represented in the RMS domain due to the inadequate system feedback, and affecting the resultant steady-state associated with converter source models. RMS simulations reflect power changes sufficiently accurately in machine-dominated systems but fail to capture the dynamics precisely with a high share of IBRs [14, 22, 23, 107, 127]. Hence, cause significant and non-evident modelling and system analysis errors. Further details on this topic have been discussed in [127] and a novel index is introduced to quantify the error in RMS domain response and its implications.

Based on the details mentioned above in Section 2.5, a mere RMS simulation is not adequate to assess the IBR-based system's stability. A worthwhile comparison between EMT and RMS results is obtained only after the first couple of cycles since RMS calculations consist of only $\underline{i}_{\mathrm{p}}$ Additionally, as described in Section 2.5.2 and 2.5.3, attention should be paid to continuous and discrete systems to obtain global stability in control system under all parameter conditions. To determine the robustness of discrete time dynamical systems, the criterion for global asymptotic stability needs to be ensured. Further, as in Section 2.5.3, distinguishing

between digital simulation and an analog system is mandated as any simulation has inherent limitations and is not injective or uniquely mapped with an analog system (hardware/real equipment).

Based on the above, a few key takeaways include:

- Time required to reach steady-state response in EMT is disregarded in RMS and induces modelling errors in RMS domain.
- RMS is unable to accurately represent converter dynamics with closed-loop power system (R, L, C as passive network elements) due to constant frequency assumption. Unless a control is developed, which achieves constant frequency at steady-state of any arbitrary power system.
- To design any discrete dynamical system, global stability under all system parameter conditions is required to be established.

The Phase Restoring Principle (PRP) introduced in this work generates a constant frequency due to the control structure. Thus, both positive sequence EMT and RMS results merge into steady-state similar responses. However, as the control development progresses the validity of each simulation domain is assessed to check the legitimacy of response as mentioned in Section 1.3.1 and shown in Section 4.

2.6 Chapter summary

This chapter discusses the operating principles of PE-based converters, and a broad-level classification of their control strategies according to the evolving grid. Two main converter control categories are discussed, namely GFL and GFM. Their functional behavior is compared under distinct operating conditions with GFM to indicate possible future network solutions. The primary inadequacy of GFL is attributed to the synchronization procedure achieved via PLL, leading to instabilities in weak grids.

Further, new developments in the power industry are highlighted with a focus on the new upcoming philosophies guiding the grid code requirements for the IBR-dominated power system in general and GFM in particular. The system demands based on the evolving grid are ranked, of which stability is most crucial. GFM recommended definition and its requirements and activities based on the deploying or deployed countries are listed. In this regard, particular importance is given to the definition published by NERC, and the feature of prioritizing disturbance over

setpoints is emphasized. Some other characteristics requested by most countries such as active power control, damping active power, inertial response, overcurrent protection etc., are also looked into and discussed.

As stability is the primary requirement for system needs hierarchy, an overview, and definitions of dynamical system stability in general and power system stability in specific, are examined. The impact and deductions of IBRs on power system stability are reviewed with a significant influence on voltage and frequency stability (magnitude and phase). A new stability class called Converter-Driven Stability focusing on harmonic interactions was recently introduced, indirectly influencing voltage and frequency stability. Followed by a synopsis of the *'Existence Theorem'* and small-signal analysis as the preferred methodology utilized for stability analysis in the forthcoming chapter of this work.

Additionally, the activities on IBR Modelling and recommendations by various WGs and national grid codes are accentuated. Therefore, modelling aspects of converter technologies as a concluding topic pertaining to converter-dominated systems is discussed. The relevance of the accurate translation of mathematical models, simulation domains, and physical systems is illustrated. Simulation models enable the assessment of any technology and, therefore, to conceive a better awareness. This section highlights probable errors or mismatches between the physical system and simulation. The insufficiency of phasor or RMS simulation for converter-dominated systems is evaluated against EMT, both analytically and simulatively. General awareness of modelling and simulation errors from stability perspective is examined. A greater emphasis on global asymptotic stability is given from nonlinear control systems aspect.

3 Grid-Forming control based on Phase Restoring Principle

This chapter introduces the novel GFM control scheme called the 'Phase Restoring Principle' (PRP) that achieves power system stability under several challenging network scenarios. The control hierarchy is elucidated with the bottom-up approach to illustrate each control loop's significance for the scheme's development. The control development consists of three distinctive phases. Phase 1 introduces a novel building block that provides fast frequency response and is fully GFM. PRP is described in Section 3.1, the mathematical proof of its operating point's validity is presented in Section 3.2 and the small-signal solution is derived in Section 3.3. Phase 2 extends and enhances this scheme with active power control (APC), as described in Section 3.4, allowing interoperability between multiple sources. Lastly, Phase 3 concludes the control scheme by implementing a unique current limiting methodology complementing Phases 1 and 2, and is depicted in Section 3.5. The details of the complete PRP GFM Scheme with DC compensation are presented in Section 3.6, and the entire control concept is summarized in Section 3.7. The theoretical proof supported by simulation and demonstration of practical case studies of this nonlinear control is depicted in the following chapters. Parts of this chapter are published in journals J1, J2 and conference contribution C1 (see Table A 7).

3.1 Novel building block

A control that achieves asymptotic stability and, consequently, frequency emerges after steady-state evolution may be defined as a GFM system. It is, therefore, worth examining the physical definition of GFM recommended by NERC and extending the definition to include a system that achieves asymptotic stability. Hence, the controller design, as pointed out by NERC, responds to disturbance, and all controllers in the power system collectively support both voltage and frequency to be restored. The regulation of active and reactive power is a secondary task.

The learnings from Siemens NGA and system requirements, as discussed in Chapter 2, initiated the development of the globally stable and novel 'Phase Restoring Principle' (PRP). The approach is based on the change of perspective from converter to grid, prioritizing response to disturbances over response to setpoint changes and attaining nominal frequency in reverse action to a PLL. As iterated in Section 2.4 and 2.5.2, stability must

be ensured under all operating conditions to design a globally stable control system, independent of the variation of network parameters.

This concept of Phase Restoration is realized by choice of transformation angle applied to the measured voltage using a novel angular transformation called $\rho_{dr}\iota_{dr}$, as displayed in Figure 3.1. The new rotating coordinate system, rotates contrary to the conventional dq used with PLL, by reacting to the phase difference as described in equation (A 3.3) of Appendix A3. Thus, no synchronization is involved with the power system frequency.

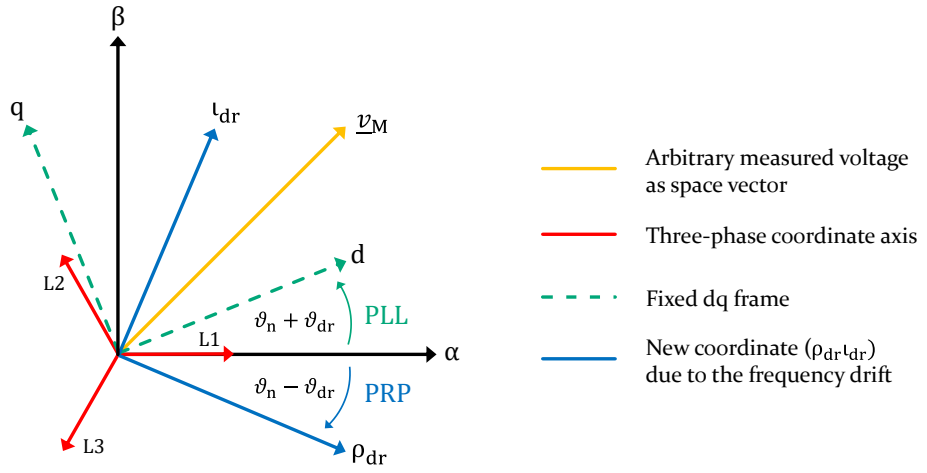

Figure 3.1: Phasor diagram interpretation of the phase drift ϑ_{dr} in αβ frame.

The control concept clamps the phase at the voltage measurement node, restoring to its initial value in the opposite direction to a disturbance in the ohmic-inductive network and achieving steady-state or constant frequency. It attains the post-disturbance operating point directly by adjusting the transformation angle applied to the converter source. The PRP represents the phase part of a voltage in the GFM principle corresponding to a complex rotation and is a nonlinear phenomenon. Thus, the proposed control scheme built is nonlinear, discrete, and the lowest building block in developing a GFM converter control.

Frequency is uniquely defined only under steady-state conditions, an essential aspect of the PRP control's property to obtain operating points. The Taylor series expansion for the complex argument of the node voltage as a function of time is given by:

$$\phi(t) = \phi_0 + \phi_1 \frac{t}{1!} + \phi_2 \frac{t^2}{2!} + \cdots \tag{3.1}$$

where, ϕ_0 is the phase of the voltage and $\phi_1 = \frac{\mathrm{d}\phi}{\mathrm{dt}}$ represents instantaneous frequency which is constant at steady-state. Argument and phase of a complex number ($\underline{z} = \mathrm{e}^{\mathrm{j}\phi}$) are used synonymously ($\phi = \arg\{\underline{z}\}$). At steady-state, other than 0th and 1st derivate, all higher derivatives are zero. Thus, asymptotic stability corresponds to these two terms. The absolute load flow phase, represented by ϕ_0, is an outcome of the dynamic network history when it reaches steady-state. PRP works on ϕ_1, mathematically defined as frequency; hence, the scheme creates frequency.

The analyzed power system displays an ohmic and inductive characteristic, resulting in an inherent phase shift. The control strategy utilizes this fundamental characteristic. PRP incorporates a new $\rho_{\mathrm{dr}}\iota_{\mathrm{dr}}$ rotating coordinate system, rotating opposite to a PLL or synchronized system response. As known, the selection of a coordinate transformation largely depends on the specific controller method being used. The current and voltage phase will depend on the choice of the coordinate or reference system dynamically. Whereas the magnitudes of voltage or current and power are invariant to the arbitrary transformations. Therefore, it is advantageous to use invariant quantities in control design and hence, utilized in PRP design. Due to the novel transformation, the transient frequency drift shifts from the power system to the control, resulting in a stabilizing response in the phase change to counteract the disturbance. The reaction is in accordance with the power system's inductive nature and participates in the creation of future operating point. PRP inherently accounts for the voltage stabilizing effect. Therefore, it is possible to maintain global stability (discussed in Section 2.4.1.) in the power system invariably achieving nominal frequency ω_{n}. It is essential to mention specifically for GFM converters; stability corresponds to maintaining the phase-frequency relationship of voltage to stabilize the network. All relevant information is extracted from the locally measured voltage for a converter control. Frequency is associated with the argument of voltage vector; a strong coupling exists between voltage and frequency stability. Attaining both voltage and frequency stability is vital.

The block diagram of PRP, an essential building block for realizing a GFM-based converter control scheme, is shown in Figure 3.2. This is further referenced as Phase 1. The naming conventions are aligned with the space vector representation in Figure 3.1 to aid understanding. The general converter output voltage is defined by $\underline{v} = \underline{\hat{V}}\mathrm{e}^{(\mathrm{j}\omega t)} + \underline{v}_{\mathrm{DC}}$, where $\underline{v}$ is the voltage space vector in time domain, $\underline{\hat{V}}$ is AC phasor voltage and $\underline{v}_{\mathrm{DC}} = \underline{\hat{V}}_{\mathrm{DC}}$ is the DC space vector. At steady-state $\underline{\hat{V}}_{\mathrm{DC}}$ is negligible and $\underline{\hat{V}}\mathrm{e}^{(\mathrm{j}\omega t)}$ is the

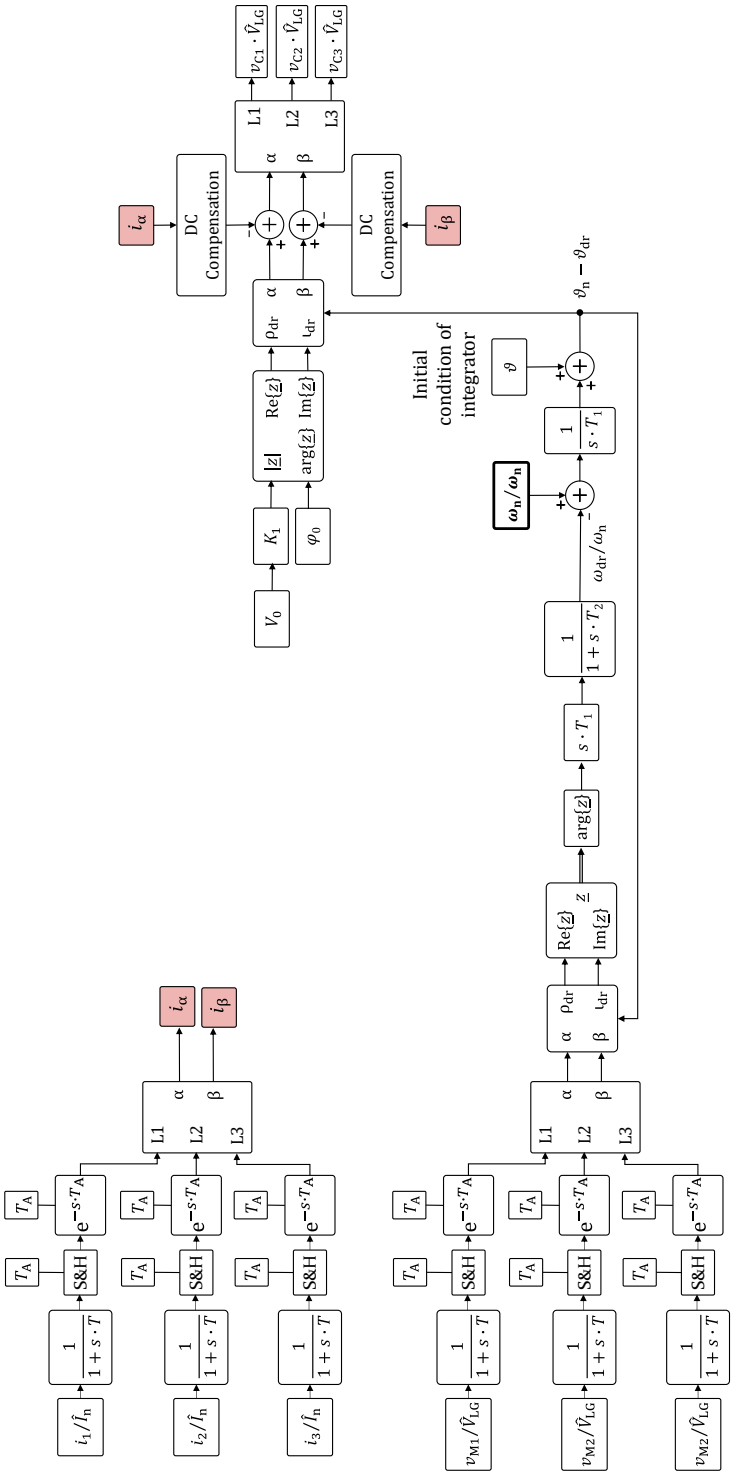

Figure 3.2: Block diagram of Phase Restoring Principle (**PRP**) for Grid-Forming converter control – **Phase 1**.

driving voltage, with $\hat{V}_{\mathrm{LG}}$ as peak magnitude. Thus, the output signal (source voltage) in EMT domain consists of an AC and DC part $\underline{v} = \underline{\hat{V}}\mathrm{e}^{(\mathrm{j}2\pi F_{\mathrm{n}} t)} + \underline{\hat{V}}_{\mathrm{DC}}$. Whereas, in RMS domain the output voltage is reduced to the phasor part $\underline{V}$, where $\underline{V} = \underline{\hat{V}}/\sqrt{2}$. Accordingly, the nominal frequency shift block (highlighted in **bold** in Figure 3.2) is set to zero in RMS domain. The network quantities are in physical units while the control requires a pu base as clarified in Appendix A4.

The block diagram in Figure 3.2 consists of the three-phase measured input voltages ($\underline{V}_{\mathrm{M}}$) which are smoothed and discretized over a sample and hold block (S&H) with an inherent delay to create and represent a realistic discrete converter control with sampling frequency. The full control is sampled with 10 kHz or time step of 100 µsec. The method shall also work with sampling frequencies starting from 5 kHz to higher values. The smoothing time constant is 100 µsec. The measured input signals are transformed from αβ reference frame to a new coordinate frame of $\rho_{\mathrm{dr}}\iota_{\mathrm{dr}}$ in terms of the frequency drift, where ρ_{dr} represents the real part of the measured voltage while ι_{dr} is the imaginary part. The phasor diagram is shown in Figure 3.1, where the new reference system $\rho_{\mathrm{dr}}\iota_{\mathrm{dr}}$ is defined by the drift frequency or Phase Restoring angle ($\vartheta_{\mathrm{n}} - \vartheta_{\mathrm{dr}}$), a rotation angle with respect to αβ. Thus, displaying the opposite behavior to the standard PLL phase defined by ($\vartheta_{\mathrm{n}} + \vartheta_{\mathrm{dr}}$) by not following the system frequency and maintaining a drift in control coordinate system. This raw drift or difference in phase of the complex input voltage ($\arg\{z\} = \tan^{-1}\frac{\mathrm{Im}\{z\}}{\mathrm{Re}\{z\}}$) is processed over a differentiator ($s \cdot T_1$) with the phase of the complex input voltage and is further smoothed with the time constant (T_2). The differentiator with the first-order filter constitutes the washout filter to suppress noise amplification. The smoothed difference (ω_{dr}) corresponds to the $1st$ term, or coefficient of the Taylor series expansion's as addressed in (3.1). The control is represented in the continuous domain for analytical treatment. The differentiator is approximated by a difference for the simulation purposes. The differentiator discards the control of the $0th$-order term or the constant load flow phase, thus deriving instantaneous frequency. The resultant frequency drift (ω_{dr}) is subtracted from the reference frequency (ω_{n}) and passed to the phase integrator (T_1). The integrator computes the linear part of the transformation angle over the control feedback loop. Reference values (V_0, φ_0) are manipulated based on the phase drift (ϑ_{n}–ϑ_{dr}) to the new coordinate system ($\rho_{\mathrm{dr}}\iota_{\mathrm{dr}}$) and cross-referenced to the rotating αβ, to obtain three-phase converter voltage ($\underline{V}_{\mathrm{C}}$)

in physical units. Here, V_0 and φ_0 represent pu nominal peak voltage and initial phase of $\underline{V_C}$ output.

The PRP control scheme is characterized by the absence of an initial reference signal and synchronizes to the measurement node and the network impedances, facilitating power sharing (initial phase and nominal frequency are required prior to PRP control release). The power sharing is then accomplished based on the ratios of the network impedances. The Phase Restoration process is accomplished by employing a voltage transformation angle at the measurement node, which is generated in response to a disturbance through the action of the phase integrator. The frequency drift archives the operating history embedded in the transient phenomenon. Following a disturbance, the phase at the measurement node is restored to its initial value. The power system moves from the initial state and converges into the steady-state solution via the action of the Phase Restoration integrator. The phase of the converter voltage exhibits a direct path from the initial state to the steady-state. This response is aligned with NERC's [31] and National Grid's requirements [16], further discussed in Chapter 4 and Chapter 5. The frequency drift (ω_{dr}) has a transient and a steady-state aspect. The latter is an aspect of active power control (APC), covered in sub-section 3.4. Therefore, PRP concentrates on the phase part of the voltage in the GFM principle and directly takes over the central part of the control [21, 29].

3.2 Mathematical proof to obtain stable operating point

To illustrate the control principle, a basic ohmic inductive test bench network is considered, as shown in Figure 3.3. This topology consists of a converter voltage source '$\underline{V_C}$', connected at node 'CON' via coupling impedance 'X_{C}' and followed by a transformer impedance 'X_{T}' at the measurement node 'MEAS'. The grid equivalent or slack node is designated as 'SLK' with voltage '$\underline{V_S}$' and the load is connected at the point of common coupling. Between the 'PCC' and 'SLK', the network impedance 'X_{N}' with a negligible resistive component 'R_{N}' is connected. The load is purely resistive, with resistance 'R'. The load is initially disconnected, and the scenario is termed as pre-disturbance. Connection of the load is termed as post-disturbance. Both the CON and SLK terminals operate at nominal voltage ($\hat{V}_{\mathrm{LG}}$) or 1 pu (Appendix A4).

The control aims to achieve power system stability by fixing the phase voltage at the measurement node 'MEAS', expressed by voltage '$\underline{V_M}$'. To reach the steady-state operating point (post-disturbance), the solution to

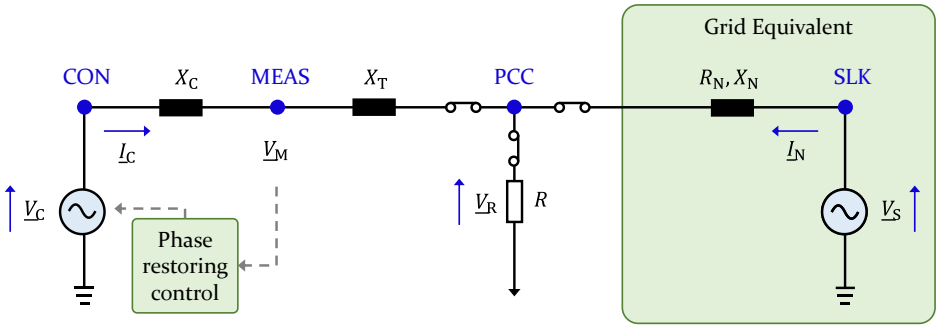

Figure 3.3: Simplified circuit diagram of the test network in post-disturbance condition.

the network equations need to be ascertained, which are unique. The network in Figure 3.3 is illustrated as a two-port network and is solved using the following two voltage loop equations:

$$\underline{V}_S - \mathrm{j}X_N\underline{I}_N - \underline{V}_R = 0 \tag{3.2}$$

$$\underline{V}_C - \mathrm{j}X_C\underline{I}_C - \mathrm{j}X_T\underline{I}_C - \underline{V}_R = 0 \tag{3.3}$$

where, $\underline{V}_C = |\underline{V}_C|\mathrm{e}^{\mathrm{j}\varphi} = \hat{V}_{LG}\mathrm{e}^{\mathrm{j}\varphi}$ is the converter source voltage, $\underline{V}_S = \hat{V}_{LG}\mathrm{e}^{\mathrm{j}0}$ is the slack voltage, $\underline{I}_C$ and $\underline{I}_N$ are the complex currents flowing in the network. $\underline{V}_R$, is the voltage across the load and the resultant is:

$$\underline{V}_R = R\left(\underline{I}_C + \underline{I}_N\right) \tag{3.4}$$

On solving (3.2), (3.3) and (3.4) given above, transpires a solution for the loops currents $\underline{I}_C$ and $\underline{I}_N$. The voltage at the measurement node $\underline{V}_M = |\underline{V}_M|\mathrm{e}^{\mathrm{j}\theta}$, is equated by:

$$\underline{V}_M = \underline{V}_C - \mathrm{j}X_C\underline{I}_C \tag{3.5}$$

As discussed in Section 2.4.3.1, the *'Existence Theorem'* is utilized to find a unique solution under given conditions in linear or nonlinear systems and thus prove the existence of solutions [120, 121]. The idea is to display the nonlinear PRP scheme's achievement of steady-state independent of the network parameters, with the phase at its measurement node reverting to its initial value. To solve for the steady-state operating point, the phase at 'SLK' is assumed to be equal to the phase at 'MEAS', approximating negligible impedance values of X_N and X_T. The assumptions allows the determination of phase at 'MEAS'. The network solution of (3.5) is described in A5 of the Appendix and its simplified form is:

$$\underline{V}_M = \mathrm{e}^{\mathrm{j}\varphi} \cdot c_1 + c_2 \tag{3.6}$$

Applying condition $\mathrm{Im}\{\underline{V}_\mathrm{M}\} = 0$, the voltage phase at 'MEAS' becomes independent of load R and of value zero. Substituting $\underline{V}_\mathrm{M}$ with its the magnitude and phase as $\underline{V}_\mathrm{M} = |\underline{V}_\mathrm{M}|e^{j0}$, allows to obtain an equation in terms of network impedances and $\arg(\underline{V}_C) = \varphi$. The solution is as follows:

$$\varphi = -\sin^{-1}\left(\frac{\mathrm{Im}\{c2\}}{|c1|}\right) - \arg(c1) \tag{3.7}$$

where, $c1$ and $c2$ are complex numbers depending on the network impedances with the complete solution of φ exhibited in equation (A 5.5 of Appendix A5. Equation (3.7) is giving in terms of the converter phase.

The geometrical representation of the analytical equation (3.6) is displayed in Figure 3.4. The solution is given by the intersection of the circle with the x-axis or $\mathrm{Re}\{\underline{V}_\mathrm{M}\}$. In (3.6), an arbitrary circle is defined in the plane of $(\mathrm{Re}\{\underline{V}_\mathrm{M}\}, \mathrm{Im}\{\underline{V}_\mathrm{M}\})$ with radius $|c1|$ shifted from the origin by $c2$. Equation (3.7) is obtained by imposing the condition $\mathrm{Im}\{\underline{V}_\mathrm{M}\} = 0$ to equation (A 5.5) or simplified form in (3.6). Figure 3.4 illustrates all possible solutions for the network with an arbitrary phase of converter voltage, denoted as φ. The PRP limits the solutions to the initial value of φ_0 (set to $\varphi_0 = 0$, in this scenario). At the instant of control release, initial value φ_0 of the converter phase is determined. An intersection of the circle with the real axis indicates a stable operating point of the new phase φ with respect to φ_0, while a non-intersection with the real axis suggests no potential operating point.

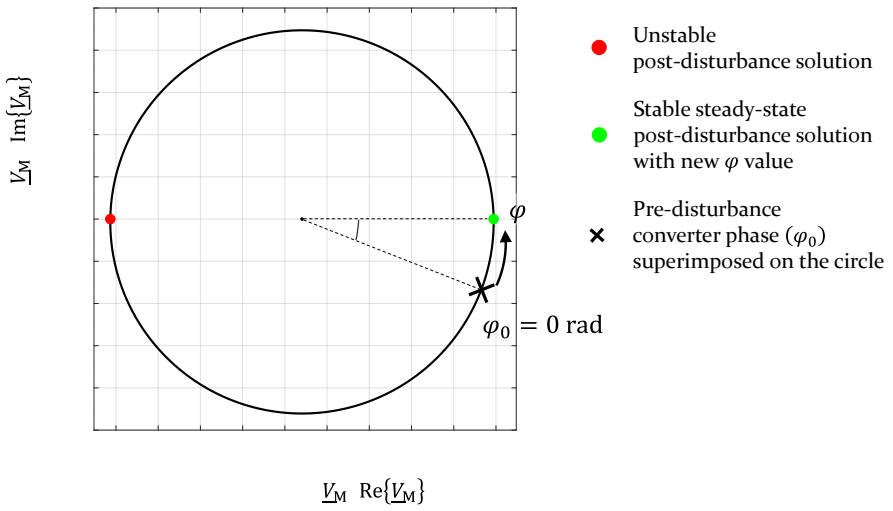

Figure 3.4: Geometrical solution of $\underline{V}_\mathrm{M}$ according to equation (3.6) parameterized by converter voltage phase φ given in equation (3.7).

As the converter phase (φ) value increases, the circle is traced counterclockwise, with 0 radians (marked ×) as the initial value. To better comprehend the post-event solution development, the initial phase is superimposed on the Figure 3.4. There exist two intersections of the circle with $\mathrm{Re}\{\underline{V}_\mathrm{M}\}$ represents regular (**green dot**) and irregular (**red dot**) conditions. Here, irregularity refers to phase opposition appearing at the initial value's far end. The Phase Restoring control achieves the steady-state value by following the direct path lying closest to the starting point (0 radians). The network solutions described here are high voltage low current (regular) or high current low voltage (irregular). From power system theory, these two solutions exist for transmitting power over long distances with minimal losses. PRP acts towards the regular solution.
The network shown in Figure 3.3 is analyzed to determine the parameter conditions under which steady-state is achieved. Equation (A 5.5) aids to achieve the following two expressions:

$$|c1|^2 = \Big(\big(X_\mathrm{N}{}^2 X_\mathrm{T}(X_\mathrm{T}+X_\mathrm{C}) + R^2(X_\mathrm{N}+X_\mathrm{T})(X_\mathrm{C}+X_\mathrm{N}+X_\mathrm{T})\big)^2 + \big(RX_\mathrm{C}X_\mathrm{N}{}^2\big)^2\Big) \tag{3.8}$$

$$\mathrm{Im}\{c2\} = -\big(RX_\mathrm{C}X_\mathrm{N}(X_\mathrm{C}+X_\mathrm{T})\big) \tag{3.9}$$

The complex form equivalent to (3.7) is presented in (3.10), and the complete solution of both is in (A 5.5) of Appendix.

$$|c1|\mathrm{Im}\{\mathrm{e}^{\mathrm{j}(\varphi+arg(c1))}\} = -\mathrm{Im}\{c2\} \tag{3.10}$$

The dependence on power system parameters is analyzed utilizing (3.10), to determine the range of validity for the PRP.

3.2.1 Determination of network parameters ranges

This section derives the constraints on parameter ranges required to obtain a steady-state solution. The application of upper bound estimates reduces the number of parameters. The objective is to identify the parameter constraints (X_T where X_C is given) under which network parameters can be arbitrarily varied (R and X_N). The mathematical estimates determined utilizing upper and lower bounds help define the basic design parameters of the PRP-based GFM system.

Equation (3.10) describes a circle with radius $|c1|$ with the origin translated by $c2$. The necessary condition for intersection with real line (in Figure 3.4)

referenced in (3.11) states that the radius must be greater than or equal to the shift origin along the imaginary line. Three assumptions are formulated and proved in the following sections to define the boundaries of the operating point.

$$|c1|^2 \geq (-\mathrm{Im}\{c2\})^2 \tag{3.11}$$

3.2.1.1 Assumption 1 - Considering $R > X_C$

Deduction. Considering the left hand side (LHS) of (3.11) and neglecting the first term to establish larger than condition for $|c1|^2$. Neglecting the last term in (3.8) as it is a square of positive terms, the following is obtained:

$$\begin{gathered} |c1|^2 > \\ \left(\left(\left(R^2(X_N + X_T)(X_C + X_N + X_T)\right)^2 + \left(RX_C{X_N}^2\right)^2\right)\right) \\ > \left(\left(R^2(X_N + X_T)(X_C + X_N + X_T)\right)^2\right) \end{gathered} \tag{3.12}$$

Additionally, neglecting X_T in the first bracket and X_N in the second bracket to establish a relation in similar terms of $\mathrm{Im}\{c2\}$. The resultant is:

$$|c1|^2 > \left(\left(R^2(X_N)(X_C + X_T)\right)^2\right) \tag{3.13}$$

Now, applying the initial condition $R > X_C$, and substituting one R term with X_C, delivers:

$$|c1|^2 > \left(RX_C(X_N)(X_C + X_T)\right)^2 > (\mathrm{Im}\{c2\})^2 \tag{3.14}$$

The final inequality hold true as it is based on the initial hypothesis that $R > X_C$. This leads to $c1^2 > c2^2 \equiv |c1| > |c2|$, since $\mathrm{Im}\{c2\} = RX_C{}^2X_N + X_CX_NX_T$ (as witnessed by comparing (3.7) and (A 5.5).

Remark 1: It is deduced that a globally stable solution is achieved by ensuring that the radius $c1$ is always greater than the shift of the origin along the imaginary axis, $\mathrm{Im}\{\underline{V}_M\}$. This implies, R must be greater than X_C. The condition above guarantees the intersection of the circle with the real axis, $\mathrm{Re}\{\underline{V}_M\}$, resulting in a steady operating point. Additionally, $R > X_C$ describe typical power system load, such as nominal load with $R \sim 10 \times X_C$.

3.2.1.2 Assumption 2 - Complement to Assumption 1, i.e., $R < X_C$

Deduction. Starting with the same consideration of as in *Assumption 1* and neglecting the first term devoid of R and the related hypothesis

dependency on X_C in the LHS of (3.11). Thus, creating inequalities and resulting in the following:

$$|c1|^2 > \left(\left(\left(R^2(X_N + X_T)(X_C + X_N + X_T)\right)^2 + \left(RX_C{X_N}^2\right)^2\right)\right) \tag{3.15}$$

Assuming $X_T = 0$, and applying to the inequality in (3.15), gives:

$$|c1|^2 > \left(\left(\left(R^2(X_N)(X_C + X_N)\right)^2 + \left(RX_C{X_N}^2\right)^2\right)\right) \tag{3.16}$$

Considering the RHS of (3.11) and using the above assumption of $X_T = 0$, and equating the resultant to (3.16), produces the expression:

$$\begin{aligned} |c1|^2 > \left(\left(\left(R^2(X_N)(X_C + X_N)\right)^2 + \left(RX_C{X_N}^2\right)^2\right)\right) \\ = \left(RX_CX_N(X_C)\right)^2 \end{aligned} \tag{3.17}$$

Applying the inference deduced in *Assumption 1* for *global stability*, $c1 > c2$, implies LHS>RHS. Using this logic in (3.17), the form below evolves:

$$\left(\left(\left(R^2(X_N)(X_C + X_N)\right)^2 + \left(RX_C{X_N}^2\right)^2\right)\right) > \left(RX_CX_N(X_C)\right)^2 \tag{3.18}$$

Considering common terms and simplifying (3.18) results into:

$$\left(R(X_C + X_N) + (X_CX_N)\right)^2 > (X_CX_C)^2 \tag{3.19}$$

For the condition in (3.19) to be untrue, implies LHS<RHS. Thus, the resultant is indicated in (3.20) and (3.21) by equating terms of each side.

$$(X_CX_N) < (X_CX_C) \Rightarrow X_N < X_C \tag{3.20}$$

$$R(X_C + X_N) < (X_CX_C) \Rightarrow R \ll X_C \tag{3.21}$$

Remark 2: It is deduced from (3.20) and (3.21), the conditions under which the network equations fail to satisfy the steady-state solution or $|c1| < |c2|$ leading to no intersection with the real axis. This suggests that a steady-state operating point for the Phase Restoring control will not be achieved with the above network conditions, $X_N < X_C$ and $R \ll X_C$ and $X_T = 0$. The transformer impedance (X_T) is a decisive parameter and cannot be disregarded in controller design.

3.2.1.3 Assumption 3 - Considering $X_T \geq X_C$

Deduction. *Assumption 3* stability criteria is based on (3.11) and the global stability inference of $|c1| > |c2|$ from *Assumption 1*. By neglecting the last term in the RHS of (3.8) the inequality condition below is established:

$$\begin{pmatrix} {X_N}^2 X_T (X_T + X_C) + R^2 (X_N + X_T) \\ (X_C + X_N + X_T) \end{pmatrix}^2 > \left(R X_C X_N (X_C + X_T)\right)^2 \tag{3.22}$$

The LHS of the inequality in (3.22) is examined, and compared with $|c2|$ to obtain similar terms. Applying the assumption that $X_T \geq X_C \Rightarrow X_C \leq X_T$ to the second term $(X_N + X_T)$ and neglecting X_N with respect to X_C in $(X_C + X_N + X_T)$ of the second term in LHS, the expression below is obtained:

$$|c1|^2 > \left({X_N}^2 X_T (X_T + X_C) + R^2 (X_N + X_C)(X_C + X_T)\right)^2 \tag{3.23}$$

Taking common terms from the LHS in (3.23) and RHS in (3.22) and applying square root on both side, the following is derived:

$$\left({X_N}^2 X_T + R^2 (X_N + X_C)\right) > (R X_C X_N) \tag{3.24}$$

Inference 3: As it has been previously concluded that $R > X_C$, always gives a globally stable solution. Further, boundary conditions are applied to (3.24) for determining the lower limits of X_C (sub-section 3.2.1.4 and 3.2.1.5).

3.2.1.4 Assumption 3a - Considering $R < X_C$ and $R < X_N$

Deduction. The LHS of (3.24) is analyzed by applying the assumption $X_T \geq X_C$, and the following condition is obtained:

$$LHS > \left({X_N}^2 X_C + R^2 (X_N + X_C)\right) \tag{3.25}$$

By applying the assumption $R < X_N$, and substituting R for X_N in the first term and X_N for R in the second term of (3.25), leads to:

$$\left({X_N}^2 X_C + R^2 (X_N + X_C)\right) \xrightarrow{yields} \left(R X_N X_C + R X_N (X_N + X_C)\right) \tag{3.26}$$

Analogizing RHS terms in (3.26) to the RHS of (3.24), the following resulting terms are concluded:

$$\left(\underbrace{(RX_{\mathrm{C}}X_{\mathrm{N}})} + RX_{\mathrm{N}}(X_{\mathrm{N}} + X_{\mathrm{C}})\right) > (RHS + additional\ terms) > \left(\underbrace{RX_{\mathrm{C}}X_{\mathrm{N}}}\right) \tag{3.27}$$

Inference 3a: The inequality demonstrated suggests that the assumptions made are valid and that the LHS > RHS based on the premises considered.

3.2.1.5 Assumption 3b - Considering $R < X_{\mathrm{C}}$ and $R > X_{\mathrm{N}}$

Deduction. By considering the initial hypothesis presented in (3.24) and applying the supposition $X_{\mathrm{C}} \leq X_{\mathrm{T}}$ to the LHS of the inequality, the result below is reached:

$$LHS > \left({X_{\mathrm{N}}}^2 X_{\mathrm{C}} + R^2(X_{\mathrm{N}} + X_{\mathrm{C}})\right) \tag{3.28}$$

Additionally applying $R > X_{\mathrm{N}}$, and simplifying:

$$\left({X_{\mathrm{N}}}^2 X_{\mathrm{C}} + RX_{\mathrm{N}}\,(X_{\mathrm{N}} + X_{\mathrm{C}})\right) \xrightarrow{yields} \left({X_{\mathrm{N}}}^2 X_{\mathrm{C}} + R{X_{\mathrm{N}}}^2 + RX_{\mathrm{N}}X_{\mathrm{C}}\right) \tag{3.29}$$

On comparing the outcome in (3.29) to the RHS of (3.24), (3.30) is inferred.

$$\left({X_{\mathrm{N}}}^2 X_{\mathrm{C}} + R{X_{\mathrm{N}}}^2 + \underbrace{RX_{\mathrm{C}}X_{\mathrm{N}}}\right) > (additional\ terms + RHS) > \left(\underbrace{RX_{\mathrm{C}}X_{\mathrm{N}}}\right) \tag{3.30}$$

Inference 3b: Therefore, the assumptions are true.

Remark 3: ***Assumption 3a*** and ***Assumption 3b*** outline the criteria for stable operating points. The condition $R < X_{\mathrm{C}}$, always hold true since the preconditions was derived from ***Assumption 2***, which defines the limits for X_{T} and $R << X_{\mathrm{C}}$. $R \to 0$, maybe inferred as a short circuit condition, irrespective of X_{N} value, and the control acts to attains stable operating point under this condition.

One significant conclusion drawn from this hypothesis is the pivotal role of transformer impedance in the overall performance of converter control. In addition, the coupling reactance X_{C} or impedance Z_{C} and the transformer reactance X_{T} or impedance Z_{T} are design parameters of the converter control system (neglecting resistive part). They are specified during the basic design process. Hence, X_{C} and X_{T} are not network branches but quintessential parts of the converter system stability. The *'Existence Theorem'* proves that control stability is independent of network impedance or X_{N}. Thus, the proceedings provide necessary and sufficient evidence for the PRP scheme [29].

3.3 Small-signal stability analysis

The devised analytical approach evaluates the stability under independent network loading of the closed-loop nonlinear Phase Restoring control scheme via *linearization*. The small-signal stability analysis approach and details have been discussed in Section 2.4.3.2.

The network model is reduced, and small-signal *linearization* is performed on the controller structure, represented by transfer functions in Laplace domain. Firstly, small-signal system stability analysis with a restriction on the load model (R) at PCC is conducted, indicating a typical small-signal disturbance. This task is intentionally enacted to display simulation responses under regular network loading conditions with sufficiently large load or R values corresponding to small phase conditions.

Subsequently, the general small-signal solution in frequency domain is derived, displaying the stability of the closed-loop system independent of network loading and, by extension, global stability of the control.

As the network topology is not of prime focus but, the control, the structure of PRP in Figure 3.2 is considered for analytical calculation and linear approximation. The reduced-order network shown in Figure 3.5 is used in conjunction with the linearized Phase 1 control model in dq representation.

The 1st order measurement delays have been ignored in the reduced order analytical and the simulative model to facilitate small-signal analysis. The reduced order network shown in Figure 3.5 is similar to the test bench depicted in Figure 3.3. The total impedance '$X = sL$' includes the coupling impedance 'X_C' and transformer impedance 'X_T' The resistive load is represented by 'R', similar to Figure 3.3. In this context, '$U(s)$' represents the converter source voltage, which is analogous to '$\underline{V_C}$', and '$V(s)$' is equivalent to the voltage at the measurement node '$\underline{V_M}$' in the frequency domain. This analogy is valid as only one equivalent impedance has been assessed.

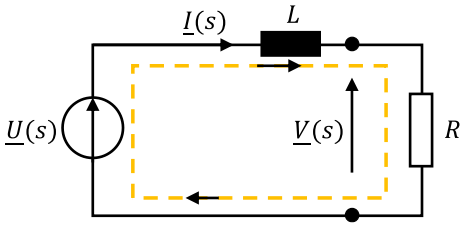

Figure 3.5. Reduced test network consisting of source and load utilized for linearization, with outer (network) loop highlighted in **yellow**.

Linear approximation is conducted by evaluating the Taylor series expansion about the point of interest. The steps involved in *linearization* and the components used to derive the transfer function are presented in the following sub-sections. At this stage, it is not mandatory to introduce the new coordinate system $\rho_{dr}\iota_{dr}$ in the derivation of the analytical results. Instead, the controller's internal quantities are directly represented in the dq coordinate system as obtained from *linearization***.** The linearization of PRP evolved in a two-step approach.

3.3.1 Small-signal analysis for typical power system loads

A solution is initially established for realistic loads in the power system ($R \geq 1$ pu) with sufficiently small phases as an operating point and is visualized by numerical methods. Here $R = 1$ pu corresponds to nominal load or regular network loading.

For facilitating small-signal analysis, the feedback loop with phase integrator is simplified as a first-order system, and eliminating inverse dynamics. The resultant reduced-order PRP control scheme is shown in Figure 3.6. This reduced order model is analyzed within the context of the reduced closed-loop test bench depicted in Figure 3.5. The closed-loop control transfer functions are derived in the Laplace domain by considering the network and converter's physical relationships. The overall transfer function is determined by assessing all individual components. Based on the analytical model, inferences are drawn to confirm the stability of the control system and verify simulatively. It is worth noting that Figure 3.5 and Figure 3.6 illustrate the presence of two loops: an outer loop comprising the network with the control (highlighted in **yellow**) and an inner feedback loop corresponding to the controller (highlighted in **blue**), respectively.

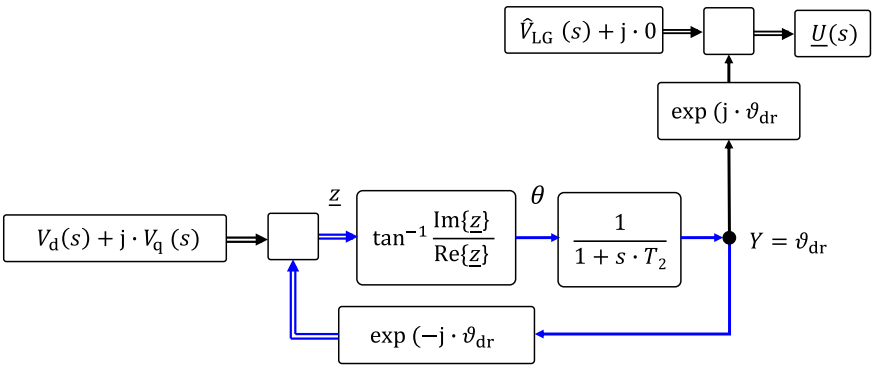

Figure 3.6.: Reduced and simplified Phase Restoring control scheme (PRP) for linearization, with inner (control) loop highlighted in **blue**.

According to the control principle, the primary assumptions for the *linearization* of the control are provided by (3.31) and (3.32). Linear approximation is performed by utilizing the Taylor series expansion (as in (2.8) and (2.9)) about the development point with converter voltage $\hat{V}_{\mathrm{LG}}$ with a phase $\varphi_0 = 0$. The assumed operating point considered is mentioned in sub-section 3.2 and is valid for all large resistive load ($R \geq 1$ pu). The choice of the dq transformation leads to a negligibly small V_{q}. The input measurement voltage to the control is decomposed in dq domain and rotated with the nominal frequency to αβ. Consequently, the dq transformation frequency corresponds to ω_{n}.

$$\underline{v}(t) = \underline{\hat{V}} \mathrm{e}^{(\mathrm{j}\omega_{\mathrm{n}} t)} = \left(V_{\mathrm{d}}(t) + \mathrm{j}V_{\mathrm{q}}(t)\right) \mathrm{e}^{(\mathrm{j}\omega_{\mathrm{n}} t)} \tag{3.31}$$

$$V_{\mathrm{d}}(t) \gg V_{\mathrm{q}}(t) \tag{3.32}$$

By *linearization* of the exponential function $\mathrm{e}^{(-\mathrm{j}\vartheta_{\mathrm{dr}})}$, in Figure 3.6, such that $\vartheta_{\mathrm{dr}} \ll 1$, leads to:

$$\mathrm{e}^{(-\mathrm{j}\vartheta_{\mathrm{dr}})} \approx (1 - \mathrm{j}\vartheta_{\mathrm{dr}}) \tag{3.33}$$

Multiplication of the linearized exponential function with the input voltage is performed, with the consideration of the initial assumption, $v_{\mathrm{d}}(t) \gg v_{\mathrm{q}}(t)$. Equation (3.35) is derived based on initial condition stated below:

$$V_{\mathrm{d}}(t) \cong \hat{V}_{\mathrm{LG}} \tag{3.34}$$

$$\underline{z} \approx \hat{V}_{\mathrm{LG}} + \mathrm{j}\left(V_{\mathrm{q}}(t) - \hat{V}_{\mathrm{LG}} \cdot \vartheta_{\mathrm{dr}}(t)\right) \tag{3.35}$$

Further *linearization* of the argument of the resultant complex function $arg\{\underline{z}\} = \tan^{-1} \frac{\mathrm{Im}\{\underline{z}\}}{\mathrm{Re}\{\underline{z}\}}$ yields:

$$\theta(t) \approx \tan^{-1}\left(\frac{V_{\mathrm{q}}(t)}{\hat{V}_{\mathrm{LG}}} - \vartheta_{\mathrm{dr}}(t)\right) \tag{3.36}$$

Applying the assumptions of (3.37) to (3.36), (3.38) is achieved.

$$V_{\mathrm{q}}(t) \cong 0.0 \tag{3.37}$$

$$\theta(t) \approx \left(\frac{V_{\mathrm{q}}(t)}{\hat{V}_{\mathrm{LG}}} - \vartheta_{\mathrm{dr}}(t)\right) \tag{3.38}$$

The inner algebraic control loop in frequency domain is determined by multiplying first order system ($\frac{-1}{(1+sT)}$), and the result attained is:

$$Y \approx -\frac{\left(V_{\mathrm{q}}(s)\middle/\hat{V}_{\mathrm{LG}}\right)}{[sT]} \tag{3.39}$$

Further calculating the converter voltage $\underline{U}(s)$ as a function of the measured input voltage $\underline{V}(s)$, the expression derived is:

$$\underline{U}(s) = \hat{V}_{\mathrm{LG}} - \mathrm{j}\frac{V_{\mathrm{q}}(s)}{[sT]} \tag{3.40}$$

A q/q controller transfer function is defined for further proceedings, with measurement voltage as output and converter voltage as input.

$$\begin{aligned} \hat{V}_{\mathrm{LG}} - \mathrm{j}\frac{V_q}{[sT]} \rightarrow \frac{Measurement\ voltage}{Converter\ voltage} \rightarrow \frac{V_{\mathrm{q}}(s)}{Im\{U(s)\}} \\ = \frac{V_{\mathrm{q}}(s)}{-V_{\mathrm{q}}(s)\middle/[sT]} = -[sT] \end{aligned} \tag{3.41}$$

Comparing (3.39) to (3.41) reveals an inverse relationship, thus indicating that the controller's transfer function corresponds to the inverse of the inner loop. This calculation aims to determine the measurement voltage $\underline{V}(s)$, a deemed output quantity.
The network equations in the Laplace domain for the reduced circuit model (as in Figure 3.5) considered for small-signal analysis are denoted by:

$$\underline{U}(s) - \underline{I}(s) \cdot sL - \underline{V}(s) = 0 \tag{3.42}$$

$$\underline{V}(s) = R \cdot \underline{I}(s) \tag{3.43}$$

By identifying $\underline{U}(s)$ as part of the network and solving the outer algebraic network loop for the complete closed-loop solution, the resulting network equations in dq frame are shown in equation (3.44). The application of frequency shifting property described in Appendix A6 to (3.42) yields the network solution in dq frame.

$$\begin{bmatrix} V_{\mathrm{d}}(s) \\ V_{\mathrm{q}}(s) \end{bmatrix} = \begin{bmatrix} -sL & \omega_n L \\ -\omega_{\mathrm{n}} L & -sL \end{bmatrix} \begin{bmatrix} I_{\mathrm{d}}(s) \\ I_{\mathrm{q}}(s) \end{bmatrix} + \begin{bmatrix} U_{\mathrm{d}}(s) \\ U_{\mathrm{q}}(s) \end{bmatrix} \tag{3.44}$$

Substituting the values of $\underline{U}(s)$ from (3.40) into the network equations (3.44) and solving for $\underline{V}(s)$ yields the final solution. On comparing to the theory mentioned in Section 2.4.3.2, the Jacobian matrix in (3.45) can be inferred. The intermediate steps are as follows:

$$\begin{bmatrix} V_{\mathrm{d}}(s) \\ V_{\mathrm{q}}(s) \end{bmatrix} = \begin{bmatrix} -sL & \omega_{\mathrm{n}}L \\ -\omega_{\mathrm{n}}L & -sL \end{bmatrix} \begin{bmatrix} I_{\mathrm{d}}(s) \\ I_{\mathrm{q}}(s) \end{bmatrix} + \begin{bmatrix} \hat{V}_{\mathrm{LG}} \\ V_{\mathrm{q}}(s) \Big/ _{[sT]} \end{bmatrix} \tag{3.45}$$

$$\begin{bmatrix} 1 + sL/_R & -\omega_{\mathrm{n}}L/_R \\ \omega_{\mathrm{n}}L/_R & 1 + sL/_R + 1/_{[sT]} \end{bmatrix} \begin{bmatrix} V_{\mathrm{d}}(s) \\ V_{\mathrm{q}}(s) \end{bmatrix} = \begin{bmatrix} \hat{V}_{\mathrm{LG}} \\ 0 \end{bmatrix} \tag{3.46}$$

The complete solution for the closed-loop system is provided by (3.47) with the determinant (det(**A**)) designated in (3.48). The solution is viable within the considered the range of *linearization* for all $R \geq 1$ pu.

$$\begin{bmatrix} V_{\mathrm{d}}(s) \\ V_{\mathrm{q}}(s) \end{bmatrix} = \frac{1}{\det(\mathbf{A})} \begin{bmatrix} 1 + sL/_R + 1/_{[sT]} & \omega_{\mathrm{n}}L/_R \\ -\omega_{\mathrm{n}}L/_R & 1 + sL/_R \end{bmatrix} \begin{bmatrix} \hat{V}_{\mathrm{LG}} \\ 0 \end{bmatrix} \tag{3.47}$$

$$\det(\mathbf{A}) = \left(1 + sL/_R + 1/_{[sT]}\right)\left(1 + sL/_R\right) + \left(\omega_{\mathrm{n}}L/_R\right)^2 \tag{3.48}$$

In order to draw conclusions, common terms in (3.47) are grouped. The resultant is denoted in (3.49) or succinct as in (3.50) with a rearranged determinant in (3.51).

$$\begin{bmatrix} V_{\mathrm{d}}(s) \\ V_{\mathrm{q}}(s) \end{bmatrix} = \frac{[sT]}{\det(\mathbf{A})} \begin{bmatrix} 1 + sL/_R + 1/_{[sT]} & \omega_{\mathrm{n}}L/_R \\ -\omega_{\mathrm{n}}L/_R & 1 + sL/_R \end{bmatrix} \begin{bmatrix} \hat{V}_{\mathrm{LG}} \\ 0 \end{bmatrix} \tag{3.49}$$

$$\begin{bmatrix} V_{\mathrm{d}}(s) \\ V_{\mathrm{q}}(s) \end{bmatrix} = \frac{-(Eq.\,(3.41))}{\det(\mathbf{A})} \begin{bmatrix} 1 + sL/_R + 1/_{[sT]} & \omega_{\mathrm{n}}L/_R \\ -\omega_{\mathrm{n}}L/_R & 1 + sL/_R \end{bmatrix} \begin{bmatrix} \hat{V}_{\mathrm{LG}} \\ 0 \end{bmatrix} \tag{3.50}$$

$$\det(\mathbf{A}) = [sT]\left[\left(1 + sL/_R\right)^2 + \left(\omega_{\mathrm{n}}L/_R\right)^2\right] + \left(1 + sL/_R\right) \tag{3.51}$$

Substituting $s = 0$ under steady-state (as in Appendix A6), in (3.47) and solving for voltages, gives:

$$\begin{bmatrix} V_{\mathrm{d}}(0) \\ V_{\mathrm{q}}(0) \end{bmatrix} = \begin{bmatrix} 1 & 0 \\ 0 & 0 \end{bmatrix} \begin{bmatrix} \hat{V}_{\mathrm{LG}} \\ 0 \end{bmatrix} \tag{3.52}$$

Remark: From (3.52) it is inferred that the Phase Restoring Principle (PRP) is valid at the nominal frequency (which corresponds to 0 frequency in dq domain). The measurement voltage $\underline{V}(s)$ is constant and, therefore, independent of the network elements, leading to a constant phase in the voltage $\underline{V}(0)$.

A significant conclusion from this section pertains to (3.41), which shows that the controller transfer function corresponds to an integrator. This integrator is responsible for achieving the operating point and, thus, the solution on the circle, as shown in Figure 3.4. Furthermore, the solution in (3.50) demonstrates the presence of integrator action. These deductions further help to confirm and provide visual support for the findings presented in Section 4.2 [29].

3.3.2 General solution in frequency domain

The small-signal solution evidenced in sub-section 3.3.1 is applicable only within the linearization range for all $R \geq 1$ pu. Therefore, the validity of the solution is restricted to load models at PCC with sufficiently large 'R' values that correspond to small phase conditions. A general small signal solution is derived by extending the restricted solution to all network loading conditions. This enables to incorporate arbitrary phase conditions with no constraints on the load (R).

A q/q controller transfer function (3.41) is obtained through the linearization technique during the small-signal analysis. This transfer function approximates the phase/phase equivalent for small values. The evaluation is valid since the quadrature component of the voltage (V_q) is comparable to the argument of the voltage, only under the range of linearization. This is further discussed with simulations in Section 4.2.

The complete solution can be separated into the network solution and the control solution. The reduced-order network shown in Figure 3.5 is used in conjunction with the linearized full control model in dq representation. The control loop shown in Figure 3.7 (in **blue**) is analyzed for the general solution, intentionally ignoring active power control (APC). It is to be noted that small-signal stability is marginally affected due to the choice of gain parameters.

Assumption 1: The network equations in Laplace domain for the reduced circuit model for small-signal analysis are presented in (3.42) and (3.43).The equations are identical to the previous sub-section for small-signal analysis. Application of frequency shifting property (Appendix A6) to (3.42) yields

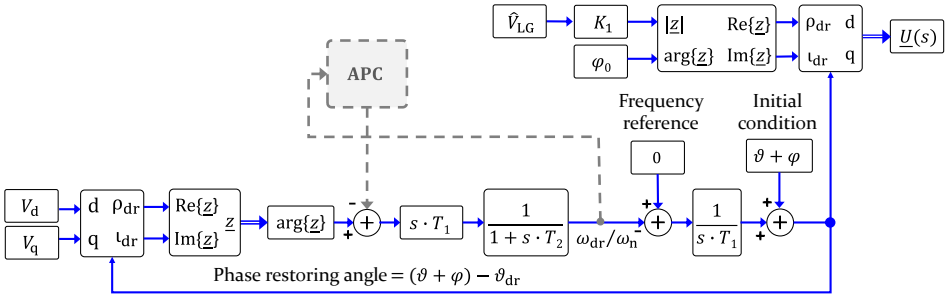

Figure 3.7.: Reduced order Phase Restoring control scheme (PRP) in dq domain for linearization marked in **blue**.

the following network solution in dq frame, expressed in terms of $U(s)$.

$$\underline{U}(s) = \underline{V}(s)\left[1 + \frac{L}{R} \cdot (s + \mathrm{j} \cdot \omega)\right] \tag{3.53}$$

Assumption 2: As mentioned in Section 2.4.3.2, *linearization* is performed around the development point. The control operating point is obtained by applying the stated development points with $|\underline{\hat{V}}| = \hat{V}_{LG} = 1$ pu and phase $\varphi_0 = 0$, as cited in Section 3.2. The result is presented in (3.54). However, for the general solution the measured voltage is decomposed into a constant and small variation (Δ) component. In PRP, *linearization* is performed for steady-state operation under the conditions $V_q \approx 0$ and $\Delta V_d \approx 0$. Based on the assumptions cited in (3.54) and on further simplification based on *complex number theory* [132], leads to (3.55).

$$\begin{aligned} \underline{V}(s) = \; & V_d(s) + \mathrm{j} \cdot V_q(s) = (V_d + \Delta V_d)(s) + \mathrm{j} \cdot (V_q + \Delta V_q)(s) \\ & = V_d(s) + \mathrm{j} \cdot \Delta V_q(s) \approx V_d(s) \cdot \mathrm{e}^{(\mathrm{j} \cdot \Delta\varphi)} \end{aligned} \tag{3.54}$$

$$\Delta V_q(s) \approx V_d(s) \cdot \Delta\varphi \tag{3.55}$$

Generalized Proof: To compute the general solution, the measurement voltage is expressed as an expansion around the development point or steady-state phase φ and the small-signal component $\Delta\varphi$ as shown in:

$$\underline{V}(s) = |\underline{\hat{V}}|\mathrm{e}^{\mathrm{j} \cdot (\varphi + \Delta\varphi)} = |\underline{\hat{V}}|\mathrm{e}^{\mathrm{j} \cdot \varphi}\mathrm{e}^{\mathrm{j} \cdot \Delta\varphi} \tag{3.56}$$

Using the block diagram shown in Figure 3.7 and expressing the converter voltage $\underline{U}(s)$ in terms of measured voltage $\underline{V}(s)$, (3.57) is obtained. The general arbitrary phase of the converter voltage is expanded around the steady-state operating point or load flow phase, $(\vartheta + \varphi)$ with a small-signal deviation of $\Delta\vartheta$.

$$\underline{U}(s) = \; \hat{V}_{LG}\mathrm{e}^{\mathrm{j} \cdot (\vartheta + \Delta\vartheta + \varphi)} \tag{3.57}$$

The solution of the inner feedback loop in the control (marked **blue**) is given by $(\vartheta + \Delta\vartheta + \varphi)$, where the input voltage phase is $(\varphi + \Delta\varphi)$. Solving the control feedback loop under the condition, where the voltage source input is equal to the transformed measured phase, results into:

$$\underbrace{\vartheta + \Delta\vartheta + \varphi}_{\text{Input Phase}} = \underbrace{\{(\varphi + \Delta\varphi) - \Delta\vartheta - (\vartheta + \varphi)\} \cdot (sT_1) \cdot \frac{1}{(1 + sT_2)} \cdot \left(-1 \cdot \frac{1}{(sT_1)}\right)}_{\text{Transformed Measured Phase}} \tag{3.58}$$

The negative input phase in the transformation is a result of the feedback in the control. Simplifying (3.58) provides:

$$\vartheta + \Delta\vartheta + \varphi = \{\varphi + \Delta\varphi - \Delta\vartheta - \vartheta - \varphi\} \cdot \frac{-1}{(1 + sT_2)} \tag{3.59}$$

Assessing steady-state frequency by rearranging and first evaluating constant terms with $s = 0$ in dq domain as in (3.59), below is attained:

$$\begin{aligned} \vartheta + \varphi &= -(\varphi - \vartheta - \varphi) \\ \Rightarrow\ \varphi &= 0\ (constant) \end{aligned} \tag{3.60}$$

Therefore, setting $s = 0$ implies $\varphi = 0$, but the differentiator is a surjection and any constant φ yields a solution. Thus, with φ as arbitrary constant $f: \partial\varphi \to 0$. Examining the rest of the terms in (3.59), including the change in phase (Δ terms). Discarding contributions from constant phase terms (as constant φ and ϑ cancelled by the differentiator) in (3.59) obtains:

$$\Delta\vartheta = -(\Delta\varphi - \Delta\vartheta) \cdot \frac{1}{(1 + sT_2)} \tag{3.61}$$

On solving for $\Delta\vartheta$, the solution achieved is:

$$\Delta\vartheta = -\frac{\Delta\varphi}{(sT_2)} \tag{3.62}$$

where, $\Delta\vartheta$ is the small-signal variation in the feedback loop.

As mentioned above, the input measurement phase is decomposed into two parts consisting of φ or the load flow phase and $\Delta\varphi$ the small change in phase such that $\Delta\varphi \approx 0$. Linearizing the input voltage signal in (3.56) around φ, results in:

$$\underline{V}(s) \approx (1 + \mathrm{j} \cdot \Delta\varphi) \cdot \left|\hat{\underline{V}}\right| \mathrm{e}^{\mathrm{j} \cdot \varphi} \tag{3.63}$$

$\underline{U}(s)$ or (3.57) is linearized around $\Delta\vartheta$ to attain:

$$\underline{U}(s) \approx \hat{V}_{\mathrm{LG}} \mathrm{e}^{\mathrm{j}\cdot(\vartheta+\varphi)} \cdot (1 + \mathrm{j} \cdot \Delta\vartheta) \tag{3.64}$$

Substituting $\Delta\vartheta$ from (3.62) in the linearized solution (3.64), the following is deduced:

$$\underline{U}(s) \approx \hat{V}_{\mathrm{LG}} \mathrm{e}^{\mathrm{j}\cdot(\vartheta+\varphi)} \cdot \left(1 - \mathrm{j} \cdot \frac{\Delta\varphi}{(sT_2)}\right) \tag{3.65}$$

By equating network solution in (3.53) to the solution in (3.65), and substituting the linearized solution for $\underline{V}$ (s) from (3.63) leads to:

$$\begin{aligned} \left|\underline{\hat{V}}\right| \mathrm{e}^{\mathrm{j}\cdot\varphi} \cdot (1 + \mathrm{j} \cdot \Delta\varphi) \left[1 + \frac{L}{R}(s + \mathrm{j} \cdot \omega_{\mathrm{n}})\right] \\ = \hat{V}_{\mathrm{LG}} \mathrm{e}^{\mathrm{j}\cdot(\vartheta+\varphi)} \cdot \left(1 - \mathrm{j} \cdot \frac{\Delta\varphi}{(sT_2)}\right) \end{aligned} \tag{3.66}$$

Equation (3.66) represents the general network solution valid in steady-state (load flow) conditions. It is derived from (3.53) and (3.57). By applying the property of equality to the constant terms, as per the $\Delta\varphi$-independent terms of (3.66), (3.67) must hold true.

$$\left|\underline{\hat{V}}\right| \mathrm{e}^{\mathrm{j}\cdot\varphi} \left[1 + \frac{L}{R}(s + \mathrm{j} \cdot \omega_{\mathrm{n}})\right] = \hat{V}_{\mathrm{LG}} \mathrm{e}^{\mathrm{j}\cdot(\vartheta+\varphi)} \tag{3.67}$$

Equating remaining $\Delta\varphi$-dependent terms of (3.66), by taking into account the deduction in (3.67), the solution arrived at is:

$$\Delta\varphi = -\frac{\Delta\varphi}{(sT_2)} \tag{3.68}$$

and hence we can conclude:

$$\Delta\varphi = 0 \tag{3.69}$$

Inference: In (3.69), it is established that decomposing the arbitrary measurement phase into its constant and small variable components results in $\Delta\varphi$ being zero for steady-state, corresponding to $s = 0$ (in dq frame). As derived in (3.60), the constant phase contribution is zero in PRP control scheme. This demonstrates the validity of linearizing the solution around zero (small phases) and thus proved for arbitrary φ. The general solution given in (3.66) holds for all values of $R > 0$ (independent of network loading). The linearized model for small-signal with arbitrary R values representing the load at the PCC, displays the control's steady-state behavior in achieving arbitrary demands at the network and therefore exhibits global stability [30].

The general solution confirms the PRP control's stable performance independent of network loading conditions (R or X_{L}). It validates the *linearization* assumption around small phases or zero value to obtain negligibly small V_{q} with respect to the dq-frame of the network. The mathematical structure is simpler since the ansatz completely reflects the system property: namely the PRP is a rotation.

3.4 Extension via active power control

The drift frequency ($\mathrm{f_{dr}}$ or ω_{dr}) determined by PRP without active power control (APC) established zero deviation through the controller's actions relying on unlimited current. As discussed in Section 3.1, frequency is a global attribute (f or ω) only if a steady-state is reached (Fourier analysis). The APC loop is integrated into the PRP control structure to adjust the frequency in response to changes in the setpoint. It corresponds to the steady-state aspect of ω_{dr} as mentioned in Section 3.1. The PRP serves as the foundational building block and is fully GFM, with the power control dynamics enforced on top of it.

As depicted in Figure 3.8, the modified block diagram highlights the APC in **green**. Here, $S_{\mathrm{n}} = 3 \cdot V_{\mathrm{RMS}} \cdot I_{\mathrm{RMS}} = 1.5 \cdot \hat{V}_{\mathrm{LG}} \cdot \hat{I}_{\mathrm{n}}$, where $\hat{V}_{\mathrm{LG}}$ is nominal peak voltage (line-to-ground) and $\hat{I}_{\mathrm{n}}$ is nominal peak current. The inputs to the control logic are measured values obtained from the power system.

The initial conditions are maintained constant until the control is released. The APC is implemented as a proportional-integral (PI) control with a constant gain K_3, and an integral component to minimize the difference with the setpoint value. The PI block input is subtracted and the argument of the complex input voltage ($\underline{z} = \mathrm{Re}\{\underline{z}\} + \mathrm{Im}\{\underline{z}\} = |\underline{z}|e^{j arg\{\underline{z}\}}$) obtained in the new coordinate system is used as an input to the differentiator. The output value is smoothed by a $1st$ order delay, which forms the drift frequency $\frac{\omega_{\mathrm{dr}}}{\omega_{\mathrm{n}}}$ in pu, serving as input to the integrator. The integrator uses an arbitrary reference frequency (initial condition) to compute the linear part of the transformation angle or Phase Restoring angle over the control feedback, described in Section 3.1. The control's steady-state achievement with reference changes is verified through simulation in Section 4.3 using analytical solution derived here. This section examines the effects of setpoint changes and impedances on ω_{dr} in a single and double converter configuration. The unique operating range under regular conditions is determined. Additionally, adaptations to the APC for varied network loading conditions and faster response time are derived in Section 3.4.3. and establishes Phase 2 of the control.

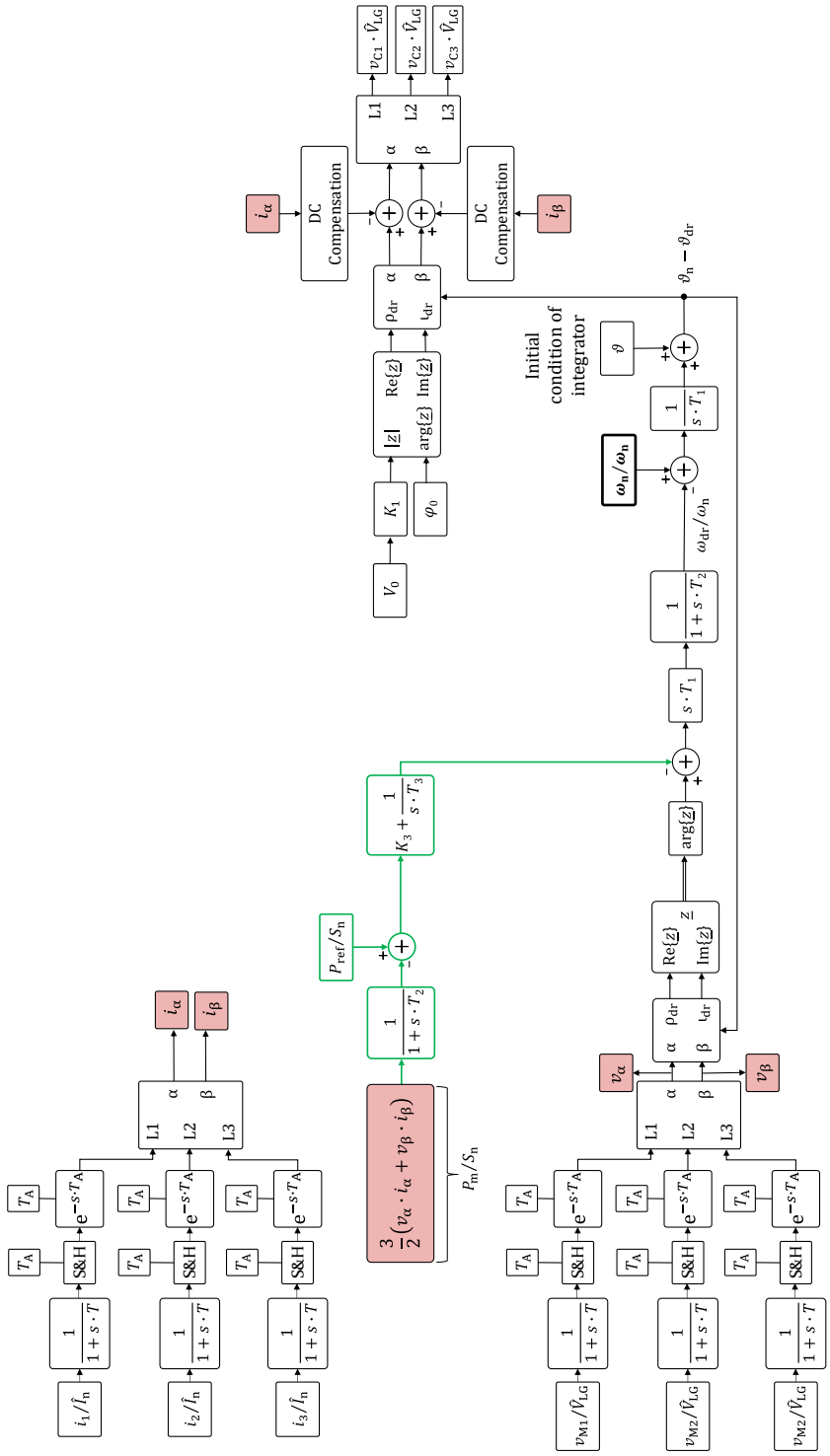

Figure 3.8: Block diagram of the Phase Restoring Principle (**PRP**) with active power control (**APC**) highlighted in **green**.

3.4.1 Mathematical deduction of single converter configuration

The single converter test setup, featuring the PRP control with APC, is depicted and highlighted in grey in Figure 3.9. The test setup is based on the previously evaluated single converter-ohmic-inductive network configuration, which is used to demonstrate the global stability conditions of the PRP control. The setup includes a source with coupling and transformer impedances (X_C and X_T), an intermediate measurement node (MEAS), and a load dynamically connected, as an event, at the PCC. The network configuration provides again a stable solution for the controller under the conditions outlined in Table 3.1 as demonstrated in Section 3.2.

This network scenario encompasses all possible ranges of applicability of the PRP control scheme and its boundary conditions. The test setup characterizes the inductive behavior under weak grid conditions ($X_N > X_C$). X_C represents 10 % nominal impedance, where the nominal impedance is given by $\frac{(V_n)^2}{S_n}$ with 1 MVA machine base (S_n). The typical range of X_C is between 6 % to 15 % of nominal impedance. The globally stable network in Table 3.1 is based on Section 3.2. The parameters may be configured as a single or two-source network described in Figure 3.9. The control stability margin increases with higher resistance in a passive network.

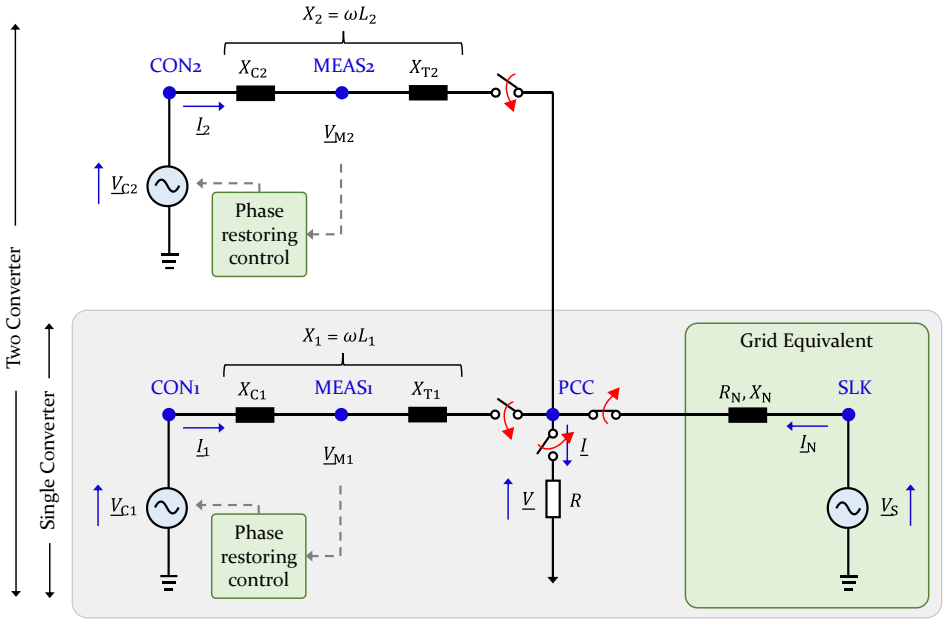

Figure 3.9: Test bench for single and double converter configurations.

Table 3.1: Network (Figure 3.9) condition and parameter considered [29].

Network condition	$X_{\mathrm{T}} = X_{\mathrm{C}}, X_{\mathrm{N}} > X_{\mathrm{C}}, R > X_{\mathrm{C}}$
Parameter	**Value**
X_{C}	0.1
X_{T}	0.1
X_{N}	$10 \times X_{\mathrm{c}}$
R	$10 \times X_{\mathrm{c}}$

To determine an operating point, it is necessary to specify two unknown variables, namely the drift frequency (f_{dr} or ω_{dr}) and active power (P_{m}). As a result, two equations are developed for deducing the solution for the operating point. In a steady-state condition, the PRP feedback loop generates a phase contribution, which is added to the output of the APC loop. The solution for the APC loop is described in (3.70), and disregards the smoothing time constant $T_2 = 0.01$ sec as it does not impact the steady-state ($s = 0$) and filters the drift frequency (F_{dr}). The active reference power (P_{ref}) is also a parameter.

$$\frac{F_{\mathrm{dr}}}{F_{\mathrm{n}}} = -\frac{(P_{\mathrm{ref}} - P_{\mathrm{m}})}{S_{\mathrm{n}}} \cdot \left(K_3 + \frac{1}{sT_3}\right) \cdot (s \cdot T_1) \tag{3.70}$$

The time constants $T_1 = 1/50$ and $T_3 = 1.0$ are in seconds. On simplifying (3.70), the control gain K_1 and $K_3 = 1$, were substituted to derive the complete steady-state control solution. The differentiation of a constant is zero and thus K_3 does not contribute to steady-state similar to PRP feedback phase. The solution is normalized in terms of angular frequency, and converter power rating, which results in the final solution represented in (3.71) and compliant with Figure 3.8. Normalization expresses equations in terms of pu.

$$\omega_{\mathrm{dr}} = 2\pi \cdot F_{\mathrm{dr}} = -\left(\frac{T_1}{T_3}\right) \cdot (P_{\mathrm{ref}} - P_{\mathrm{m}}) \cdot \left(\frac{\omega_{\mathrm{n}}}{S_{\mathrm{n}}}\right) \tag{3.71}$$

where, S_{n} signifies the rating of the converter. Here, $S_{\mathrm{n}} = 1.5 \cdot \hat{V}_{\mathrm{LG}} \cdot \hat{I}_{\mathrm{n}}$, where $\hat{V}_{\mathrm{LG}}$ is the peak voltage line-to-ground and $\hat{I}_{\mathrm{n}}$ is the peak current.

As indicated by (3.71), it is inferred that f_{dr} (ω_{dr}) is proportional to P_{m}. By solving (3.71) in terms of P_{m} and expressing in pu, it culminates in:

$$\frac{P_{\mathrm{m}}}{S_{\mathrm{n}}} = \frac{P_{\mathrm{ref}}}{S_{\mathrm{n}}} + \frac{\omega_{\mathrm{dr}}}{\omega_{\mathrm{n}}} \cdot \frac{T_3}{T_1} \tag{3.72}$$

The control is evaluated in the inductive network depicted in Figure 3.9. Evaluating P_m as the steady-state solution of the network, (3.73) is obtained. Constant magnitude is prescribed by the voltage source.

$$P_\mathrm{m} = 1.5 \cdot \mathrm{Re}\{\underline{\hat{V}} \cdot \underline{\hat{I}}^*\} = 1.5 \cdot \underline{\hat{V}} \cdot \left(\underline{\hat{V}}/R\right)^* = \frac{{V_\mathrm{LL}}^2}{R} \tag{3.73}$$

By utilizing the general solution presented in Section 3.3.2 and equating (3.53) and (3.57), voltage $\underline{\hat{V}}$ is derived. Here, $\hat{V}_\mathrm{LG} = \frac{\sqrt{2}.V_\mathrm{n}}{\sqrt{3}}$. This yields (3.74) as converter's power contribution at steady-state (i.e., $\Delta\varphi = 0$). The total inductance (L) includes the coupling (L_C) and transformer (L_T) inductance.

$$\underline{\hat{V}} = \frac{\sqrt{2}}{\sqrt{3}} \frac{V_\mathrm{n}\, \mathrm{e}^{\mathrm{j}\cdot\vartheta}}{\left[1 + \frac{L}{R} \cdot (s + \mathrm{j} \cdot \omega)\right]} \tag{3.74}$$

Substituting the value for $\underline{\hat{V}}$ from (3.74) in (3.73) gives:

$$P_\mathrm{m} = \frac{V_\mathrm{n}\mathrm{e}^{\mathrm{j}\cdot\vartheta}}{\left[1 + \frac{L}{R} \cdot (s + \mathrm{j} \cdot \omega)\right]} \cdot \frac{V_\mathrm{n}\mathrm{e}^{-\mathrm{j}\cdot\vartheta}}{\left[1 + \frac{L}{R} \cdot (s + \mathrm{j} \cdot \omega)\right]^*} \cdot \frac{1}{R} \tag{3.75}$$

Under steady-state consideration $s = 0$ (in dq frame as described in Appendix A6), with a transformation frequency $\omega = \omega_\mathrm{n} - \omega_\mathrm{dr}$, simplification of (3.75), results in (3.76). Equation (3.77) is the per-unitized form of (3.76), similar to (3.72).

$$P_\mathrm{m} = \frac{{V_\mathrm{n}}^2}{\left[1 + \left\{(\omega_\mathrm{n} - \omega_\mathrm{dr})^2 \cdot \left(\frac{L}{R}\right)^2\right\}\right]} \cdot \frac{1}{R} \tag{3.76}$$

$$\frac{P_\mathrm{m}}{S_\mathrm{n}} = \frac{{V_\mathrm{n}}^2}{\left[1 + \left\{(1 - \frac{\omega_\mathrm{dr}}{\omega_\mathrm{n}})^2 \cdot \left(\frac{\omega_\mathrm{n} L}{R}\right)^2\right\}\right]} \cdot \frac{1}{R} \cdot \frac{1}{S_\mathrm{n}} \tag{3.77}$$

Inference and remark: Both (3.72) and (3.77) are in pu and provide expressions in terms of P_m and ω_dr. Equation (3.72) geometrically represents a line equation independent of the absolute phase. The solution to these equations is defined by the intersection of the line (3.72) with (3.77) which illustrates the steady-state solution (operating point) of the proposed PRP with APC scheme in the considered network. Figure 3.10 (a) illustrates this solution at $P_\mathrm{ref} = 0$ with the resulting measured power P_m and drift frequency ω_{dr}. The internal control ω_dr is defined as the negative

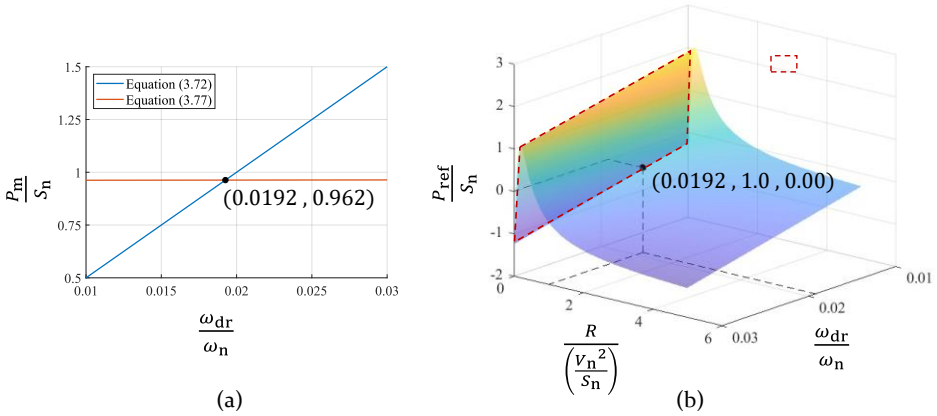

Figure 3.10:
(a) Steady-state solution of single converter in terms of P_{m} and ω_{dr}, with $P_{\mathrm{ref}} = 0.0$ pu;
(b) Steady-state solution plane dependent on network conditions (R) and operating ranges (P_{ref}) (from equations (3.72) and (3.77)).

deviation of the power system frequency (ω) from the nominal frequency (ω_{n}), i.e., $\omega_{\mathrm{dr}} = -\Delta\omega = -(\omega - \omega_{\mathrm{n}})$, as exhibited in the simulation result Figure 4.10 (c). This phenomenon is attributed to the novel transformation block $\rho_{dr}\iota_{dr}$ in the scheme counteracting to the event and shifting the transient frequency drift from power system to control as explained in Section 3.1. Hence, the slope in Figure 3.10 (a) is negative when displayed against $\Delta\omega$ and is positive when plotted against ω_{dr}.

Simulation is utilized to verify the analytical results, which are presented in Table 4.6 under Section 4.3.1. Figure 3.10 (b) illustrates the reference values (P_{ref}) and its corresponding network load R and ω_{dr}. The solutions from (3.72) and (3.77) depicted in Figure 3.10 (b) are unique, within the regular operating ranges with $\Delta|\underline{\hat{V}}| < 0.1$ pu of $\hat{\mathrm{V}}_{\mathrm{LG}}$ $(\leq\ 150\% \cdot \hat{I}_{\mathrm{n}})$. In power system dynamics, small values of R or $X = R$ (optimum adjustment) result in high current solutions (ca. $>\ 5\ \hat{I}_{\mathrm{n}}$), which necessitate the capability for current limitation in control. As a result, solutions that are irregular in relation to these values of load are disregarded in this context (marked **red** in Figure 3.10 (b)). The necessary measures for implementation of current limitation are covered in sub-section 3.5.

3.4.2 Mathematical deduction of two converter configuration

This section provides a detailed examination of the theoretical implications of arbitrary reference values and power balance conditions in the context of two converter configurations. Equation (3.71) in sub-section 3.4

establishes a proportionality between drift frequency (ω_{dr}) and active power (P_{m}) for a single converter. This association is expanded to encompass two converters utilizing PRP with active power control. A star topology is examined to establish the power distribution among multiple converter sources. Figure 3.9 illustrates the network configuration, which includes two converters and power measurements, denoted as $P_{1\mathrm{m}} \equiv P_1$ and $P_{2\mathrm{m}} \equiv P_2$. The control parameters are consistent with mentioned values in sub-section 3.4.1 and Figure 3.8. Three unknowns ($\omega_{\mathrm{dr}}, P_1, P_2$) must be determined to achieve a steady-state operating point, which requires the derivation and resolution of three equations similar to sub-section 3.4.1. From (3.71), a single converter solution, leads to the inference:

$$\omega_{dr} \propto (P_{\mathrm{ref}} - P_{\mathrm{m}}) \tag{3.78}$$

Therefore, by the law of '*direct proportionality*', a non-zero constant '*c*' exists. Equations (3.79) and (3.80) are derived from this principle given in (3.78), where '*c*' is weighted gain or power-frequency droop in the control.

$$\omega_{dr} = -c(P_{\mathrm{ref1}} - P_1) \tag{3.79}$$

$$\omega_{dr} = -c(P_{\mathrm{ref2}} - P_2) \tag{3.80}$$

The network solution for two converters is computed utilizing the '*Superposition theorem*' [133, 134]. Equation (3.81) presents the general solution, which is a combination of intermediate solutions represented by $\underline{\hat{V}}_{C1}$ and $\underline{\hat{V}}_{C2}$. It is structurally similar to (3.74) under steady-state conditions with *s* variable as described in Appendix A6.

$$\underline{\hat{V}} = \frac{\underline{\hat{V}}_{C1} L_2 + \underline{\hat{V}}_{C2} L_1}{L_1 + L_2} \cdot \frac{1}{1 + \frac{(s + \mathrm{j} \cdot \omega) \cdot L_1 L_2}{(L_1 + L_2) R}} \tag{3.81}$$

The control response is inspected by calculating the *common-mode* and *differential-mode* voltage signals, as derived from (3.79) and (3.80), the *common-mode* and *differential-mode* are calculated to inspect the control response. *Common-mode* voltage signals represent the common or average input to the two voltage sources, whereas *differential-mode* voltage signal represents the difference between the two [135, 136]. Equations (3.82) to (3.85) are derived to further facilitate the calculations, taking into account the converter voltage magnitude with $\hat{V}_{\mathrm{LG}} = \sqrt{2} \cdot V_{\mathrm{n}} / \sqrt{3}$.

$$\underline{\hat{V}}_{C1} = \frac{\sqrt{2} \cdot V_{\mathrm{n}}}{\sqrt{3}} \mathrm{e}^{\mathrm{j} \cdot \varphi_1} \tag{3.82}$$

$$\underline{\hat{V}}_{C2} = \frac{\sqrt{2} \cdot V_{\mathrm{n}}}{\sqrt{3}} \mathrm{e}^{\mathrm{j} \cdot \varphi_2} \tag{3.83}$$

$$\varphi = \varphi_1 + \varphi_2 \tag{3.84}$$

$$\Delta\varphi = \varphi_1 - \varphi_2 \tag{3.85}$$

The phase φ_1 is obtained by adding (3.84) and (3.85) as sum of *common-mode* and *differential-mode*. Similarly, subtracting (3.84) and (3.85) results in φ_2. The calculated phase values of φ_1 and φ_2 are substituted in (3.82) and (3.83). By utilizing the updated equations and substituting the values of $\underline{\hat{V}}_{C1}$and $\underline{\hat{V}}_{C2}$ in (3.81), the following equation is arrived:

$$\underline{\hat{V}} = \frac{\sqrt{2}\cdot V_{\mathrm{n}}}{\sqrt{3}} e^{\mathrm{j}\cdot\varphi_0} \cdot \frac{e^{\mathrm{j}\cdot\left(\Delta\varphi/2\right)}\cdot L_2 + e^{\mathrm{j}\cdot\left(-\Delta\varphi/2\right)}\cdot L_1}{L_1 + L_2} \cdot \frac{1}{1+(s+\mathrm{j}\cdot\omega)\tau} \tag{3.86}$$

where $\varphi_0 = {}^{\varphi}/_{2}$, and $\tau = \frac{L}{R} = \frac{L_1 \| L_2}{R} = \frac{L_1 . L_2}{[(L_1+L_2)\cdot R]}$

The total power contribution at PCC is ascertained by $P = 1.5 \cdot \mathrm{Re}\{\underline{\hat{V}} \cdot \underline{\hat{I}}^*\}$. Substituting the value of voltage gained in (3.86) and solving for the total power contribution or *common-mode* ($P_1 + P_2 = P$), results in:

$$P_1 + P_2 = \frac{{V_{\mathrm{n}}}^2}{R} \cdot \left\{\frac{{L_1}^2 + {L_2}^2 + 2\cdot L_1 L_2 \cdot \cos[\Delta\varphi]}{(L_1+L_2)^2}\right\} \cdot \frac{1}{1+(\omega\tau)^2} \tag{3.87}$$

where, $\omega = (\omega_{\mathrm{n}} - \omega_{\mathrm{dr}})$.

The *differential-mode* power is computed by utilizing the *principle of superposition* to calculate the branch currents. These currents aid in the evaluation of the *differential-mode* power. The current response in each branch is represented by the following equations:

$$\underline{\hat{I}}_1 = \frac{R\cdot\left(\underline{\hat{V}}_{C1} - \underline{V}_{C2}\right) + \underline{\hat{V}}_{C1}\cdot(s+\mathrm{j}\cdot\omega)L_2}{(s+\mathrm{j}\cdot\omega)^2\cdot L_1 L_2 + (s+\mathrm{j}\omega)(L_1+L_2)\cdot R} \tag{3.88}$$

$$\underline{\hat{I}}_2 = \frac{R.\left(\underline{\hat{V}}_{C2} - \underline{V}_{C1}\right) + \underline{\hat{V}}_{C2}\cdot(s+\mathrm{j}\cdot\omega)L_1}{(s+\mathrm{j}\cdot\omega)^2\cdot L_1 L_2 + (s+\mathrm{j}\omega)(L_1+L_2)\cdot R} \tag{3.89}$$

The *differential-mode* or difference of power between the two sources. is represented by (3.90). It is important to note that only the real part is taken into consideration, as setpoint modifications impact active power values.

$$P_1 - P_2 = \mathrm{Re}\{S_1 - S_2\} = 1.5\cdot\mathrm{Re}\left\{\underline{\hat{V}}_{C1}\cdot{\underline{\hat{I}}_1}^* - \underline{\hat{V}}_{C2}\cdot{\underline{\hat{I}}_2}^*\right\} \tag{3.90}$$

The solution for the *differential-mode* is represented by (3.91), which is obtained by substituting voltage from (3.82) and (3.83) while currents from (3.88) and (3.89), into (3.90). The term '*S*' represents the complex power.

$$\Delta P = \frac{{V_{\mathrm{n}}}^2}{R} \cdot \frac{\left\{\left(\frac{(L_2-L_1)}{(L_1+L_2)}\right) + \left(\frac{R}{\omega\cdot(L_1+L_2)}\cdot 2\sin[\Delta\varphi]\right)\right\}}{(1+(\omega\tau)^2)} \tag{3.91}$$

where, $\omega = (\omega_{\mathrm{n}} - \omega_{\mathrm{dr}})$.

Equation (3.87) is in terms of cosine function while (3.91) is in terms of sine function. Further simplifying the two equations to obtain known trigonometric identities. Hence, considering *common-mode* and adding (3.79) and (3.80), the resultant is:

$$(P_1 + P_2) = (P_{\mathrm{ref1}} + P_{\mathrm{ref2}}) + 2 \cdot c' \cdot \omega_{\mathrm{dr}} \tag{3.92}$$

The value of 'c' in (3.79) and (3.80), is derived from (3.71). Its reciprocal 'c''' is calculated in (3.93) and is subsequently substituted into (3.92).

$$c' = \frac{1}{c} = \frac{S_{\mathrm{n}}}{\omega_{\mathrm{n}}} \cdot \frac{T_3}{T_1} \tag{3.93}$$

The equations (3.87) and (3.92) are equated, and the resultant is solved for $\cos[\Delta\varphi]$, leading to:

$$\cos[\Delta\varphi] = \frac{\left\{\begin{array}{c}(P_{\mathrm{ref1}} + P_{\mathrm{ref2}} + 2 \cdot c' \cdot \omega_{\mathrm{dr}}) \cdot \left(\frac{R}{{V_{\mathrm{n}}}^2}\right) \\ \cdot (L_1 + L_2)^2 \cdot (1 + \ [(\omega_{\mathrm{n}} - \omega_{\mathrm{dr}}) \cdot \tau]^2) - {L_1}^2 - {L_2}^2\end{array}\right\}}{(2 \cdot L_1 \cdot L_2)} \tag{3.94}$$

For calculating *differential-mode* in (3.95), (3.79) is subtracted from (3.80).

$$P_1 - P_2 = \ P_{\mathrm{ref1}} - P_{\mathrm{ref2}} \tag{3.95}$$

Equating (3.91) and (3.95), for solving $\sin[\Delta\varphi]$, the outcome is:

$$\begin{aligned}&\sin[\Delta\varphi] \\ &= \frac{\left\{(P_{\mathrm{ref1}} - P_{\mathrm{ref2}}) \cdot \left(\frac{R}{{V_{\mathrm{n}}}^2}\right) \cdot \{1 + \ [(\omega_{\mathrm{n}} - \omega_{\mathrm{dr}}) \cdot \tau]^2\} - \left[\frac{(L_2 - L_1)}{(L_2 + L_1)}\right]\right\}}{(2 \cdot R)} \\ &\qquad \cdot [(\omega_{\mathrm{n}} - \omega_{\mathrm{dr}}) \cdot (L_1 + L_2)]\end{aligned} \tag{3.96}$$

The network solution in terms of a ω_{dr} is determined by utilizing trigonometric identity (3.97) in (3.94) and (3.96). The above equations are derived under the assumption of constant voltage magnitude.

$$cos^2[\Delta\varphi] + sin^2[\Delta\varphi] = 1 \tag{3.97}$$

When considering symmetrical network elements ($L_1 = L_2 = L \Longrightarrow \tau = \frac{L}{2 \cdot R}$), equation (3.94) and (3.96) maybe further simplified. The validity of

(3.94) and (3.96) in terms of (3.97) is verified simulatively and the results are listed in Table 4.7 of Section 4.3.2.

Remark: The equations presented demonstrate that the power flow solution depends on the phase difference rather than on the absolute phase of the source voltage. The drift frequency ω_{dr} is defined by *common-mode* power and is characterized by a power-frequency droop 'c'. The power dispatch is adjusted by the *differential-mode* power, which is obtained through dissimilar reference powers (P_{ref}) [30].

3.4.3 Self-stabilizing setpoint via droop

The APC response is based on fixed setpoint values. It is not practical as the arbitrary setpoint is unknown to the power system operator to reach an asymptotic stable operating point (defined in Section 2.4.1). Therefore, an additional power-frequency droop via K_2 is incorporated into the APC to create an auto-adjustable and self-stabilizing response of the control to the power system.

It covers a wide range of network loading conditions indicated by the EMT domain investigations in Section 4.3.3. Via this droop, the complete control response is adjusted to increase the reference value further in case of load increase. Thus, pushing additional active power during the disturbance's transient phase and lowering the frequency or phase difference towards the nominal value. The droop K_2 is supplemented to the APC loop, and the modified block diagram is seen in Figure 3.11. This completes Phase 2 of the control development.

Modifying the original APC equations ((3.70) to (3.72)), in sub-section 3.4.1 by incorporating the additional power-frequency droop (K_2). The updated control solution in pu is (3.101), with intermediated steps emphasized from (3.98) to (3.100) The parameters of the complete APC are in Table 3.2.

Table 3.2: Complete parameter set of the active power frequency droop control.

Parameter	Unit	Value
K_1	pu	1.0
K_2	pu	0.25×50
K_3	pu	1.0
T_1	sec	$1.0/(50 \times 2\pi)$
T_3	sec	$1.0/2\pi$
T_2	sec	0.01

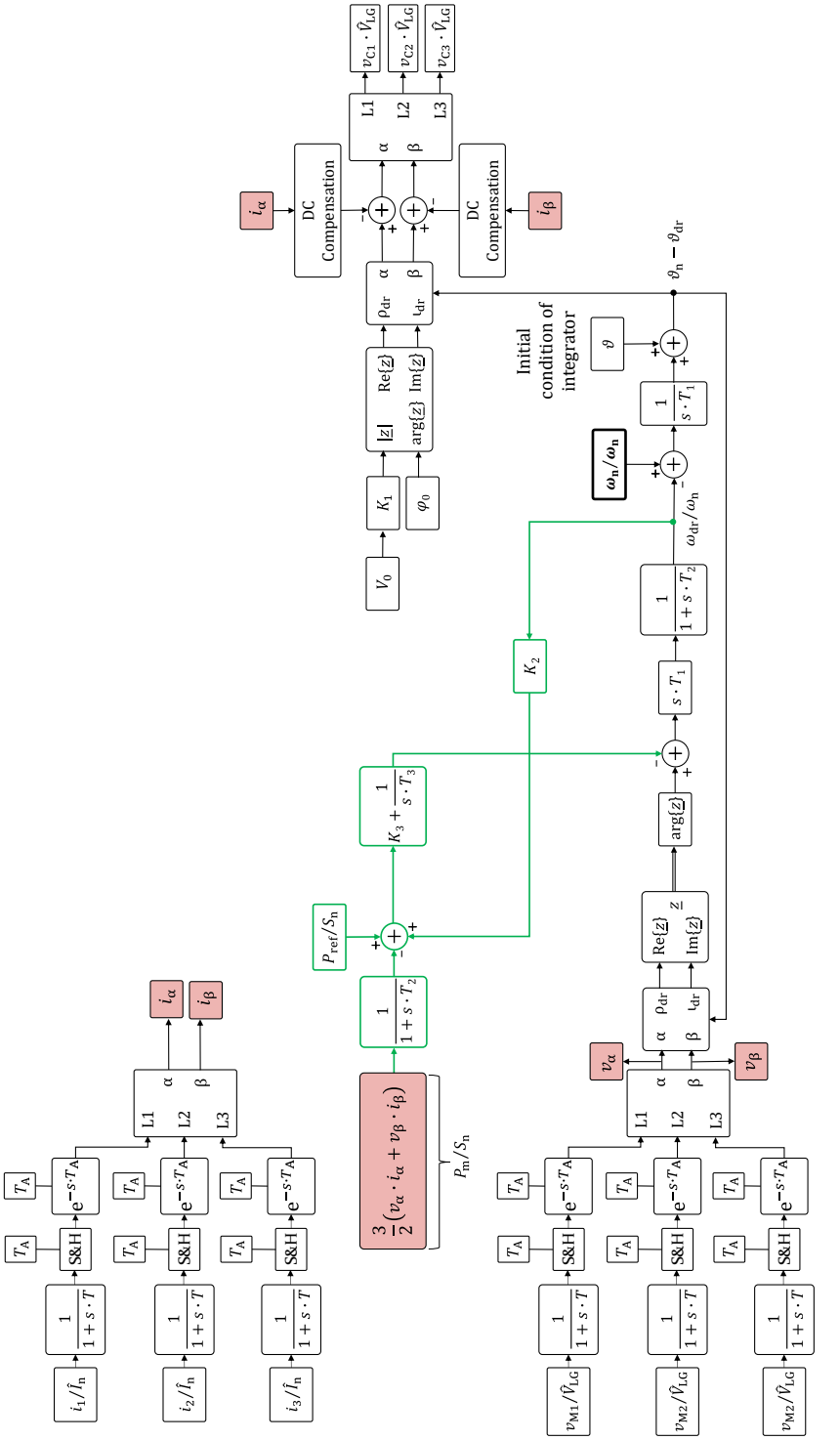

Figure 3.11: Modified Block diagram of the Phase Restoring Principle (**PRP**) with active power control (**APC**) considering self-stabilizing droop K_2 (in **green**) – **Phase 2**.

The network solution remains unchanged as derived in (3.77).

$$\frac{F_{\mathrm{dr}}}{F_{\mathrm{n}}} = -\left(\frac{P_{\mathrm{ref}} - P_{\mathrm{m}}}{S_{\mathrm{n}}} + K_2 \cdot \frac{F_{\mathrm{dr}}}{F_{\mathrm{n}}}\right).\left(K_3 + \frac{1}{sT_3}\right).(s \cdot T_1) \tag{3.98}$$

$$\frac{F_{\mathrm{dr}}}{F_{\mathrm{n}}} = -\left(\frac{P_{\mathrm{ref}} - P_{\mathrm{m}}}{S_{\mathrm{n}}} + K_2 \cdot \frac{F_{\mathrm{dr}}}{F_{\mathrm{n}}}\right) \cdot \left(\frac{T_1}{T_3}\right) \tag{3.99}$$

$$\frac{F_{\mathrm{dr}}}{F_{\mathrm{n}}} \cdot \left(1 + K_2 \cdot \frac{T_1}{T_3}\right) = -\left(\frac{T_1}{T_3}\right) \cdot \left(\frac{P_{\mathrm{ref}} - P_{\mathrm{m}}}{S_{\mathrm{n}}}\right) \tag{3.100}$$

$$\frac{P_{\mathrm{m}}}{S_{\mathrm{n}}} = \frac{P_{\mathrm{ref}}}{S_{\mathrm{n}}} + \frac{\omega_{dr}}{\omega_{\mathrm{n}}} \cdot \left(\frac{T_3}{T_1} + K_2\right) \tag{3.101}$$

Remark: Similar to (3.72) and (3.77) in sub-section 3.4.1, (3.101) is in terms of P_{m} and ω_{dr}. The solution to these equations is defined by the intersection of the lines (Figure 3.12), which display the steady-state solution (operating point) of the proposed control PRP with APC incorporating additional self-stabilizing droop K_2. Figure 3.12 displays the intersection shift closer to nominal frequency when accounting for K_2. The parameter P_m in constant, and the small difference is due to numerical error.

Similarly, for the two converter configuration (sub-section 3.4.2), only 'c' or the weighted gain in the control needs to be modified to (3.102) and its reciprocal is (3.103). All the other equations derived in sub-section 3.4.2 remain unaltered.

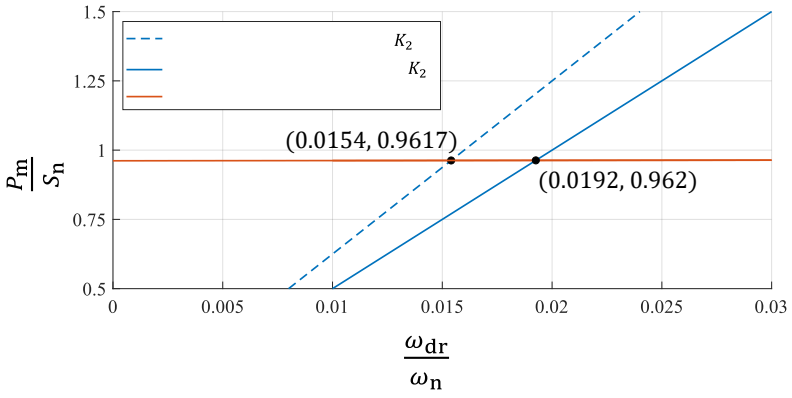

Figure 3.12: Comparison of steady-state solution of single converter in terms of $P_{\mathrm{m}}$and ω_{dr} with and without self-stabilizing droop K_2 and $P_{\mathrm{ref}} = 0.0$ pu.

$$c = \frac{\omega_{\mathrm{n}}}{S_{\mathrm{n}}} \cdot \frac{T_1}{T_3} \cdot \left(1 + K_2 \cdot \frac{T_1}{T_3}\right)^{-1} \tag{3.102}$$

$$c' = \frac{1}{c} = \frac{S_{\mathrm{n}}}{\omega_{\mathrm{n}}} \cdot \frac{T_3}{T_1} \cdot \left(1 + K_2 \cdot \frac{T_1}{T_3}\right) \tag{3.103}$$

Equation (3.97) utilizing (3.94) and (3.96) is solved to determine ω_{dr} under the selected P_{ref} values. The value of the reciprocal 'c'' is replaced with (3.103). Similarly, ω_{dr} is calculated employing (3.101) and (3.77), displayed in Figure 3.12 and cross-checked simulatively in Section 4.3.3. The modified equations for single and two converters incorporating self-stabilizing droop K_2 are verified simulatively in both EMT and phasor (RMS) domains. Additionally, the two-converter configuration (Figure 3.9) is simulated under a wide range of impedance values to display the response of the modified control (Figure 3.11) under different loading (Z) conditions and exhibited in Section 4.3.3.

3.5 Current limiting control method under symmetrical disturbances

Limiting the converter current magnitude is relatively simple, but maintaining stability and exiting the current limiting mode is challenging. A less complex and elegant current limitation methodology in the GFM converter is to consider implementing a simple saturation block and maintaining its original control strategy. Power and voltage amplitude are the reference values to be included in the GFM converter control. A successful current limiting technique should restrict the power and voltage amplitude to maintain stable synchronization and simultaneously curtail the current. However, it should be noted that limiting the power also limits the voltage phase angle [62]. Examining the discussion above and based on known current limiting methodologies, an effective current limitation approach by voltage magnitude adjustment is proposed. The proposed approach creates higher transient peak current demand to stabilize the power system. The Phase 2 control is extended to implement this current limiting strategy. This is the last phase of control development, named Phase 3, illustrated in Figure 3.13.

The method realized is based on the voltage limiter concepts discussed in Section 2.2, with additional trigger level selections corresponding to the current limits defined for different grid conditions. The objective of the voltage limiter is to limit the current magnitude. By allowing the current to be controlled and eventually fixed at PCC, the converter output voltage

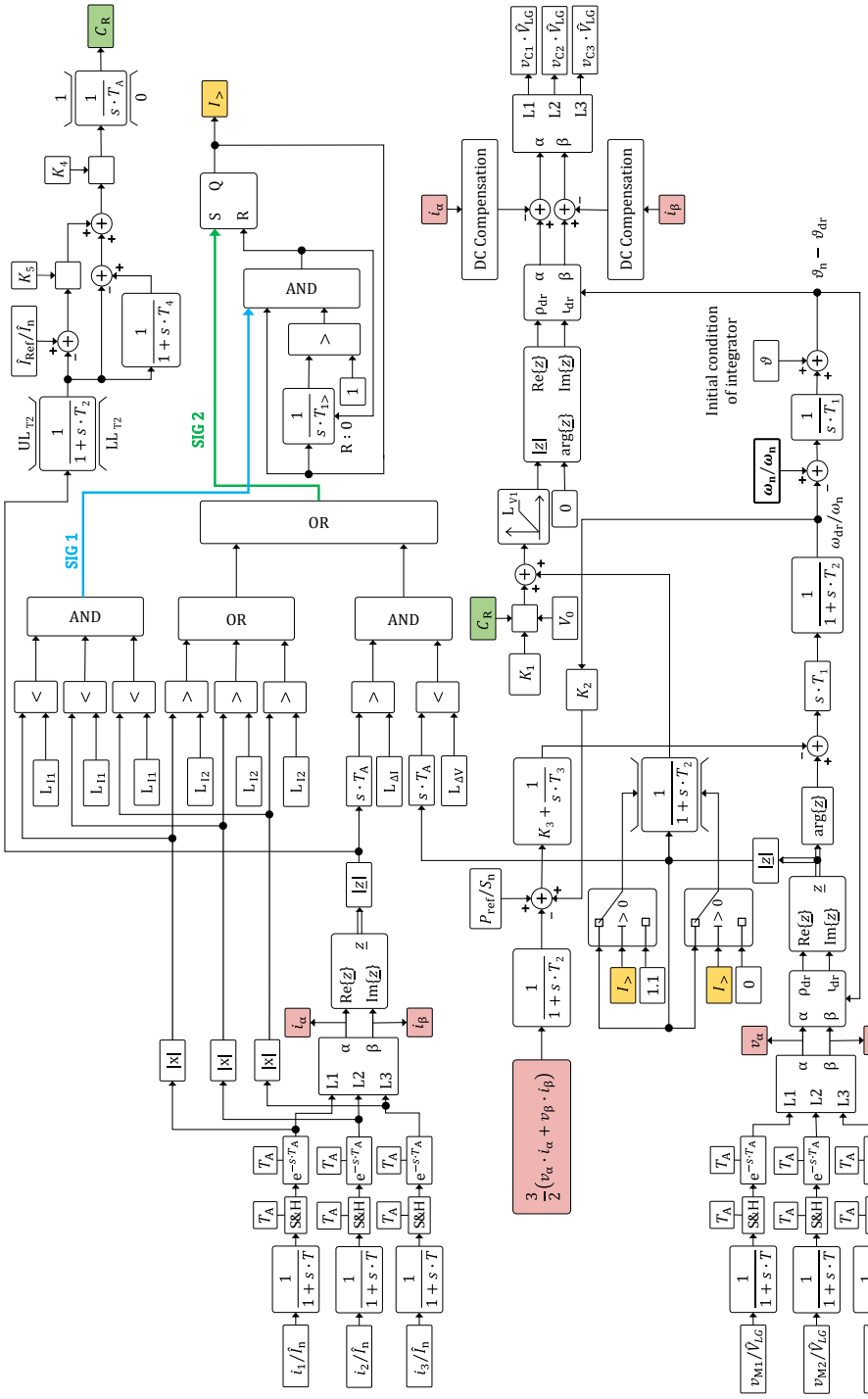

Figure 3.13: PRP scheme including modified APC and current limit control – **Phase 3**.

changes accordingly. Conversely, if the converter output voltage is actively controlled and held constant, the resultant current automatically changes to the desired value.

The parameters for the block diagram in Figure 3.13 are listed in Table 3.3. In the proposed control, instantaneous three-phase currents are utilized to determine the violation of current limits. These currents are compared against two trigger levels. **SIG 1** determines the regular operation with any instantaneous current magnitude below the limit set at $L_{I1} \leq 1.05$ pu (105 %) and is marked in **blue**. **SIG 2** actuates the current limitation strategy if a minimum of one instantaneous current magnitude exceeds the upper threshold of $L_{I2} > 1.15$ pu and is labeled in **green**. The trigger levels may be adapted to provide other levels of response. The range between 1.05 pu to 1.15 pu allows slow development of the reactive current and, thus, voltage magnitude. The trigger signals SIG 1 and SIG 2 are the outputs of a conjunction and a disjunction evaluating current magnitudes. They constitute Set and Reset of the Flip-flop together with a delayed feedback ($T_{1>}$) from Flip-flop's Q state. The trigger levels with the Flip-flop constitute a basic state machine whose output is highlighted in **yellow** and symbolized by $\boldsymbol{I}_{>}$. This output determines the corresponding dynamic current limiting or steady-state operation.

Since there is no closed-loop current control, additional measures are taken to avoid the hunting effect. A proportional differentiator (PD), whose

Table 3.3: Paremters assocaiated with current limitation.

Parameter	Unit	Value
L_{I1}	pu	1.05
L_{I2}	pu	1.15
T_2	sec	0.01
UL_{T2}	pu	1.15
LL_{T2}	pu	0.70
T_4	sec	0.02
K_1	pu	0.10
K_4	pu	0.005
K_5	pu	0.50
$T_{1>}$	sec	0.001
T_A	sec	$1 \cdot E - 4$
L_{V1}	pu	1.15
$L_{\Delta I}$	pu	0.001
$L_{\Delta V}$	pu	0.0001

output signal feeds an input to the discrete integrator (DI) serving as a counter, is developed. The PD controller has a gain K_5 and a differentiator time constant T_4. The input to the PD is a smoothed magnitude of the complex-valued current with time constant T_2, and the output is multiplied with gain K_4. The total gain is sufficiently high and tuned. The integrator's output signal is utilized to calculate the reactive current and adjust the voltage magnitude for limitation. The output of the discrete integrator is denoted by $\boldsymbol{Cr}$ and marked in **green**. The aggregated arrangement forms a PD-DI block. The present scenario is configured by $\hat{I}_{\mathrm{Ref}}/\hat{I}_{\mathrm{n}} = 1.0$ pu. Therefore, below 105 %, a rapid response is desired, while above 105 %, a slower reduction to bring the current back to its nominal value is devised. The discrete integrator is reset to zero when the current magnitude limiter is triggered to improve the fault recovery capability of the GFM converter.

As known, the derivative component is effective for slow dynamic errors. Hence, it creates a damped output and stabilizes the response with a rapid current increase. The derivative response is proportional to the rate of change of the process variable and predicts error in the control loop, while the proportional gain increases the speed of the response. Together, this creates a fast and improved transient damped reaction on the current magnitude and accelerates the global system response. Hence, the PD-DI block is active for a small range of deviations around the nominal current, allowing the voltage to settle smoothly at its limits with minimal overshoot.

The output $\boldsymbol{Cr}$ of the discrete integrator with the output $\boldsymbol{I_>}$ of the Flip-flop constitutes an anti-windup method for voltage limit controller that guarantees the converter's fault recovery capability. The resultant converter voltage magnitude is composed of a constant part K_1 adjusted by the reduction gain $\boldsymbol{Cr}$ and a smoothed measured voltage magnitude with saturation limits set to 1.1 pu and 0.0 pu.

In steady-state operation the output voltage magnitude results from a superposition of measured voltage magnitude and scaled feedforward part K_1 comprising nominal reactive current injection (K_1 reflecting the coupling reactance X_{C}). Contrary, in current limitation the converter output voltages approaches the measured voltages leading to a zero voltage drop across the coupling inductor after the decay of natural response.

Thus, there are two contributions from the current limitation strategy implemented, an active reduction and feedback. The active part is limited to 10 % reflecting the coupling impedance, whereas the feedback is obtained by the smoothing of measured voltage magnitude. The present parameter configuration sets the steady-state converter terminal voltage at

a maximum of 1.15 pu with 10 % coupling and 10 % transformer impedance, amounting to a 20 % voltage drop at PCC for a nominal, inductive current. The steady-state limit of the current is 1 pu. In the benchmarked case, the tested upper limits are adjusted to $L_{V1} = 1.15$ pu and lower limit to 0.0 pu. The output signal is further transformed from $\rho_{dr}\iota_{dr}$ to $\alpha\beta$ to obtain the voltage magnitude and argument of the converter

As mentioned in Section 2.3.5 and in [7, 92–95], an essential requirement of GFM is to maintain a constant magnitude and phase of the voltage within the transient time frame following a disturbance. Therefore, the voltage regulation is realized by constant magnitude under normal conditions. An adjustment via scaling is performed in case of overcurrent. If the voltage control bandwidths for regulation of the terminal voltage are sufficiently small, the control loops' response time is slow, implying longer rise and settling times. The GFM control must maintain stability under low short circuit ratio (SCR) conditions and even 'form' grid voltage when necessary. Adhering to the above, the voltage magnitude limitation in conjugation with PRP allows to maintain the voltage source behavior during the severe disturbances. In case of deep faults, a reactive, viz. capacitive current is injected to stabilize the power system. Otherwise, a mix of active and reactive currents, as implied by Phase 2, interacts with the power system impedance. A swift and stable response is ensured with the underlying PRP scheme such that the slower response is guaranteed around nominal values. The prime difference to existing voltage limiter methods is that the phase is not controlled via the current limiting control, rather current is limited via magnitude only. Thus, no restriction is applied to the voltage phase, preserving the phase-frequency coherence and the original control characteristic. The concept can be extended to include additional measures for negative sequence as the trigger levels are based on peak values of the instantaneous currents. The control scheme is simulated, tested intensively and the results are displayed and discussed in Section 4.4. During testing, some high residual peak currents under transients for improbable network conditions were witnessed. An oversizing is anticipated as a necessary trade-off for stability in these cases, amounting to a maximum peak current of 1.5 pu. However, the steady-state current remains 1 pu.

3.6 Complete Grid-Forming control

The block diagram of the complete control is shown in Figure 3.14, and the parameters are listed in Table 3.4. The parameter selection allows the desired optimal performance. It enables the response of disturbances to dominate over setpoint changes. Further, it maintains the voltage source

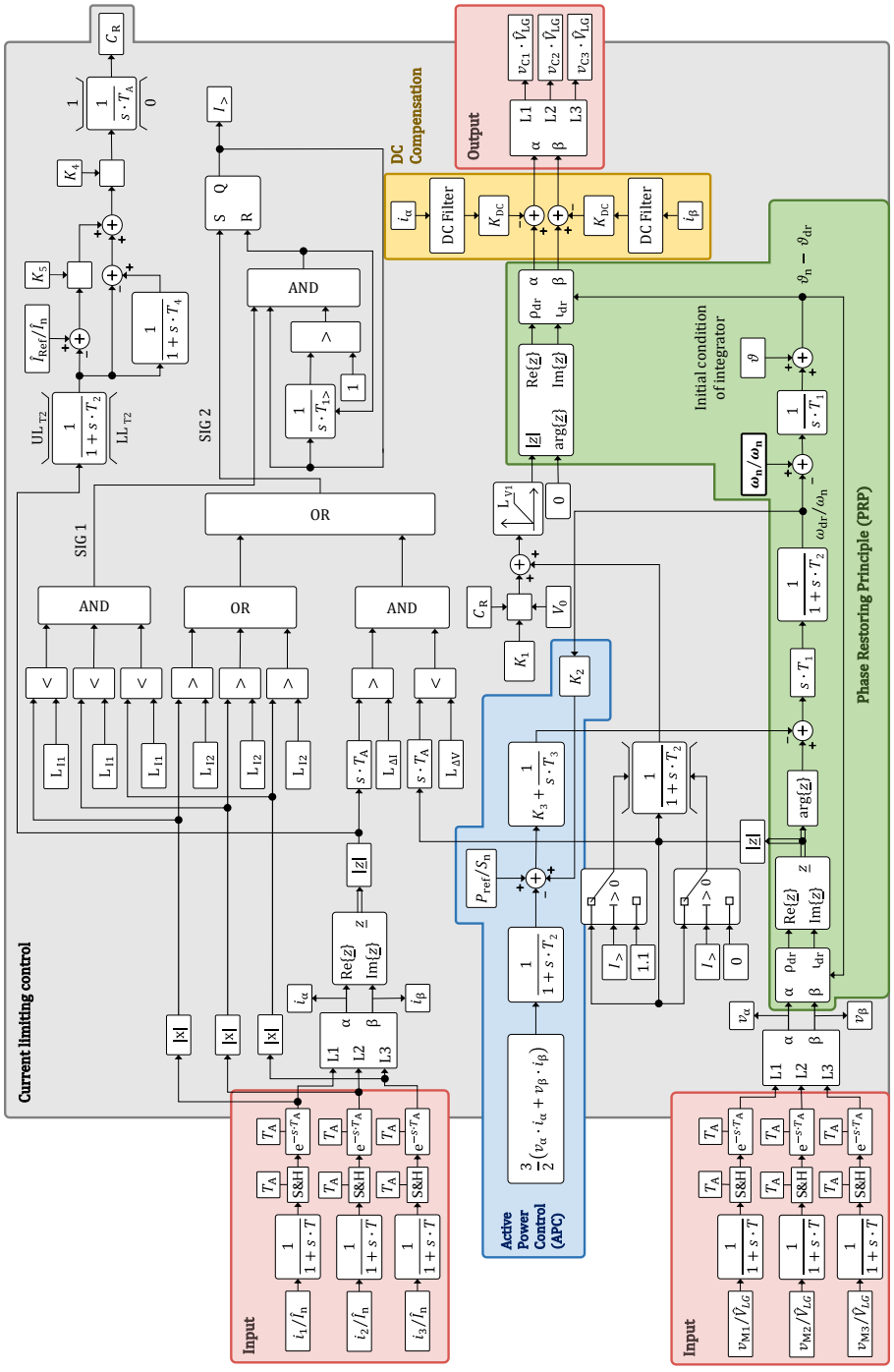

Figure 3.14 Phase-Restoring Principle (PRP) based full GFM control – **Phase 3**.

characteristic with current limitation control. This GFM scheme also allows inertial support and active power dispatch.

The DC compensation is also incorporated into the control principle. It is added to mitigate the undesirable slow DC component in the output current to improve dynamic system performance. For EMT simulations it is necessary to superpose a DC voltage compensating the transient DC current as seen in Figure 3.14. The DC compensation is a proportional controller estimating the transient voltage difference (ΔV_{CTR}) as discussed in Section 2.5.1. The DC control is implemented as a discrete controller (DFT) with a sampling frequency of 5 kHz, while the full control is sampled with 10 kHz. All the measured input signals are smoothed with a time constant of 100 µsec to reduce aliasing effects. These sampling frequencies are viable choices though PRP is not restricted to these exemplary values.

Table 3.4: Complete paremters list of the GFM scheme based on PRP.

Parameter	Unit	Value
T_1	sec	$1.0/(50 \times 2\pi)$
T_2	sec	0.01
T_3	sec	$1.0/2\pi$
T_4	sec	0.02
$T_{1>}$	sec	0.001
$\mathrm{UL_{T2}}$	pu	1.15
$\mathrm{LL_{T2}}$	pu	0.70
K_1	pu	0.10
K_2	pu	0.25×50
K_3	pu	1.00
K_4	pu	0.005
K_5	pu	0.5
K_{DC}	pu	0.02
T_{A}	sec	$1 \cdot E - 4$
$\mathrm{L_{I1}}$	pu	1.05
$\mathrm{L_{I2}}$	pu	1.15
$\mathrm{L_{V1}}$	pu	1.15
$\mathrm{L_{\Delta I}}$	pu	0.001
$\mathrm{L_{\Delta V}}$	pu	0.0001
V_0	pu	1.00
F_{n}	Hz	50.00
T	sec	$1 \cdot E - 4$

3.7 Chapter Summary

This chapter presents a theoretical basis of an unconventional control strategy for a GFM converter based on a 'Phase Restoring Principle' (PRP) by which a constant steady-state frequency is achieved. The development of the control scheme is distributed across three distinct phases.

In Phase 1, the basic block of the GFM control scheme, namely PRP, is introduced, and its realization is described in context to GFM converters. The unique control structure with minimal order dynamics, operating principle and frequency drift as a local phenomenon is discussed. It is deduced that the internal frequency drift (ω_{dr}) is the negative deviation of the power system frequency $\Delta\omega$, under disturbances. The scheme utilizes a novel angular transformation of the reference frame in the opposite direction to a disturbance in the ohmic-inductive network and is inherently without a PLL. PRP generates the frequency actively by restoring the phase at the measurement node and not by following it passively, thus providing equivalence to infinite virtual inertia. The mathematical investigations in a realistic test bench under different operating scenarios with necessary boundary conditions to obtain a solution based on the control principle were described. The existence of the operating point of the proposed concept is proved via the *'Existence Theorem'*. An essential outcome of the theorem was the role of the transformer impedance as a decisive constituent in the overall converter control performance. The ratio between the coupling and transformer impedance is vital in obtaining a regular operating point. Hence, coupling and transformer impedances are not network branches but quintessential parts of the converter system stability. Evidence of small-signal system stability by analytical evaluation of the linearized closed-loop transfer function is provided, and the generalized small-signal solution of the control independent of network loadings is proved. Global stability is derived from the general small-signal solution and operating point's existence exhibited with a suitable choice of network parameters, with the solution's uniqueness defined by the shortest path. PRP takes over the central part of the control task of responding to an event, with power dispatch capacity and current limitations superimposed. Thus, the scheme response reflects that frequency ranks over the constant load flow phase by prioritizing disturbance over setpoint changes.

Further, in Phase 2 of controller development, PRP is supplemented with active power control (APC), which allows the control scheme to cooperate with other sources. Analytical deductions of the APC are displayed in single

and double converter configurations under weak grid scenarios. Self-stabilizing droop is incorporated into the APC to enhance performance dynamics and robustness. The development of steady-state operating point and hence drift frequency using the principle of PRP with active power, along with the additional droop control, is examined. Discussions based on reference values and weighted gain '*c*' selection are also performed. The enhanced PRP control structure also displays controller stability for sufficiently small drift frequencies and achieves nominal frequency with dedicated parameters.

Finally, in Phase 3, the underlying Phase 2 control is extended with the current limitation concept. This current limiting concept is based on voltage magnitude control with phase administered by PRP. The control consists of novel usage of an anti-windup limiter, discrete integrator and a current magnitude triggered Flip-flop, which defines the control state. These assist in better recovering from the undesired current saturation and hunting effects to detect and respond to symmetrical fault conditions. The voltage magnitude is constant under normal operation and scaled under overcurrent conditions. The current limiting control blocks help preserve the GFM functionality and provide the best possible control response under severe faults. Thereby complying with the GFM characteristics or requirements mentioned in Section 2.3.

The last section of this chapter includes the complete block diagram with DC compensation and details of the chosen parameter based on optimal performance.

4 Simulative validation of Phase Restoring Principle

This chapter displays and discusses simulative evidence of the control response and its robustness based on the mathematical investigations and proofs delivered in Chapter 3. Steady-state operating point development to validate global stability and control responses are simulatively verified in Section 4.1. The small-signal stability and the analytical conclusions of the nonlinear Phase Restoring Principle are demonstrated in Section 4.2. The prioritization of disturbances over setpoints and the restoration of the nominal frequency with PRP and APC is displayed in Section 4.3. Additionally, a variegated panorama of scenarios is simulated, and the control's robustness responses are contrasted with and without current limits in Section 4.5 and Section 4.4, respectively. Finally, the chapter provides a summary in Section 4.6. The offline simulation tools utilized here are PSS®NETOMAC in both EMT and RMS domains and MATLAB-Simulink® for small-signal analysis. Please refer to Appendix A4 for per-unit definition. Fragments of this chapter are published in journals J1, J2 and conference paper C1 as provided in Table A 7.

4.1 Steady-state operating point development in single converter configuration

The Phase 1 PRP based GFM control scheme displayed in Figure 3.2 is applied to a basic network model shown in Figure 4.1. The assumed network is inductive, and as such, the resistive component of the network equivalent R_{N}, is considered negligible compared to the impedances of the other network elements. This section deals with the response of PRP as fully GFM with no additional control loops. Based on the mathematical boundaries defined in Section 3.2, four distinct scenarios are considered, and the results demonstrate global stability. This sub-section is organized into two parts. The first part, or sub-section 4.1.1, presents the different conditions of the simulated test bench simulated. While the second part or 4.1.2 includes time-domain results utilizing PSS®NETOMAC software tool for both EMT and RMS domains of the various cases.

The test bench as described in Figure 4.1 is represented in PSS®NETOMAC in a per-unit MVA system. The converter voltage source is defined by 1 pu. The control is sampled with 10 kHz and the test system including control is simulated with an integration time step of $T_{\mathrm{INT}} = 100\ \mu\mathrm{sec}$. It

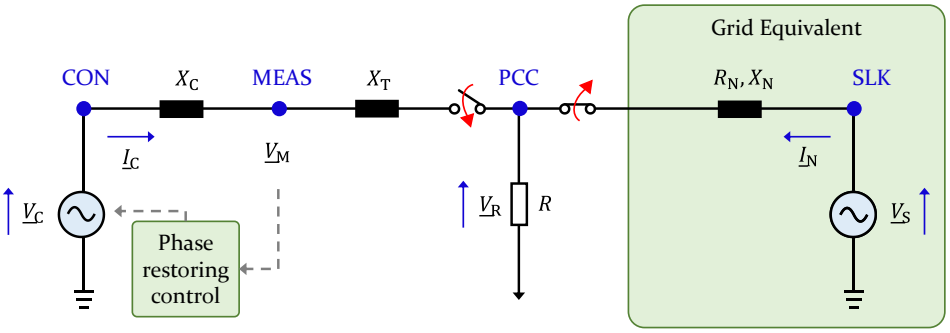

Figure 4.1: Simulated test bench based on Figure 3.3.

synchronizes with the network at $t = 0.2$ sec. At $t = 5.04$ sec, the shunt load designated as R is connected creating a disturbance in the system. The network configuration is simulated for a duration of 15 sec. The coupling impedance in the circuit (X_C) is set at 10 % of a nominal impedance 1 MVA machine base power as described in (4.1). All the other impedance values are described and varied in relation to the coupling impedance. The test bench is simulated in EMT and RMS domains and the responses are evaluated.

$$X_C = 0.1 \frac{(0.69\ \text{kV})^2.}{1\ \text{MVA}} = 10\% \times \text{nominal impedance} \tag{4.1}$$

4.1.1 Simulated scenarios

Case A: The network model exhibits a weakly coupled grid configuration. The network parameters are determined based on the conditions specified in *Assumption 3a* (Section 3.2.1.4) for the steady-state operating point.

Case B: This network model highlights a strongly coupled grid configuration. The requirements derived in *Assumption 3b* of Section 3.2.1.5 for the steady-state operating point describe the network parameters.

Case C: The network model exhibits a globally stable solution for the Phase 1 control under *Assumption 1* of Section 3.2.1.1. The steady-state operating point and network parameters satisfy these conditions.

Case D: The simulation results for this case display an unstable network solution with the chosen network parameters. The case conforms to the conditions in *Assumption 2 of* Section 3.2.1.2. It should be noted that the instability, corresponds to an oscillating frequency condition.
The network parameters fulfilling the conditions for each described scenario are described in Table 4.1.

Table 4.1: Parameters considered for the simulated scenarios.

Case	A	B	C	D
Network condition	$X_T = X_C$, $X_N > X_C$, $R < X_C$, $R < X_N$	$X_T = X_C$, $X_N \ll X_C$, $R < X_K$, $R > X_N$	$X_T = X_C$, $X_N > X_C$, $R > X_C$	$X_T = 0$, $X_N < X_C$, $R < X_C$
Parameters	Value	Value	Value	Value
X_C	0.1	0.1	0.1	0.1
X_T	X_C	X_C	X_C	1.E-6× X_C
X_N	$10 \times X_C$	$0.00001 \times X_C$	$10 \times X_C$	$X_C/2$
R	$X_C/10$	$X_C/10$	$X_C \times 10$	$X_C/10$

4.1.2 Results and inferences

Figure 4.2 visualizes the results for all four simulated cases. Each circle represents the general solution of the corresponding network condition ((3.5) or abridged (3.6)). The dots indicate the steady-state operating phase of the converter voltage (3.7). The circles for each case are interpretable, as explained in Figure 3.4. The phase values obtained from the simulation are also cross-verified with equations (3.7) or (A 5.5). The arbitrary solution used for plotting each scenario is given in equation (A 5.4) of Appendix A5. The values displayed in Figure 4.2 for Cases A, B, and C match the simulated results shown in Figure 4.4 to Figure 4.6, supporting the hypothesis.

The Phase Restoring control demonstrates that each stable case achieves the steady-state value through the direct path (described in Section 3.2), for the topology in Figure 4.2. The direct path is observable through the movement of the operating point's development from the pre-disturbance (**x**) to the post-disturbance value (**dot**) in the close-up views of Figure 4.2. The intersection of the circles with the real axis ($\mathrm{Re}\{\underline{V}_M\}$) visualize the solution in accordance with equation (3.5) or extended equation (A 5.4). The circles represent all possible converter voltage phases depending on measurement voltage real and imaginary parts for a defined impedances (network parameters with R and X values). Pre-disturbance both the converter and measurement voltage phases are zero. The intersection of the circles with the real axis display the post disturbance solutions for the converter voltage phase. Since PRP fixes the phase of the measurement phase at zero the post disturbance converter phase is shifted to positive values corresponding to ohmic loading. The change of converter phase is marked on the circles by a (x) and (•) labeling pre- and post-disturbance respectively.

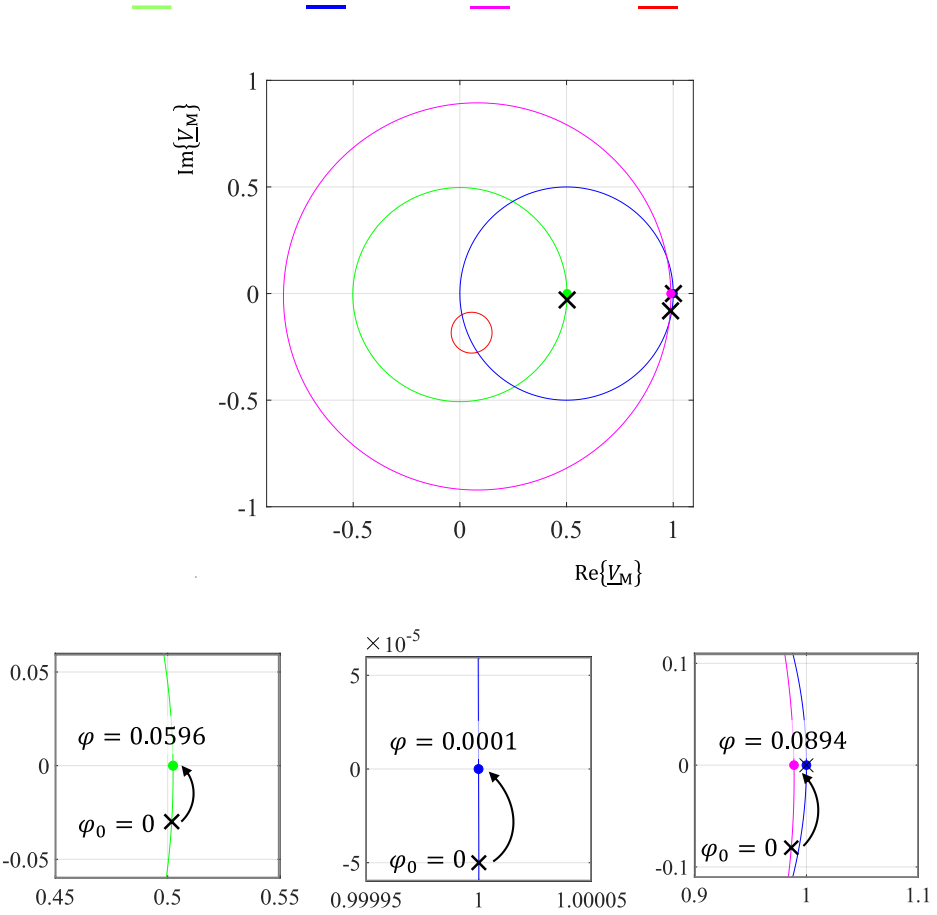

Figure 4.2: Solution circles (3.5) parameterized by converter phase (φ) with close-ups of operating points defined by $\mathrm{Im}\{\underline{V}_M\} = 0$, where (**x**) is phase of pre-disturbance and (•) is phase of post-disturbance**.** The values are displayed in radians**.**

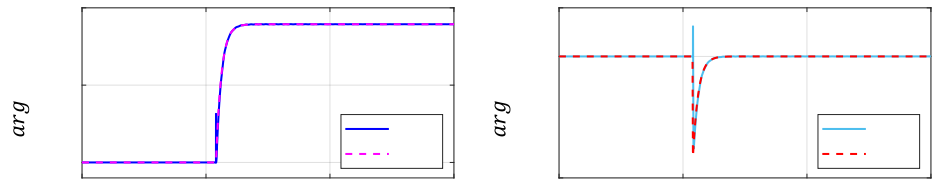

(a) (b)

Figure 4.3: Case C (a) Under disturbance conditions at CON, phase jump in phasor of converter voltage $\underline{V}_C$, undertaking the direct path; (b) Under disturbance conditions at MEAS, phase restored by the control of the measurement voltage $\underline{V}_M$.

The simulation plot in Figure 4.3 (a) additionally illustrates a smooth response in the converter voltage argument ($\arg\{\underline{V}_C\}$), demonstrating the direct path from the pre- to post-disturbance values. The argument of the measurement voltage $\arg\{\underline{V}_M\}$ in Figure 4.3 (b) displays a minor delayed control action, which returns to its initial value after a short jump (network response) in opposite direction, corresponding to steady-state frequency. The choice of the transformation angle based on the voltage at the measurement node allows the realization of a true virtual inertia principle, leading to global stability**.** The response is analogous to a large source and thus comparable to the inertia concept providing support during a disturbance. Moreover, under the above-mentioned conditions, the controller is stable without a slack connection, corresponding to $X_N \to \infty$.

Simulation results for cases A to D are displayed in Figure 4.4 to Figure 4.7. For better visualization of the plots, the abscissa range is fixed between 4 sec to 6 sec, while the ordinate is variable. Results for Cases A, B, and C demonstrate that the control and power system reach a steady operating point after a disturbance if the necessary parameter requirements are satisfied. In contrast, Case D (Figure 4.7) illustrates an unstable network condition in which no operating point for the Phase Restoration control is possible, and the integrator is unable to achieve steady-state operation, resulting in oscillations. This case is not asymptotically unstable but rather a limit cycle oscillation with oscillatory behavior characterized by constant periodicity. True instability is unbounded, leading to an exponential response, described as Lyapunov's unstable in Section 2.4. In Figure 4.2, Case D solution does not intersect with the real axis ($\mathrm{Re}\{\underline{V}_M\}$) and offers a clear distinction in response compared to the other scenarios.

Switching on the load introduces a disturbance that causes a voltage drop and increases the converter's reactive and active power, as demonstrated in variant (c and d) of Figure 4.4 to Figure 4.7. In response to this disturbance, the control adjusts to a new operating point to compensate for the disturbance event and restore the phase at the measurement node, as shown in variant (b) of Figure 4.4 to Figure 4.7. This new operating point is achieved by adjusting the argument of the converter voltage, which leads to an increase in active power. The network also imposes additional reactive power requirement. The proportion of reactive power share is determined by the ratio of the impedances between the converter node and PCC, specifically, X_C and X_T. The choice of transformer impedance plays a crucial role in the determination of the PRP scheme's ability to achieve a feasible operating point, as illustrated in the plots for Case A (Figure 4.4),

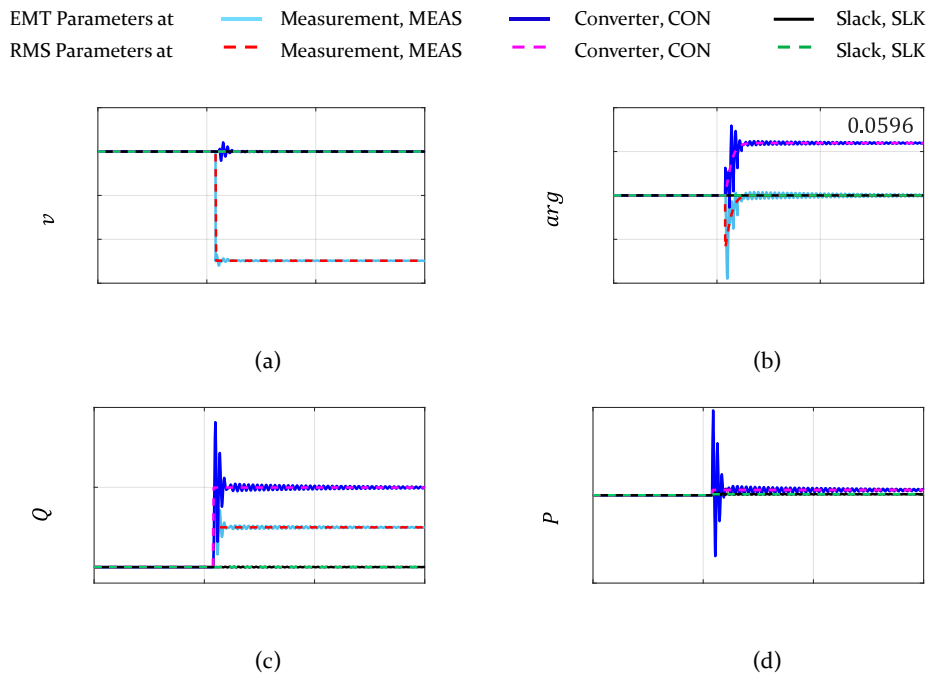

Figure 4.4. Phase Restoration Principle (PRP) simulation for Case A (a)Voltage magnitude; (b)Voltage argument; (c) Reactive power and (d) Active power.

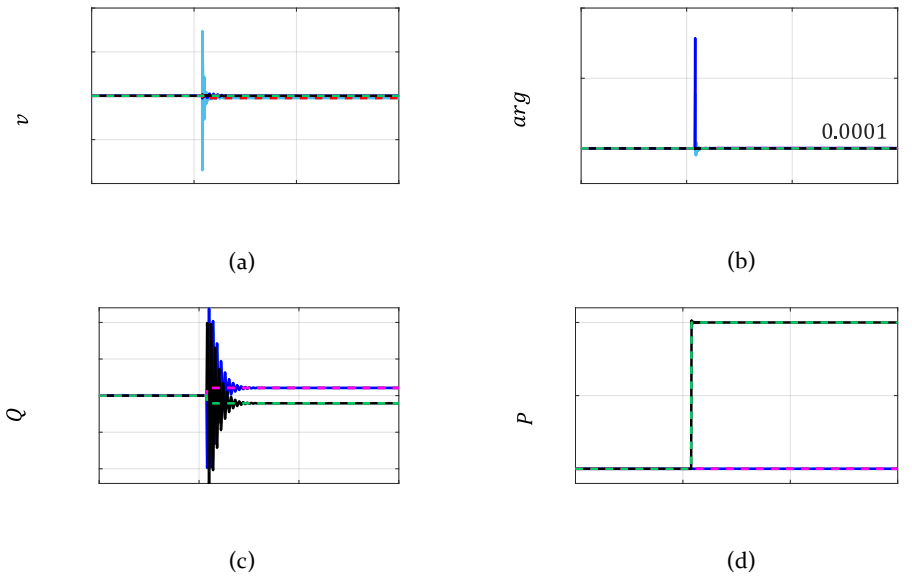

Figure 4.5. Phase Restoration Principle (PRP) simulation for Case B (a)Voltage magnitude; (b)Voltage argument; (c) Reactive power and (d) Active power.

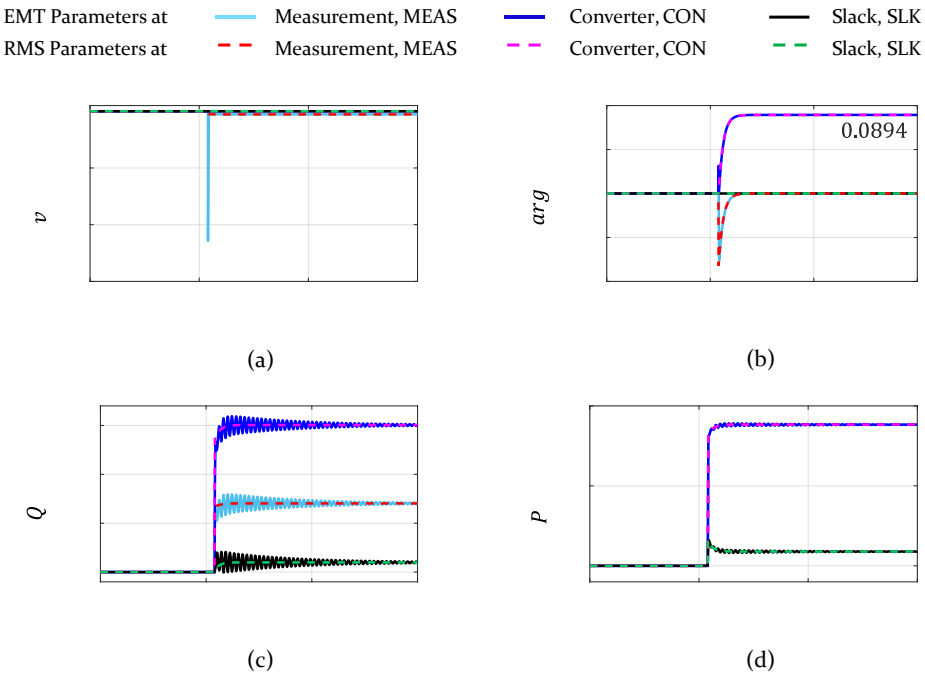

Figure 4.6. Phase Restoration Principle (PRP) simulation for Case C (a)Voltage magnitude; (b)Voltage argument; (c) Reactive power and (d) Active power.

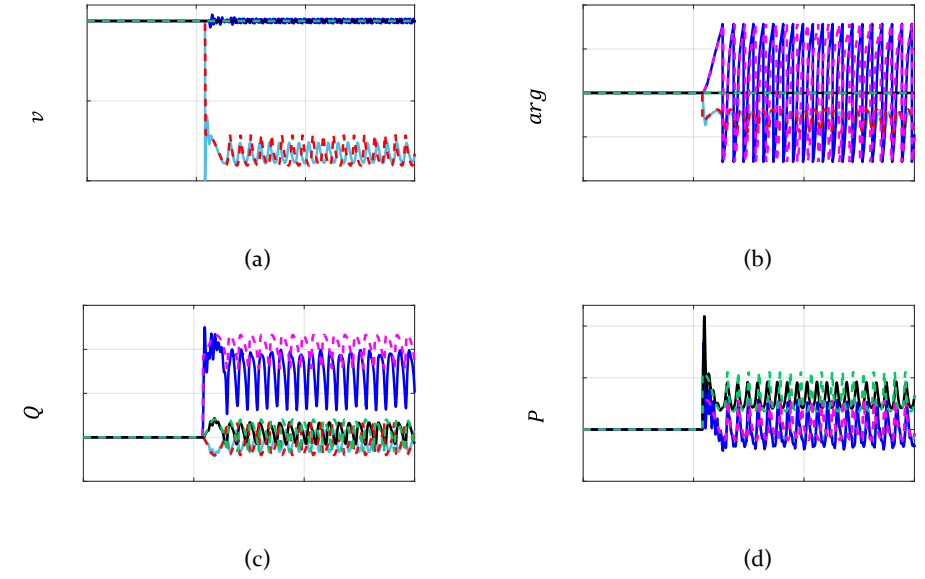

Figure 4.7. Phase Restoration Principle (PRP) simulation for Case D (a)Voltage magnitude; (b)Voltage argument; (c) Reactive power and (d) Active power.

Case B (Figure 4.5), and Case C (Figure 4.6). The impact of the grid (SLK) on the system is greatly dependent on the network configuration. Case A, in which the grid or network equivalent has minor or non-existent influence (weak grid), exhibits significant differences in system responses compared to Case B, where the grid has a more substantial impact (strong grid). In Case A, the PRP scheme operates under weak grid conditions and plays a dominant role in the post-disturbance interaction.

Comparing stable Cases, A to C reveals that the power system responses in the positive sequence EMT and RMS domains are similar. The operating points achieved through both simulation methods align. However, in unstable Case D, the responses differ due to the violation of the constant frequency condition inherent to the RMS domain solution. The findings of the mathematical analysis presented in Section 3.2 are visualized through simulation [29].

4.2 Small-signal evidence

In this sub-section, the theoretical small-signal deductions derived in Section 3.3 are corroborated via numerical simulations. Since the small-signal numerical analysis is conducted in MATLAB-Simulink®, the PRP control results are benchmarked against the native simulation program PSS®NETOMAC (EMT and RMS) (sub-section 4.2.1). The transfer functions are determined by applying perturbation frequencies to the network. The analytical evaluation is presented in sub-section 4.2.2 and further compared and verified against the numerical simulations. The obtained results are presented and described via visualization in sub-section 4.2.4.

4.2.1 Benchmark scenarios

The control model from PSS®NETOMAC is replicated in MATLAB-Simulink® with the converter voltage source set at $\hat{V}_{\mathrm{LG}} = \frac{\sqrt{2}}{\sqrt{3}} \cdot 0.69\ \mathrm{kV}$. This control is reproduced in two different network configurations, the reduced and the complete model as described in Figure 3.3 and Figure 3.5, respectively. The control structure built in MATLAB-Simulink® is not linearized and represents full control as in Figure 3.2. Case C, as described in Table 4.1, is chosen as the base network case to demonstrate a comparable match in control responses across the two tools. This test case is a superset of all global stable solutions, as seen in Figure 4.2 containing all network scenarios.

The control in the complete network model built in MATLAB-Simulink®, is

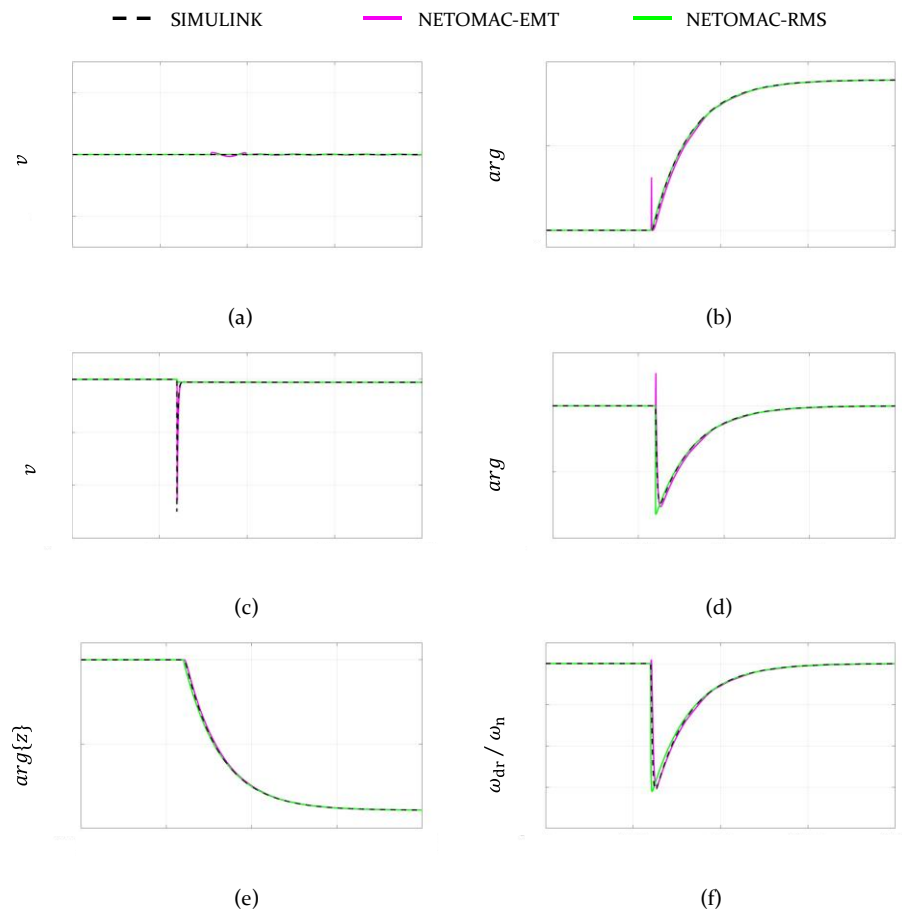

Figure 4.8: Phase 1 PRP response (Figure 3.2) in test bench Figure 3.3 validated among tools (PSS®NETOMAC and MATLAB-SIMULINK®) and domain (EMT and RMS)
(a) Voltage magnitude at CON ($\underline{V}_C$); (b) Voltage argument at CON ($\underline{V}_C$);
(c) Voltage magnitude at MEAS ($\underline{V}_M$); (d). Voltage argument at MEAS ($\underline{V}_M$);
(e) Control's argument of phase; (f) Control's internal drift frequency.

benchmarked against the control model built in PSS®NETOMAC (both EMT and RMS domains) prior to conducting stability analysis. The benchmarking serves to validate the consistency of interpretation in the two different tools as observed from the comparison in Figure 4.8. Time traces displaying the comparison of voltage magnitude and argument at the converter node and measurement node are presented in the Figure 4.8 (a to d). Additionally, the controller's internal signals of the phase's argument and the drift frequency are consistent between the two tools as witnessed in Figure 4.8 (e and f). Figure 4.8 (f) provides better visualization of the drift frequency ω_{dr}, and the control's behavior in restoring the phase after

a disturbance. As previously demonstrated, comparing EMT and RMS simulation responses exhibit similar behavior.

4.2.2 Theoretical deductions

Section 3.3.1 presents the results for small-signal stability analysis obtained through closed-loop transfer functions derived through *linearization* at an operating point for $R \geq 1$ pu. To enhance the clarity of the results, selected scenarios of Case C are simulated to provide additional support for the theoretical conclusions.

In the previous section, the system is calculated in the Laplace domain. However, for spectral analysis, the evaluation is performed using $s = \mathrm{j}\omega$ on the imaginary axis, which corresponds to a Fourier Transform (discussed in Section 2.4.3.2). The Phase Restoring Principle linearized through small-signal methods demonstrates a constant d component, $V_\mathrm{d} = \hat{V}_\mathrm{LG}$ in dq domain, as derived in (3.52). The value of the converter source voltage $\hat{V}_\mathrm{LG}$ is constant for all $-\infty < t < \infty$. As a result, the constant voltage V_d transforms into a Dirac distribution ($\delta(\mathrm{j}\omega)$) in Fourier domain. By applying this principle to the analytical deduction in (3.49), (4.2) is obtained with the determinant of matrix **A** in (3.51).

$$\begin{bmatrix} V_\mathrm{d}(\mathrm{j}\omega) \\ V_\mathrm{q}(\mathrm{j}\omega) \end{bmatrix} = \frac{[\mathrm{j}\omega T]}{\det(\mathbf{A})} \begin{bmatrix} 1 + {}^{\mathrm{j}\omega L}/_{R} + {}^{1}/_{[\mathrm{j}\omega T]} & {}^{\omega_\mathrm{n} L}/_{R} \\ -{}^{\omega_\mathrm{n} L}/_{R} & 1 + {}^{\mathrm{j}\omega L}/_{R} \end{bmatrix} \begin{bmatrix} \hat{V}_\mathrm{LG} \cdot \delta(\mathrm{j}\omega) \\ 0 \end{bmatrix} \tag{4.2}$$

For steady-state analysis, substituting $s = 0$ in dq frame (refer Appendix A6), in (4.2) produces:

$$\begin{bmatrix} V_\mathrm{d}(\mathrm{j}\omega) \\ V_\mathrm{q}(\mathrm{j}\omega) \end{bmatrix} = \begin{bmatrix} \hat{V}_\mathrm{LG} \cdot \delta(\mathrm{j}\omega) \\ 0 \end{bmatrix} \tag{4.3}$$

Equation (4.3), demonstrates that $V_\mathrm{d} = 0$ and is valid for all frequencies dissimilar to zero. Therefore, the q/q controller transfer function $-[sT]$ derived in (3.41) is chosen for numerical evaluation. The q/q controller transfer function is evaluated at a predetermined set of perturbation frequencies in EMT domain. These frequencies are incrementally increased in steps of 0.1 Hz, starting from 50 to 51 Hz. For evaluation, the frequency difference to nominal ($F_\mathrm{n} = 50\ Hz$) is considered. The results of evaluation are presented in Table 4.2 and are compared with corresponding simulation results. The argument of the transfer function illustrates the impact of $-[sT]$. With time constant of $T = 0.02$ sec $= T_1$ (Figure 3.6), the argument computes -1.5708 rad or $-\pi/2$ rad, which corresponds to an ideal integrator phase. This relationship is verified through simulations discussed in subsequent sections.

Table 4.2: Analytical evaluation of transfer function at various perturbation frequencies.

Frequency difference to nominal	**Mag $\lvert -sT \rvert$ (pu)**	**Arg $\{-sT\}$ i.e., Phase (rad)**
0	0	0
0.1	0.0126	-1.5708
0.2	0.0251	-1.5708
0.3	0.0377	-1.5708
0.4	0.0503	-1.5708
0.5	0.0628	-1.5708
0.6	0.0754	-1.5708
0.7	0.088	-1.5708
0.8	0.1005	-1.5708
0.9	0.1131	-1.5708
1	0.1257	-1.5708

4.2.3 Numerical simulations

The linear superposition principle is employed to establish a correlation between the theoretical results presented in Section 3.3.1 and numerical simulations. The linear superposition principle states that in a linear system, the system's response to multiple stimuli is the sum of the response of each stimulus [137]. Therefore, the fundamental input voltage is superimposed with a small sinusoidal perturbation at a frequency (F_{p}), and various scenarios are simulated and evaluated based on this principle [138, 139]. Following the general conditions for small-signal analysis, the injected perturbation should be of a single frequency but with arbitrary magnitudes and phases and assumes the sinusoidal form. However, it is challenging to handle mathematically and generate, during simulation or experiment, such arbitrary unbalanced three-phase signals. Therefore, a three-phase current source with positive sequence perturbation at a frequency (F_{p}) is injected. The range of the perturbed frequency is restricted to $+1$ Hz and varied in steps of 0.1 Hz with respect to nominal ($F_{\mathrm{n}} = 50\ Hz$).

The methodology employed to simulate small-signal behavior through the application of the superimposition principle is outlined as follows:

1. The application of a current source, characterized by a perturbed frequency (F_{p}), is superimposed on the converter voltage $\underline{V_{\mathrm{C}}}$ to obtain the total voltage output, which is the result of the summation of the two sources.

2. The steady-state response of the input and output voltage magnitude and phase is periodically calculated over a single phase (0 to 2π). It is worth noting that the phase values of the extracted voltage responses are determined at each perturbation frequency. Due to the *linearization* technique, a q/q controller transfer function is obtained, which approximates the phase/phase equivalent for small values (proven in Section 3.3.2). This conclusion is valid as the voltage's quadrature component (V_{q}) is similar to the voltage's argument ($\arg\{\underline{V}\}$) within the range of *linearization* ($R \geq 1$ pu)*.*
3. A Fourier analysis is performed to extract the magnitude and phase of measurement voltage $\underline{V}_{\mathrm{M}}$ and converter voltage $\underline{V}_{\mathrm{C}}$ at the perturbation frequency (F_{p}).
4. At disturbance frequency, the ratio of these voltages' argument ($\arg\{\underline{V}\}$) is evaluated.

The above methodology is applied to both the reduced (Figure 3.5) and complete (Figure 3.3) networks, and the results are subsequently compared. Table 4.3 provides a summary of the considered network parameters with X_{C} defined in (4.1). Furthermore, the value of the resistive load 'R' is varied to validate the response under linearized boundary conditions ($R \geq 1$ pu). Two specific values of 'R' with 1 pu and 16 pu, are chosen at a base of 1 MVA and 0.69 kV, respectively, to perform this validation.

Table 4.3: Parameters for the simulated scenarios

Network configuration	X_{C}	X_{T}	X_{N}	R
Reduced	1 pu	-	-	1 pu, 16 pu
Complete	1 pu	1 pu	10 pu	1 pu, 16 pu

4.2.4 Results and inferences

The small-signal results obtained by evaluating the transfer functions for two simulated scenarios are presented in Table 4.4 and Table 4.5 for $R = 1$ pu and $R = 16$ pu, respectively. Figure 4.9 comprises the converter's steady-state responses and measurement voltage's argument at various disturbance frequencies and network configurations. For the disturbance range, the evaluation of the transfer function of the voltage phases confirms the analytical results described in Table 4.2. Additional visual confirmation is provided in Figure 4.9, demonstrating that the converter and measurement voltage phase is shifted by $\pi/2$ rad for all perturbed frequencies. Hence, it supports the conclusion in (3.41), corresponding to

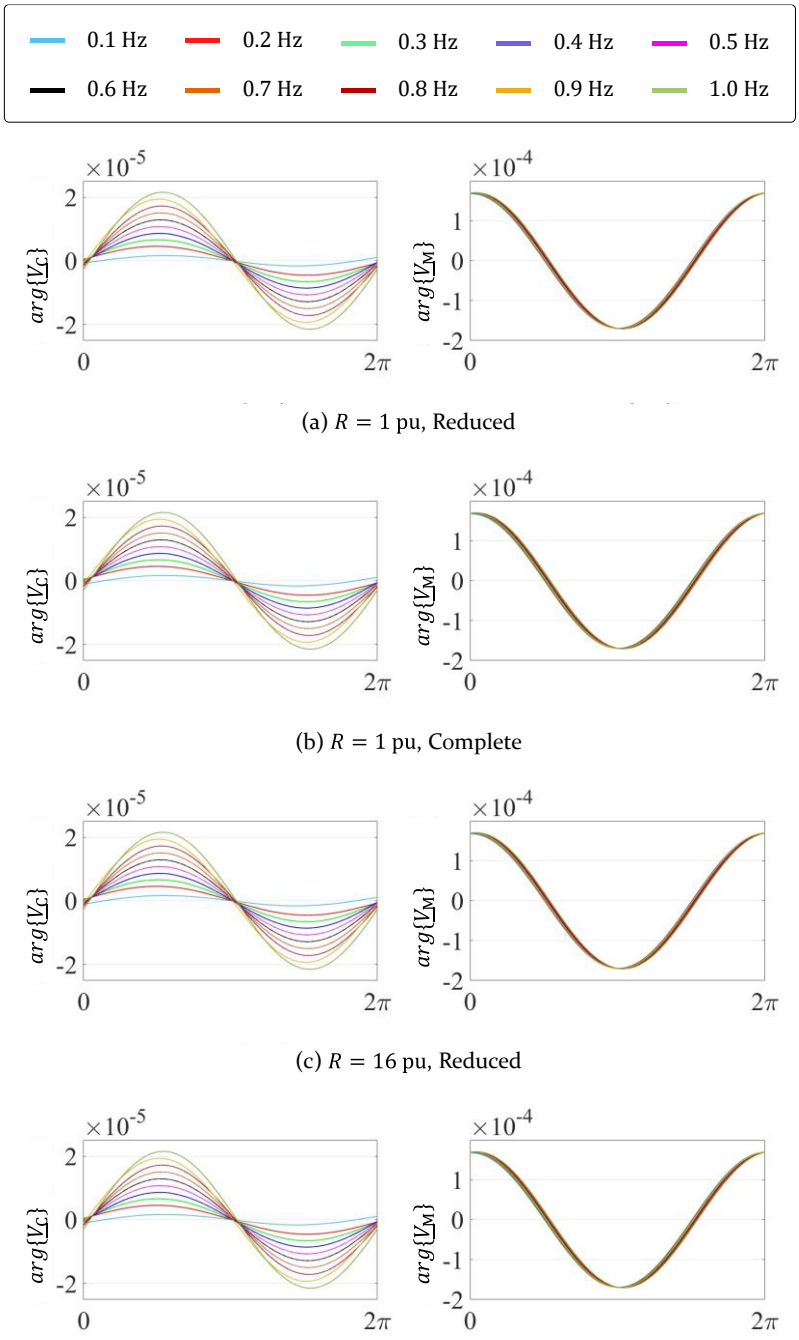

(a) $R = 1$ pu, Reduced

(b) $R = 1$ pu, Complete

(c) $R = 16$ pu, Reduced

(d) $R = 16$ pu, Complete

Figure 4.9: Argument of converter voltage ($\underline{V_C}$) and measurement voltage ($\underline{V_M}$) at specified disturbance frequencies over one respective cycle

an integrator. Both the reduced and complete network models show that the transfer function corresponds to the inverse of the inner feedback loop.

The values obtained in Table 4.4 and Table 4.5 are consistent with those presented in Table 4.2. Minor deviations from the analytical results are observed at lower frequencies. The challenges associated with numerical investigations of low-frequency phenomena through long-term simulations are well-known [47, 140, 141]. The sub-plots in Figure 4.9 demonstrate that steady-state is not achieved at low frequencies. This explains the minor deviations observed in the tabular data from expected values.

The simulation results confirm the independence of the control response on the network parameters. The evaluation of the defined controller transfer function illustrates the dominant role of the inverse inner feedback loop. As a result, the influence of the network is not apparent at the disturbance frequency (F_p), while the converter control dominates the system response as per the controller transfer $-[sT]$ characteristic. The $\underline{V}_C$ ensures the superposition of its response on $\underline{V}_M$. Thereby $\underline{V}_C$ guaranteeing invariance of $\underline{V}_M$ to variations in network parameters, provided both operating point's existence and the viability of the small-signal approach are upheld.

Table 4.4: Simulative evaluation of transfer function at various disturbance frequencies.

Disturbance frequency ($\boldsymbol{F_p}$) difference to nominal ($\boldsymbol{F_n}$)	$\boldsymbol{R = 1}$, **Reduced network**		$\boldsymbol{R = 1}$, **Complete network**	
	Mag (pu)	Arg i.e., Phase (rad)	Mag (pu)	Arg i.e., Phase (rad)
0.1	0.0097	-1.5657	0.0098	-1.5662
0.2	0.0268	-1.5678	0.0267	-1.5684
0.3	0.0387	-1.5687	0.0387	-1.5683
0.4	0.0505	-1.5716	0.0505	-1.5716
0.5	0.0629	-1.5707	0.0629	-1.5707
0.6	0.0754	-1.5709	0.0754	-1.5709
0.7	0.088	-1.5708	0.088	-1.5708
0.8	0.1006	-1.5706	0.1006	-1.5706
0.9	0.1131	-1.5709	0.1131	-1.5709
1	0.1257	-1.5709	0.1257	-1.5709

Table 4.5: Simulative evaluation of transfer function at various frequencies.

Disturbance frequency ($\boldsymbol{F_p}$) difference to nominal ($\boldsymbol{F_n}$)	$\boldsymbol{R}$ = 16, **Reduced network**		$\boldsymbol{R}$ = 16, **Complete network**	
	Mag (pu)	Arg i.e., Phase (rad)	Mag (pu)	Arg i.e., Phase (rad)
0.1	0.0096	-1.5659	0.0097	-1.5664
0.2	0.0267	-1.5677	0.0267	-1.5685
0.3	0.0387	-1.5688	0,0387	-1.5684
0.4	0.0505	-1.5716	0.0505	-1.5716
0.5	0.0629	-1.5707	0.0629	-1.5707
0.6	0.0754	-1.5709	0.0754	-1.5709
0.7	0.088	-1.5708	0.088	-1.5708
0.8	0.1006	-1.5706	0.1006	-1.5706
0.9	0.1131	-1.5709	0.1131	-1.5709
1	0.1257	-1.5709	0.1257	-1.5709

The results presented in this section, obtained through both analytical and simulation methods, indicate that both voltage V_d and V_q are zero for all frequencies, excluding V_d equal to $\hat{V}_\mathrm{LG}$ at nominal frequency.

The general solution derived in Section 3.3.2 is valid for all values of $R > 0$ pu confirming the non-dependence on network loading parameters at steady-state frequency condition in dq reference frame ($s = 0$), hence global stable. Thus, by extension the large loads are also small-signal stable, and the analytical statement is valid within the range of *linearization* specified in Section 3.3. The small development point ($\Delta\varphi \sim 0$) is valid due to the phase integrator and therefore the phase/phase function approaches q/q transfer function with large loads ($V_\mathrm{q} \approx 0$). However, the Phase Restoring Principle is valid under the conditions specified by the *'Existence Theorem'* [29].

4.3 Response of power dispatch capacity with active power extension

This section displays the influence of PRP with APC and is divided into single converter, double converter configurations and self-stabilizing droop's (K_2) role in sub-sections 4.3.1, 4.3.2 and 4.3.3 respectively. Simulations are conducted to validate the analytical deductions presented

in sub-section 3.4, utilizing the test bench depicted in Figure 3.9. Additionally, the effects due to droop K_2 is also assessed under a vast range of network loading conditions. The network topology employed in these simulations included both coupling impedance and transformer impedance, in order to construct a basic yet realistic model. The inclusion of a slack element facilitated the initialization process, though it is not obligatory, and its disconnection was carried out as per the equations derived. The values P_{m} and ω_{dr} are determined under constant load and varying impedances. The test bench is simulated with PSS®NETOMAC in RMS and EMT domain, displaying Phase 2's development and results.

4.3.1 Single converter configuration

The test bench depicted in Figure 3.9 in a single converter configuration is considered under one selected loading condition to verify the P_{m} and ω_{dr} deductions of sub-section 3.4.1 This section is segmented into scenario description (sub-section 4.3.1.1), discussion of results and inferences drawn (sub-section 4.3.1.2) and evidence for priority of disturbance over setpoints is also displayed in sub- section 4.3.1.3. The test bench is simulated with the software tool PSS®NETOMAC in phasor-domain in a per-unit MVA system. The sequence of events for the simulation is as follows.

- A load of 1 pu is connected to the network equivalent at 2.5 sec.
- Connection and synchronization of the first converter at 7.5 sec.
- Disconnection of the slack or network equivalent occurs at 12.5 sec.
- The simulation runs for 16 sec.

The period from 12.5 sec onwards corresponds to the solution with a constant P_{ref} of 0.0 pu. Therefore, the results of interest can be found in Table 4.6 for this period ($\geq$ 12.5 sec). The frequency deviation, designated by $\Delta\omega$, was calculated relative to the nominal value (ω_{n}) for the test bench before and after the disconnection of the grid equivalent. The sequence of events is simulatively evidenced in Figure 4.10 (a) to Figure 4.10 (c) for Case 2. The area of interest is shaded in grey.

4.3.1.1 Simulated scenarios

Case 1: The present network configuration encompasses lumped impedances (X_{C}+X_{T}) as previously employed in sub-section 3.4.1. The reference value is maintained constant throughout the simulation. Table 4.6 presents a reiteration of the network parameters from Table 3.1 for ease

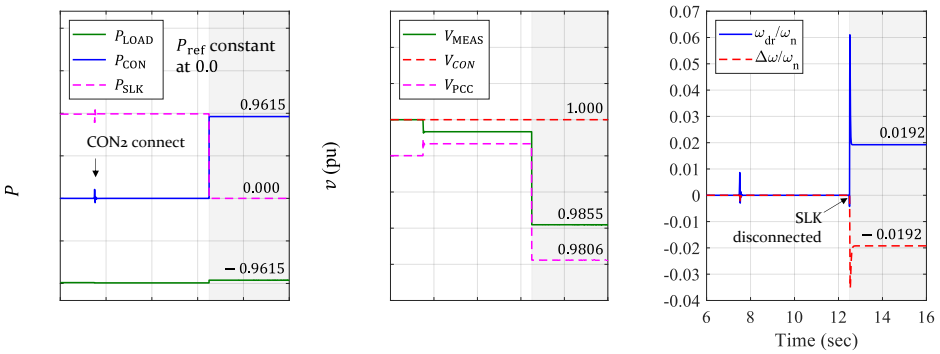

Figure 4.10: Case 2: (a) Active power flows with a constant reference of 0.0 pu; (b) Voltage magnitudes; (c) Frequency drift in control (ω_{dr}) and network ($\Delta\omega$).

of comparison with Case 2 and displays the resulting steady-state operating points.

Case 2: This case represents an elaboration of Case 1 with segregated coupling and transformer impedances, as per network requirements outlined in Table 3.1. The steady-state solution and the selected network values are available in Table 4.6.

4.3.1.2 Results and inferences

Simulation results supporting the mathematical equations ((3.72) and (3.77)) are illustrated in Table 4.6. Case 1 and Case 2 demonstrate the achievement of the steady-state operating point with a resultant ω_{dr} of 0.0192 pu in control. The network frequency deviation is $\Delta\omega$ with value $\Delta\omega = -\omega_{\mathrm{dr}}$, owing to load increase. The primary distinction between Case 1 and Case 2 is the additional voltage drop at the measurement node in Case 1, resulting from the segregated impedances ($2X = X_{\mathrm{C}} + X_{\mathrm{T}}$), despite the load flow remaining unchanged. These results thus demonstrate the viability of the equations and the development of ω_{dr} due to active power control. The importance of transformer impedance in Case 1 and Case 2 further display that the resultant ω_{dr} is determined by the total load and is thus equivalent [29]. With appropriate selection of reference value as in Case 2 (Figure 4.10), ω_{dr} can be compensated, and nominal frequency is restored as discussed in the next section.

4.3.1.3 Evidence for priority of disturbance over setpoints

The effectiveness of the active power control (APC) response in conjugation with the fundamental block of PRP or Phase 1 is validated and demonstrated in Case 2 through the development of an operating point and

Table 4.6: Parameters and results for single converter scenarios.

Network parameters	**Case 1**	**Case 2**
X_{C} (as in (4.1))	0.2	0.1
X_{T}	$0.1 * 10^{-6}$	0.1
R	$X_{\mathrm{C}} * 5.0$	$X_{\mathrm{C}} * 10.0$
CON - P_{ref}	0.0	0.0
Results ($t \geq 12.5\ sec$) – setpoint changes		
$\omega_{\mathrm{dr}}/\omega_{\mathrm{n}}$ in control(Analytical) (pu)	0.0192	0.0192
$\omega_{\mathrm{dr}}/\omega_{\mathrm{n}}$ in control (Simulative) (pu)	0.0192	0.0192
$\Delta\omega/\omega_{\mathrm{n}}$ in network (pu)	-0.0192	-0.0192
F (Hz)	49.0385	49.0385
P_{CON} – Active power (MW)	$0.9615 \cong 0.962$	$0.9615 \cong 0.962$
P_{SLACK} – Active power (MW)	0.00	0.00
P_{LOAD} - Load power (MW)	-0.9615	-0.9615
V_{CON} – Voltage (pu)	1.00	1.00
V_{MEAS} – Voltage (pu)	0.9806	0.9855
V_{PCC} – Voltage (pu)	0.9806	0.9806

the resulting non-zero drift frequency (ω_{dr}). Utilizing dedicated parameters in PRP with APC, deviation of ω_{dr} from zero is eliminated via PI control action, resulting in the achievement of nominal frequency (ω_{n}) in the complete control scheme . The performance of the PRP with and without superimposed APC is compared through the simulation of the test scenario, Case 2, utilizing the following three variants:

a. PRP without APC (Figure 3.2)
b. PRP with APC and $P_{\mathrm{ref}} = 0.0$ (identical to Case 2 - Figure 3.8)
c. PRP with APC and $P_{\mathrm{ref}} = 0.9615$ at $t = 14\ sec$

In Variant (a), the steady-state drift frequency (ω_{dr}) is observed to be zero, as illustrated in Figure 4.11 (displaying the time scale of interest). This is demonstrated by the immediate response to a disturbance, such as the disconnection of grid equivalent and return to nominal frequency ω_{n}. However, the absence of APC, limits the ability for arbitrary power dispatch and interaction with other devices. Therefore, the inclusion of APC is necessary. Variant (b) illustrates the superposition of the PRP and APC in response to a disturbance, with no changes to the setpoint. The resulting

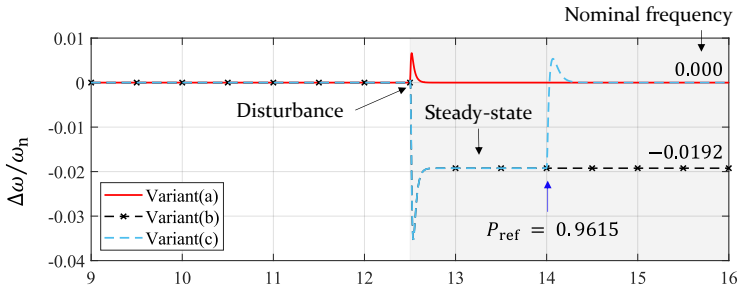

Figure 4.11: Comparison of frequency drift in the network ($\Delta\omega$) of Case 2 variants.

steady-state of $\omega_{dr} = -0.0192$ pu, indicating deviation from the nominal frequency ω_n. Variant (c) extends the previous Variant (b) by incorporating tuned reference values that result in nominal frequency or $\omega_{dr} = 0.0$ pu.

The nominal frequency is achieved through a delayed response by prioritizing responding to the disturbance to attain steady-state. The selection of apt APC parameters (K_3, T_3) such that the reaction to the event governs over the response to setpoint changes. The $\Delta\omega$ trajectories in pu for all three variants are visible in Figure 4.11.

4.3.2 Two converter configuration

The control scheme is evaluated in a two converter symmetrical network configuration, utilizing the coupling and transformer impedances outlined in Table 4.7 and depicted in Figure 3.9. The content in this section is structured with scenario descriptions in sub-section 4.3.2.1 and discussion of results and inferences in sub-section 4.3.2.2. The simulation is conducted using PSS®NETOMAC software in RMS and aimed to examine the response to setpoint changes and attainment of steady-state. The test bench is constructed in a per-unit MVA system. The sequence of the simulation events is as follows:

- At 0.5 sec, the first converter (CON1) is connected and synchronized with a reference value of 0.0 pu.
- At 2.5 sec, a load of 2 pu is connected to the network.
- At 7.5 sec, the second converter (CON2) is connected and synchronized with a reference value of 0.0 pu.
- At 12.5 sec, the disconnection of the slack is simulated.

- At 7.0 sec and 14 sec, the reference value P_{ref} of CON1 and CON2 were altered from their initial values of 0.0 pu to the values given in Case 4 and Case 5.
- The simulation was run for a duration of 16 sec.

The timeline from 14.0 sec onwards corresponds to the solution equations with a step-change in P_{ref} in both converters. The deviation of the system frequency from ω_{n} is represented by $\Delta\omega = (\omega - \omega_{\mathrm{n}})$, where ω is the resultant system frequency. Time frame of interest is shaded in grey and is shown in Figure 4.12 to Figure 4.14 and Table 4.7.

4.3.2.1 Simulated scenarios

Case 3: The present scenario demonstrates the accomplishment of a constant P_{ref} of 0.0 pu to display the achievement of that the same ω_{dr} by the two converters as by one in Case 2. This is achieved via symmetrical network and control parameters. The two converters equally contribute to the load of 2 pu. The steady-state values, obtained through analytical and simulation methods utilizing grid parameters, are presented in Table 4.7.

Table 4.7: Parameters and results for the two converter scenarios.

Network parameters	**Case 3**	**Case 4**	**Case 5**
X_{C1} and X_{C2} (as X_{C} given in (4.1))	0.1	0.1	0.1
X_{T1} and X_{T2}	0.1	0.1	0.1
R	$X_{\mathrm{C}} * 5.0$	$X_{\mathrm{C}} * 5.0$	$X_{\mathrm{C}} * 5.0$
CON1 - P_{ref1}	0.0	0.9615	0.9615
CON2 - P_{ref2}	0.0	-0.9615	0.9615
Results ($t \geq 14\ sec$) – setpoint changes			
$\omega_{\mathrm{dr}}/\omega_{\mathrm{n}}$ in control(Analytical) (pu)	0.01922	0.01848	0.0
$\omega_{\mathrm{dr}}/\omega_{\mathrm{n}}$ in control (Simulative) (pu)	0.0192	0.0184	0.0
$\Delta\omega/\omega_{\mathrm{n}}$ in network (pu)	-0.0192	-0.0184	0.0
F (Hz)	49.0385	49.0786	50.000
P_{CON1} – Active power (MW)	0.9615	1.8829	0.9615
P_{CON2} – Active power (MW)	0.9615	-0.0401	0.9615
P_{LOAD} – Load power (MW)	-1.9230	-1.8427	-1.9230
V_{CON1} – Voltage (pu)	1.0000	1.0000	1.0000
V_{CON2} – Voltage (pu)	1.0000	1.0000	1.0000
$V_{\mathrm{MEAS\_C1}}$ – Voltage (pu)	0.9855	0.9601	0.9855
$V_{\mathrm{MEAS\_C2}}$ – Voltage (pu)	0.9855	0.98	0.9855
V_{PCC} – Voltage (pu)	0.9806	0.96	0.9806

Case 4: This scenario demonstrates unequal P_{ref} setpoint changes and the resultant ω_{dr} at steady-state. Both $P_{\mathrm{ref1}} = 0.9615$ and $P_{\mathrm{ref2}} = -0.9615$ in CON1 and CON2, respectively, altering from 0.00 pu of their initial value. Table 4.7 presents the correlation between ω_{dr} and network parameters, as determined through both analytical and simulation methods.

Case 5: This case highlights the ability to eliminate ω_{dr} through the implementation of suitable setpoints values or P_{ref} and demonstrate power system dynamics and control stability. Table 4.7 provides a comprehensive overview of the network and control parameters that are instrumental in achieving nominal frequency.

4.3.2.2 Results and inferences

The steady-state solution for Case 3 with a constant P_{ref} at 0.0 pu are tabulated in Table 4.7 and Figure 4.12. Please refer Appendix A4 for per-unitization definition of voltage. This scenario is analogous to Case 1 or Case 2 as both converters share the load equally under pure symmetrical conditions and without any additional step-change in P_{ref}. The resultant drift frequency (ω_{dr}) achieved is equivalent to that of the single converter configuration, thus confirming the deductions outlined in Section 3.4. The network deviation is represented by $\Delta\omega = -\omega_{\mathrm{dr}}$, which indicates that the system frequency (F or ω) is lower than the nominal value. The common and differential modes are 0.0 pu.

In Case 4 both *common-mode* and *differential-mode* effects are perceptible and shown in Figure 4.13. The choice of the setpoint P_{ref} defines the frequency which is determined by the *common-mode*. The *differential-mode* defines the power-sharing between the two sources. In this scenario, due to the change in P_{ref} after 14 sec, the resultant *differential-mode* is 2 pu, with CON1 participating in the overall load sharing. In contrast, CON2 does not contribute to the share ascribed to the P_{ref} selection. The *common-mode* is 0.0 pu, and contrary to expectation, ω_{dr} is dissimilar to that of Case 3. The difference in ω_{dr} is attributed to the different voltage at PCC compared to Case 3 and in accordance with (3.87). In order to obtain the same ω_{dr}, the measured power should be identical. With the same *common-mode* but unequal *differential-mode*, the loop currents at PCC vary, and the phase of total voltage (φ) at the load is different, resulting in a different redistribution of power among the sources, as presented in Table 4.7. Finally, Case 5 exhibits only *common-mode* and no *differential-mode* with an appropriate choice of P_{ref} values displayed Figure 4.14. The resulting ω_{dr} is 0.0 pu, and the system attains nominal frequency ($\omega = \omega_n$).

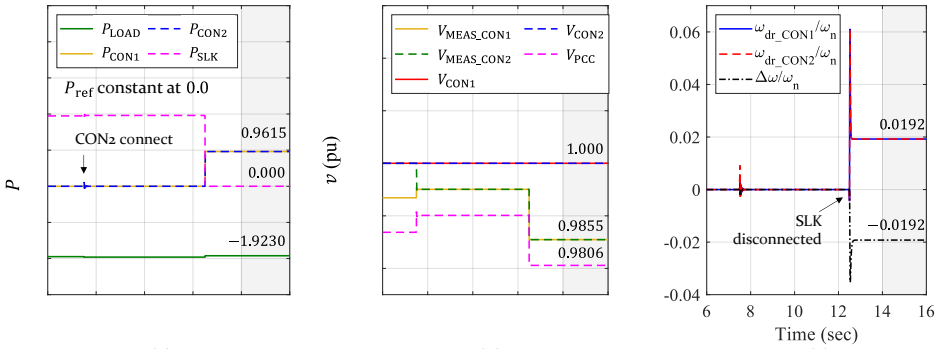

Figure 4.12: Case 3: (a) Active power flows with no reference change for CON1 and CON2; (b) Voltage magnitudes; (c) Frequency drift in converter control (ω_{dr} in CON1 and CON2) and network ($\Delta\omega$).

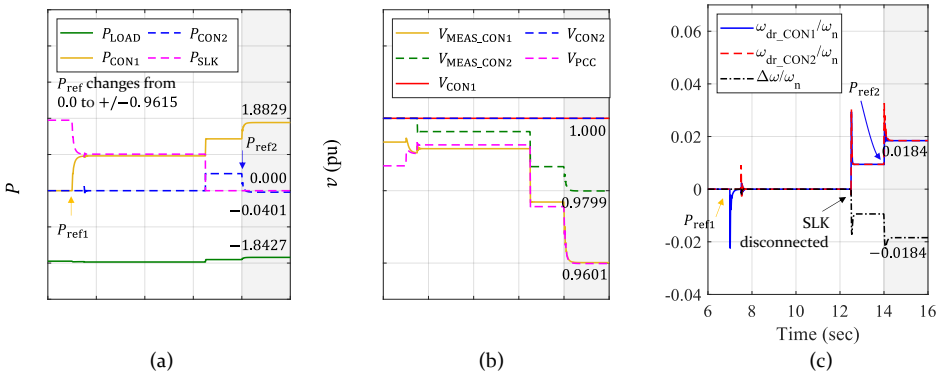

Figure 4.13: Case 4: (a) Active power flows with reference change to +0.9615 pu for CON1 and −0.9615 pu for CON2; (b) Voltage magnitudes; (c) Frequency drift in converter control (ω_{dr} in CON1 and CON2) and network ($\Delta\omega$).

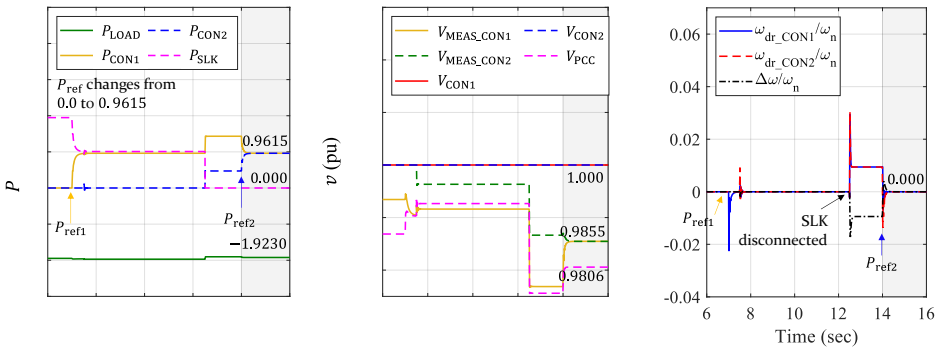

Figure 4.14: Case 5: (a) Active power flows with reference change to +0.9615 pu for CON1 and CON2; (b) Voltage magnitudes; (c) Frequency drift in converter control (ω_{dr} in CON1 and CON2) and network ($\Delta\omega$).

The presented examples illustrate the converters, when operating without any network equivalent or SM, achieve a steady-state operating point to satisfy the load requirements. Thus, PRP in conjugation with the APC achieves control stability with ω_{dr} which may deviate from nominal frequency (ω_{n}). Upon reaching steady-state, a common frequency throughout the power system develops, with same absolute value in control and network. The manipulation of the weighted gain or power-frequency droop 'c', references (P_{ref}) and initial conditions results in steady-state at a unique frequency for a given total load. The sum of the references ($P_{\mathrm{ref1}} + P_{\mathrm{ref2}}$) interplay with the total measured load (P_{LOAD}). This, P_{LOAD} defines the ω_{dr} and may return to ω_{n} through the selection of appropriate controller setpoints.

Additionally, dissimilar power-sharing or *differential-mode* in converters may arise due to variations in coupling impedance, reference values, or both. The time traces provided to assist in visualizing that the step-responses are comparable to 1st order transfer functions, whilst double integrators act for the power balance control and the differentiator creates phase stability. The likelihood of possible instability is frequent with integrator control of higher order than one [30, 142].

Performance of APC with PRP in unsymmetrical delta configuration is presented in [142].

4.3.3 Self-stabilizing setpoint via droop

The impacts of the self-stabilizing droop (K_2) are displayed via various simulation scenarios. The presented Cases 2, Cases 2(c), Cases 3, and Cases 5 are restimulated considering the K_2 in different simulation domains and cross-examined with the analytical results. The ω_{dr} obtained from equations (3.101) and (3.77) are verified for a single converter, while (3.94) and (3.96) are solved with 'c'' in (3.94) for two converter configurations accounting for the additional droop K_2. The analytical results are matched simulatively which are shown in Figure 4.15 and Figure 4.16 for Case 2(c) and Case 5, respectively. While Case 2 and3 are available in the Appendix A9 (Figure A 5 and Figure A 6). The values are tabulated in Table 4.8 for comparison.

Initial simulation in EMT, RMS and frequency dependent RMS (enhanced RMS) simulations are performed for the scenarios mentioned with the resistive load. The frequency dependent RMS simulation results in additional network element manipulation where the impedances are modelled as frequency dependent (linear dependency) to incorporate the

system response and create a realistic network response under dynamics (similar to EMT domain). Additionally, a wide range of network loading conditions supporting the implementation of K_2 is simulated in the EMT domain and discussed in Section 4.3.3.2.

The section first discusses the comparison of responses across simulation domains considering K_2 (sub-section 4.3.3.1), followed by extensive testing of the droop under different loadings confirming the advantage if this self-stabilizing droop (sub-section 4.3.3.2) which is further divided into scenario description and discussion of results.

4.3.3.1 Comparison of responses across simulation domains

As mentioned above EMT, RMS and frequency dependent RMS (enhanced RMS) simulations are performed for the scenarios Case 2, Case 2(c), Case 3, and Case 5 with the resistive load with the identical sequence of events. The prime purpose of this section is to evaluate the stability incurred due to the additional droop K_2 verified by mathematical derivation and to understand the simulation domain boundary conditions with regards to accuracy.

The analytical and simulative responses in all domains are comparable as tabulated in Table 4.8. However, the analytical values better matched the steady-state response obtained in EMT and enhanced RMS. The minor deviation in pure RMS domain results is attributed to the constant frequency assumption or missing homogenous solution ($\underline{i}_{\mathrm{h}}$) in simulation

Table 4.8 : Comparison of analytical and simulation results for the cases simulated in RMS, enhanced RMS and EMT domain.

Scenario	$\boldsymbol{P}_{\mathbf{ref1}}$	$\boldsymbol{P}_{\mathbf{ref2}}$	**Analytical** $\frac{\omega_{\mathrm{dr}}}{\omega_{\mathrm{n}}}$ (pu)	**RMS** $\frac{\omega_{\mathrm{dr}}}{\omega_{\mathrm{n}}}$ (pu)	**RMS with frequency dependency** $\frac{\omega_{\mathrm{dr}}}{\omega_{\mathrm{n}}}$ (pu)	**EMT** $\frac{\omega_{\mathrm{dr}}}{\omega_{\mathrm{n}}}$ (pu)
Case 2	0,00	-*	0.015403	0.015384	0.015406	0.015399
Case 2(c)	0.961523	-*	0	0	0	0.000001
Case 3	0.0	0.0	0.015405	0.015384	0.015406	0.015399
Case 5	0.961523	0.961523	4.00E-07	0	0.000002	0.000001

-* **:** CON2 is not connected in this scenario

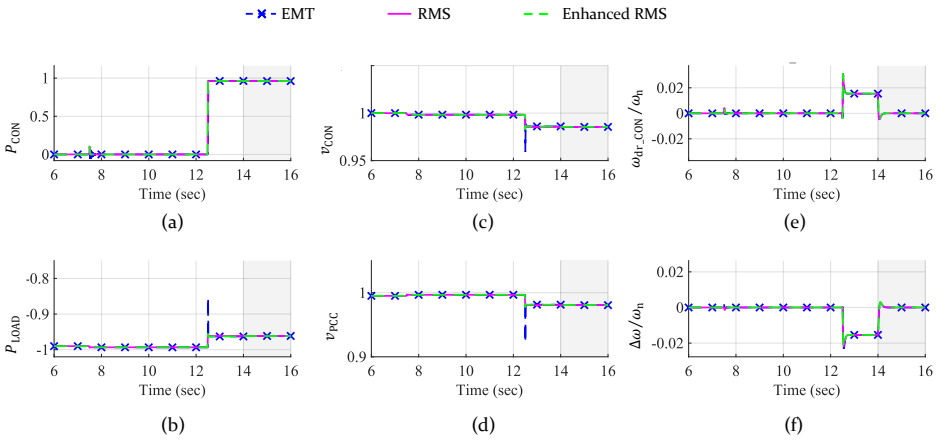

Figure 4.15: Case 2(c):
(a) Active power flow with reference change to +0.9615 pu;
(b) Load active power flow; (c) and (d) Voltage magnitude; (e) Frequency drift in converter control; (f) Frequency deviation in network.

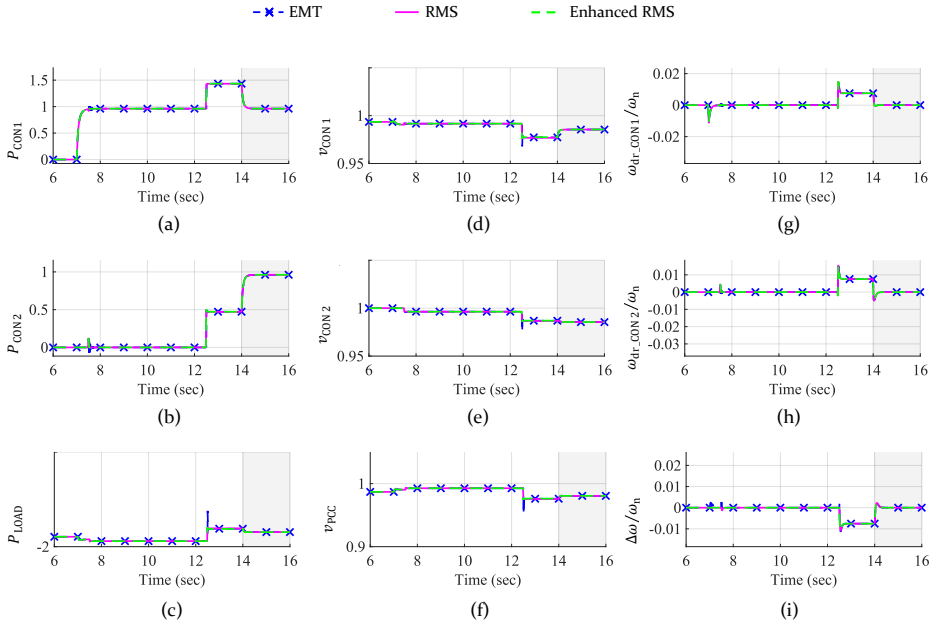

Figure 4.16: Case 5 :
(a) and (b) CON1 and CON2 active power flow with reference change to +0.9615 pu; (c) Load active power flow; (d), (e) and (f) Voltage magnitude; (g) and (h) Frequency drift in converter control; (i) Frequency deviation in network.

as discussed in Section 2.5 (at 4th decimal place). The intermediate simulation procedure examines the RMS sufficiency and the overestimation of the network responses in this domain. The active reference is adjusted via the additional droop K_2 without a supplemental P_{ref} tuning. The frequency deviation is further reduced to attain ω_{n}, compared to Cases 2 and 3 simulated in sub-section 4.3.1 and 4.3.2 of this chapter. The self-stabilizing gain, as described in Section 3.4.3, injected additional active power, helps damp the transient response, and attains steady-state. On manipulating P_{ref}, the frequency deviation is reduced to zero as seen in Figure 4.15 and Figure 4.16.

4.3.3.2 Current response under arbitrary loadings

An exhaustive combination of load (shunt impedance) parameters is performed to demonstrate the effectiveness of self-stabilizing droop (K_2) and display the response of the modified APC with PRP (Phase 2) under different loading conditions. The test bench is displayed in Figure 4.17 is simulated in PSS®NETOMAC and the sequence of events include:

- The connection and synchronization of converter (CON1) at 0.5 sec with a 0.0 pu reference value.
- The slack is disconnected at 2.0 sec.
- The load is connected at 2.5 sec with varied impedance values.
- The second converter (CON2) is connected and synchronized at 12.5 sec with a reference value of 0.0 pu.
- At 22.5 sec, the load is disconnected.
- The load is reconnected at 32.5 sec.

The resultant network at $t = 12.5$ sec is a star-connected network with Phase 2 PRP-based GFM converters. The complete simulation is run for 40 sec. The test bench network parameters are tabulated in Table 4.9. The following resistance and inductance values are considered for the load impedance given by $Z = \sqrt{R^2 + X^2}$ in ohms.

$$R = X_{\text{C1}} \times R_{\text{Fact}} \tag{4.4}$$

$$X = X_{\text{C1}} \times X_{\text{Fact}} \tag{4.5}$$

$$\text{where, } R_{\text{Fact}} = \{0.001, 1.0, 2.0, 3.0, 4.0, 5.0, 6.0, 7.0, 8.0, 9.0, 10.0\} \tag{4.6}$$

$$\text{and } X_{\text{Fact}} = \{0.001, 1.0, 2.0, 3.0, 4.0, 5.0, 6.0, 7.0, 8.0, 9.0, 10.0\}. \tag{4.7}$$

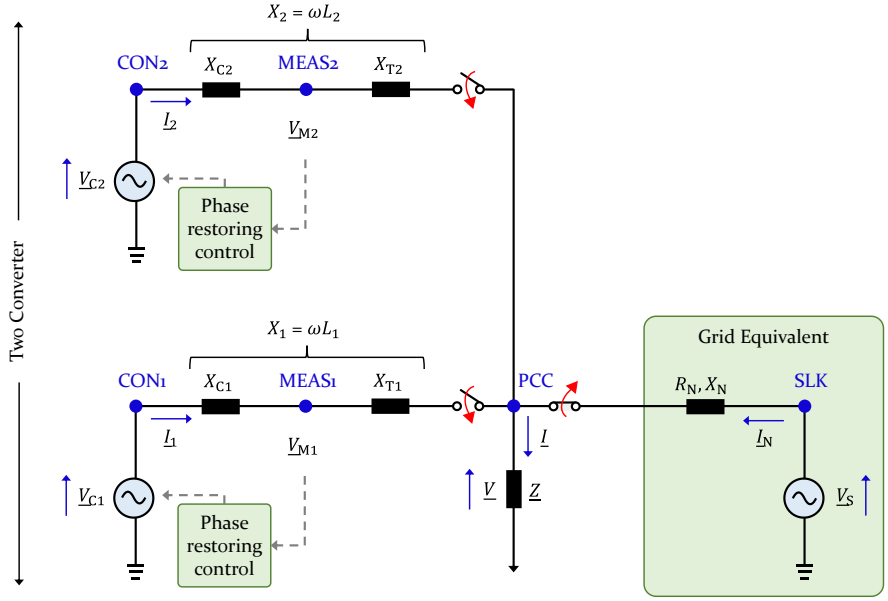

Figure 4.17 : Test bench for vary network loading conditions.

Employing (4.4) and (4.5), a resultant of 121 scenarios are created with unique R_{Fact} and X_{Fact} from (4.6) and (4.7) respectively.

Simulated Scenarios

A total of 121 load variants $(\underline{Z})$ are simulated as scenarios under different network loadings with parameters given in Table 4.9. The stability responses of both converters are evaluated with the unrestricted Phase 2 PRP and serves as a prerequisite test before the implementation of the current limits on the control concept. The term unrestricted here relates to the absence of current limitation on the control concept. The responses help assess and inspect PRP's stability under vast conditions. Appendix A8 describes each scenario ordered in ascending Z value with its explicit R_{Fact} and X_{Fact}. The load model implemented is of shunt type, i.e., small impedance leads to large currents indicating a large load and vice versa. The current value displayed in the plots is in pu with peak nominal current value given by:

$$\hat{I}_{\text{n}} = 1\text{MVA} \cdot \frac{\sqrt{2} \cdot 0.69\text{kV}}{\sqrt{3}} = 1.183\ \text{kA}. \tag{4.8}$$

Similarly, the voltage is displayed in pu and a network frequency of 50 Hz is considered. The simulation time step is $T_{\text{INT}} = 10\ \mu\text{sec}$ in EMT domain.

Results and Inferences

The 121 scenarios display a vast combination of results to assess the stability of the unrestricted PRP with modified APC. As mentioned, this intensive testing is required to determine the robustness of the control scheme before implementing any limitations. A steady-state ω_{dr} is achieved in each scenario, and therefore frequency evolves (Figure A 15 and Figure A 16). Uniquely tuning P_{ref} for each scenario, nominal frequency (ω_{n}) shall be accomplished.

A crucial element of this unrestricted control displays exceptionally high currents in the range of 5-7 pu (Figure 4.18 and Figure 4.19) and hence high powers (Figure A 9 and Figure A 10) delivered by the source to attain a stable operating point. The reactive power response are also attached in the Appendix A9 (Figure A 11 and Figure A 12). A significant load connection results in a large voltage drop at the measurement nodes (MEAS1 and MEAS2), as expressed in Figure A 13 and Figure A 14. The response describes the control's unrestrained reaction to an event to create a stable operating point for the power system without respecting converter hardware limits. This reaction is comparable to a synchronous machine (SM) capable of providing 5–7 times fault current during a disturbance. However, as known in the PE industry, semiconductor devices rated for regular operation cannot withstand high overcurrent and thermal stresses [48, 50–53]; hence limiters are required. Typical limit values have been covered in Section 2.2. These uninhibited responses are later contrasted and discussed in Section 4.4, where the current limitation is implemented on the overall control hierarchy, and the differences in response are noticeable.

Table 4.9 : Test bench parameters for two converter with different network loadings.

Network parameters	**Unit**	**Value**
X_{C1} and X_{C2} (as X_{C} given in (4.1))	pu	0.1
X_{T1} and X_{T2}	pu	0.1
R_{T1} and R_{T2}	pu	1.E-9
R_{L}	pu	$X_{\mathrm{C}} \times R_{\mathrm{Fact}}$
X_{L}	pu	$X_{\mathrm{C}} \times X_{\mathrm{Fact}}$
CON1 - P_{Pref1}	pu	0.0
CON2 - P_{Pref2}	pu	0.0

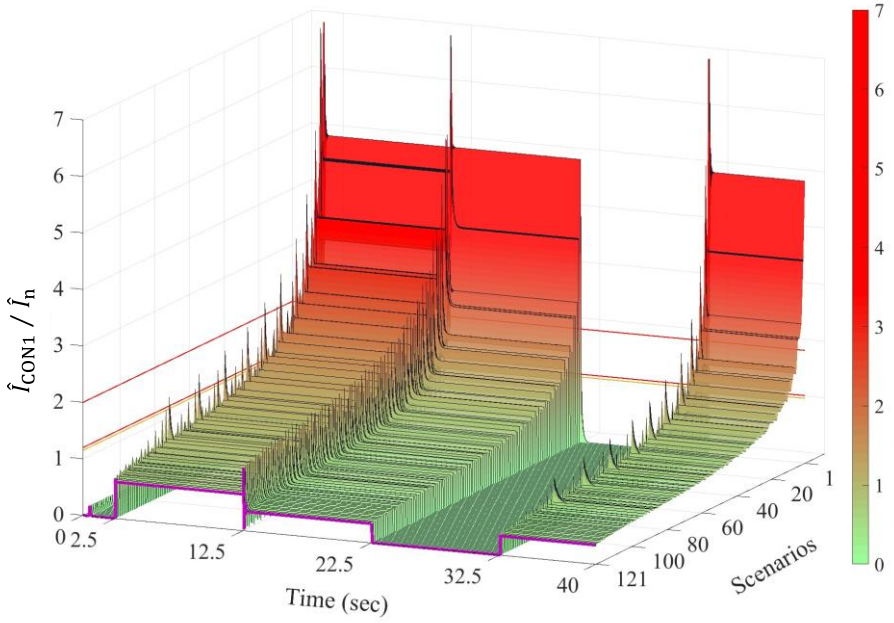

Figure 4.18: CON1 current space vector magnitude ($\hat{I}$) responses without current limiter for 121 shunt impedance variation.

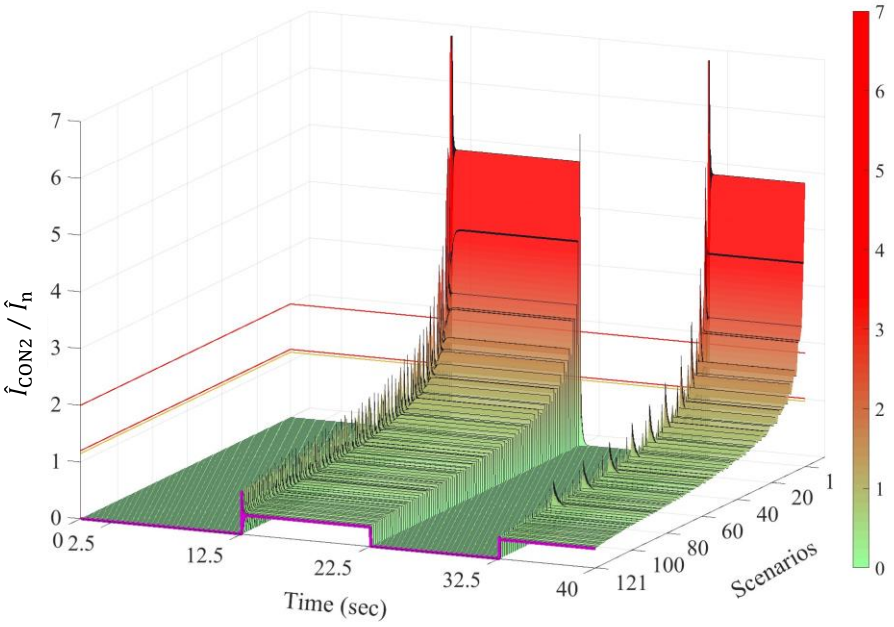

Figure 4.19: CON2 current space vector magnitude ($\hat{I}$) responses without current limiter for 121 shunt impedance variation.

4.4 Response of current limiting control

A broad range of network loading conditions are tested to validate the response of the voltage magnitude-based current limiter incorporated into the PRP-based GFM control (Phase 3). A heuristic approach is adapted to test the control's robustness with tuned optimum parameters. Robustness is the minimum requirement a control system has to satisfy to be beneficial in a practical environment [143]. Upon completion of the designed controller, the parameters are unchanged, and control performance is measured against changing system conditions. The primary focus is to evaluate the operation of the control to achieve stability with the current limit under normal operating ranges.

The performance is demonstrated under a single set of parameters as described in Table 3.4. The identical test bench in Figure 4.17 with the same sequence of events as in sub-section 4.3.3.2 (Phase 2 under different loads) is considered. The simulation is carried out in PSS®NETOMAC, with load modelled as shunt impedance and the events are described as follows:

- The first converter (CON1) is connected and synchronized at 0.5 sec with a 0.0 pu reference value.
- The disconnection of the slack is performed at 2.0 sec.
- Load connection at PCC is performed at 2.5 sec.
- The second converter (CON2) is connected and synchronized at 12.5 sec with a reference value of 0.0 pu.
- Followed by the load is disconnected at 22.5 sec and forms a network with $SCR = 0$ or a weak grid scenario.
- At 32.5 sec, the load is reconnected.

The resultant network at $t = 12.5$ sec, is a star configuration with 100 % IBRs. The load disconnected at 22.5 sec forms a network with $SCR = 0$ due to the absence of any other voltage source, resulting in a viable testing condition for control's robustness. A low SCR implies the system is weak and very sensitive to active/reactive power injections [144]. Each connection and disconnection of either load or slack or converter source is a disturbance event. The various faults for testing current limiting mode for GFM are documented in [82, 90, 92–96]. Thus, combination of voltage faults, frequency and phase faults are incorporated into the event sequence.

The simulation run is for 40 sec considering EMT models in PSS®NETOMAC with control sampling frequency of 10 kHz and simulation

time step of 10 µsec. RMS or phasor-based modelling is justified as long as the system voltages are nearly sinusoidal, as in case of SM, GFL converters in strong grids, and GFM operating in forming mode [90]. However, for GFM with active current limiting, this is no longer valid, as the voltage provided may not be sinusoidal and is not represented adequately by a RMS. The plots are available in Section 4.4.2.

4.4.1 Simulated scenarios

The network parameters for the test bench are described in Table 4.9 with varying impedance ($Z = \sqrt{R^2 + X^2}$) values. The value of R and X are computed based on (4.4) and (4.5), under unique combinations of R_{Fact} and X_{Fact} from (4.6) and (4.7) respectively. The resultant produces a large combination of impedance values or load parameters in ohms to test the control response. 121 variants or scenarios are simulated, so the responses of both converter controls and the entire system are evaluated. Thus, a combination of voltage, frequency, and phase faults encompassing voltage jump reactive current, phase jump, inertial, and damping active current effects may activate current limiting mode. For better comprehension, the voltage jump reactive current may be mapped to voltage drop or short circuit event, the inertia active current to the loss of generating unit or connection of load, phase jump is correlated to line opening or frequency event and damping active power to sub-synchronous oscillations in the system [92]. These events in various combinations are a subset of the 121 simulated scenarios to sufficiently display the GFM characteristics current under faults. Appendix A8 (Figure A 4) describes each scenario ordered in ascending Z value with its explicit R_{Fact} and X_{Fact}.

The load model implemented is of shunt type, i.e., small impedance leads to large currents, implies large load and vice versa. The currents are displayed in pu with nominal continuous value $\hat{I}_{\text{n}} = 1.183$ kA, calculated in (4.8). The voltage displayed is also in pu for a 50 Hz system. The simulated scenarios are identical to sub-section 4.3.3.2 with unrestricted Phase 2 PRP to exhibit a contrast in responses with and without current limit control. Please note that the sequence of events selected with the shunt load display island operation ($t \geq 2$ sec) including short-circuit with 0 pu residual voltage at PCC considering impedance factor of $R_{\text{Fact}} = 0.001$, $X_{\text{Fact}} = 0.001$ and $SCR = 0$ event due load disconnected ($22.5 \text{ sec} \leq t \leq 32.5$ sec) with parallel operated converters. These disturbances constitute large events. Thus, ensuring stable Phase 3 PRP control operation and withstanding fault ride-through represents the control's robustness in these challenging scenarios.

4.4.2 Results and inferences

The solution of the 121 variants is displayed in Figure 4.20 to Figure 4.25. As seen from the voltage, current, and power tendencies, a steady-state operating point (Figure 4.24 and Figure 4.25) is achieved after each event. The considered parameter selection allows both the convert controls to approach a quasi-steady state asymptotically under the described circumstances with the examined control structure plots.

The test network, with its events, describes a set of challenging scenarios to assess the transient and steady-state current limitation under the influence of two converters. The control's robustness is assessed by evaluating responses considering wide ranges of load parameters and their interaction. The connection of CON1 with slack is for initial synchronization with the network followed by its disconnection resulting in the creation of a weak system or island complete IBR dominated. The time span $t = 22.5$ sec to $t = 32.5$ sec with the load disconnection and both converters in operation corresponds to a network with $SCR = 0$. The connection of CON2 at $t = 12.5$ sec describes the differential mode since CON1, in an already connected state, reacts to the event in a stabilizing manner and eventually shares the load power with CON2. Whilst the event at $t = 22.5$ sec describes common mode when both converters have matching contributions to the event.

Under dynamic events, the evaluation of Phase 3 PRP, due to implemented current limiter scheme, may be segregated into the steady-state and transient responses. The steady-state response is visible under all loading conditions with the attainment of maximum values of 1 pu peak current for both converters. The corresponding results of Phase 3 PRP with different loadings are shown in Figure 4.20 to Figure 4.25. Examining the trends with larger loads (small R and X values), it is noticeable that a significant voltage drop results leading to a temporary overcurrent with a peak value ≥ 1.2 pu. Inspecting the peak currents in Figure 4.20 and Figure 4.21 shows that the maximum peak occurs due to the connection of CON2 or the unrealistic load (small R value with smaller X value) connected to the system; however, the temporary overcurrent values are well below 1.5 pu. The maximum peak current ($\hat{I}$) as a function of scenario's impedances (R and X values) are plotted in Figure 4.26 and Figure 4.27. displaying values < 1.5 pu. The connection of CON2 results in an interaction with CON1 and a resulting differential mode between them. Connection of large loads is performed to establish control's robustness.

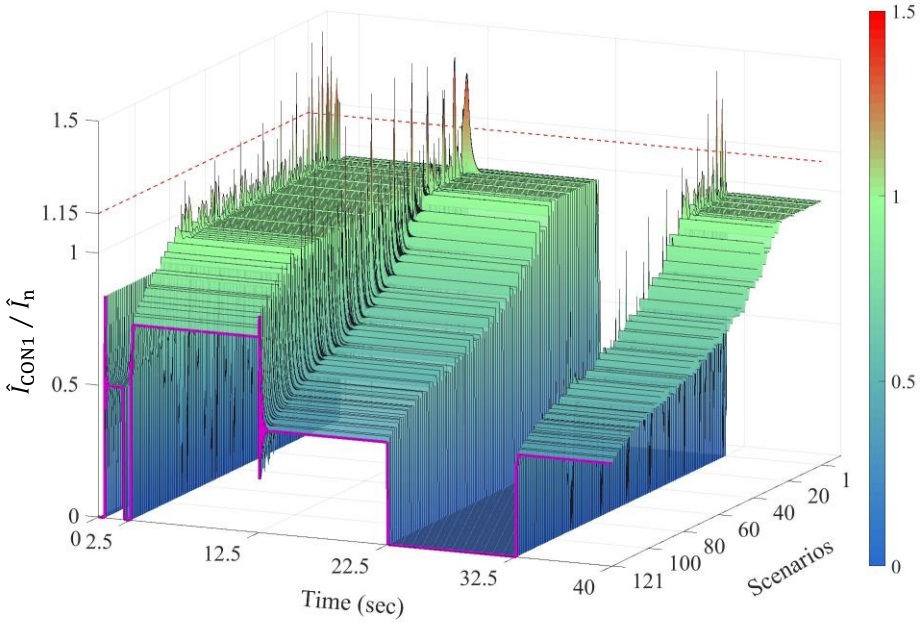

Figure 4.20: CON1 current space vector magnitude ($\hat{I}$) responses with current limiter for various shunt impedance values (121 cases) and no reference change.

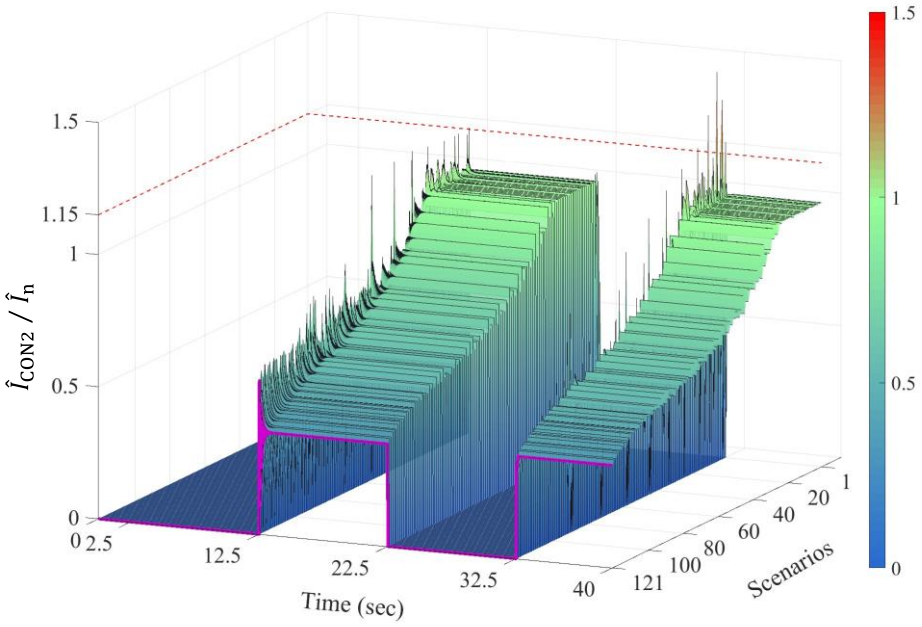

Figure 4.21: CON1 current space vector magnitude ($\hat{I}$) responses with current limiter for various shunt impedance values (121 cases) and no reference change.

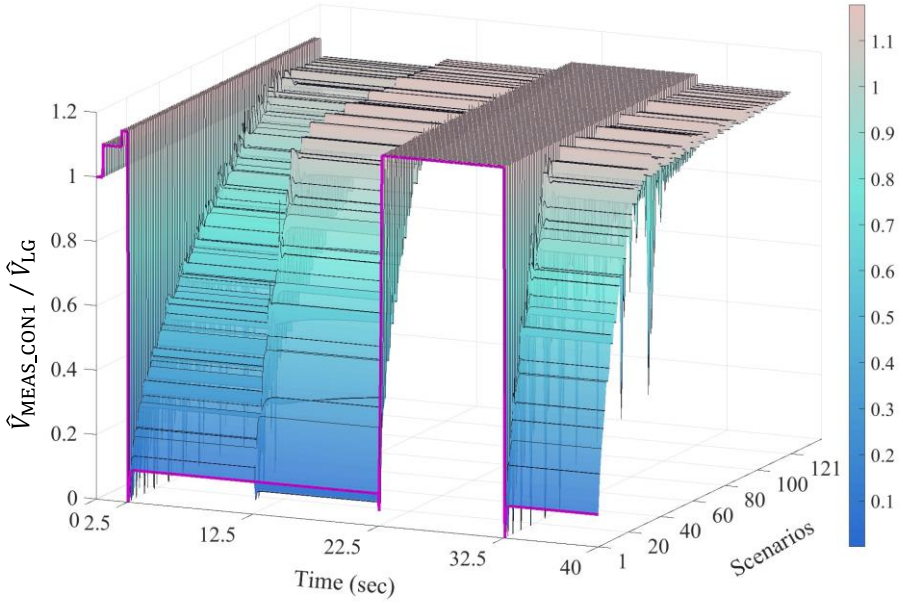

Figure 4.22 : CON1 voltage space vector magnitude ($\hat{V}$) at MEAS1 node with current limiter for various shunt impedance values (121 cases) and no reference change.

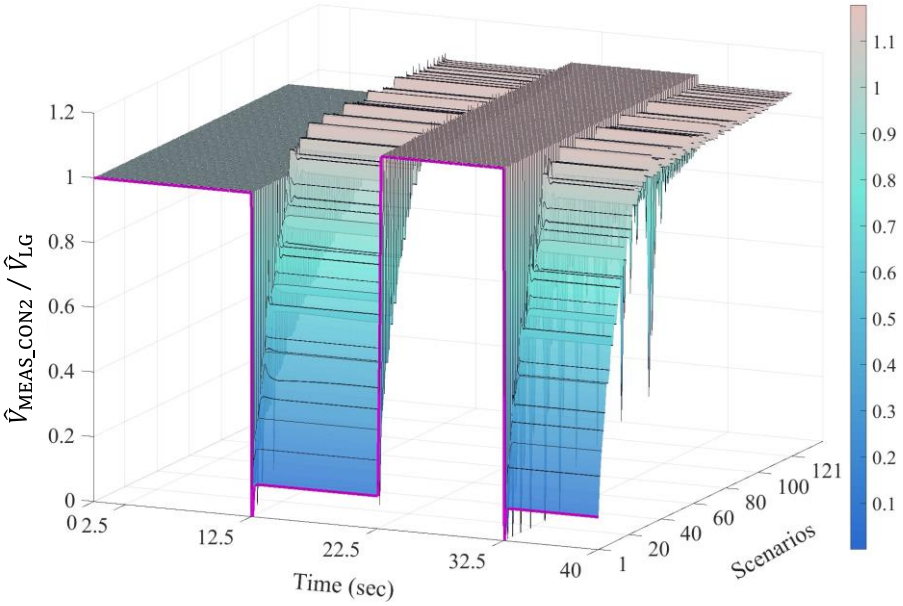

Figure 4.23: CON1 voltage space vector magnitude ($\hat{V}$) at MEAS2 node with current limiter for various shunt impedance values (121 cases) and no reference change.

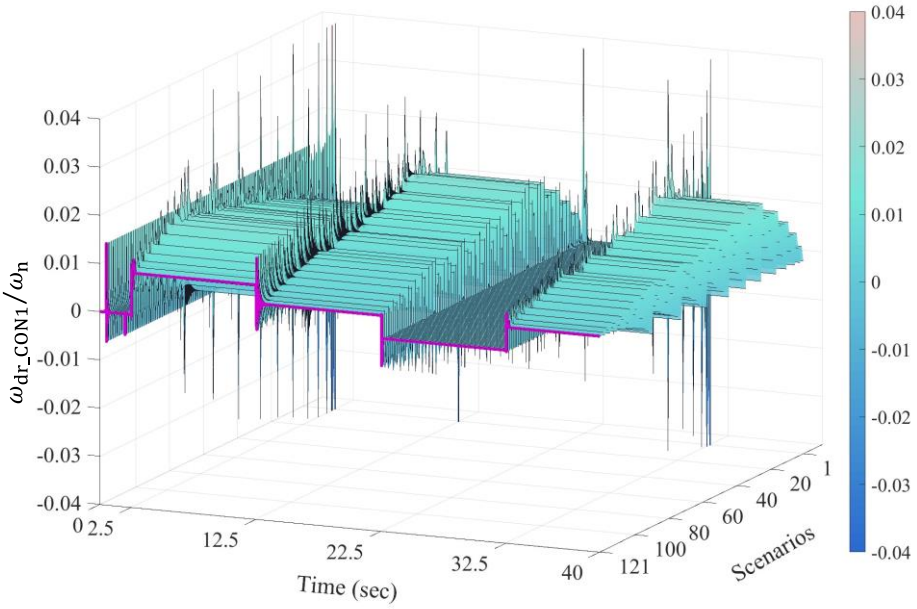

Figure 4.24: Frequency drift in converter control CON1 (ω_{dr}) with current limiter for various shunt impedance values (121 cases) and no reference change.

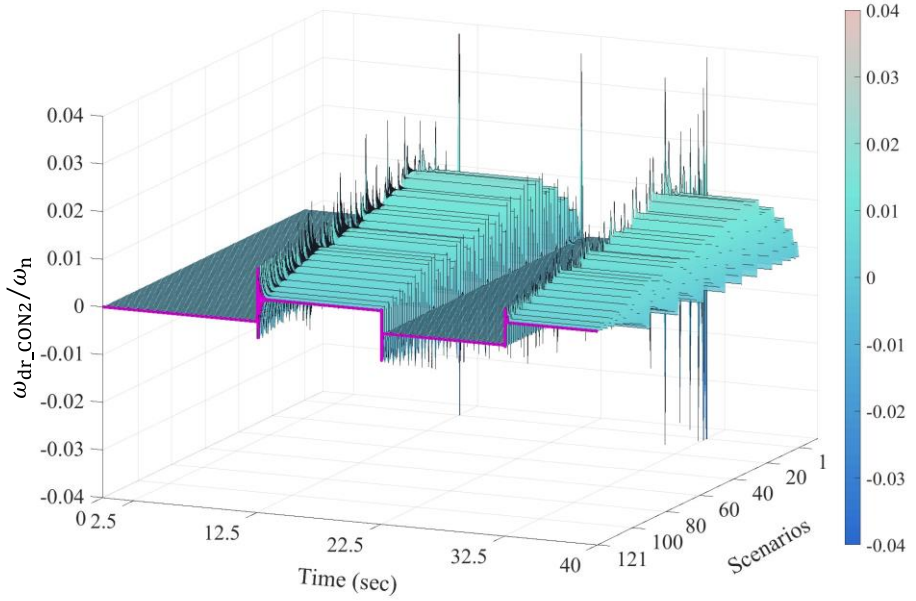

Figure 4.25: Frequency drift in converter control CON2 (ω_{dr}) with current limiter for various shunt impedance values (121 cases) and no reference change.

The highest peak current ($\hat{I}$) is 1.45 pu at CON1 (Figure 4.26) when CON2 is connected with load values ($\underline{Z}$) of $R_{\mathrm{Fact}} = 5.0$, $X_{\mathrm{Fact}} = 0.001$, as a result of the *differential-mode*. Whereas at CON2, the highest $\hat{I}$ is 1.37 pu (Figure 4.27.) with load connection as a disturbance event with Z of $R_{\mathrm{Fact}} = 0.001, X_{\mathrm{Fact}} = 2.0$. The maximum duration for the peak value is ca. 40 msec with $R_{\mathrm{Fact}} = 0.001, X_{\mathrm{Fact}} = 2.0$ resulting due to the switching on CON2. The detected temporary transient overcurrent value (max. 1.45 pu) may result in an oversizing of the converter for certain network conditions, depending on the permissible peak/continuous current ratio of applied semiconductors. It is a necessary bargain for stability and outweighs the price aspect. Furthermore, the peaks due to such high-power resistors are not encountered in reality. In the power system, typical loads are inductive, and in small-signal theory, loads are also inductive in nature. Therefore, considering and evaluating typical inductive loads with power factor (PF) 0.95 the peak value is $\hat{I} = 1.15$ pu, while with a PF of 0.8 the $\hat{I} = 1.05$ pu. These values are well within the trip levels of $1.2 - 2.0$ pu of the nominal continuous current ($\hat{I}_{\mathrm{n}}$) [48, 50–53].

As described in Table 4.9, the network considered is highly undamped, with Q-factor ≥ 1000 depending on the connected loads. The Q-factor determines the damping response of a system, where an underdamped system is described with higher values and vice-versa. The control response demonstrated does not rely on passive damping and is resilient to the weakly damped DC component. Post transient current overshoot, the phase current magnitude is well maintained within 1.0 pu (Figure 4.20 and Figure 4.21). The active and reactive power flows are visible in Figure A 17 to Figure A 20 of Appendix A10. The necessary reactive power supply is maintained and determined by the ratio of the impedances between the converter node and PCC as required by grid code upon the voltage drop. Furthermore, the control response is sufficiently fast and requires approx. 500 msec ($R_{\mathrm{Fact}} = 0.001, X_{\mathrm{Fact}} = 5$) to restore its 90 % normal operational voltage evaluated form Figure 4.22 and Figure 4.23. Please note that the performance values mentioned above are for the worst-case scenarios, and the full spectrum of scenario values are displayed in the figures.

Due to the wide range of load impedance ($\underline{Z}$) parameters, an essential observation is the dominant influence of the reactance (X). It creates a more significant voltage drop and results in critical events than a dominant resistive (R) part of an impedance. It can be remedied with higher reactive voltage with small phases to remain small-signal stable.

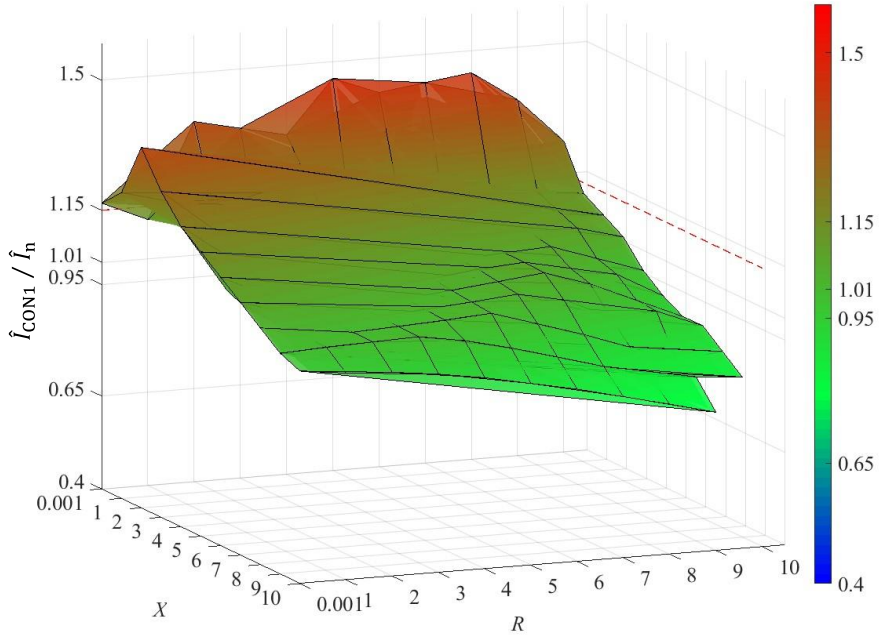

Figure 4.26: Maximum $\hat{I}$ for CON1 as a $f(R, X)$ in each of the 121 scenarios.

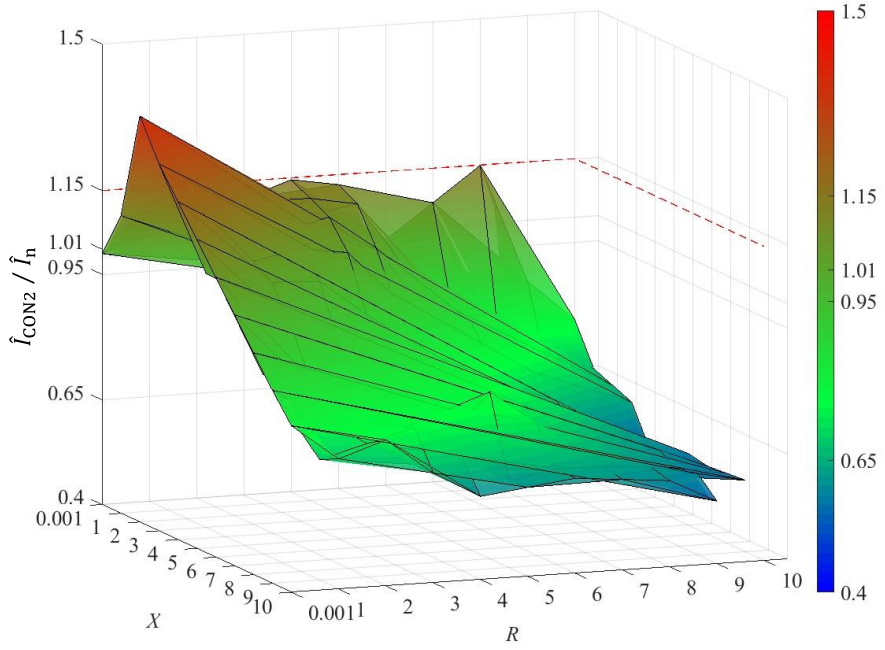

Figure 4.27: Maximum $\hat{I}$ for CON2 as a $f(R, X)$ in each of the 121 scenarios.

The new and improved current control methodology is applied on voltage magnitude. The orthogonal part (quadrature component $\underline{V}_q$) has negligible impact on the voltage magnitude under small phases. Therefore, the implemented limitation with PRP helps to stabilize critical scenarios. As mentioned in Section 3.1, the PRP acts on the phase part of the rotational voltage, thus creating stabilizing reaction to events where the resistive characteristics of the load are dominant. In contrast, the current limit control is applied to the voltage magnitude. A dominant resistive load results in increased phase difference, while a dominant reactance results in a significant drop in voltage magnitude. However, the effects are no longer decoupled for an impedance with substantial contributions from both resistive and inductive facets. To address a broad spectrum of network loading conditions and control interaction, the parameter selection is performed as a comprise between the stability and dynamics in all investigated cases, keeping in mind one set of parameters has been considered for all scenarios.

Comparing the response with Section 4.3.3.2, where Phase 2 did not include a current limitation control, the $\hat{I}$ in Phase 3 is reduced significantly. The steady-state current is limited to the designed rated value. The unrestricted response of Section 4.3.3.2 displays $5-7$ pu $\hat{I}$ (Figure A 7 and Figure A 8) with corresponding high powers (Figure A 9 and Figure A 10). An apparent reduction in the power flows (Figure A 17 to Figure A 20) is also visible with limits. Due to the additional enhancements in the overall Phase 3 control structure, the frequency deviations (ω_{dr}) are also improved (Figure 4.24 and Figure 4.25). The unrestricted Phase 2 PRP displays a direct correlation to the largest load creating the most significant frequency deviations. However, due to the controlled responses in Phase 3, the ω_{dr} is minimized. The control response is stable and shows a resilient performance under challenging conditions. Additional discussion on current limitation implications is presented in Section 5.3.

4.5 Response of complete Grid-Forming control

As a concluding test, a sequence of dynamic events is performed on the Phase 3 control (Figure 3.14) considering current limits and setpoint changes. The test describes the overall dynamic performance of the control by restoring the network frequency to nominal. The network conditions are identical to Section 4.4, with test bench in Figure 4.17 and parameters given in Table 4.10 for two cases. A realistic load impedance (pu) based on power factor (PF) of 0.95 with $R_{\mathrm{Fact}}=6,\ X_{\mathrm{Fact}}=2$ and PF of 0.80 with $R_{\mathrm{Fact}}=7$, $X_{\mathrm{Fact}}=5$ is considered. The sequence of events is similar to Section 4.4,

with the additional events of reference changes (P_{ref}). It ascertains the nonlinear Phase 3 control's stable response under both small and large events. The event sequence for the concluding test are as follows:

- The connection of first converter (CON1) and its synchronization is performed at 0.5 sec with an initial reference value of 0.0 pu.
- The slack is disconnected at 2.0 sec.
- The following event is the load connection at PCC at 2.5 sec with a case-specific power factor.
- The reference value P_{ref1} of CON1 is changed from initial values of 0.0 pu at 7.0 sec.
- The second converter (CON2) is connected and synchronized at 12.5 sec with a reference value of 0.0 pu.
- The reference value P_{ref2} of CON2 is altered from the initial values of 0.0 pu at 17.0 sec.
- The load (shunt impedance) is disconnected at 22.5 sec.
- Subsequent reconnection of the load is performed at 32.5 sec.
- Both $P_{\text{ref1}}$and P_{ref2} are switched back to 0.0 pu at 38.5 sec.

The complete simulation run is for 40 sec. The control sampling frequency is 10 kHz, and the simulation time step for the whole system is 10 μsec in EMT domain using PSS®NETOMAC.

4.5.1 Simulated scenario

Case 1: This case depicts the load with PF 0.95 and asymmetrical reference change values. The reference value P_{ref1} of CON1 is changed at 7.0 sec from 0.0 pu to $P_{\text{ref1}} = 0.811523$ pu. The reference value P_{ref2} of CON2 is altered to $P_{\text{ref2}} = 0.951523$ pu from the initial values of 0.0 pu at 17.0 sec. Both $P_{\text{ref1}}$and P_{ref2} are switched back to 0.0 pu at 38.5 sec. The test bench parameters and results are tabulated in Table 4.10.

Case 2: This scenario exhibits realistic inductive load with PF 0.80 with symmetrical reference change values. The simulated scenario is identical to the previous case of load with PF 0.95. However, the reference values are turned to $P_{\text{ref1}} = P_{\text{ref2}} = 0.540$ pu to match the different load value and hence reduce the frequency deviation to 0.0 pu. The network parameters and results are provided in Table 4.10.

The simulated scenario displays the reference value changes to attain nominal frequency with current limits under realistic loading conditions, with both converters tuned to unequal (Case 1) and equal (Case 2) reference values.

4.5.2 Results and inferences

The comparative responses are visible in Figure 4.28 and Figure 4.29, displaying the events of interest. Both the scenarios present the attainment of steady-state and frequency evolution (ω) since it is uniquely defined under steady-state only (Taylor series definition). The enhanced concept imports the global stability of Phase 1 PRP with apt choice of parameters and when conferring to the coupling-transformer impedance relation. Steady-state is achieved within a certain range of frequencies close to nominal frequency (ω_{n}) due to the choice of active power setpoints and control parameters.

The connection and disconnection of Z and the disconnection of grid equivalent are disturbance events. The two converters immediately respond to the disturbance and share the network loading. Case 1 utilizes asymmetrical reference values with additional active power contribution due to $P_{\mathrm{ref1}} = 0.811523$ pu and $P_{\mathrm{ref2}} = 0.951523$ pu as in Figure 4.28 (d). Without additional reference change, the contribution is equal from converters in Case 1. The frequency drift (ω_{dr}) development is visible in Figure 4.28 (c), with 0.0 pu deviation with tuned P_{ref1} and P_{ref2} from $16.5\ \mathrm{sec} \leq t \leq 22.5\ \mathrm{sec}$ and $32.5\ \mathrm{sec} \leq t \leq 38.5\ \mathrm{sec}$. In contrast Case 2 describes symmetrical reference changes of $P_{\mathrm{ref1}} =$ to $P_{\mathrm{ref2}} = 0.54$ pu resulting in equal power share from both converters to minimize ω_{dr} as seen in and Figure 4.29 (e). The control achieves ω_{n} under the effects of setpoint change with dedicated parameters in both cases and are demarcated in grey. Non-zero ω_{dr} result from unsuitable active power setpoints and F_{n} ($50\ Hz$) of the test bench is not attained. The steady-state current is limited to 1.15 pu with additional setpoint adaptation (Figure 4.28 (b) and Figure 4.29 (b)), and converter voltages ($\underline{V}_{\mathrm{CON}}$) are controlled at 1.15 pu (Figure 4.28 (a) and Figure 4.29 (a)) due to the development of the disturbance event. The temporary transient overcurrent with a peak value $\hat{I}$ of 1.23 pu for 5.0 msec is visible at the disturbance inception in case 1 (marked as 'Peak' - Figure 4.28 (b)). With a load of PF 0.80 or dominant inductive behavior displays a transient peak ($\hat{I}$) of 1.15 pu.

Typical protection trip levels are around $1.2 - 2.0$ pu [50, 53, 145] with trip periods of only a few milliseconds (< 20 msec) [146]. The simulated peak

results are well within this range. Thus, the scenarios depict the superposition of response to disturbance (Phase 1) with Phase 2 PRP to eliminate ω_{dr} with an appropriate choice of parameters considering current limits. The Phase 3 configuration demonstrates that the control scheme is viable, with effective active and reactive power sharing and resulting in a steady-state operating point despite the current limitation in a realistic system.

Table 4.10: Parameters and results for the simulation scenario with network loading of $\mathbf{PF} = \mathbf{0.95}$ (Case 1) and $\mathbf{PF} = \mathbf{0.80}$ (Case 2).

Network parameters	**Unit**	**Case 1**	**Case 2**
X_{C1} and X_{C2} (as X_{C})	pu	0.1	0.1
X_{T1} and X_{T2}	pu	0.1	0.1
R_{T1} and R_{T2}	pu	1.E-9	1.E-9
R_{L}	pu	$X_{\mathrm{C}} * 6$	$X_{\mathrm{C}} * 7$
X_{L}	pu	$X_{\mathrm{C}} * 2$	$X_{\mathrm{C}} * 5$
CON1 - P_{Pref1}	pu	0.811523	0.54
CON2 - P_{Pref2}	pu	0.951523	0.54
Results ($16.5\ sec \leq t \leq 22.5\ sec$) – setpoint changes			
$\omega_{\mathrm{dr}}/\omega_{\mathrm{n}}$ (Analytical)	pu	0.0	0.0
$\omega_{\mathrm{dr}}/\omega_{\mathrm{n}}$ (Simulative)	pu	0.0	0.0
$\Delta\omega/\omega_{\mathrm{n}}$	pu	0.0	0.0
F	Hz	50.000	50.000
P_{CON1} – Active power	MW	0.81369	0,542104
P_{CON2} – Active power	MW	0.953891	0,542104
P_{LOAD} – Load power	MW	-1.783836	-1,08463
Q_{LOAD} – Load power	Mvar	-0,585698	-0,783038
$\lvert\hat{V}\rvert_{\mathrm{CON1}}$ – Voltage	pu	1.150000	1.150000
$\lvert\hat{V}\rvert_{\mathrm{CON2}}$ – Voltage	pu	1.150000	1.150000
$\lvert\hat{V}\rvert_{\mathrm{MEAS\_C1}}$ – Voltage	pu	1.115100	1.110165
$\lvert\hat{V}\rvert_{\mathrm{MEAS\_C2}}$ – Voltage	pu	1.114200	1.110165
$\lvert\hat{V}\rvert_{\mathrm{PCC}}$ – Voltage	pu	1.108500	1.072517
$\lvert\hat{I}\rvert_{\mathrm{CON1}}$ – Current	pu	0.799183	0.623655
$\lvert\hat{I}\rvert_{\mathrm{CON2}}$ – Current	pu	0.915900	0.623655

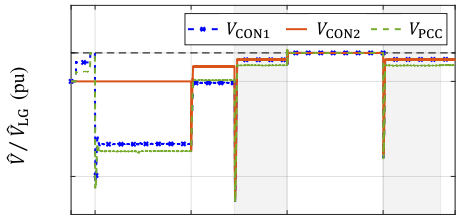
V_{CON1}
V_{CON2}
V_{PCC}
$\hat{V}$ / $\hat{V}_{LG}$ (pu)

(a)

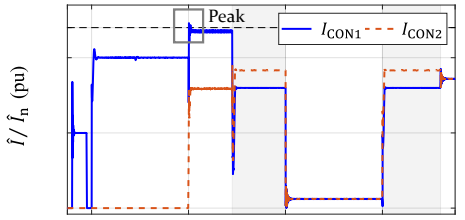
Peak
I_{CON1}
I_{CON2}
$\hat{I}$ / $\hat{I}_n$ (pu)

(b)

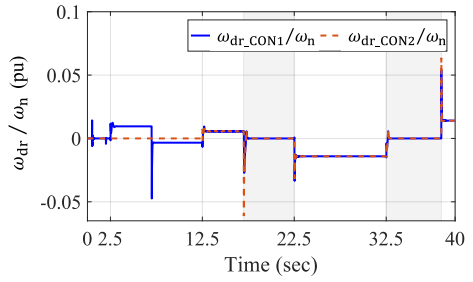
$\omega_{dr\_CON1}/\omega_n$
$\omega_{dr\_CON2}/\omega_n$
ω_{dr} / ω_n (pu)
0.1
0.05
0
-0.05
0 2.5
12.5
22.5
32.5
40
Time (sec)

(c)

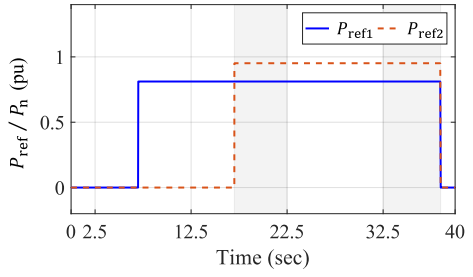
P_{ref1}
P_{ref2}
P_{ref} / P_n (pu)
1
0.5
0
0 2.5
12.5
22.5
32.5
40
Time (sec)

(d)

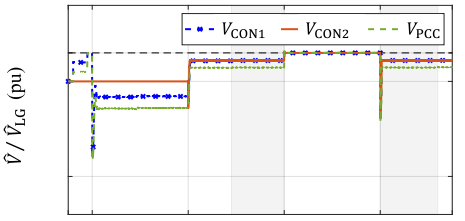
V_{CON1}
V_{CON2}
V_{PCC}
$\hat{V}$ / $\hat{V}_{LG}$ (pu)

(a)

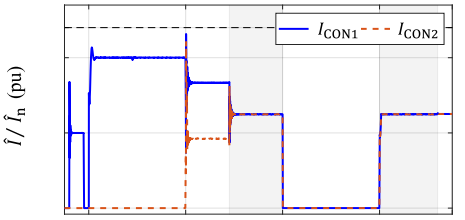
I_{CON1}
I_{CON2}
$\hat{I}$ / $\hat{I}_n$ (pu)

(b)

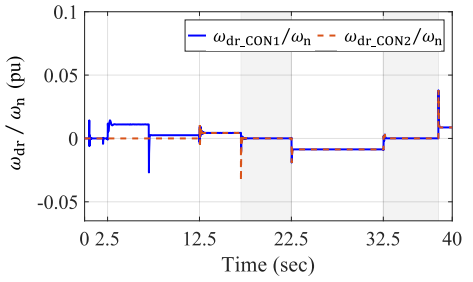
$\omega_{dr\_CON1}/\omega_n$
$\omega_{dr\_CON2}/\omega_n$
ω_{dr} / ω_n (pu)
0.1
0.05
0
-0.05
0 2.5
12.5
22.5
32.5
40
Time (sec)

(c)

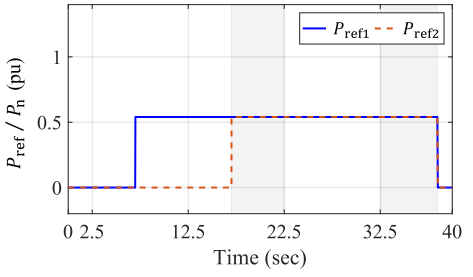
P_{ref1}
P_{ref2}
P_{ref} / P_n (pu)
1
0.5
0
0 2.5
12.5
22.5
32.5
40
Time (sec)

(d)

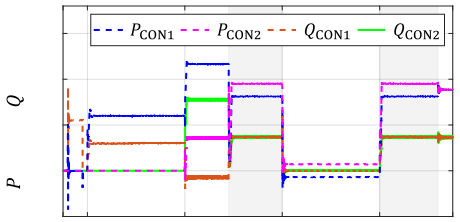

(e)

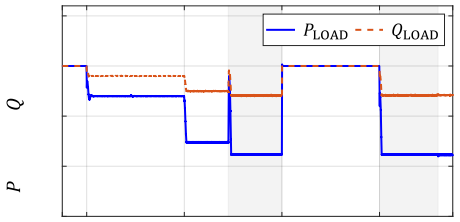

(f)

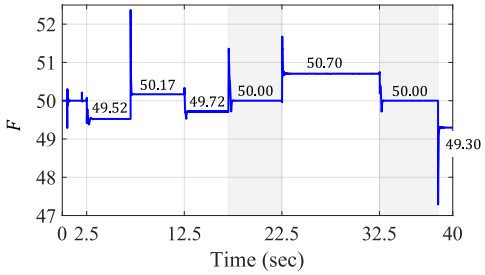

(g)

Figure 4.28: Responses with realistic loadings for Case 1

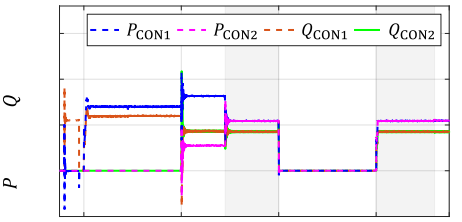

(e)

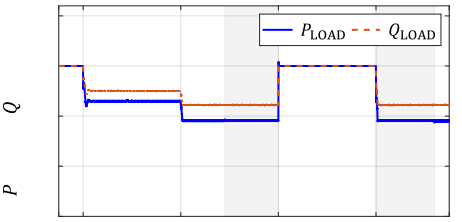

(f)

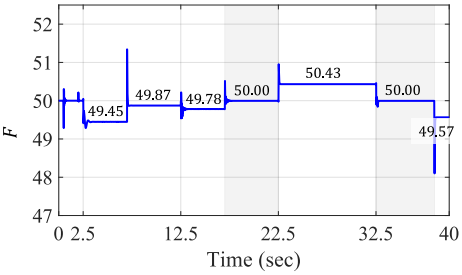

(g)

Figure 4.29: Responses with realistic loadings for Case 2

(a) Voltage space vector magnitudes;
(b) Current space vector magnitudes;
(c) Frequency drift in converter control (ω_{dr} in CON1 and CON2);
(d) Active power reference (P_{ref1}, P_{ref2});
(e) Converter power flows;
(f) Load's active and reactive power;
(g) Network frequency with ($F_n = 50\ Hz$).

4.6 Chapter summary

This chapter illustrates and discusses the simulative results evidenced by the analytical deductions. It verifies the foundation of a novel GFM converter concept achieving steady-state frequency and ensuring global stability. The development of the operating point via the control principle is visualized via simulations of a basic, inductive network. Applying the *'Existence Theorem'* helped to establish the necessary and sufficient conditions for obtaining an operating point. By the application of linearized theory for small-signal stability investigations, evidence for the Phase Restoring Principle (PRP) is highlighted under two network topologies and encompassing global stability. The ability to attain the shortest path displays uniqueness for the nonlinear scheme corresponding to the regular operating point from the two possible solutions. Additionally, the control achieves stability independent of network parameters if the constraint on X_T is obeyed. Furthermore, Phase 1 PRP demonstrated that RMS results are similar to positive sequence EMT phasor simulation results, as expected in the network's case of constant frequency conditions.

The extension of Phase 1 or the base structure of PRP to incorporate the active power control (APC) assists in arbitrary power dispatch and cooperation with other active sources. Numerical simulation results confirm that the proposed control inherently by choice of gains prioritizes the response to disturbances over setpoint changes. Thus, the response to disturbance or inertial support and APC, the two key aspects of GFM control mentioned by various grid code requirements are realized in this scheme. This modified Phase 2 control scheme is no longer restricted to Converter Operated Power System (COPS). Stable operation with other devices with setpoint adaptions is envisaged for single and two converter configurations. PRP with active power control in multiple converters work jointly to find a steady-state operating point according to load requirements. The control can achieve nominal frequency by using properly tuned weighted gain 'c' (power frequency droop) and dedicated control parameters. Additional modification to the APC is performed by supplementing a self-stabilizing drop K_2, which allows for displaying control stability under a variegated panorama of network loading conditions. The obligatory DC compensation is incorporated and part of the complete control development. A stable response is obtained by cascading a differentiator with a double integrator system for power balance with step-responses comparable to a 1st order transfer function response. The Phase 2 responses are additionally corroborated in both EMT and RMS domains and are comparable.

After assessing the stability of the unrestricted Phase 2 control, the necessary augmentation for the current limitation strategy is performed, and a stable response over a wide range of network loading conditions is obtained. The stability of a linear system does not depend on the size of a disturbance. Therefore, a linear system, which is stable for a small disturbance, is also globally stable for any large event. Considering the previously established small-signal stability, large disturbances on the Phase 3 control scheme are performed. These include three-phase faults ($^{X}/_{R} \geq 1$), islanding, maximum phase jumps (pure R), etc., under weak grids. As PRP is nonlinear, its stability is established under both small and large disturbances. The simulation results accentuate that an impedance with a dominant reactance component (X) causes a more significant voltage drop and is more critical than a dominant resistive component (R) under a wide range of load parameters. This issue can be expiated by increasing the quadrature part of voltage while keeping the phase small to maintain small-signal stability. The quadrature part has a negligible impact on the voltage magnitude under small phases. While the implemented current limiting methodology controls voltage magnitude. PRP acts on the phase or quadrature component of the voltage stabilizing critical scenarios where the resistive element in the load is dominant. However, the effects are no longer decoupled when both resistive and inductive elements are present. The parameter selection is based on optimal performance under one set of values for all cases to ensure stability under all investigated dynamic scenarios. Additionally, the present current limiting technique functions as a saturation limiter with enhanced anti-windup elements and maintains PRP's original control strategy as a simple, elegant control development approach mentioned in Section 3.5. The robustness of the control is ensured under a single set of parameters with current limitations in two converter interaction. The highest transient peak current is 1.45 pu, while steady-state value is limited to 1.0 pu.

Since some of the events simulated were idealistic, a conclusive test of the Phase 3 control with realistic distribution loads of PF 0.95 and 0.80 are performed to validate the stable control response. The event included additional setpoint modifications and the previous disturbances. The transient peaks are at 1.2 pu and hence well within typical semiconductor protection limits. The Phase 3 scheme achieves a steady-state and can restore nominal frequency with tuned reference values.

5 Characterization and discussion on Phase Restoring Principle

To define the Phase Restoring Principle's capabilities as a GFM resource, added services, performance, test procedures, and comparison are necessary to characterize this resource's capabilities to serve various system requirements. GFM converters schemes are still under development, and a complete understanding of the capabilities of each methodology is necessary to meet the system requirements. The prime purpose of this chapter is to ascertain system perspective requirements, including the implications of hardware limitations on PRP, and to understand the extent to which grid code procedures can be fulfilled. The first part of the chapter provides a phase-frequency comparison of PRP with typical voltage sources in Section 5.1, followed by its comparison with known GFM concepts in Section 5.2. Section 5.3 discusses the Phase 3 control performances with current limitations to better judge the control scheme with the GFM requirements. Additionally, the fundamental features of PRP are presented in Section 5.4. Section 5.5 abridges the chapter. Segments of this chapter are published in conference paper C1 and C13, as presented in Table A 7.

5.1 Comparisons of phase-frequency responses

A slack is an ideal voltage source characterized by constant phase and frequency, providing an exemplary power system response. Its closest equivalent is an ideal machine with infinite inertia and time constant.

The principle of PRP prioritizes the response to perturbations over setpoints and aims to reach the future steady-state operating point through a direct trajectory. Therefore, to demonstrate the performance and behavior of PRP dynamics, compared against known typical source dynamics, the connection of a significant load is employed as a simulation event. The performance of a source as a slack, a GFM converter with Phase 1 PRP as the source element, a synchronous machine with both infinite and finite inertia, and an ideal PLL are contrasted through analysis of both short-term dynamics (until 120 msec) and long-term dynamics (until 600 msec) in a test environment. Riemann sheets are constructed based on the time curves for the long-term dynamic response to assist in describing and visualizing the reactions. Additionally, the effect of a machine's field time constant and inertia response on voltage stability concerning stability in small-signal domain is emphasized.

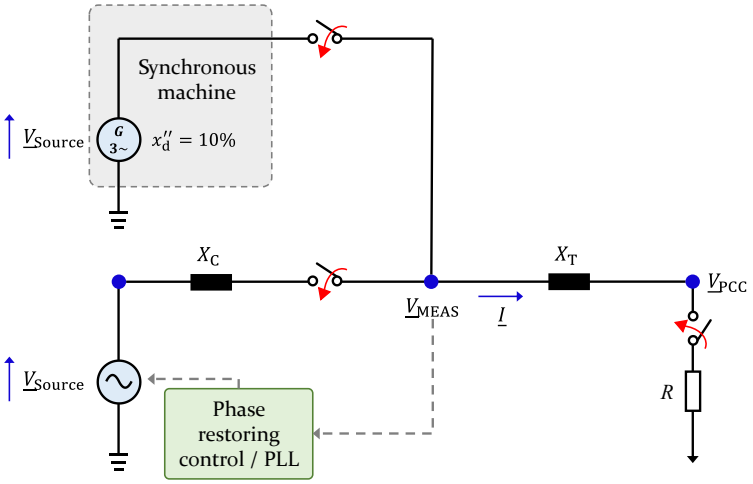

Figure 5.1: Test bench for comparison of sources.

Figure 5.1 presents the circuit configuration of the test bench to demonstrate the PRP principle against established sources. The test setup is analogous to the network configuration illustrated in Section 4.1 to display the global stability conditions of PRP. The network layout is representative of a weak grid scenario, consisting of a basic source and load connected at the PCC with coupling and transformer impedances (X_{C} and X_{T}) and an intermediate measurement node (MEAS). The synchronous machine's equivalent sub-transient impedance ($x''_{\text{d}} = 10\,\%$) is matched to the converter coupling impedance to establish a comparable scenario. The network parameters are detailed in Table 5.1. At $t = 5.04$ sec, the load 'R' is switched, generating a disturbance event. Prior to the load connection, the source ($\underline{V}_{\text{Source}}$) is in phase with the PCC node. The connection of the load (R) results in a post-event voltage drop at the PCC, and the voltage phase at PCC ($\underline{V}_{\text{PCC}}$) lags the source ($\underline{V}_{\text{Source}}$).

Table 5.1: Electrical test bench parameters.

Network parameters	**Symbol**	**Value**
Nominal Voltage (LL)	V_{n}	0.69 kV
Nominal frequency	F_{n}	50 Hz
Coupling impedance	X_{C}	0.1 pu
Transformer impedance	X_{T}	0.1 pu
Load resistance	R	0.1 pu

Performance time curves of PRP as a GFM source are evaluated against a slack, a synchronous generator with two inertia configurations ($H = \infty$ and 5 sec), and an ideal PLL with a source element ($\underline{V}_{\text{Source}}$) on the cited test bench, utilizing the software tool PSS®NETOMAC in EMT domain.

5.1.1 Short-term dynamic response

As illustrated in Figure 5.2 (a and c), a comparison of slack and PRP responses reveals similar trajectories with comparative phase gradients up to 20 msec. However, as the phase of the measurement voltage (arg_{MEAS}) returns to its initial value due to the control action, PRP displays a higher Nadir frequency than slack. The slack settles at its new operating point after 50 msec post-event. Nevertheless, PRP, with slower dynamics resulting from its choice of control parameters, attains steady-state after 110 sec, as depicted in Figure 5.2 (c), with the same phase difference between the MEAS node and PCC as in slack. A machine's initial 2-3 cycle response during an event (phase shift) results from field time constants and is identical in Figure 5.2 (b) and Figure 5.2 (d). The decay time of the field current is influenced by the sub-transient time constant (T_{d}''). As elucidated in Section 5.1.2, the inertial and steady-state response becomes apparent after this period. Analyzing the curve tendencies of PRP reveals that its initial change in phase gradient enables it to settle to a stable

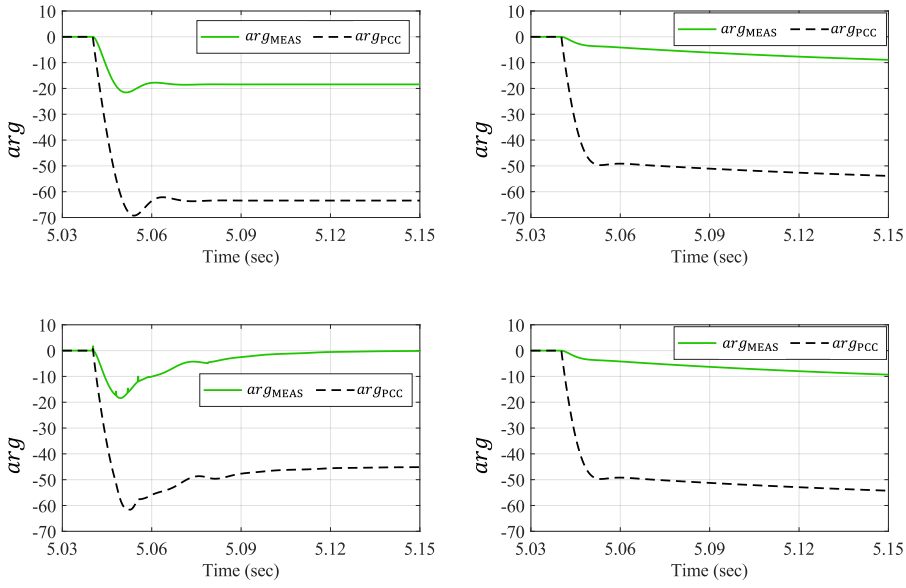

Figure 5.2: Voltage argument for short-term dynamic responses of (a) Slack; (b) Machine ($\boldsymbol{H = \infty}$); (c) PRP; (d) Machine ($\boldsymbol{H}$ **= 5 sec**).

operating point with increased rapidity than a machine, which exhibits a divergent behavior due to its 2nd-order swing dynamics. The overshoot at 5.05 sec in all plots results from large load dynamics.

5.1.2 Long-term dynamic response

The requirement for leading phase response at the source node with respect to the PCC arises due to the connection of an ohmic-inductive load as an event. The long-term responses of the source models in the topology depicted in Figure 5.1 are analyzed and evaluated. Applying the concept of Riemann Sheets from complex function theory facilitates the visualization and analogizing of the source models' responses to disturbances in the context of PRP-based GFM control. Each white-blue sheet in Figure 5.3 (b), Figure 5.3 (f) or Figure 5.3 (h) is interpreted as a plane of constant frequency encompassing phase values between $\pm\pi + k \cdot 2 \cdot \pi, k \in \mathbb{Z}$ (where $\mathbb{Z}$ represents set of all integers). At steady-state, the operating point resides on the main sheet ($k = 0$); however, in the event of a slip frequency, the phasor will traverse the sheets. At steady-state, the PRP is considered equivalent to a slack or infinite source, while during transients, the response is differentiated against an idealized PLL with no additional control in the converter source.

A slack is modelled as an ideal voltage source with a constant phase in an electrical network. The behavior of the slack in the specified network topology is simulated and depicted in Figure 5.3 (a) with the post-event steady-state phasors in Figure 5.3 (b). Prior to the event, the phasors of the slack ($\arg_{\mathrm{SLACK}}$), measurement ($\arg_{\mathrm{MEAS}}$) and PCC ($\arg_{\mathrm{PCC}}$) nodes are aligned in phase. However, post-event, while the phase at the slack ($\arg_{\mathrm{SLACK}}$) remains fixed and thus unchanged, the measurement ($\arg_{\mathrm{MEAS}}$) and the PCC ($\arg_{\mathrm{PCC}}$) phases experience a shift and lag in relation to the slack node based on the impedance ratios as portrayed in Figure 5.3 (a) and Figure 5.3 (b). The phase difference ($\Delta\varphi = 63.432°$) between $\arg_{\mathrm{SLACK}}$ and $\arg_{\mathrm{PCC}}$ provides the total network solution and not absolute phase values at the nodes. As a result, slack source ($\underline{V}_{\mathrm{SLACK}}$) leads PCC ($\underline{V}_{\mathrm{PCC}}$) post-fault. The PRP response is illustrated in Figure 5.3 (g) and Figure 5.3 (h), which portrays that both source ($\arg_{\mathrm{CON}}$) and PCC ($\arg_{\mathrm{PCC}}$) are in phase pre-fault. Upon load connection, the measurement phase ($\arg_{\mathrm{MEAS}}$) remains fixed and hence constant, whereas the source phase ($\arg_{\mathrm{CON}}$) leads and the PCC phase ($\arg_{\mathrm{PCC}}$) lags with respect to the measurement node ($\arg_{\mathrm{MEAS}}$). Thus, PRP demonstrates a leading source phase in accordance with network requirements. The network solution is established through the phase difference ($\Delta\varphi = 63.432°$) between PRP ($\arg_{\mathrm{CON}}$) and PCC ($\arg_{\mathrm{PCC}}$).

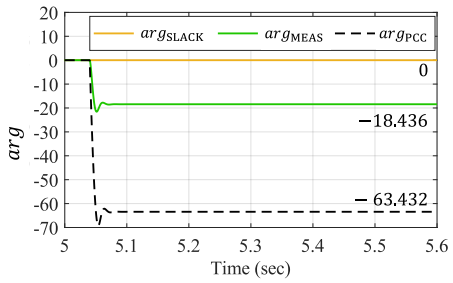

(a) Slack dynamic response

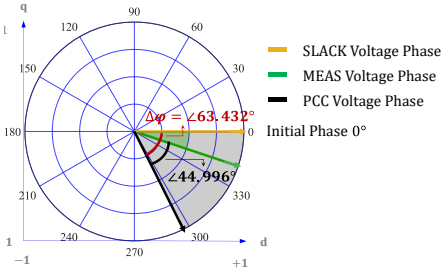

(b) Slack steady-state response (post-event)

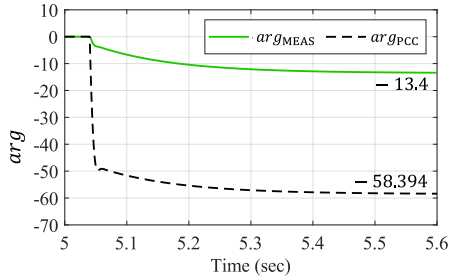

(c) Machine ($H = \infty$) dynamic response

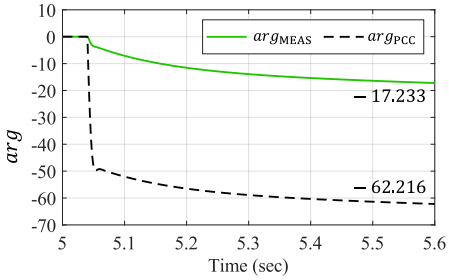

(d) Machine (H = 5 sec) dynamic response

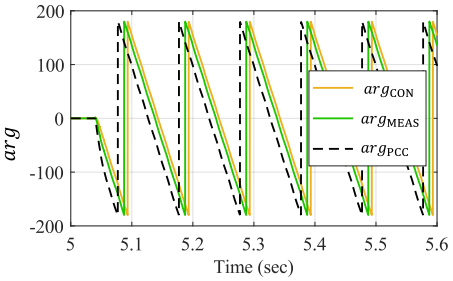

(e) PLL dynamic response

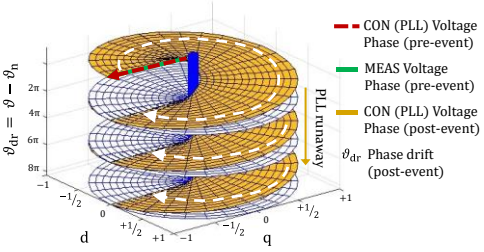

(f) PLL response representation to event

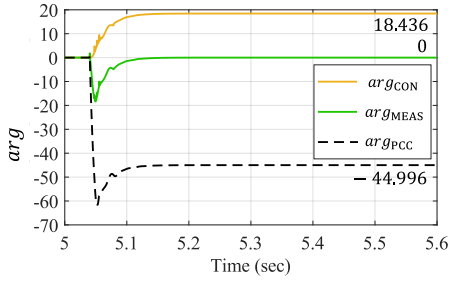

(g) PRP dynamic response

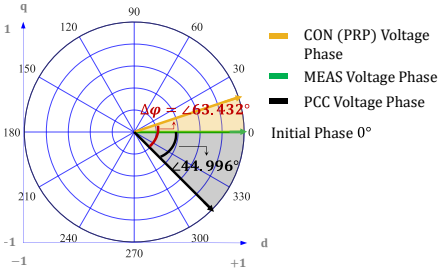

(f) PRP dynamic response (post-event)

Figure 5.3: Dynamic and post-event voltage argument responses for different sources.

The steady-state response of both slack and PRP configurations, prior to and after a disturbance, exhibits similarities in phase and lie on the same plane due to the evolution of constant frequency. In PRP, constant frequency is maintained by restoring the measurement node's phase, while in slack, the source node remains fixed. The network solution or phase difference ($\Delta\varphi$) between the source (slack or PRP) and PCC in both configurations remains equal post-disturbance due to the development of an identical load flow solution. Thus, highlighting that only the phase difference (small-signal) is controllable, not the absolute phase. Due to the comparable responses of PRP and slack, generating constant frequency and inducing the same relative phase responses ($\Delta\varphi$), it is reasonable to attribute PRP with infinite inertia from frequency perspective. This comparison underscores the importance of considering phase difference as a criterion in the design of GFM controllers and renunciation of absolute phase reference. As described in Appendix A12, each load flow remains unchanged with the addition of any constant value to the phase of any node voltage.

The long-term dynamics of a SM reveals the inherent inertial response of the rotating mechanical components. An idealized SM with infinite inertia, as depicted in Figure 5.3 (c), displays a steady-state response delayed by the field time constant and is devoid of non-beneficial dynamical swing. Conversely, a machine with a realistic inertial value (Figure 5.3 (d)) experiences an initial drift due to swing dynamics that is subsequently adjusted by the governor and exciter dynamics. Thus, the smaller the inertial time constant, the quicker the divergence, resulting in higher dynamics and stability challenges in the power system (referred to as small-signal stability). This phenomenon is evident in Figure 5.3 (c) and Figure 5.3 (d) at 5.4 sec, where the machine with $H = \infty$ attains a steady-state. In contrast, the machine with $H = 5$ sec undergoes a short-term divergence due to the initial swing, ultimately leading to power oscillations. A machine with infinite inertia is analogous to a slack in its long-term dynamic behavior and, by extension, comparable to a PRP. Also, SM with finite inertia is not globally stable and is not a paradigm for global stability of a converter control. Besides, SM is stable in many aspects but not in all [147].

To provide further insight into Phase 1 PRP under transient conditions, a comparison between the response of PRP and an ideal PLL is performed, as both systems exhibit similarities at a functional level. PRP operates on the phase difference and incorporates the 1st term of the Taylor series, which represents instantaneous frequency, $^{\Delta\vartheta}/_{\mathrm{d}t}$. Conversely, an ideal PLL

without additional control features follows the power system response or the lagging measurement phase ($\arg_{\mathrm{MEAS}}$) and does not offer a conducive response to disturbance under a weak or island grid scenario. As a result, PLLs require further modification to provide a robust response to disturbances in weak grids or systems dominated by converters. Numerous studies have been published in this field to address this issue [41, 148, 149].

Pre-event, the PRP and PLL voltage phasors are aligned on the same plane. As depicted in Figure 5.3 (e), the dynamic response exhibits a downward spiral movement or runaway effect upon load connection. Similarly, a downward movement is illustrated in Figure 5.3 (f). An ideal PLL under disturbance will experience either a spiraling upward or downward trend on the yellow sheet or plane, corresponding to an increase or decrease in frequency, with no stabilizing influence. To achieve steady-state or synchronism in conventional PLL-based converter control, it is necessary to incorporate an additional control block in conjunction with the PLL. Hence, an ideal PLL exhibits a runaway effect during an event that follows the network frequency, serving as a pure observer with no controllability. Thus, leading to a lack of stabilizing response in weak power grids.

PRP is characterized by its self-stabilizing property, achieved via a minimal control order. The response to disturbances is stabilizing as a result of a novel transformation implemented in the PRP control scheme, operating directly from pre-event to post-event in the control loop. As a result, it can effectively achieve the desired future operating point, as depicted in Figure 5.3 (g). Thus, the design feature displays limited Vector Shifts (Figure 5.3 (h)) and a constant frequency, enabling the response to remain on the same plane post-disturbance. The interpretation of Figure 5.3 (f) in the context of PRP highlights the association of the drift frequency f_{dr} and phase ϑ_{dr} determines the rate of movement on the spiral plane [21].

Table 5.2 and Table 5.3 provide an overall comparison of PRP from a functional level and source point of view based on three key performance indicators (KPIs), respectively. The notation in the table indicates, ϕ_0 is the load flow phase or constant part and $\phi(t)$ is the general phase as in (3.1).

Table 5.2 : Comparison of PRP at functional level.

Functional point of view	**Control of phase ($\boldsymbol{\phi(t)}$)**
Phase Restoring Principle (PRP)	Yes
PLL (observer)	No

Table 5.3 : Comparison of dynamic responses (up to 1/2 sec range) of PRP to typical voltage sourced models.

Source point of view	Active control of phase (ϕ_0)		Control of frequency	Swing (frequency overshoot)
	CON/SLACK	MEAS		
Slack	Fixed	No	Fixed	No
Machine without control ($H = \infty$)	-	No	Fixed	No
Machine without control ($H = 5\ sec$)	-	No	No	Yes
Phase Restoring Principle (PRP)	Yes	Fixed	Fixed	No

5.2 Comparison of Phase Restoring Principle with other Grid-Forming Methodologies

Several GFM concepts are under research and display their characteristic behavior to meet the system's needs. Hence understanding the advantages of each control scheme is vital. The emerging PRP concept is contrasted and discussed against well-known Droop (Figure 2.4) and Virtual Synchronous Machine (Figure 2.5) GFM schemes. Each control methodology is implemented in the IEEE 9-bus test system in the EMT domain to highlight their characteristics in the network with a high proliferation of renewables ($> 66.67\ \%$). Details of the test bench and scenario are available in Appendix A11.

Each control approach provides inertia support and ensures stability under disturbance. For a better comparison, the inertial PRP response without APC and current limit activation or Phase 1 is evaluated against Droop and VSM, to create a reasonable comparison at the functional level. The reaction of each scheme after generation loss of SRC 3 (machine) is displayed in Figure 5.4. Both Droop and VSM return to a lower operating point after the disturbance, whereas PRP increases its active power contribution, as visible in active power plots of Figure 5.4, displaying better support to the grid. Droop- and VSM-based controls exhibit similar responses as discussed in Section 2.1.2.2. With its reduced control order, PRP features its prioritizing response to disturbance over setpoint changes with higher participation under disturbance. Hence, PRP may serve as a viable alternative. Additional details on this test scenario and deeper analysis is available in [32]. The voltages displayed in the plots are peak line-to-ground values where, $V_{\mathrm{LL}} = 230\ \mathrm{kV}$.

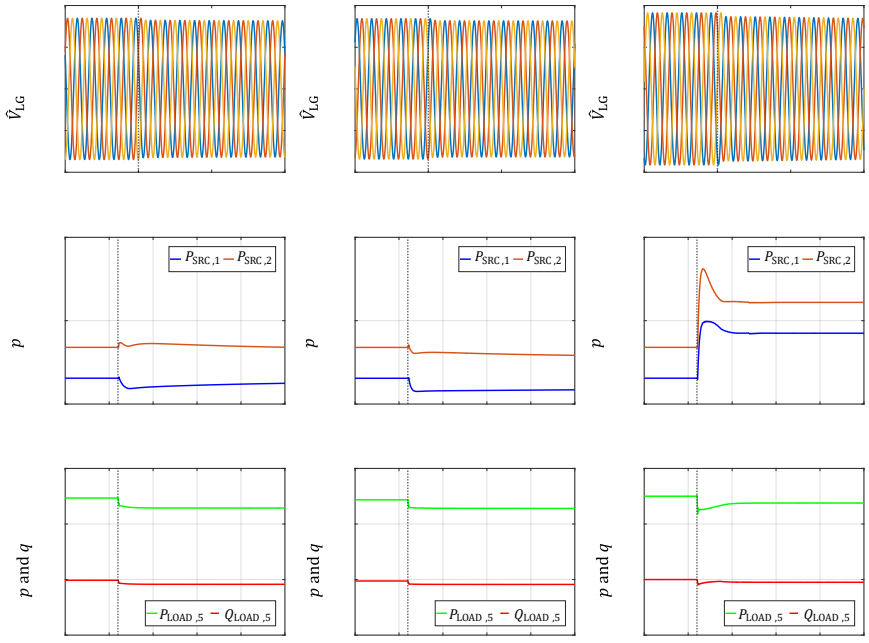

(a) (b) (c)

Figure 5.4: Responses of Voltage at Bus 5, Active and reactive power at Bus 1 & 2 and dynamic load at Bus 5 in IEEE 9 bus system due to event (a) Droop; (b) VSM; (c) PRP.

5.3 Deliberation of Phase Restoring Principle with current limiting control

The prime characteristic feature of GFM is defined as a voltage source behind an impedance with the provision of inertial response under regular operation. Support for maintaining power system stability is the utmost essential requirement for a GFM converter. The overall complexity of dynamics pertaining to low-inertia systems is well described through characteristic timescales presented in Figure 5.5. Conventional power systems based on SMs have a distinct difference in time constants for frequency and voltage regulation. However, with the inclusion of fast-acting converter-based generation, the system dynamics become more complex and convoluted and may lead to unexpected couplings [20]. The voltage and frequency related dynamics in Figure 5.5 refers to the voltage and frequency regulation associated with controllers, respectively. A degree of association exists, but these are not directly correlated with the standard voltage and frequency stability terms [117], particularly regarding complex dynamics of weak systems. The main difference between conventional and

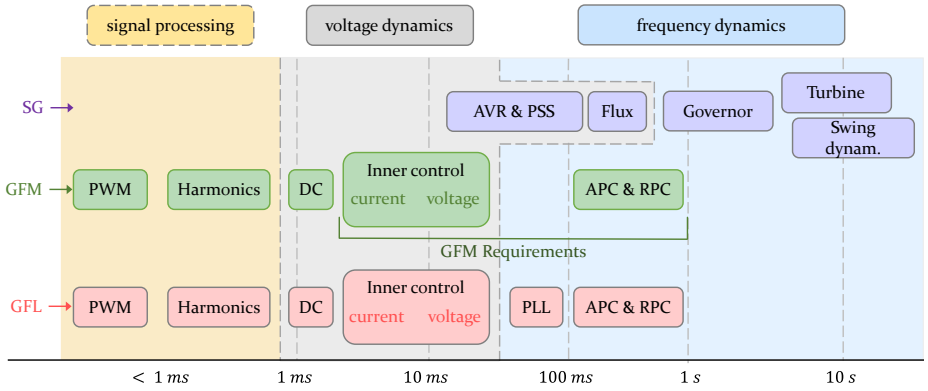

Figure 5.5: Characteristic timescales of different physical and control dynamics in a low-inertia system (modified and adapted from [150]).

low-inertia systems is the timescale of separation between the respective controllers of SMs and IBR, which leads to instability under high penetration [24, 150]. As seen in Figure 5.5, the inner control loop, which includes current limit control, defines the stability boundary limit of the cascaded structure, viewing from the GFM control requirement perspective. Therefore, grid-stabilizing behavior of GFM during grid fault or overload situations that exceed the converter's current limits needs to be guaranteed. Therefore, a technical requirement of the GFM converter is the capability to contribute to system needs even in situations when the converter's physical current and power limits are exceeded [7]. Due to the current limited nature of PE converters, GFM controls have to operate in abnormal operation modes in case of overload and grid fault situations [82, 90, 92–96]. Therefore, GFM needs to be tested under different overload and grid fault conditions to ensure grid stabilizing behavior.

Various fault scenarios include voltage-driven overload scenarios like over and under-voltage events. Phase-driven overload scenarios such as phase jumps, RoCoF events, and system split scenarios need to be addressed. The GFM should retain grid-synchronicity and inject stabilizing current for all these scenarios [80, 82, 90, 92–96]. With GFM, coupling of phase, and frequency need to be controlled for stabilization. A recently implemented grid code requires the GFM converters to inject reactive current into the power system in < 5 msec, when the voltage at PCC drops below 0.9 pu [16, 151]. During an event, frequency stabilization needs to be preserved, a trait of GFM that requires active power; however, the necessary share of power to stabilize the system is unknown. The only evident fact is the need to control frequency and magnitude of local voltage towards nominal

conditions. It is not imperative that the reactive current alone is stabilizing, depending on the power system condition. During the short fault period, a suitable alternative would be to maintain the voltage source behavior of the GFM converter for the duration with a natural fault current response instead of controlling the output current of the GFM converter [50, 151].

The current limitation is not a system requirement but a curtailment that needs to be superimposed on the control. For a successful disturbance ride-through and converter protection, the converter needs to withstand these overcurrents. A similarity may be drawn to the machine controller is the OEL, which essentially limits the field currents under steady-state. The OEL's purpose is to restrict the field current value so that the generator operating point does not exceed the field current limit. Albeit under the transient time frame, the machine may be temporarily overloaded and deliver $5-7$ pu of fault current [46, 48]. The high currents are delivered due to the superimposed field and swing dynamics [147] and are not system stabilizing requirements as discussed in sub-section 5.1. Furthermore, after the decay of the transients, the phase-frequency relationship of voltage needs to be maintained, or the machine slips away, known as rotor angle stability [117].

The virtual impedance approach is the most prevalent and discussed method of current limit control in voltage-controlled or GFM converters. The converters, under disturbances, behave as a voltage source behind adaptive impedances. The voltage difference determines the output current vector angle and the X/R ratio of the virtual impedance. An accurate design of the X/R ratio is required to meet the fault current contribution requirement, which implicitly requires the power system impedance information across the entire frequency spectrum. Thus, the impedance needs to be defined over the full frequency range to ensure stability, and this is a challenging task. An alternative solution to relax this parameter selection requirement is combining the virtual impedance methods with the power reference adjustment method proposed in [152]. However, the voltage source behavior of the converter may be lost, implying the GFL condition [50].

In contrast, the voltage magnitude limiter combined with PRP does not rely on the precise impedance parameter values of the power system. PRP has a dependence on the inductive small-signal characteristic provided by the X_{C} and X_{T} reactances. Since the network is unknown, the current cannot be deduced; therefore, only voltage magnitude control is implemented. The angle spread with IBR is an outcome of 1-2 cycle dynamics (Figure 5.5). PRP

first minimizes the angle spread and thus helps attain the new operating point through the shortest path. Large angles lead to instabilities eventually approaching the irregular solution branch. The voltage magnitude control limits the current, whereas PRP performs voltage-frequency control for all voltage magnitudes, which is not apparent by all converter controls leading to current injections and instabilities. As mentioned in [29], frequency is associated with the linear part of the argument of the voltage space vector, the essential aspects of voltage stability [153], and PRP acts on the phase part of voltage implying frequency. Another, vital consideration of the current limiting mode of operation is the 'stiffness' factor of the voltage source emulated as a GFM converter, hinting at the control response time. The performance of many of the system services of the GFM converter relies on the stiffness of the source [7]. Therefore, the voltage magnitude limiter with PRP is tuned to react sufficiently prompt without compromising on stability. Additionally, the voltage source behavior with a natural current response is maintained in this scheme, as discussed in [50]. Simulation results for large disturbances under weak grid conditions, three-phase bolted faults, and islanding show both converters' stable performance and low voltage ride-through (see Section 4.4).

Furthermore, it is crucial to characterize GFM controls' behavior during operation in the current limiting mode and the transition into and out of the current limiting mode. As discussed in [50], one main challenge in the fault recovery process is caused by the windup of voltage controllers. Hence, the realized voltage magnitude limiter includes the anti-windup methods such as a Flip-Flop and counter with unique conditional triggers to enable the GFM converter control to recover from the undesired current saturation. The current limitation control loop is restored to its normal operation from the current limiting mode when disturbances are cleared.

5.4 Characteristics of complete Grid-Forming control

The following section summarizes the key findings of PRP-based GFM control. PRP is developed based on setting stability as the most crucial power system need as determined by NERC [31] and various working groups [7, 90]. Due to its novel angle transformation, PRP inherently creates a response according to the power system. Thus, generating and maintaining a constant voltage magnitude at normal ranges and a scaling in case of overcurrent at the IBR terminal. From control hierarchy, it prioritizes response to disturbances over response to setpoint changes. PRP attains synchronization, frequency stability, voltage regulation and damped response with minimal control order compared to the popular VSM. At

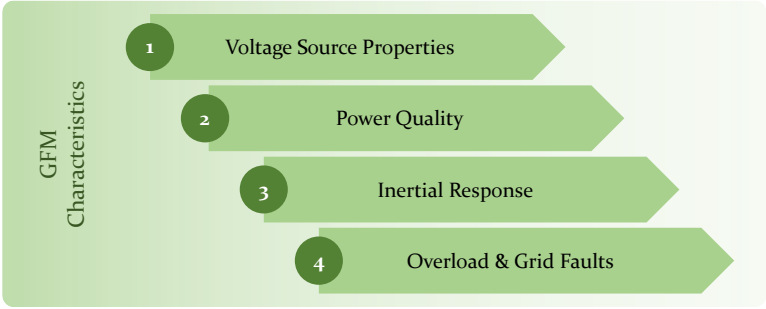

Figure 5.6: GFM converter characteristics (adapted from [92]).

steady-state, the response is equivalent to a slack in frequency perspective. Thus, by fixing the phase at the measurement node ($\arg_{\mathrm{MEAS}}$), PRP delivers an infinite inertia frequency reaction to the power system under disturbance and fulfills one of the necessary attributes of a GFM converter. The response is free of the non-beneficial dynamical swing, damped, and attains the new operating point directly by displaying the limited Vector Shift criteria as proposed by National Grid, UK [16]. *Vector Shift (VS)* relates to a protection mechanism that monitors sudden changes in the mains voltage angle caused by a change in output from generating unit or demand connected to the network. Hence, the protection may respond quickly to network impedance changes during islanding [81]. PRP fixes the measurement phase and minimizes phase shift at the PCC and thus avoids unnecessary protection trips.

Furthermore, the response of PRP is similar to a first-order system. Global stability is secured under independent variations of network parameters, with a suitable choice of controller values. Due to the active power control (APC), PRP can operate with other devices in the network, which is a central requirement for GFM, e.g., according to the UK Grid Code [16, 90, 154].

Another technical requirement of GFM is the capability to contribute to system demands in situations where the converter's physical current and power limits are exceeded [7]. Due to the current limited nature of PE converters, GFM has to operate in abnormal operating modes in case of overload and grid fault situations. With the implemented voltage magnitude limited current control, PRP achieves this feature by preserving hardware limits. A consequence of this prioritizing property is considering frequency over power (load flow phase). Furthermore, the voltage source behavior, a higher critical requirement [50], is maintained.

Based on the discussion above, PRP correlates to GFM characteristics as in Figure 5.6 and satisfies most of the grid code requirements mentioned in Section 2.3 The essential qualities and services offered by the full scheme are as follows:

- *Global stability* when meeting an impedance relationship (coupling-transformer impedances)
- Infinite inertia-based frequency response, damped and no oscillation due to direct path response. Overall cascaded control structure displays first-order system response
- Limited phase or Vector Shift
- GFM controller hierarchy, response to disturbances over response to setpoint changes
- Control scheme provides multi-instance functionality allowing arbitrary dispatches with APC activation
- Current limited response is robust and stable under normal operating ranges, severe faults and weak grid scenario maintaining voltage source behavior
- Application includes converters interfaced with batteries or capacitor banks (as shown in Figure A 22 of Appendix A13)

5.5 Chapter summary

This chapter highlights the characteristic response and services delivered by the recently introduced control concept, the 'Phase Restoring Principle' (PRP), developed from the power system perspective. It is a basic block of a novel GFM control scheme based on attaining nominal frequency in reverse action to a PLL. Comparisons based on voltage source's phase-frequency responses and similar converter control applicable techniques are performed to describe the scheme's benefits. The intention and significance of voltage magnitude-based current limiter on PRP scheme responses, a hardware limitation, is delivered.

Initially, the Phase 1 PRP is compared against typical active voltage sources. Usually, a phase synchronized coordinate system such as a PLL is employed for synchronization and serves as a reference frame for the control design and is therefore designed to respond to setpoint changes. In contrast, Phase 1 PRP is self-stabilizing and demonstrates an equivalent behavior to a slack (for frequency only) since the power system frequency always returns to its nominal value. The response described in this chapter shows

PRP providing an ideal reaction to the power system under disturbance and outperforming a SM with its undesirable swing dynamics. This non-linear concept avoids the runaway effects produced by a PLL by directly participating in the power exchange caused by the disturbance and attaining the post-disturbance operating point with reduced or no additional higher-order control block. Thus, it is opposed to rotating in the direction of the standard dq frame of a PLL.

On comparison of Phase 1 PRP with other GFM methodologies, all schemes provide inertial support and stable response. However, due to its distinguishing feature, PRP represents a faster and higher contribution to the event and may serve as a viable alternative to the upcoming GFM schemes.

As mentioned in Section 2.3, an essential requirement of GFM is to maintain a constant magnitude and phase of the voltage within the transient time frame following a disturbance. If the voltage control bandwidths for regulation of the terminal voltage are sufficiently small, the control loops' response time is slow, implying longer rise and settling times. Thus, GFM resources should maintain stability under low short circuit ratio (SCR) conditions and even 'form' grid voltage when necessary. The slower APC control dynamics are built over Phase 1 PRP in developing Phase 2 control. With the current limit incorporated into the scheme, this Phase 3 GFM control forms the grid and achieves a steady-state response under islanding and grid-tied scenarios. The voltage magnitude limited current control enables to respect of hardware limits with adequate speedy reactions. PRP minimizes angle spread to achieve a new operating point through the shortest path and helps avoid instabilities caused by large angles. Additionally, the voltage magnitude limiter with PRP is tuned to respond promptly to current output while maintaining stability. The voltage source behavior is maintained throughout the Phase 3 control scheme during the current limiting mode in operation and transitioning in and out, a demanded requirement. Anti-windup methods such as Flip-Flop and counter are included in the voltage magnitude limiter to support post-fault voltage recovery.

Lastly, PRP is fully GFM and satisfies several grid code criteria, hence forming the basis for building all additional control blocks over it. Its key features are summarized in Section 5.4 to provide a better overview and gauge the GFM IBR behavior.

6 Demonstration and validation of Phase Restoring Principle in real-time

A real-time simulation is performed to experimentally demonstrate and validate the novel GFM control concept's ability to stabilize an extended electric power system with other grid assets. The demonstration is performed in a realistic medium voltage direct-current (MVDC) network consisting of a high-fidelity, real-time simulator (RTS) using Power-Hardware-in-the-loop (PHiL) simulation. A PHiL simulation allows the connection of actual hardware to a computer simulation model running in real-time such that the hardware converter and the power system interact dynamically. Thus, a PHiL simulation allows experimental validation using real hardware without risking customers and utility equipment. It helps to bridge the gap between pure computer (digital) simulations and live field testing [13, 155–158]. It is a step toward validating realistic model responses of IBR considering digital and analog systems, as noted in Chapter 2.

In chapters 3 and chapter 4, the theoretical proof of the control concept is displayed with simulative evidence, respectively. The PRP control scheme can operate in grid-tied and island-based systems, exclusively IBRs based. This demonstration further strengthens and improves confidence in the control scheme to obtain stable operation and displays the interaction with real hardware and other converter control schemes (GFL and GFM) under selected test scenarios. PRP is employed as a control firmware. This chapter describes the PHiL and initial rapid control prototyping responses of PRP in a star interconnected system. The workflow allows to rapidly perform experimental iterations in order to identify and resolve potential issues [159]. This chapter is divided into four sections. Section 6.1 describes the experimental test bench, followed by scenario description and responses as plots in Section 6.2, results obtained in the previous section are discussed in Section 6.3. Finally, Section 6.4 recapitulates the chapter. The work presented in this chapter is developed within the framework of the project Kopernikus **ENSURE** (Neue EnergieNetzStruktURen für die Energiewende) and a part of the results are published in J4, J5 and C14.

6.1 Topology of the MVDC-HVDC test bench for Grid-Forming operation

The topology consists of an interconnected MVDC-HVDC (high voltage direct-current) link connected to an extended AC network to include

simulated assets such as a GFM-based converter source, constant loads, and a dynamic photovoltaic plant. The entire setup is connected and interfaced with a microgrid laboratory. Figure 6.1 provides a visualization of the test bench. Closeup views of the real-time simulator (RTS) from RTDS Technologies Inc. AMETEK and laboratory equipment are visible in Figure A 23 (Appendix A14). The MVDC collector system (in **blue**) with the HVDC link is modelled based on [160]. The simulated topology is developed in RSCAD® software. Two GFM control schemes are integrated and investigated, with this work's focus on the PRP control scheme. The microgrid laboratory (in **orange**) is linked to the RTS by optical fibers via a linear power amplifier. Based on Figure 3.11, the Phase 2 PRP scheme is implemented at the converter source highlighted in **green** with sufficient headroom and a rating of 100 MVA. The converter is an aggregated IBR, such as PV with an integrated battery, or battery storage, or capacitor bank.

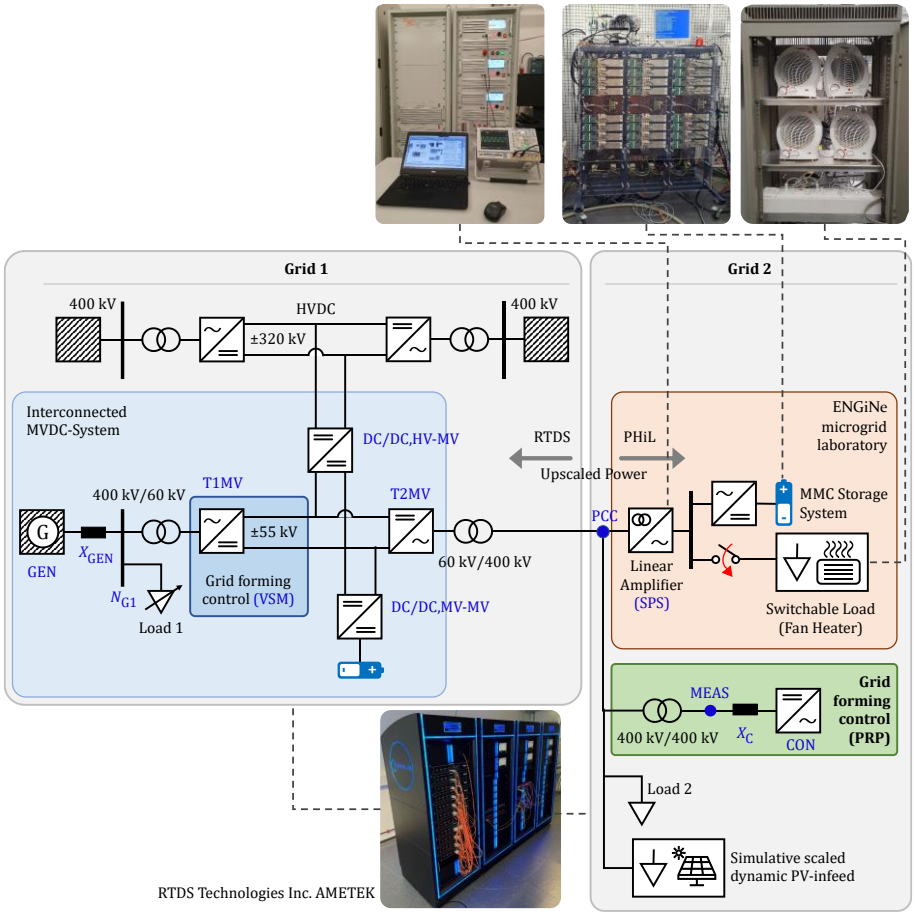

Figure 6.1: MVDC-HVDC test bench featuring PRP based GFM.

Test bench is an MVDC network with downscaled medium voltage (MV) converter stations, aggregated IBRs, and loads connected to an AC network, derived from [161, 162]. To ease system interpretation, the topology is divided into two grids. Grid 1 consists of the Virtual Synchronous Machine based GFM (VSM-Figure 2.5) at terminal 1 (T1MV) of the interconnected MVDC-HVDC terminals, which is further connected to AC network equivalents of weak system strengths with a scalable variable load. While the microgrid laboratory assets as PHiL, PRP control based-GFM converter source, simulated constant load, and a dynamic PV plant constitute Grid 2.

6.1.1 Grid 1 - HVDC-MVDC interconnection and battery storage system integrated via DC/DC converters

The MVDC grid is designed as a symmetrical monopole configuration with a rated DC voltage of ± 55 kV. Each terminal has a rated active power capacity of ± 100 MW, and a reactive power of ± 30 Mvar. The MVDC is connected to a DC link of the HVDC via a multilevel DC/DC converter (110 kV/640 kV) with a triggered droop control between HVDC and MVDC link, with an initial droop value set to zero implying no participation. Thus, a multi- terminal system with two DC voltage levels is formed with a droop-based DC-side control. The coupling converter connecting the MVDC and HVDC grid is based on [163]. The head stations of the MVDC feed into the 400 kV system. The VSM control scheme is adopted at converter station T1MV of the MVDC and can provide inertia only. Primary control reserve is possible in combination with setpoint adaptions at the MVDC terminals and other assets to maintain system balance.

A highly scaled lithium-ion battery storage (Li-ion) model is integrated into the DC link of the MVDC. It is interfaced via a cascaded three-phase dual-active bridge (3Ph-DAB) modelled via the state-space-averaging (SSA) method. To reduce computational power, the 3Ph-DAB is modelled using the least detailed modelling approach as in [164–166]. The output currents are averaged by considering all switching intervals within one switching period instead of employing a detailed switching model. The resulting DC current on the primary and secondary sides are coupled via controlled current sources, with reference values calculated as a function of controlled load angle and the current output voltages. The large-scale grid battery storage system has a power rating of 55 MW and is connected to the MVDC grid via a multilevel 3Ph-DAB or DC/DC converter. Its original design is derived from [165]. The Li-ion battery packs used for storage system is based on [167], with a target nominal secondary DC voltage of 1 kV. A comprehensive electrical battery model based on Min/Rincon-Mora [168],

is implemented to capture the Li-ion battery's dynamic and nonlinear characteristics. The multilevel 3Ph-DAB or DC/DC converter is rated at 110 kV/1 kV with the primary side (110 kV) connected to 22 DAB3 modules in series, while the secondary outputs (1 kV) are connected in parallel on the 1 kV battery connection point. Two battery racks are connected to each 3Ph-DAB power module resulting in an overall battery storage system of 44 battery racks. With each rack containing 22 battery packs connected in series. The chosen topology is an isolated Modular Multilevel Converter dual-active bridge (MMC-DAB) with a front-to-front configuration. The design parameters of the MVDC-HVDC link are derived from [163] and given in Table A 5 with a rated power of 200 MW and frequency up to 150 Hz at the front-to-front AC link, while the parameters of large-scale battery interfaced via DC/DC converter are in Table A 6.

The external HVAC grids are represented as network equivalents of weak system strength modelled as thévenin sources coupled via transformers connecting the HVDC link. The HVDC is further coupled to the MVDC via the DC/DC converter. The terminal 1 (T1MV) of the MVDC via transformer (60 kV/400 kV) is connected to a network equivalent, modelled as a generator source of 1220 MVA rating capacity and a short circuit power $Sk'' = 903.7$ MVA at 400 kV with $X_{\mathrm{d,GEN}}{}'' = 0.175$ pu. The generator source (GEN) has an inertia constant of $H = 4.70$ sec, with exciter and power system stabilizer dynamics, but without a frequency-droop or governor control. A constant power variable load of 100 MW initial consumption is connected at the N_{G1} node. The T1MV converters are simulated as MMC average models, and control implemented in MATLAB-Simulink® and is exported to RSCAD® as C-code. DC voltage support may be provided via T2MV or DC/DC converter connected battery unit. Additionally, T2MV of the MVDC is modelled as a switching-level to provide blocking capabilities for island investigations in Grid 2. These elements jointly comprise Grid 1.

6.1.2 Grid 2 – Phase Restoring Principle integrated with microgrid laboratory and other MV assets

The Institute of Electrical Energy Systems' microgrid and energy storage laboratory (ENGiNe) communicates with the RTS using the Xilinx Aurora-based protocol. Three optical cables are interconnected to RTDS and to a linear power amplifier, which amplifies each phase up to 5 kW. The linear amplifier connected is the *'Typ DM 15000/APS/PHIL'* from the company Spitzenberger & Spies (SPS). The ideal transformer method [156, 169] is used as an interface between the simulator and the amplifier. The simulator sends the voltage signal at a selected connection point and transfers it to

the power amplifier. The power amplifier sets an output voltage, which leads to a current flow with connected hardware or device under test. The current and voltage are measured within the power amplifier and are transferred back to the RTS. A resultant one-time step delay in the closed signal feedback between the sent and received voltage signal along the communication path is gauged.

Various static and dynamic power hardware of the microgrid ENGiNe and PHiL Laboratory is scaled by a factor of 1000 at the communication interface and applied to the simulated test bench in different modes of operation. The PHiL includes a purely resistive three-phase fan-heater of up to 7 kW power rating, connected as an adjustable load for the simulation. An MMC converter with integrated Li-ion batteries in charging configuration or load operation is coupled. The MMC includes 4 submodules per branch, a total apparent power rating of 25 kVA, with diverse operation concepts. The MMC and the three-phase fan heater are interfaced through the power amplifier, enabling the usage of either one or both during tests. In addition, dynamic photovoltaic plant data is simulated based on the installed SMA Solar Technology rooftop PV System. Three strings of *'Sunny Tripower 7000TL'* and *'Sunny Tripower 9000TL'* inverters with a maximum AC apparent power of 7 kVA and 9 kVA, respectively, are measured and archived in second-by-second resolution to allow the creation of time series, which is used as input for simulated PV systems. A converter with the Phase 2 PRP scheme (CON) scaled up to 100 MVA at 400 kV from a base value of 1 MVA at 0.69 kV (as Section 4) and a constant power simulated load of 40 MW are interconnected to form Grid 2. Except for Scenario 9, the active power control (APC) of Phase 2 PRP is deactivated with no arbitrary dispatch. The APC is a slow control, and the present testing focuses on fast frequency responses (FFR) and system interactions.

The combined system is simulated in EMT domain and in real time to examine dynamic interactions and islanding. The equipment itself is modeled in RSCAD®FX on RTDS. A NovaCor Chassis from RTDS licensed with eight cores is applied for the test bench. The common time step or main step applied in this work is 50 µsec, applicable to the electrical elements like cables, generators, and all controls, including PRP, MMC, PV, SPS, and generator controls. The switching or sampling frequency of the MMC and DC/DC converter (MVHV) interconnection between MVDC and HVDC is implemented in a substep frame with a time step of 5 µsec. The various disturbances, such as variable load steps, islanding, and setpoint operations, are applied to the considered test bench (Grid 1 and Grid 2) to obverse the stability and interaction of the converter control and system.

6.2 Scenarios, responses, and system interaction

The test scenarios are simulated to display the interaction between the different control schemes and their ability to work in a coordinated manner under various events. The plot notations are designated in Table 6.1. The operating points of the assets in distinct scenarios are given in Table 6.2.

Table 6.1: Notation adopted in figures (Figure 6.1 to Figure 6.9).

Active Power MVDC Terminal 1	$P_{\mathrm{AC,T1MV}}$
Active Power MVDC Terminal 2	$P_{\mathrm{AC,T2MV}}$
AC network equivalent modelled as generator	P_{GEN}
PRP as GFM IBR	P_{CON}
Simulated PV model (constant and dynamic profile	P_{PV}
Linear amplifier (SPS)	P_{SPS}
Battery interfaced DC/DC converter	$P_{\mathrm{DC/DC,MV-MV}}$
DC/DC converter between MVDC-HVDC	$P_{\mathrm{DC/DC,HV-MV}}$
Frequency of Grid 1	ω_{GEN}
Frequency emulation of VSM GFM	ω_{VSM}
Frequency at PCC (Grid 2)	f_{PCC}
Voltage argument at the measurement node of PRP GFM (CON)	arg_{MEAS}

Table 6.2: Steady-state operating points of active elements in test bench (in MW).

Scenario / **Operating Point**	Heater switch ON/ OFF (Scenario 1,2 & 6)		Heater switch ON/ OFF (Scenario 7 to 9)		Load step at Grid 1 (Scenario 3)	Step increments at MMC (0→3→6→3→0) (Scenario 4&5)
Linear Amplifier Status	OFF	ON	OFF	ON	ON	ON
Grid 1			**BLOCKED**			
AC, T1 MV	+60	+60	0	0	+60	+60
AC, T2 MV	-40	-40	0	0	-40	-40
Const. load 1	-100*	-100*	0	0	-100*	-100*
Grid 2			**OPERATIONAL**			
CON - PRP	+60	+66	+20	+26	+71	+66
PV	+20	+20	+20	+20	+20	+20
Const. load 2	-40*	-40*	-40*	-40*	-40*	-40*
MMC	0	0	0	0	-5*	0
Fan heater	0	-6*	0	-6*	-6*	-6*

*__Note:__ Negative power indicate load operation or consumption

To create a more reasonable comparison and showcase PRP's functionality, the plots are displayed for interconnected systems (Grid 1 and Grid 2) and island operation (Grid 2); however, scenario descriptions are sequential.

Scenario 1: The scenario displays the performance and interaction of the complete system with a focus on the response of PRP (APC is deactivated). The two networks (Grid 1 and Grid 2) are stable and connected, while a disturbance at Grid 2 is created by the connection and disconnection of the three-phase fan heater creating a step event. The event stages are as follows:

- Complete system in normal operation with MVDC terminal 2 (T2MV) in non-blocking mode.
- Constant PV infeed with other stable operation of all connected loads and sources.
- Three single-phase heaters are interfaced via SPS. The SPS is initially offline. It is switched ON for approx. 3 sec, followed by switching OFF and disconnecting the SPS. The connection leads to the load step of the heaters of approx. 6 MW.
- The response of the converter based on PRP's scheme and other resources are monitored.
- MMC is offline with both DC/DC converters at zero participation.

The responses are documented in Figure 6.2.

Scenario 2: This scenario is an extension of Scenario 1, considering dynamical PV infeed with consolidated PV profile injection instead of constant PV characteristics. The rest of the system and procedures are identical to Scenario 1 (as such, MMC is offline, and DC/DC converters have zero participation). The steps include:

- Initial conditions as Scenario 1 with dynamical PV infeed with fast varying PV profile characteristics.
- Similar to Scenario 1, SPS is initially offline, followed by an online connection. As a result, the heaters are switched on, leading to a load increase of approx. 6 MW.
- After approx. 3 sec, SPS is switched OFF, and the heaters are disconnected by extension.
- Similar to the previous case, the converter's response based on PRP's scheme and other resources are monitored.

The diagram displaying PRP's responses and associated elements of interest is available in Figure 6.4.

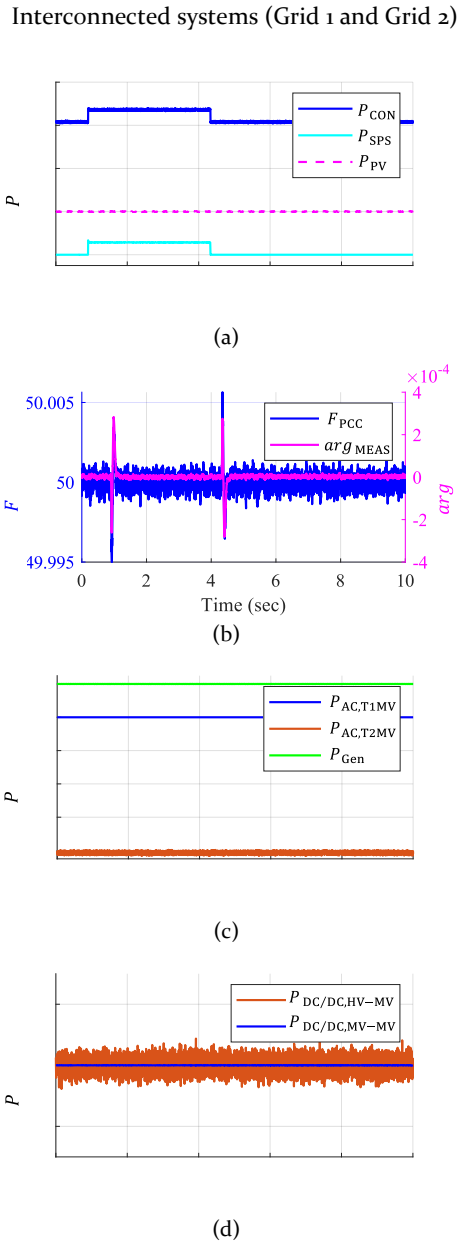

Figure 6.2: Responses of Scenario 1:

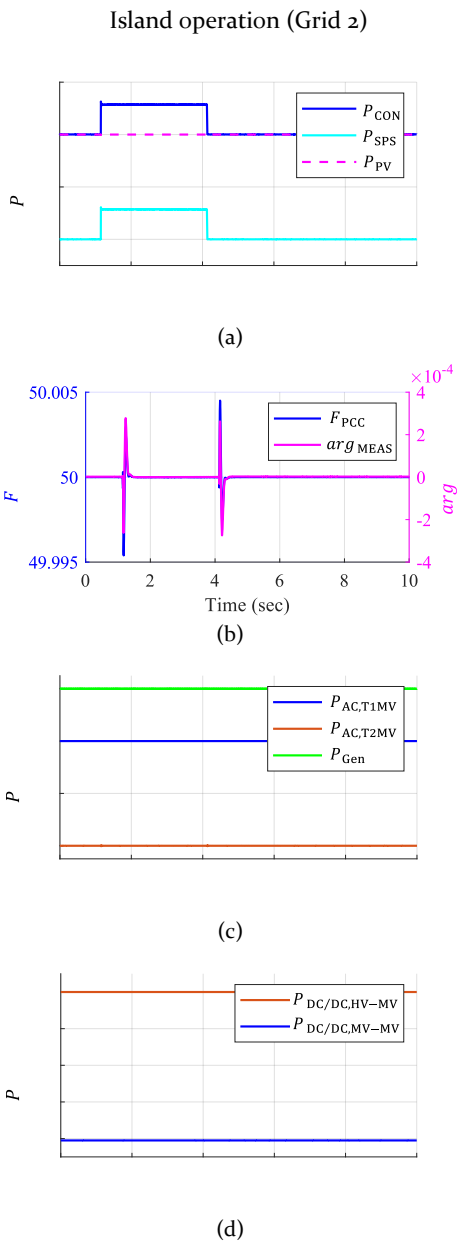

Figure 6.3: Responses of Scenario 7:

(a) Active power responses in Grid 2;
(b) Measurement voltage phase at PRP MEAS terminal and frequency at PCC;
(c) Active power responses in Grid 1;
(d) DC power flows in HV-MV and MV-MV converters.

Interconnected systems (Grid 1 and Grid 2)

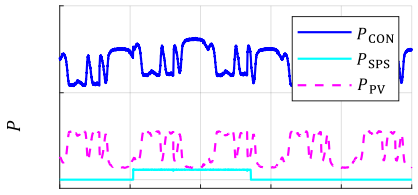

(a)

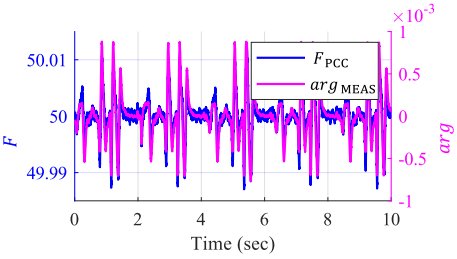

(b)

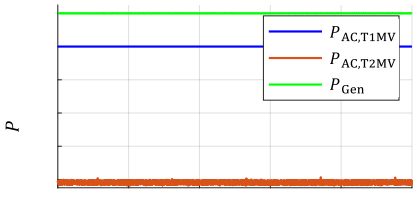

(c)

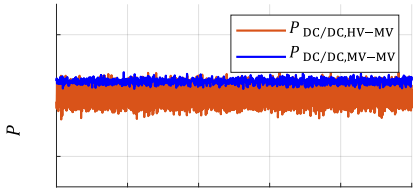

(d)

Island operation (Grid 2)

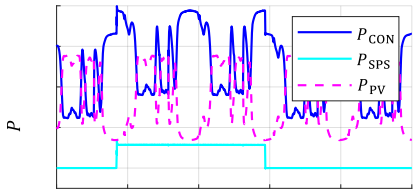

(a)

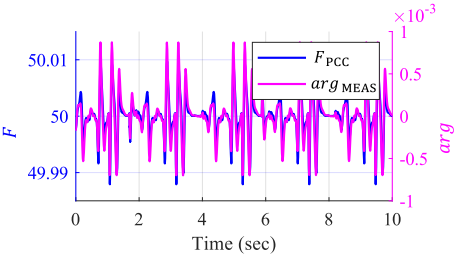

(b)

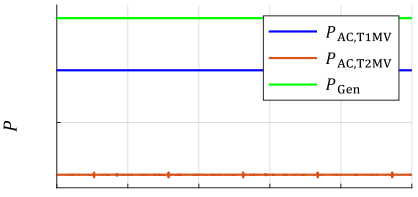

(c)

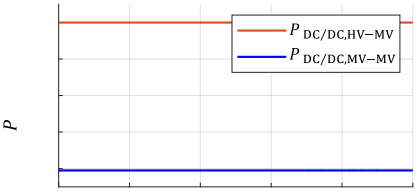

(d)

Figure 6.4: Responses of Scenario 2:

Figure 6.5: Responses of Scenario 8:

(a) Active power responses in Grid 2;
(b) Measurement voltage phase at PRP MEAS terminal and frequency at PCC;
(c) Active power responses in Grid 1;
(d) DC power flows in HV-MV and MV-MV converters.

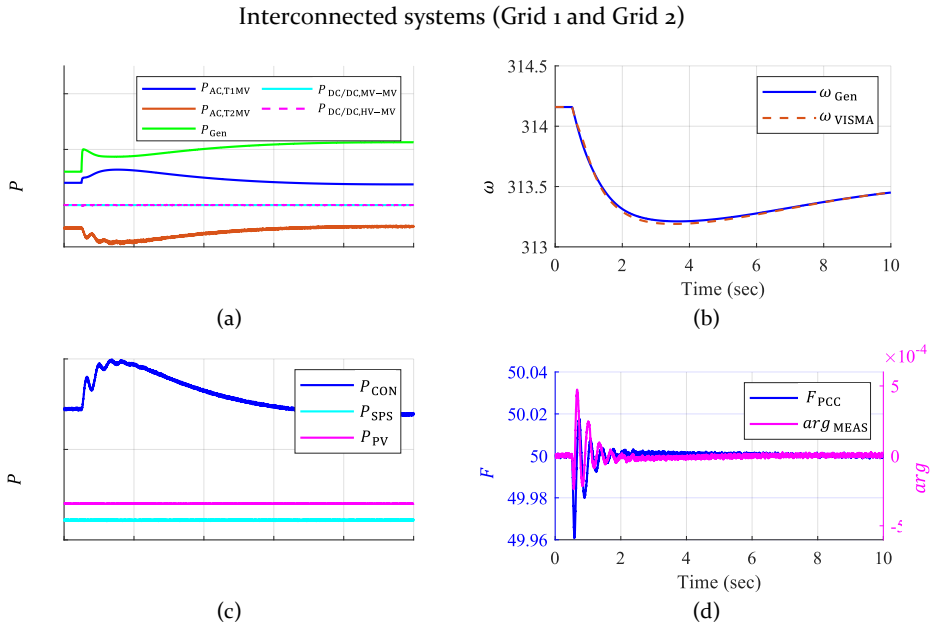

Figure 6.6: Responses of Scenario 3:
(a) Active power responses in Grid 1;
(b) Frequency response at Grid 1;
(c) Active power responses in Grid 2;
(d) Measurement voltage phase at PRP MEAS terminal and frequency at PCC.

Scenario 3: This case describes the combined MVDC system response with a load step increase in Grid 1. Grids 1 and 2 are at steady-state operation, and the response concerning PRP is highlighted and discussed.

- Normal steady-state operation of Grid 1 and Grid 2.
- A load step increase of 50 MW is performed for load 1 from an initial loading of 100 MW to final loading of 150 MW.
- Droop constants of DC/DC converters connected between HV-MV and MV-MV link are set to zero with no participation of these converters and hence ensuring no power flow from the HVAC grid or 3Ph-DAB large-scale battery.
- Grid 1, along with VSM and PRP control, are evaluated, and responses stabilizing the system are observed.

The scenario responses are depicted in Figure 6.6.

Scenario 4: This test case describes the response to disturbance with additional setpoint adaptions applied to the system. The MMC in load operation is switched in multi-step responses, and the entire system response is evaluated for the step events. The actions include:

- Loads steps at the MMC via the linear amplifier are performed in Grid 2 with an initial loading of 0 MW.
- The heaters are ON at constant loading of 6 MW and PV with constant infeed of 20 MW.
- Droop constants of DC/DC converters connected between HV-MV and MV-MV link are set to zero with no power flow.
- The load sequence follows: 0 MW →3 MW →6 MW →3 MW →0 W. Thus, two step-ups followed by two step-downs.
- An immediate setpoint change is applied to the active power infeed at the node marked PCC of Grid 2, which is forwarded as setpoint change to T2MV and T1MV of the MVDC. The setpoint change is performed via Human-Machine Interface (HMI).
- The power dispatch is forwarded to MVAC Grid 1, relieving PRP's contribution to the event. System response is noted.

The associated findings are illustrated in Figure 6.7.

Scenario 5: This test is an amendment to Scenario 6, replacing the source of power dispatch from MVAC Grid 1 to the DC/DC battery storage unit. The rest of the procedure is identical and is as follows:

- The MMC is initially at 0 MW loading with the fan heater at 6 MW consumption and PV with 20 MW constant infeed.
- Droop constant of DC/DC converter between HV-MV is zero with no participation while MVDC battery has a non-zero droop factor.
- Load step increase and decrease events are applied at the MMC in the following sequence: 0 MW →3 MW →6 MW→3 MW→0 W.
- Manual setpoint adaptation via HMI is performed at PCC of Grid 2, in which the T2MV and the integrated battery unit of the MVDC overtake power dispatch due to non-zero droop factor.
- PRP responds to the event, and the complete system is monitored.
- The active power loading is forwarded to battery storage unit.

The test results are displayed in Figure 6.8.

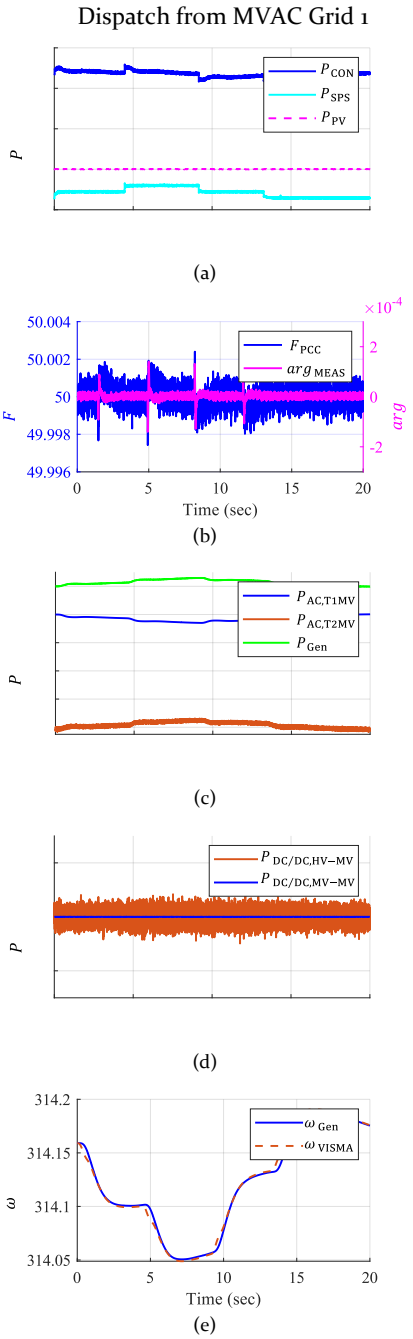

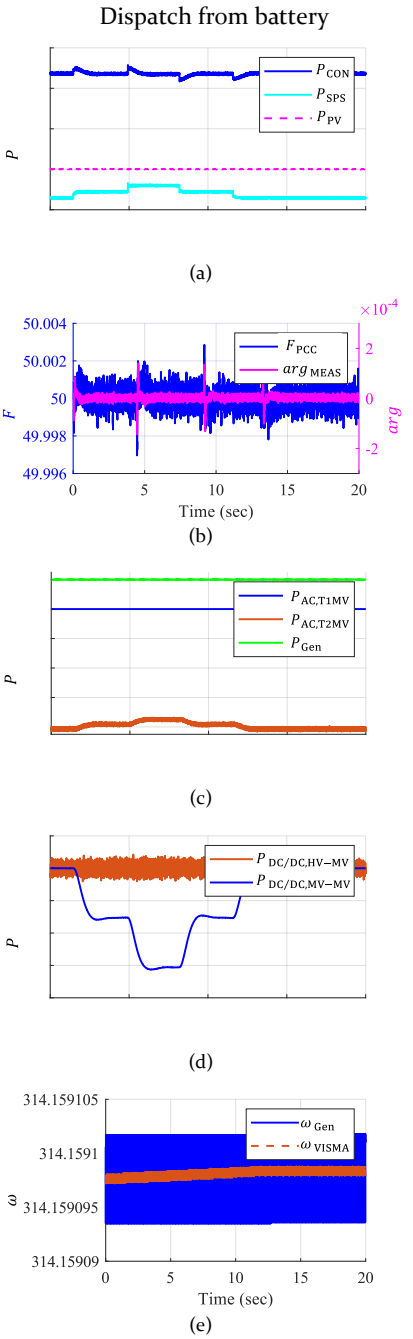

Figure 6.7: Responses of Scenario 4:

Figure 6.8: Responses of Scenario 5:

(a) Active power responses in Grid 2; (b) Measurement voltage phase at PRP MEAS terminal and frequency at PCC; (c) Active power responses in Grid 1; (d) DC power flows in HV-MV and MV-MV converters; (e) Frequency response at Grid 1.

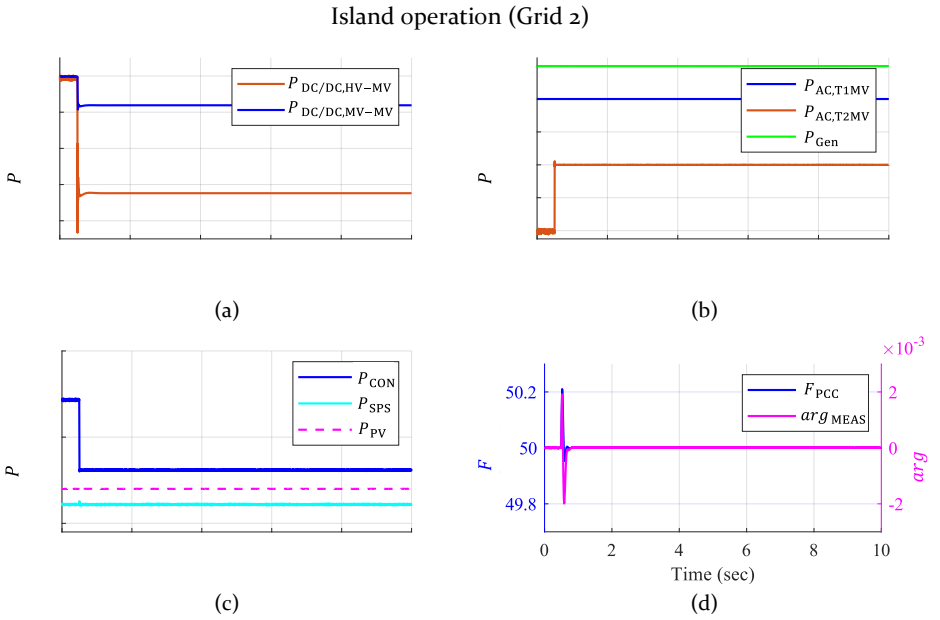

Figure 6.9: Responses of Scenario 6:
(a) DC power flows in HV-MV and MV-MV converters;
(b) Active power responses in Grid 1;
(c) Active power responses in Grid 2;
(d) Measurement voltage phase at PRP MEAS terminal and frequency at PCC.

Scenario 6: This scenario describes the islanding case of Grid 2, and the associated steps involved in triggering of the event:

- Normal operation of Grid 1 and Grid 2 at steady-state with sufficient headroom in PRP-controlled source.
- MVDC terminal 2 (T2MV) is blocked.
- PRP responds to disturbance and forming capability of the network is observed. Other elements' response in Grid 2 are tracked.
- DC side power of MVDC terminal 1 (T1MV) is taken over by both DC/DC converters by non-zero droop factors. $P_{DC/DC,MV-MV}$ and $P_{DC/DC,HV-MV}$ have power flows.
- All assets connected at Grid 2 function at the same operating point.

The associated plots are shown in Figure 6.9.

Scenario 7: This test case is an extension of Scenario 6 and shows additional disturbance created by switching ON and OFF the fan heater with constant PV injection. The testing procedures followed are similar to

Scenario 1, with the exception of the disconnection of Grid 1 (T2 of MVDC blocked). A detailed description is provided below:

- Successful creation and stabilization of Scenario 6 is the starting point with Grid 2 in island operation and T2 is in blocking mode.
- Static or constant PV infeed in Grid 2.
- Steady-state operation of other sources and load.
- Three single-phase heaters interfaced via SPS are switched ON from the initially OFF position for approx. 3 sec. It is subsequently switched OFF, disconnecting the SPS. The load step event of the heaters is with a step size of approx. 6 MW.
- PRP's response to the disturbance and influence on the island network is checked, along with the stable operation of other elements in the island.
- MMC system is offline and MVDC battery with non-zero droop.

The associated responses are shown in Figure 6.3.

Scenario 8: This case is an extension of Scenario 7 and is analogous to procedures followed in Scenario 2, considering dynamic PV characteristics, and connecting the three-phase fan heater, followed by its disconnection. This case includes the following:

- Initial conditions as Scenario 7 with dynamical PV infeed data with time scale compressed PV profile injection instead of constant PV characteristics.
- Similar to Scenarios 7 and 2, SPS is switched ON. As a result, the heaters are connected, leading to the load step increase by the heaters to approx. 6 MW for ca. 3 sec.
- Thereafter, disconnection of SPS and by extension of the heaters is performed after the stipulated time.
- Similar to the previous case, the stability of the island system is recorded and studied. MMC storage system is offline.

The observations are recorded in Figure 6.5.

Scenario 9: This case describes the islanded Grid 2, with APC active and setpoint adaptations on Phase 2 PRP converter control. The disturbance is created by switching ON and OFF the fan heater with constant PV injection. The Grid 1 is disconnected by blocking T2 of MVDC. A detailed

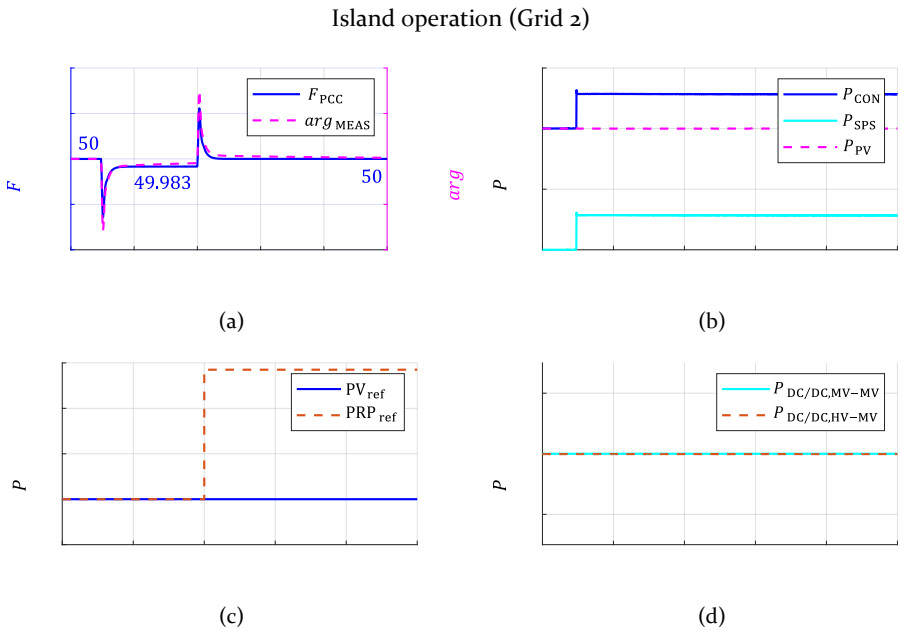

Figure 6.10: Responses of Scenario 9:
(a) Measurement voltage phase at Phase 2 PRP MEAS terminal and frequency at PCC ;
(b) Active power responses in Grid 2;
(c) Active power setpoint changes in Grid 2;
(d) DC power flows in HV-MV and MV-MV converters.

detailed description is provided as follows:

- Successful islanding of Scenario 6 serves the starting point of this case with Grid 2 in island operation and T2MV blocked.
- Constant PV infeed in Grid 2 and MMC storage system is offline.
- Steady-state operation of other sources and load.
- Three single-phase heaters interfaced via SPS are switched ON from the initially OFF position at approx. 1 sec. The connection of the load leads to step event with a step size of approx. 6 MW.
- PRP with APC response to the disturbance with a stable steady-state response to the event, however frequency is not restored to nominal due to the APC activation.
- Manual setpoint adaptations via HMI is performed on PRP after an inherent control delay of 0.5 sec to restore the nominal frequency.

The scenario responses are depicted in Figure 6.10.

6.3 Discussion of results

The tests display a wide range of scenarios and operating conditions that demonstrate the PRP control scheme's performance and key behavior. The APC and current limitation is initially not considered to evaluate the GFM control responses for the distinctive inertial attribute (FFR) of each scheme (PRP and VSM) without enhancements and restrictions. The various hardware connected to the test bench is operated to create a dynamic event, and the responses are monitored. A supplementary Scenario 9 with APC activation in islanding is performed to highlight the response of Phase 2 (PRP+APC) control with tuned setpoints.

Scenarios 1 and 2 focus on PRP's response in the interconnected system under disturbance. Providing immediate response to the step event and restoring the phase, thus, nominal frequency in the network is displayed. The system is at steady-state prior to the event, and the initial power dispatches are seen in Table 6.2. PRP provides a quick damped response to disturbances by restoring the phase in the system and stabilizing, a prime differentiator of the control scheme, which is prominent with a small delay in both Scenario 1 and 2 with the switching ON/OFF event of the heater as displayed in Figure 6.2 (a and b) and Figure 6.4 (a and b). The converter equipped with the PRP control scheme has sufficient capacity and delivers adequate power to the increased and decreased loading. Similarly, for Scenario 2, PRP stabilizes the power system by acting on the disturbance supplying the necessary power based on the dynamic infeed from PV and the active power variation due to the switching of pure resistive fan load as portrayed by (Figure 6.4 (a)). Grid 1 does not participate in the event, as seen in the plots (Figure 6.2 (c and d) and Figure 6.4 (c and d)), with no variation in frequency and active power dispatches. Similarly, all other loads and sources (GFL) remain connected without additional power infeed in both cases (Figure 6.2 (a) and Figure 6.4 (a)). Due to the switching function model of the T2MV MVDC, the power responses at Grid 2 contain unfiltered current ripples.

Scenario 3 describes PRP's interaction with the VSM GFM scheme to provide inertial support to stabilize the system. A load increase (Load 1) in Grid 1 results in the inertial provision of VSM control attached at T1MV. The event in Grid 1 leads to a steep frequency drop partially relieved by a temporary power increase of VSM due to the inertia emulation. The power difference to stabilize the frequency is retrieved from the MVDC Grid 2, which is stabilized by the other head station T2MV by the action of the droop control. The temporary power increase of T2MV is balanced by Grid 2

and, more specifically, by the PRP GFM control resulting in an immediate inertial response from PRP to the disturbance event, as visible Figure 6.6 (c and d). As seen in Figure 6.6 (a and b), the VSM, based on its characteristic swing response, initially increases its active power infeed in coordination with PRP's temporary increase in active power infeed before the reaction from Grid 1 dominates. The VSM initially provides inertial support to Load 1 using DC-linked storage systems and energy stored in the MMC sub-modules. The inherent characteristic to react to the disturbance in a stabilizing manner results in a quick PRP response in coordination with the VSM control returning both GFM schemes to their initial operation point pre-event. The network equivalent (Grid 1) takes over the primary control or provides additional power dispatch to compensate for the load increase. No permanent power increase of T1MV is viable as only inertia provision is available (in this scenario). At lower control inertias, local area oscillations are observed between the VSM-controlled converter and the upscaled generator. The addition of a power system stabilizer (PSS) to the VSM enhances the damped response of the control scheme.

Scenarios 4 and 5 focuses on displaying PRP's prioritizing of disturbance over setpoints changes. Sequential load steps are performed, resulting in an immediate or inertial and stabilizing response from PRP. The measurement phase is restored to its initial value after each disturbance, as seen in Figure 6.7 (b) and Figure 6.8 (b). The DC voltage support and APC is redirected to either the MVDC Grid 1 or the DC/DC battery model. Firstly, a temporary increase of delivered active power by PRP converter is visible due to inertia support in Figure 6.7 (a) and Figure 6.8 (a), followed by the slow manual setpoint adaption through the HMI at the PCC node. Hence, allowing active power forwarding to be taken over by T2MV and T1MV in Scenario 4 with Grid 1 increased infeed or T2MV (Figure 6.7 (c and d)). In comparison, the MVDC battery storage ($P_{\mathrm{DC/DC,MV-MV}}$) provides the additional power infeed to the load variation in Scenario 5 (Figure 6.8 (c and d). Thus, the PRP converter is relieved to increase its admissible power margins for incoming Grid 2 power imbalances, and additional power dispatch or APC feature of Phase 2 PRP control is not utilized. The necessary power for Grid 1 is retrieved from other sources. Nominal frequency is restored. Setpoint adaptation in PRP control is possible with some delay ($>$ 300 msec). Therefore, setpoint adaption at PRP is not displayed as a fast system response. The incorporation of APC with multiple sources and its responses is evidenced in Chapter 4. In both cases (Scenario 4 and 5), the overall system can deliver a fast inertial response from PRP and coordinated

dispatch from other sources as an alternative, with a comparative display in Figure 6.7.and Figure 6.8.

Scenarios 6, 7, and 8 demonstrate the islanding of Grid 2 with additional disturbances created by dynamic switching of the fan heaters with constant and fluctuating PV profiles. Scenario 6 displays the successful and stable isolation of the controlled AC network or Grid 2 by blocking T2MV, as seen in Figure 6.9 (a and b). PRP responds to the disturbance and stabilizes the network. The phase is restored, and nominal frequency is achieved, as witnessed in Figure 6.9 (d). It additionally takes over the power difference caused by the blocking of T2MV with initial loading (before blocking) of 40 MW (consumer or passive component). The power flow plots due to the events are available in Figure 6.9 (c), with a decreased output by the PRP-based converter. At the same time, all other active elements maintain their pre-event operating points, shown in Figure 6.9 (c). The activation of APC relaxes on the constant frequency assumption of PRP, allowing steady-state frequency deviation, which is restored to nominal by the control after a minimum period of 600 msec, as shown in [32] and further in Scenario 9. The Scenario 6 forms the prequel to Scenarios 7 and 8. These two test cases are analogous to Scenarios 1 and 2, but under islanding conditions, and are an addendum to the stable operation in Scenario 6. Due to the absence of the effects of the switched MVDC terminal, the response in Grid 2 is ripple free, as described by the active power trends in Figure 6.3 and Figure 6.5 when compared to Scenario 1 (Figure 6.2) and 2 (Figure 6.4). The test procedure is identical to Scenarios 1 and 2 to scaled load jumps. Similar stable responses in island operation with PRP forming the network and adjusting its power infeed depending on the network requirements are displayed. The plots are visible in Figure 6.3 and Figure 6.5 and comparable to Scenarios 1 and 2.

Scenario 9 is a supplementary test of Phase 2 control with active APC to display the constant frequency relaxation and the possibility of arbitrary power dispatches via setpoint adaptions. The event portrays the control's immediate response to the disturbance with increased active power to balance the 6 MW load increase due to the switching ON of heaters. A steady-state operating point and hence frequency develops (49.983 Hz), differing from nominal frequency, as in Figure 6.10. A manual setpoint adaption is performed on Phase 2 PRP via HMI with an inherent delay of 0.5 sec to restore nominal frequency. Other elements remain undisturbed (Figure 6.10).

As mentioned in [170] demonstration experiences have shown to be good performers and capable of achieving their objectives. When introducing a new concept, it is vital to perform rigorous testing to enhance understanding, reliability, and performance. This demonstration is a step towards the same.

6.4 Chapter summary

This chapter aims to demonstrate the unique value propositions of the novel PRP control scheme. The experiments' results confirm the analysis reported in Chapter 4, and assess the GFM capabilities reported in Chapter 5 of the PRP control structure. The interactions between the PRP control scheme with other GFL and GFM converters, along with the most noteworthy observations, have been presented. The inherent characteristic of counteracting to disturbances is displayed. The ability to achieve nominal frequency with limited phase shift (arg_{MEAS}), thus acquiring the new operating point via a direct path, is also portrayed. The primary features of PRP are demonstrated in different network combinations of an MVDC test bench with a high proliferation of IBRs and non-linear loads as PHiL.

The interaction of this scheme with other GFM control concepts, in this case, VSM, has been illustrated and shows a coordinated response to disturbance by providing inertial support. An alternative to the inbuilt APC in PRP (Phase 2), power sharing or slow response, is highlighted from other assets in a coordinated approach, whereas PRP provides only inertial or fast response. Setpoint adaption is also displayed with Phase 2 PRP, including APC control restoring to nominal frequency but with some delay, allowing multisource operation with arbitrary dispatches. The control response is oscillation free. Furthermore, global stability criteria is also displayed when meeting the impedance relationship of coupling and transformer impedance.

Various tests were conducted in PHiL under challenging network conditions in an MVDC test bench with a high proliferation of IBRs and non-linear loads. The focus of the test bench was on FFR and stabilization. PRP's swift response to any fault to form and stabilize the power system is perceived in all scenarios. Therefore, this chapter further reinforces this control scheme's performance under the influence of various hardware and converter controls.

7 Conclusion and Outlook

To tackle future power system challenges with a high proliferation of IBRs, the topic of GFM converters has emerged as a promising technology. An exact definition of this technology is still being shaped in concert with the changing needs of the power system. However, maintaining a voltage source behavior with an immediate, stable response to disturbance is expected. Additional services and advanced performances, like load sharing, damped response, limited Vector Shift, and improved voltage profile during disturbed conditions, to name a few, are also requested. The early adopters of GFM include Australia, Germany, Great Britain, and Hawaii, with NERC placing a high importance on frequency stability.

NERC emphasizes that the primary objective of the GFM converter is to immediately respond to changes in the external system and maintain control stability, followed by active and reactive power regulation. ENTSO-E hints at stable response under normal, disturbed, and emergency states. The UK Grid Code and various projects worldwide provide valuable insights into synchronizing power, active control-based power requirements, and compatibility with devices in the power system. Therefore, a control that achieves asymptotic stability and, as a result, frequency evolves after steady-state may be defined as a GFM system. In other words, all controllers collectively share a coordinated control response to support voltage and frequency to restore nominal values constructively. Different GFM concepts that fulfill these requirements are being established. However, these schemes provide only some of the services or do not provide the ideal responses.

This work introduces a novel globally stable GFM control scheme developed in three phases. Phase 1 comprises of the fundamental building block of the control hierarchy called the 'Phase Restoring Principle' (PRP). It fully reflects the above-mentioned requirements by prioritizing response to disturbance over setpoint changes. It is based on the change of perspective from the converter to the grid. The PRP utilizes a novel angular transformation $\rho_{dr}\iota_{dr}$ of the reference frame in the opposite direction to a disturbance in an ohmic-inductive network. It creates a stabilizing response by reacting to the difference in phase. The PRP transformation comprises the central part of the control and is fully Grid-Forming. A similar structural designation of a PLL is sublimated into the PRP main block. This block creates a constant frequency response by returning the phase at the measurement node back to the original operating point

(nominal frequency). PRP is, therefore, controllable and actively participates in creating future operating points after a disturbance.

To achieve interoperability between multiple sources, relaxation is applied to the constant frequency condition, resulting in unbounded currents. In Phase 2, the control scheme is extended to include enhanced active power control (APC), envisaging stable operation with other devices (SM, IBRs) in a power system and allowing arbitrary power dispatches. Thus, the control scheme contains two loops for voltage phase output: the main control loop processes transformed frequency and is supplemented by the APC loop, which is added to the primary frequency loop. As a result, one output phase is obtained for the converter voltage, with the response of the frequency loop dominating the APC loop by the choice of gains. Hence, the phase contributing to frequency dominates the constant phase part of power flow, leading to the desired response to disturbances dominating over the response to setpoint changes. Additionally, the cascaded differentiator with a double integrator system produces a stable first-order transfer function response free of higher-order swing dynamics.

Appropriate current limiting control methods are required for GFM inverters to realize these GFM control concepts by meeting hardware requirements and successfully riding through disturbances. Currently, three known current limiting methodologies are being applied to GFM converters: current limiter, virtual impedance, and voltage limiter. However, these concepts serve as broad guidelines but do not provide exact implementation templates. Additionally, these broad methods need adaptations to offer tangible advantages.

To cater to better performance and recovery from undesired current saturation, new and improved current limiting controls are required to be developed to help GFM converters. Therefore, in Phase 3, a current limiting control is developed to account for the converter's hardware constraints. The concept is inspired by the voltage limiter methodology. The control algorithm proposed complements the Phase 2 scheme. It employs novel usage of an anti-windup limiter and other control logics/blocks necessary for symmetrical fault conditions to create a foundational GFM converter control. The current limiting control helps maintain all the advantages of Phases 1 and 2 of the PRP scheme, making the scheme usable under various network conditions.

The state-of-the-art GFL converters utilize pure observers, e.g., an ideal PLL, whereas PRP offers controllability and adheres to the GFM requirements. The GFM control concepts like Droop or VSM emulate a

synchronous machine and, therefore, have an inherent swing response and do not achieve nominal frequency independently. Phase 1 PRP offers a 1st order system response and is highly damped, allowing to attain nominal frequency. It exhibits minimum Vector Shift, which assists in protection schemes by avoiding unnecessary trips. Existing GFM concepts, like matching control and VOC, are based on different control methodologies and are currently in research.

Furthermore, the PRP control scheme is globally stable, unlike the GFM control schemes mentioned above controls, which operate under the underlying principle of an operating point's existence determined by external frequency. PRP functionality, either in the pure version or in the APC adjoined version, can be related to a virtual asynchronous machine with a controlled rotor or rather a virtual double fed-induction generator, to be precise, in contrast to VSM. The former acts directly on the relative phase (change in phase, viz. frequency), whereas the latter acts directly on the absolute phase.

The novel PRP concept requires a tailored current limiting strategy to help preserve its GFM features. Compared to the state-of-the-art current limiter methods for GFM, the implemented strategy maintains the voltage source behavior in PRP-based GFM under severe fault (overcurrent conditions) scenarios. Further, it does not require any mode switching.

The virtual impedance method and its variants highly depend on the network conditions (X/R ratio) and need an additional adaptive control to cover a spectrum of fault scenarios. An appropriate design of the X/R ratio is thus needed since it may destabilize the system under certain conditions.

Unlike the virtual impedance method, the developed voltage magnitude limiter method requires no additional adaptive control scheme to address a wider range of system overcurrent conditions. The prime difference to existing voltage limiter methods is that the phase is not controlled via the current limiting control; rather, the current is limited via the magnitude only. Thus, no restriction is applied to the voltage phase, preserving the phase-frequency and the original control characteristic.

The derived mathematical relations and numerical simulations confirm the stable response of the control under different operating conditions and independent of grid loading. PRP acts to ensure that the network approaches and obtains the high voltage, low current (regular) solution. The reaction of PRP is comparable to an ideal slack at steady-state due to the accomplishment of constant frequency with the same relative phase

response ($\Delta\varphi$). Hence, it is reasonable to compare the response of PRP, without supplemental control loops, to infinite inertia. The robustness of the control is ensured by evaluating stable control performance under a wide range of network conditions.

The control response results for each phase are verified by simulation for challenging scenarios such as weak grids and large disturbances. The corresponding power system responses are numerically bounded and compliant with global stability conditions. The coupling and transformer impedance ratio determines the existence of the operating point, with the role of transformer impedance as a decisive constituent of the overall converter control performance. Simulative investigations are carried out in both RMS and EMT domains. The control response is also demonstrated as further validation in a real-time laboratory environment utilizing PHiL simulations on a real-time simulator (RTS). The interaction of PRP with other control schemes (GFM and GFL) and its operation with a real MMC hardware converter is investigated in a laboratory setup. The analysis results show that PRP demonstrates a stable control response under various scenarios, including islanding. Experimental investigations, including PHiL simulations with detailed converter models and hardware, further confirmed the analytical proofs and pure simulative analyses.

The new control scheme presented in this thesis is a viable choice for future GFM field applications. The present development status serves as a template that may be extended to fulfill specific project or grid code requirements to form a comprehensive and field-ready GFM converter control. The application includes converters interfaced with batteries, a capacitor bank, a power plant controller with an added energy source, or a microgrid controller with an added energy source. It can have a transformative influence on attaining stability and reliability for networks with a high penetration of IBRs.

This thesis explores a topic of considerable scope, which necessitates multifaceted examinations encompassing proficiency in power system analysis, control theory, and fundamentals of power electronics. An interdisciplinary approach is crucial for appropriately addressing the subject matter at hand. Some future aspects extending this thesis's contribution may include the following:

- Negative sequence control structure when exposed to unbalanced faults: Studying the control response under unbalanced fault scenarios and investigating if further measures may be required for negative sequence voltage feedback components.

- Energy limitation schemes in cases of HVDC or FACTS: The control scheme considers a free energy exchange between AC and DC power systems via a battery or a capacitor bank. An alternate application of the control scheme is for HVDC or FACTS, whose limited energy capacity will require some assessment and modification.
- Interoperability with other converter controls: The proposed current limitation relies on the structural self-similarity of all connected IBRs. To achieve full interoperability with other converter controls, the current limiting strategy needs to be assessed under heterogeneous control conditions, and extensions may need to be devised.
- Minimum energy transfer: One main objective of converter rating is minimum energy transfer between the converter's internal energy storage and power system for any power system disturbance. PRP is a highly promising candidate to meet this requirement and is also considered for future investigations.
- Black start and power quality: Both black start and power quality are feasible to meet but need verification.
- Hardware implementation: The next steps include the implementation of the PRP control scheme in a real hardware. A hybrid plant consisting of a GFM battery incorporating the PRP control and other IRB assets, such as PV infeed with a power plant controller, is foreseen as a future project.

Bibliography

[1] J. Matevosyan *et al.,* "A Future With Inverter-Based Resources: Finding Strength From Traditional Weakness," *IEEE Power and Energy Mag.*, vol. 19, no. 6, pp. 18–28, 2021, doi: 10.1109/MPE.2021.3104075.

[2] Y. Lin *et al.,* "Research Roadmap on Grid-Forming Inverters: Golden, CO: National Renewable Energy Laboratory. NREL/TP-5D00-73476," 2020. [Online]. Available: https://www.nrel.gov/docs/fy21osti/73476.pdf

[3] H. Holttinen et al., "System impact studies for near 100% renewable energy systems dominated by inverter based variable generation," *IEEE Transactions on Power Systems*, vol. 37, no. 4, pp. 3249–3258, Jul. 2022. doi: 10.1109/TPWRS.2020.3034924. [Online]. Available: https://ieeexplore.ieee.org/document/9246271

[4] M. Ndreko, S. Rüberg, and W. Winter, "Grid forming control scheme for power systems with up to 100% power electronic interfaced generation: a case study on Great Britain test system," *IET Renewable Power Generation*, vol. 14, no. 8, pp. 1268–1281, 2020, doi: 10.1049/iet-rpg.2019.0700.

[5] North American Electric Reliability Corporation (NERC), "Inverter-Based Resource Strategy: Ensuring Reliability of the Bulk Power System with Increased Levels of BPS-Connected IBRs," Jun. 2022. [Online]. Available: https://www.nerc.com/comm/Documents/NERC_IBR_Strategy.pdf

[6] Wei Du, "Grid-Forming Inverters: A journey from a single microgrid to an integrated T&D system with 10,000+inverters," *IEEE PES University*, 2022. [Online]. Available: https://eesg.mit.edu/eesg-seminar/2023-sp/dwei/

[7] High Share of Inverter-Based Generation Task Force. 2022., "Grid-Forming Technology in Energy Systems Integration: High Share of Inverter-Based Generation Task Force Reliability Working Group of the Energy Systems Integration Group," Reston, VA: Energy Systems Integration Group. [Online]. Available: https://www.esig.energy/reports-briefs

[8] B. Kroposki, "Understanding Grid-forming Inverter Specifications.,"

[9] A. Larkins, "Power Converters: A Growing Challenge To Grid Stability? [Viewpoint]," *IEEE Electrific. Mag.*, vol. 9, no. 2, pp. 85–88, 2021, doi: 10.1109/MELE.2021.3070944.

[10] European Commission (EC), "'The European Green Deal,' Communication from the Commission to the European Parliament, The Council, The European Economic and Social Committee and The Committee of the Regions: COM(2019) 640 final," Brussels, Dec. 2019.

[11] Y. Latief. "Grid Booster: World's largest storage-as-transmission project gets green light: 09.10.2022." [Online]. Available: https://www.smart-energy.com/industry-sectors/storage/grid-booster-worlds-largest-storage-as-transmission-project-gets-green-light/

[12] B. P. Heard, B. W. Brook, T. Wigley, and C. Bradshaw, "Burden of proof: A comprehensive review of the feasibility of 100% renewable-electricity systems," *Renewable and Sustainable Energy Reviews*, vol. 76, pp. 1122–1133, 2017, doi: 10.1016/j.rser.2017.03.114.

[13] U. Muenz *et al.*, "Operational Security in 100% Inverter-Based Power Systems: Experiences from Hawai'i," *IEEE Electrific. Mag.*, vol. 10, no. 3, pp. 10–19, 2022, doi: 10.1109/MELE.2022.3187632.

[14] B. Badrzadeh et al., "Electromagnetic transient simulation models for large-scale system impact studies in power systems having a high penetration of inverter-connected generation: Technical Brochure - WG C4.56, Power system technical performance," (Reference: 881), Sep. 2022.

[15] B. Badrzadeh, N. Modi, J. Lindley, A. Jalali, and J. Lu, "Power System Operation With a High Share of Inverter-Based Resources: The Australian Experience," *IEEE Power and Energy Mag.*, vol. 19, no. 5, pp. 46–55, 2021, doi: 10.1109/MPE.2021.3088744.

[16] National Grid ESO, "GC0137:Minimum Specification Required for Provision of GB Grid Forming (GBGF) Capability (formerly Virtual Synchronous Machine/VSM Capability): Final Modification Report GC0137," Nov. 2021. [Online]. Available: https://www.nationalgrideso.com/industry-information/codes/grid-code-old/modifications/gc0137-minimum-specification-required

[17] European Network of Transmission System Operators for Electricity (ENTSO-E), "Continental Europe Synchronous Area Separation on 08 January 2021: ICS Investigation Expert Panel,Final Report,15 July 2021 Main Report," Jul. 2021.

[18] "Netzentwicklungsplan Strom 2035, Cersion 2021: NEP_2035_V2021_1_Entwurf_Teil1_1," Berlin, Dortmund, Bayreuth, Stuttgart: 50Hertz Transmission GmbH, Amprion GmbH, TenneT TSO GmbH, TransnetBW GmbH, Jan. 2021. [Online]. Available: https://www.netzentwicklungsplan.de/sites/default/files/paragraphs-files/NEP_2035_V2021_1_Entwurf_Teil1_1.pdf

[19] North American Electric Reliability Corporation (NERC), "Reliability guideline: Improvements to interconnection requirements for BPS-connected inverter-based resources," North American Electric Reliability Corporation (NERC), Atlanta, GA,, Sep. 2019. [Online]. Available: https://www.nerc.com/comm/RSTC_Reliability_Guidelines/Reliability_Guideline_IBR_Interconnection_Requirements_Improvements.pdf

[20] F. Milano, F. Dorfler, G. Hug, D. J. Hill, and G. Verbic, "Foundations and Challenges of Low-Inertia Systems (Invited Paper)," in *2018 Power Systems Computation Conference (PSCC)*, Dublin, Jun. 2018 - Jun. 2018, pp. 1–25.

[21] A.Kuri, R.Zurowski, G.Mehlmann, D.Audring, and M.Luther, "Phase Restoring Principle: Concept of a novel grid-forming converter scheme," *ETG/GMA Fachtagung- "Netzregelung und Systemführung"*, pp. 19–24, Sep. 2022.

[22] D. Audring and A. Kuri, "Modelling and challenges of integration of large renewable power plants," in *2021 56th International Universities Power Engineering Conference (UPEC)*, Middlesbrough, United Kingdom, Aug. 2021 - Sep. 2021, pp. 1–6, doi: 10.1109/UPEC50034.2021.9548197.

[23] J.Matevosyan *et al.,* "Grid-Forming Inverters: Are They the Key for High Renewable Penetration?," *IEEE Power and Energy Mag.*, vol. 17, no. 6, pp. 89–98, 2019, doi: 10.1109/MPE.2019.2933072.

[24] D. B. Rathnayake *et al.,* "Grid Forming Inverter Modeling, Control, and Applications," *IEEE Access*, vol. 9, pp. 114781–114807, 2021, doi: 10.1109/ACCESS.2021.3104617.

[25] R. Rosso, "Stability Analysis of Converter Control Strategies for Power Electronics-Dominated Power Systems," (PhD thesis), *Technische Fakultät der Christian-Albrechts-Universität zu Kiel*, 2020. [Online]. Available: https://nbn-resolving.org/urn:nbn:de:gbv:8:3-2021-00603-4

[26] R. Rosso, X. Wang, M. Liserre, X. Lu, and S. Engelken, "Grid-Forming Converters: Control Approaches, Grid-Synchronization, and Future Trends—A Review," *IEEE Open J. Ind. Applicat.*, vol. 2, pp. 93–109, 2021, doi: 10.1109/OJIA.2021.3074028.

[27] D. Audring and A. Kuri, "Leistungselektronische Netze: (Siemens AG)," (in Berlin & online : 26.01.2022), *Zukünftige Stromnetze 2022*. [Online]. Available: https://www.zukunftsnetz.net/

[28] J. Rocabert, A. Luna, F. Blaabjerg, and P. Rodríguez, "Control of Power Converters in AC Microgrids," *IEEE Trans. Power Electron.*, vol. 27, no. 11, pp. 4734–4749, 2012, doi: 10.1109/TPEL.2012.2199334.

[29] A. Kuri, R. Zurowski, G. Mehlmann, D. Audring, and M. Luther, "A Novel Grid Forming Control Scheme Revealing a True Inertia Principle," *IEEE Trans. Power Syst.*, vol. 36, no. 6, pp. 5369–5384, 2021, doi: 10.1109/TPWRS.2021.3071126.

[30] A. Kuri, R. Zurowski, G. Mehlmann, and M. Luther, "Power Dispatch Capacity of a Grid-Forming Control Based on Phase Restoring Principle," *IEEE Systems Journal*, pp. 1–12, 2022, doi: 10.1109/JSYST.2022.3229103.

[31] North American Electric Reliability Corporation (NERC), "White Paper: Grid Forming Controls|: Grid Forming Technology, Bulk Power System Reliability Considerations," Atlanta, GA, Dec. 2021.

[32] A. Kuri, A. Raab, A. Takhtaganov, G.Mehlmann, and M.Luther, "Comparison of Phase Restoring Principle with other Grid-Forming Methodologies," *2023 IEEE Power & Energy Society General Meeting (PESGM), Orlando, FL, USA, 2023*, pp. 1–5, doi: 10.1109/PESGM52003.2023.10252387.

[33] Y. Li, Y. Gu, and T. C. Green, "Revisiting Grid-Forming and Grid-Following Inverters: A Duality Theory," *IEEE Trans. Power Syst.*, vol. 37, no. 6, pp. 4541–4554, 2022, doi: 10.1109/TPWRS.2022.3151851.

[34] Y. Teng, W. Deng, W. Pei, Y. Li, L. Dingv, and H. Ye, "Review on grid-forming converter control methods in high-proportion renewable energy power systems," *Global Energy Interconnection*, vol. 5, no. 3, pp. 328–342, 2022, doi: 10.1016/j.gloei.2022.06.010.

[35] N. Lidula and A. D. Rajapakse, "Microgrids research: A review of experimental microgrids and test systems," *Renewable and Sustainable Energy Reviews*, vol. 15, no. 1, pp. 186–202, 2011. doi:

10.1016/j.rser.2010.09.041. [Online]. Available: https://www.sciencedirect.com/science/article/pii/S136403211000328X

[36] K. de Brabandere, B. Bolsens, J. van den Keybus, A. Woyte, J. Driesen, and R. Belmans, "A Voltage and Frequency Droop Control Method for Parallel Inverters," *IEEE Trans. Power Electron.*, vol. 22, no. 4, pp. 1107–1115, 2007, doi: 10.1109/TPEL.2007.900456.

[37] S. D'Arco and J. A. Suul, "Equivalence of Virtual Synchronous Machines and Frequency-Droops for Converter-Based MicroGrids," *IEEE Trans. Smart Grid*, vol. 5, no. 1, pp. 394–395, 2014, doi: 10.1109/TSG.2013.2288000.

[38] S. Anttila, J. S. Döhler, J. G. Oliveira, and C. Boström, "Grid Forming Inverters: A Review of the State of the Art of Key Elements for Microgrid Operation," *Energies*, vol. 15, no. 15, p. 5517, 2022, doi: 10.3390/en15155517.

[39] P. Unruh, M. Nuschke, P. Strauß, and F. Welck, "Overview on Grid-Forming Inverter Control Methods," *Energies*, vol. 13, no. 10, p. 2589, 2020, doi: 10.3390/en13102589.

[40] H. -P. Beck and R. Hesse, Ed., *Virtual synchronous machine*. Barcelona, Spain, 2007, doi: 10.1109/EPQU.2007.4424220.

[41] R. Hose, A. Kuri, G. Mehlmann, R. Zurowski, D. Audring, and M. Luther, "Performance of synchronizing units under reduced system strength," in *2021 IEEE PES Innovative Smart Grid Technologies Europe (ISGT Europe)*, Espoo, Finland, Oct. 2021 - Oct. 2021, pp. 1–6, doi: 10.1109/ISGTEurope52324.2021.9640080.

[42] S. Seman, N. Tuan Trinh, R. Zurowski, and S. Kreplin, Eds., *Modeling of the Diode-Rectifier Based HVDC Transmission Solution for Large Offshore Wind Power Plants Grid Access*. International Workshop on Large-Scale Integration of Wind Power into Power Systems as well as on Transmission Networks for Offshore Wind Power Plants, Nov. 2016.

[43] S.Seman, R. Zurowski, and C. Taratoris, Eds., *Interconnection of advanced Type 4 WTGs with Diode Rectifier based HVDC solution and weak AC grids*, Oct. 2015.

[44] S. Seman, R. Zurowski, and T.Christ, "Investigation of DC Converter Nonlinear Interaction with Offshore Wind Power Park System," 2015, doi: 10.13140/RG.2.1.2179.4400.

[45] A. Tayyebi, F. Dörfler, F. Kupzog, Z. Miletic, and W. Hribernik, Eds., *Grid-Forming Converters – Inevitability, Control Strategies and Challenges in Future Grids Application*. CIRED 2018 Ljubljana Workshop on Microgrids and Local Energy Communities, 2018.

[46] G. Benmouyal, *The Impact of Synchronous Generators Excitation Supply on Protection and Relays: Schweitzer Engineering Laboratories, Inc.* (October 2007). Synchronous Generator Protection and Control: A Collection of Technical Papers Representing Modern Solutions, 2019. [Online]. Available: https://selinc.com/api/download/3490

[47] P. Kundur, *Power System Stability and Control*. McGraw-Hill Education Ltd; New edition (1 Mar. 1994).

[48] R. Li, C. Booth, A. Dysko, A. Roscoe, H. Urdal, and J. Zhu, "Protection challenges in future converter dominated power systems: Demonstration through simulation and hardware tests," *International Conference on Renewable Power Generation (RPG 2015), Beijing, 2015; IET*, pp. 1–6, Oct. 2015, doi: 10.1049/cp.2015.0392.

[49] R. Wilson, "EU connection codes GB implementation – mod 1: Final Modification Rep. GC0100," National Grid ESO, Feb. 2018. [Online]. Available: https://www.nationalgrideso.com/document/107236/download

[50] B. Fan, T. Liu, F. Zhao, H. Wu and X. Wang, "A Review of Current-Limiting Control of Grid-Forming Inverters Under Symmetrical Disturbances," *IEEE Open Journal of Power Electronics*, vol. 3, pp. 955–969, 2022, doi: 10.1109/OJPEL.2022.3227507.

[51] R. H. Lasseter, "MicroGrids," in *2002 IEEE Power Engineering Society Winter Meeting. Conference Proceedings (Cat. No.02CH37309)*, New York, NY, USA, Jan. 2002, pp. 305–308, doi: 10.1109/PESW.2002.985003.

[52] A. Hooshyar and R. Iravani, "Microgrid Protection," *Proc. IEEE*, vol. 105, no. 7, pp. 1332–1353, 2017, doi: 10.1109/JPROC.2017.2669342.

[53] Ahmed Faheem Zobaa, Ed. *Energy Storage -Technologies and Applications,*. Rijeka: IntechOpen, 2013. [Online]. Available: https://doi.org/10.5772/2550

[54] L. Zhang, L. Harnefors, and H.-P. Nee, "Power-Synchronization Control of Grid-Connected Voltage-Source Converters," *IEEE Trans. Power Syst.*, vol. 25, no. 2, pp. 809–820, 2010, doi: 10.1109/TPWRS.2009.2032231.

[55] M. G. Taul, X. Wang, P. Davari, and F. Blaabjerg, "Current Limiting Control With Enhanced Dynamics of Grid-Forming Converters During Fault Conditions," *IEEE J. Emerg. Sel. Topics Power Electron.*, vol. 8, no. 2, pp. 1062–1073, 2020, doi: 10.1109/JESTPE.2019.2931477.

[56] N. Bottrell and T. C. Green, "Comparison of Current-Limiting Strategies During Fault Ride-Through of Inverters to Prevent Latch-Up and Wind-Up," *IEEE Trans. Power Electron.*, vol. 29, no. 7, pp. 3786–3797, 2014, doi: 10.1109/TPEL.2013.2279162.

[57] Energy Development & Power Generation Committee, Electric Machinery Committee, and Power System Relaying & Control Committee of the IEEE Power and Energy Society, *2800-2022 - IEEE Standard for Interconnection and Interoperability of Inverter-Based Resources (IBRs) Interconnecting with Associated Transmission Electric Power Systems*. S.l.: IEEE, 2022. [Online]. Available: https://ieeexplore.ieee.org/servlet/opac?punumber=9762251

[58] M. Brucoli and T. C. Green and J. D. F. McDonald, "Modelling and Analysis of Fault Behaviour of Inverter Microgrids to Aid Future Fault Detection," *2007 IEEE International Conference on System of Systems Engineering, San Antonio, TX, USA, 2007*, pp. 1–6, Sep. 2007, doi: 10.1109/SYSOSE.2007.4304253.

[59] M. N. Marwali and A. Keyhani, "Control of Distributed Generation Systems— Part I: Voltages and Currents Control," *IEEE Trans. Power Electron.*, vol. 19, no. 6, pp. 1541–1550, 2004, doi: 10.1109/TPEL.2004.836685.

[60] S. Barsali, M. Ceraolo, P. Pelacchi, and D. Poli, Eds., *Control techniques of Dispersed Generators to improve the continuity of electricity supply*. IEEE, Jan. 2002, doi: 10.1109/PESW.2002.985115.

[61] M. A. Zamani, A. Yazdani, and T. S. Sidhu, "A Control Strategy for Enhanced Operation of Inverter-Based Microgrids Under Transient Disturbances and Network Faults," *IEEE Trans. Power Delivery*, vol. 27, no. 4, pp. 1737–1747, 2012, doi: 10.1109/TPWRD.2012.2205713.

[62] J. Chen, F. Prystupczuk, and T. O'Donnell, "Use of Voltage Limits for Current Limitations in Grid-forming Converters," *CSEE Journal of Power and Energy Systems*, vol. 6, no. 2, pp. 259–269, Jun. 2020, doi: 10.17775/CSEEJPES.2019.02660.

[63] H. Wu and X. Wang, "Design-Oriented Transient Stability Analysis of PLL-Synchronized Voltage-Source Converters," *IEEE Trans. Power*

Electron., vol. 35, no. 4, pp. 3573–3589, 2020, doi: 10.1109/TPEL.2019.2937942.

[64] Y. Yang, H. Miao, H. Chen, and C. Zhang, Eds., *Voltage sag ride-through control strategy with reactive power compensation for virtual synchronous generator*. IEEE, 2018, doi: 10.1109/ICIEA.2018.8397882.

[65] C. Liu, X. Cai, R. Li, and R. Yang, "Optimal short-circuit current control of the grid-forming converter during grid fault condition," *IET Renewable Power Gen*, vol. 15, no. 10, pp. 2185–2194, 2021, doi: 10.1049/rpg2.12149.

[66] P. Piya, M. Ebrahimi, M. Karimi-Ghartemani, and S. A. Khajehoddin, "Fault Ride-Through Capability of Voltage-Controlled Inverters," *IEEE Trans. Ind. Electron.*, vol. 65, no. 10, pp. 7933–7943, 2018, doi: 10.1109/TIE.2018.2803765.

[67] M. Chen, D. Zhou, A. Tayyebi, E. Prieto-Araujo, F. Dorfler, and F. Blaabjerg, "Generalized Multivariable Grid-Forming Control Design for Power Converters," *IEEE Trans. Smart Grid*, vol. 13, no. 4, pp. 2873–2885, 2022, doi: 10.1109/TSG.2022.3161608.

[68] Y. M. Li, D. M. Vilathgamuwa, and P. C. Loh, Eds., *A grid-interfacing power quality compensator for three-phase three-wire microgrid applications*. IEEE, 2004, doi: 10.1109/PESC.2004.1355426.

[69] F. Salha, F. Colas and X. Guillaud, "Virtual resistance principle for the overcurrent protection of PWM voltage source inverter," *2010 IEEE PES Innovative Smart Grid Technologies Conference Europe (ISGT Europe), Gothenburg, Sweden, 2010*, pp. 1–6, doi: 10.1109/ISGTEUROPE.2010.5638965.

[70] A. D. Paquette and D. M. Divan, "Virtual Impedance Current Limiting for Inverters in Microgrids With Synchronous Generators," *IEEE Trans. on Ind. Applicat.*, vol. 51, no. 2, pp. 1630–1638, 2015, doi: 10.1109/TIA.2014.2345877.

[71] R. Rosso, S. Engelken, and M. Liserre, "On The Implementation of an FRT Strategy for Grid-Forming Converters Under Symmetrical and Asymmetrical Grid Faults," *IEEE Trans. on Ind. Applicat.*, vol. 57, no. 5, pp. 4385–4397, 2021, doi: 10.1109/TIA.2021.3095025.

[72] J. He and Y. W. Li, "Analysis, Design, and Implementation of Virtual Impedance for Power Electronics Interfaced Distributed Generation," *IEEE Trans. on Ind. Applicat.*, vol. 47, no. 6, pp. 2525–2538, 2011, doi: 10.1109/TIA.2011.2168592.

[73] A. Gkountaras, S. Dieckerhoff and T. Sezi, "Evaluation of current limiting methods for grid forming inverters in medium voltage microgrids," *2015 IEEE Energy Conversion Congress and Exposition (ECCE), Montreal, QC, Canada, 2015*, pp. 1223–1230, doi: 10.1109/ECCE.2015.7309831.

[74] J. M. Bloemink and M. R. Iravani, "Control of a Multiple Source Microgrid With Built-in Islanding Detection and Current Limiting," *IEEE Trans. Power Delivery*, vol. 27, no. 4, pp. 2122–2132, 2012, doi: 10.1109/TPWRD.2012.2198497.

[75] L. Zhou *et al.,* "Harmonic Current and Inrush Fault Current Coordinated Suppression Method for VSG Under Non-ideal Grid Condition," *IEEE Trans. Power Electron.*, vol. 36, no. 1, pp. 1030–1042, 2021, doi: 10.1109/TPEL.2020.3000522.

[76] C. Schöll and H. Lens, "Impact of Current Limitation of Grid-forming Voltage Source Converters on Power System Stability," (IFAC-PapersOnLine), vol. 53, no. 2, pp. 13520–13524, 2020. doi: 10.1016/j.ifacol.2020.12.766. [Online]. Available: https://www.sciencedirect.com/science/article/pii/S2405896320310909

[77] E. Afshari *et al.,* "Control Strategy for Three-Phase Grid-Connected PV Inverters Enabling Current Limitation Under Unbalanced Faults," *IEEE Trans. Ind. Electron.*, vol. 64, no. 11, pp. 8908–8918, 2017, doi: 10.1109/TIE.2017.2733481.

[78] B.Kroposki, B.Johnson Y.Zhang, V.Gevorgian, P.Denholm, B-M.Hodge, B.Hannegan, "Achieving a 100% Renewable Grid: Operating Electric Power Systems with Extremely High Levels of Variable Renewable Energy," *IEEE Power and Energy Mag.*, vol. 15, no. 2, pp. 61–73, 2017, doi: 10.1109/MPE.2016.2637122.

[79] Nikos Hatziargyriou *et al.,* "Stability definitions and characterization of dynamic behavior in systems with high penetration of power electronic interfaced technologies," *IEEE Power System Dynamic Performance Committee (PSDPC) and CIGRE*, vol. IEEE PES Technical Report PES-TR77, Apr. 2020, doi: 10.17023/zwwp-vv02.

[80] J. Bialek *et al.,* "System Needs and Services for Systems with High IBR Penetration," Research Agenda Group of the Global Power System Transformation Consortium, October 8th, 2021. [Online]. Available: https://globalpst.org/wp-content/uploads/GPST-IBR-Research-Team-System-Services-and-Needs-for-High-IBR-Networks.pdf

[81] Western Power Distribution, "Loss of Mains Protection," Jun. 2018. [Online]. Available: file://C:/Users/z003kefe/Downloads/9.%20Loss%20of%20Mains%20Protection.pdf

[82] National Grid ESO, "NOA Stability Pathfinder Phase 3: Technical Performance Requirements," Nov. 2020. [Online]. Available: https://www.nationalgrideso.com/document/208351/download

[83] R. Ierna and A. Roscoe, "Effects of VSM / Option 1 (Grid Forming) Convertor Control on Penetration Limits of Non-Synchronous Generation (NSG) in the GB Power System," Nov 2016 / Jun 2017. [Online]. Available: https://www.nationalgrid.com/sites/default/files/documents/GC0100%20Annex%209%20%20VSM_0.pdf

[84] R. Ierna *et al.,* "Effects of VSM Convertor Control on Penetration Limits of Non-Synchronous Generation in the GB Power System," *2016 15th Wind Integration Workshop*, p. 8, Nov. 2016. [Online]. Available: https://www.researchgate.net/publication/316242328_Effects_of_VSM_Convertor_Control_on_Penetration_Limits_of_Non-Synchronous_Generation_in_the_GB_Power_System/citations

[85] European Network of Transmission System Operators for Electricity (ENTSO-E), "Frequency Stability In Long-Term Scenarios And Relevant Requirements: Project Inertia Team," ENTSO-E, Dec. 2021. [Online]. Available: https://eepublicdownloads.azureedge.net/clean-documents/Publications/ENTSO-E%20general%20publications/211203_Long_term_frequency_stability_scenarios_for_publication.pdf

[86] European Network of Transmission System Operators for Electricity (ENTSO-E), "Technical Report: High Penetration of Power Electronic Interfaced Power Sources and the Potential Contribution of Grid forming Converters," Jan. 2020. [Online]. Available: https://euagenda.eu/upload/publications/untitled-292051-ea.pdf

[87] European Network of Transmission System Operators for Electricity (ENTSO-E), "ENTSO-E workshops on Connection Network Code Amendments on (RoCoF and Grid Forming) & Stability Management: ENTSO Public Workshop, 23rd November 2022," [Online]. Available: https://eepublicdownloads.entsoe.eu/clean-documents/Network%20codes%20documents/SO%20ESC/2022/221123_ENTSO-E_Workshop_on_Grid_Forming_and_RoCoF.pdf

[88] VDE|FNN. 2020a, "FNN Guideline Grid forming behaviour of HVDC systems and DC-connected PPMs: Supplement to VDE-AR-N 4131 for dynamic frequency/active power behaviour and dynamic voltage

control without reactive current specification," (August 2020), *Offenbach am Main, Germany.* [Online]. Available: https://shop.vde.com/en/fnn-guideline-hvdc-systems-2

[89] European Commission (EC), "Commission Regulation (EU) 2016/1447 of August 2016 Establishing Network Code and Requirements for Grid Connection of High Voltage Direct Current Systems and Direct Current Connected Power Part Modules.," 27 April 2016; Brussels, Belgium. [Online]. Available: https://eur-lex.europa.eu/legal-content/EN/TXT/PDF/?uri=CELEX:32016R1447&from=EN

[90] S. Rogalla *et al.,* "Grid Forming Converters in Interconnected Systems - Final Results from the Joint Research Project VerbundnetzStabil: 20th International Workshop on Large-Scale Integration of Wind Power into Power Systems as well as on Transmission Networks for Offshore Wind Power Plants (WIW 2021)," *IET*, pp. 135–140, 2021. doi: 10.1049/icp.2021.2611. [Online]. Available: https://publica-rest.fraunhofer.de/server/api/core/bitstreams/b11161e1-13f7-4851-8d3c-1cf1e3b1324f/content

[91] E. Phillip *et al.,* "Verbundnetzstabil - Stabiles Verbundsystemverhalten bei umrichterbasierter Erzeugung : Schlussbericht : Forschungsprojekt "Verbundnetzstabil"," Fraunhofer ISE, Freiburg, 2022, doi: 10.2314/KXP:1832906531. [Online]. Available: https://www.tib.eu/de/suchen?tx_tibsearch_search%5Baction%5D=download&tx_tibsearch_search%5Bcontroller%5D=Download&tx_tibsearch_search%5Bdocid%5D=TIBKAT%3A1832906531&cHash=cd4acbbbc12e255c9e519a30c1c6970a#download-mark

[92] M. Kersic et al., "Testing Characteristics of Grid Forming Converters Part I: Specification and Definition of Behaviour: 19th Wind Integration Workshop Virtual Conference, 11-12 November 2020," [Online]. Available: https://www.researchgate.net/profile/Manuel-Kersic/publication/349041906_Testing_Characteristics_of_Grid_Forming_Converters_Part_I_Specification_and_Definition_of_Behaviour/links/6078390 72fb9097c0ce5dd38/Testing-Characteristics-of-Grid-Forming-Converters-Part-I-Specification-and-Definition-of-Behaviour.pdf

[93] R. Denninger, S. Reichert, S. Rogalla and K. Jalili, Ed., *Testing Characteristics of Grid Forming Converters Part II: Voltage Source Properties and Contribution to Power Quality*. 19th Wind Integration Workshop Virtual Conference, 11-12 November 2020, 2020.

[94] A. Dyśko et al., "Testing Characteristics of Grid Forming Converters Part III: Inertial Behaviour: 19th Wind Integration Workshop Virtual Conference, 11-12 November 2020," [Online]. Available: https://pure.strath.ac.uk/ws/portalfiles/portal/113644507/Dysko_etal_WIW_2020_Testing_characteristics_of_grid_forming_converters_part_III_inertial_behaviour.pdf

[95] P. Ernst, R. Singer, S. Rogalla, R. Denninger and K. Jalili, Ed., *Testing Characteristics of Grid Forming Converters Part IV: Overload Behavior and Response to Grid Faults*. 19th Wind Integration Workshop Virtual Conference, 11-12 November 2020, 2020.

[96] National Grid ESO, "Stability Pathfinder Phase 2 FAQ," National Grid ESO, Dec. 2020. [Online]. Available: https://www.nationalgrideso.com/document/178406/download

[97] ARENA, *ARENA backs eight big batteries to bolster grid: Eight of the largest batteries ever built in Australia will boost grid-forming storage capacity tenfold.*, 2022. [Online]. Available: https://arena.gov.au/blog/arena-backs-eight-big-batteries-to-bolster-grid/#:~:text=The%20150%20MW%20%2F%20194%20MWh,grid%20forming%20battery%20in%20Australia.

[98] R. Todesco, "The largest approved grid-forming battery in Australia: Batteries & Storage, Demand management, Features, Renewable Energy," *Utility Magazine*, 31 Oct., 2022. [Online]. Available: https://utilitymagazine.com.au/the-largest-approved-grid-forming-battery-in-australia/

[99] Australian Energy Market Operator (AEMO), "Application of Advanced Grid-Scale Inverters in the NEM- White paper: August 2021 An Engineering Framework report on design capabilities needed for the future National Electricity Market," Melbourne, Australia., Aug. 2021. [Online]. Available: https://aemo.com.au/-/media/files/initiatives/engineering-framework/2021/application-of-advanced-grid-scale-inverters-in-the-nem.pdf

[100] B. Badrzadeh. "Electromagnetic transient simulation models for large-scale system impact studies in power systems having a high-penetration of inverter connected generation." [Online]. Available: https://www.nerc.com/comm/PC/Documents/EMT_simulation_models_for%20large-scale_system_impacts.pdf

[101] Hawai'i Electric Light (HEL), "Model Energy Storage Power Purchase Agreement," 2019. [Online]. Available: https://hawaiianelectric.com/

clean-energy-hawaii/selling-power-to-the-utility/competitive-bidding-for-system-resourceshttps://www.hawaiianelectric.com/documents/clean_energy_hawaii/selling_power_to_the_utility/competitive_bidding/20190822_hawaii_model_energy_storage_ppa.docx

[102] North American Electric Reliability Corporation (NERC), "2022 Odessa Disturbance, Texas Event: June 4, 2022: Joint NERC and Texas RE Staff Report," North American Electric Reliability Corporation (NERC), Atlanta, GA, Dec. 2022. [Online]. Available: https://www.nerc.com/comm/RSTC_Reliability_Guidelines/NERC_2022_Odessa_Disturbance_Report%20(1).pdf

[103] D. Ramasubramanian, W. Baker, P. Mitra, S. Dutta, and A. Gaikwad, "Differentiating between Applicability of Simulation Domains and Inverter Mathematical Models in these Domains," no. 3002025063, Jun. 2022. [Online]. Available: https://www.epri.com/research/programs/067417/results/3002025063

[104] North American Electric Reliability Corporation (NERC), "Inverter-Based Resource Performance Subcommittee (IRPS)," NERC, Aug. 2022. [Online]. Available: https://www.nerc.com/comm/RSTC/Pages/IRPS.aspx

[105] North American Electric Reliability Corporation (NERC), "Inverter-Based Resource Strategy: Ensuring Reliability of the Bulk Power System with Increased Levels of BPS-Connected IBRs," Atlanta, Georgia, Jun. 2022. [Online]. Available: https://www.nerc.com/comm/Documents/NERC_IBR_Strategy.pdf

[106] R. D. Quint, "IBR Modeling Update: Review of Findings and Recommendations from NERC Disturbance Reports and Guidelines," (North American Electric Reliability Corporation (NERC)), *ESIG Webinar Series – December 2022*.

[107] A. Kuri and E. Brackenhammer, "Challenges for integration of renewable energy in public grid," *21st Wind & Solar Integration Workshop (WIW 2022), Hybrid Conference, The Hague, Netherlands, 2022*, pp. 599–606, 2022, doi: 10.1049/icp.2022.2829.

[108] S. Wiggins, *Introduction to Applied Nonlinear Dynamical Systems and Chaos* (2). New York: Springer-Verlag, 2003.

[109] M. Paolone *et al.,* "Fundamentals of Power Systems Modelling in the Presence of Converter-Interfaced Generation," *21st Power Systems*

Computation Conference, vol. 189, no. 106811, 2020, doi: 10.1016/j.epsr.2020.106811.

[110] A. Papoulis, *Signal analysis*. New York, London: McGraw-Hill, 1977.

[111] J. Machowski, J. W. Bialek, and J. R. Bumby, *Power System Dynamics* (2nd Edition). John Wiley & Sons, Ltd., 2012.

[112] J-J. E. Slotine and W. Li, *Applied nonlinear control*. New Jersey: Prentice Hall, 1991.

[113] M. N. Anthony and L. Hou, "Stability theory of discrete-time dynamical systems involving non-monotonic Lyapunov functions," (Nonlinear Studies 21.1), *Mathematics in Engineering, Science and Aerospace*, vol. 1, 2014. [Online]. Available: https://openurl.ebsco.com/EPDB%3Agcd%3A11%3A14343483/detailv2?sid=ebsco%3Aplink%3Ascholar&id=ebsco%3Agcd%3A94786595&crl=c

[114] A. Ibrahima, S. I. Bala, I. Ahmed, Md. J. Ibrahim, and F. Jaradd, "Numerical Construction of Lyapunov Functions Using Homotopy Continuation Method," *Advances in the Theory of Nonlinear Analysis and its Application*, 2022, doi: 10.31197/atnaa.1018208.

[115] B. A. La Leon de Barra and F. J. Salazar, "Discrete-time systems with monotonic step responses and complex conjugate poles and zeros," *IEEE Trans. Automat. Contr.*, vol. 47, no. 12, pp. 2098–2101, Dec. 2002, doi: 10.1109/TAC.2002.805668.

[116] S. N. Dashkovskiy, B. S. Rüffer and F. R. Wirth, "Discrete-time monotone systems: Criteria for global asymptotic stability and applications," *Proc. 17th Int. Symp. Math. Theory Netw. Syst*, pp. 89-97, 2006. [Online]. Available: https://www.fim.uni-passau.de/fileadmin/dokumente/fakultaeten/fim/lehrstuhl/wirth/Publikationen/MTNS06-monotone.pdf

[117] P. Kundur *et al.,* "Definition and Classification of Power System Stability IEEE/CIGRE Joint Task Force on Stability Terms and Definitions," *IEEE Trans. Power Syst.*, vol. 19, no. 3, pp. 1387–1401, 2004, doi: 10.1109/TPWRS.2004.825981.

[118] X. Wang and F. Blaabjerg, "Harmonic Stability in Power Electronic-Based Power Systems: Concept, Modeling, and Analysis," *IEEE Trans. Smart Grid*, vol. 10, no. 3, pp. 2858–2870, 2019, doi: 10.1109/TSG.2018.2812712.

[119] M. Amin and M. Molinas, "Small-Signal Stability Assessment of Power Electronics Based Power Systems: A Discussion of Impedance- and Eigenvalue-Based Methods," *IEEE Trans. on Ind. Applicat.*, vol. 53, no. 5, pp. 5014–5030, 2017, doi: 10.1109/TIA.2017.2712692.

[120] H. Amann, *Ordinary Differential Equations. An Introduction to Nonlinear Analysis* (Translated from the German by Gerhard Metzen) (de Gruyter Studies in Mathematics, vol. 13). de Gruyter Studies in Mathematics, vol. 13: Walter de Gruyter, Berlin, 1990.

[121] R. F. Baum, "An Existence Theorem for Optimal Control Systems with State Variable in C, and Stochastic Control Problems," *Journal Of Optimization Theory And Applications*, vol. 5, no. 5, 1970.

[122] M. Watanabe, Y. Mitani, and K. Tsuji, "A Numerical Method to Evaluate Power System Global Stability Determined by Limit Cycle," *IEEE Trans. Power Syst.*, vol. 19, no. 4, pp. 1925–1934, 2004, doi: 10.1109/TPWRS.2004.836205.

[123] K. Ogata, *Modern Control Engineering: Fifth Edition*. Upper Saddle River, NJ, USA: Prentice Hall, 2001.

[124] H-K-Khalil, *Nonlinear-Systems--,* 3rd ed. New York, NY: Prentice Hall,Inc, 2002.

[125] C. K. Alexander and M. N. O. Sadiku, *Fundamentals of Electric Circuits,* 4th ed. New York, NY: McGraw-Hill, 2009.

[126] Dr.-Ing. O. Ruhle, *Eigenvalue and Modal Analysis (NEVA)* (2016). Erlangen, Germany: Siemens.

[127] A. Kuri, R. Zurowski, G. Mehlmann, and M. Luther, "Converter Modelling Aspects at the Boundary between EMT and RMS Domain," in *2022 International Conference on Smart Energy Systems and Technologies (SEST)*, Eindhoven, Netherlands, Sep. 2022 - Sep. 2022, pp. 1–6, doi: 10.1109/SEST53650.2022.9898501.

[128] H. Freeman, *Discrete-Time Systems: An Introduction to the Theory*. John Wiley & Sons Inc, 1965.

[129] Operational Analysis and Engineering, Australian Energy Market Operator (AEMO), "POWER SYSTEM MODEL GUIDELINES," AEMO, Mar. 2018. [Online]. Available: https://aemo.com.au/-/media/files/stakeholder_consultation/consultations/electricity_consultations/2018/psm/power_system_model_guidelines_dfc.pdf?la=en&hash=F7301DE2450A0B803E8F92D348E3D519

[130] *DIN_40110-1 : Quantities used in alternating current theory; two-line circuits,* Deutsche Kommission Electrotechnik Electronik Informationstechnik im DIN und VDE, Berlin, Mar. 1994.

[131] A. Al-Bahrani, "Induction Machine Transient Model Using Complex Variables and Trapezoidal Integration," *Journal of King Saud University - Engineering Sciences*, vol. 7, no. 2, pp. 289–306, 1995. doi: 10.1016/S1018-3639(18)30631-7. [Online]. Available: https://www.sciencedirect.com/science/article/pii/S1018363918306317

[132] R. A. Adams and C. Essex, *Calculus - A Complete Course,* 7th ed. Toronto: Pearson Canada Inc., 2013.

[133] N.O. Sadiku and Charles K. Alexander & Matthew, *Fundamentals of Electric Circuits,* 4th ed. New York, NY: McGraw-Hill Science, 2013.

[134] R. R. Singh, *ELECTRICAL NETWORKS*. Tata McGraw-Hill Education, 2009.

[135] R. L. Boylestad and L. Nashelsky, *Electronic devices and circuit theory,* 11th ed. Upper Saddle River N.J.: Pearson Prentice Hall, 2013.

[136] I. SANYU Electric. "Differential Signal and Common Mode Signal in Time Domain." [Online]. Available: https://sanyu-usa.com/wp-content/uploads/2016/09/Part3_Web.pdf

[137] M. Urbano, Ed. *Introductory electrical engineering with math explained in accessible language*. Hoboken, NJ: John Wiley & Sons Inc, 2020.

[138] A. Gelb and W. E. V. Velde, *Multiple-Input Describing Functions and Nonlinear System Design.* New York: McGraw-Hill, 1968.

[139] J. Sun, "Small-Signal Methods for AC Distributed Power Systems–A Review," *IEEE Trans. Power Electron.*, vol. 24, no. 11, pp. 2545–2554, 2009, doi: 10.1109/TPEL.2009.2029859.

[140] J Shair, H Li, J. Hu, and X. Xie, "Power system stability issues, classifications and research prospects in the context of high-penetration of renewables and power electronics," *Renewable and Sustainable Energy Reviews*, vol. 145, p. 111111, 2021. doi: 10.1016/j.rser.2021.111111. [Online]. Available: https://www.sciencedirect.com/science/article/pii/S1364032121003993

[141] R. Shah, N. Mithulananthan, R.C. Bansal, and V.K. Ramachandaramurthy, "A review of key power system stability challenges for large-scale PV integration," *Renewable and Sustainable*

Energy Reviews, vol. 41, pp. 1423–1436, 2015. doi: 10.1016/j.rser.2014.09.027. [Online]. Available: https://www.sciencedirect.com/science/article/pii/S1364032114008004

[142] F.Tyan and D.S. Bernstein, "Global stabilization of systems containing a double integrator using a saturated linear controller," vol. 9, no. 15, pp. 1143–1156, Dec. 1999. [Online]. Available: https://doi.org/10.1002/(SICI)1099-1239(19991230)9:15<1143::AID-RNC455>3.0.CO;2-W

[143] J. Ackermann, *Robuste Regelung: Analyse und Entwurf von linearen Regelungssystemen mit unsicheren physikalischen Parametern: (German Edition),* 1st ed. Berlin, Heidelberg: Springer Berlin Heidelberg, 1993.

[144] National Grid ESO, "Provision of Short Circuit Level Data | February 2022: A System Operability Framework Document," Feb. 2022. [Online]. Available: https://www.nationalgrideso.com/document/238741/download #:~:text=It%20is%20defined%20as%20the,power%20injections%20(or%20absorptions).

[145] F. Blaabjerg, *Control of Power Electronic Converters and Systems: Volume 3*. Elsevier Science, 2021. [Online]. Available: https://books.google.de/books?id=5eL7DwAAQBAJ

[146] V. Staudt, C. Heising, and A. Steimel, "Short-Circuit Protection Issues in Converter Topologies for High-Voltage DC Transmission: Short-Circuit Protection for HVDC," Ruhr-Universitat Bochum and Avasition GmbH, Jul. 2012. [Online]. Available: https://www.enesys.ruhr-uni-bochum.de/mam/enesys/images/schutzkonzepte_in_dc-netzen_.pdf

[147] G. Yang and K. V. Kkuni, "Effects of Current Limit for Grid Forming Converters on Transient Stability: Analysis and Solution," (2022), *SSRN Electronic Journal*, 2022. doi: 10.2139/ssrn.4356280. [Online]. Available: https://ssrn.com/abstract=4356280

[148] Z. Zou, B. Besheli, R. Rosso, M. Liserre, and X. Wang, "Interactions Between Two Phase-Locked Loop Synchronized Grid Converters," *IEEE Trans. on Ind. Applicat.*, vol. 57, no. 4, pp. 3935–3947, 2021, doi: 10.1109/TIA.2021.3081611.

[149] S. Golestan, J. M. Guerrero, and J. C. Vasquez, "A Robust and Fast Synchronization Technique for Adverse Grid Conditions," *IEEE*

Trans. Ind. Electron., vol. 64, no. 4, pp. 3188–3194, 2017, doi: 10.1109/TIE.2016.2636206.

[150] U. Markovic, O. Stanojev, P. Aristidou, E. Vrettos, D. Callaway, and G. Hug, "Understanding Small-Signal Stability of Low-Inertia Systems," *IEEE Trans. Power Syst.*, vol. 36, no. 5, pp. 3997–4017, 2021, doi: 10.1109/TPWRS.2021.3061434.

[151] A. Johnson, "GB Grid Forming Converters / Virtual Synchronous Machines: Workgroup 2," September 2020. [Online]. Available: https://www.nationalgrideso.com/document/181626/download

[152] T. Liu, X. Wang, F. Liu, K. Xin, and Y. Liu, "A Current Limiting Method for Single-Loop Voltage-Magnitude Controlled Grid-Forming Converters During Symmetrical Faults," *IEEE Trans. Power Electron.*, vol. 37, no. 4, pp. 4751–4763, 2022, doi: 10.1109/TPEL.2021.3122744.

[153] J. Pyrhönen, S. Semken, and V. Hrabovcová, *Electrical machine drives control: An introduction*. Chichester, West Sussex, United Kingdom: John Wiley & Sons Ltd, 2016. [Online]. Available: http://search.ebscohost.com/login.aspx?direct=true&scope=site&db=nlebk&AN=1366125

[154] G. Denis, T. Prevost, M.-S. Debry, F. Xavier, X. Guillaud, and A. Menze, "The Migrate project: the challenges of operating a transmission grid with only inverter-based generation. A grid-forming control improvement with transient current-limiting control," *IET Renewable Power Generation*, vol. 12, no. 5, pp. 523–529, 2018, doi: 10.1049/iet-rpg.2017.0369.

[155] A. Hoke *et al.*, "Stabilizing Inverter-Based Transmission Systems: Power hardware-in-the-loop experiments with a megawatt-scale grid-forming inverter," *IEEE Electrific. Mag.*, vol. 10, no. 3, pp. 32–44, 2022, doi: 10.1109/MELE.2022.3187634.

[156] A. A. Memon and K. Kauhaniemi, "Real-Time Hardware-in-the-Loop Testing of IEC 61850 GOOSE-Based Logically Selective Adaptive Protection of AC Microgrid," *IEEE Access*, vol. 9, pp. 154612–154639, 2021, doi: 10.1109/ACCESS.2021.3128370.

[157] Y. Deng, H. Li, and S. Foo, "Controller Hardware-In-the-Loop simulation for design of power management strategies for fuel cell vehicle with energy storage," in *2009 IEEE Vehicle Power 07-10 September 2009*, pp. 866–870.

[158] M. Barragán-Villarejo, F. d. P. García-López, A. Marano-Marcolini, and J. M. Maza-Ortega, "Power System Hardware in the Loop (PSHIL): A Holistic Testing Approach for Smart Grid Technologies," *Energies*, vol. 13, no. 15, p. 3858, 2020, doi: 10.3390/en13153858.

[159] Speedgoat GmbH, *Accelerate Your Research Projects: RCP - Rapid Control Prototyping.* [Online]. Available: https://www.speedgoat.com/solutions/academia/research

[160] S.Rupp and M.Hiller, Eds., *Betrieb netzbildender Umrichter im Mittelspannungsnetz (DE): (Grid forming converters in medium voltage grids)*. Berlin, Offenbach: VDE, 2021.

[161] J. Yu et al., "Medium Voltage DC Distribution Systems: CIGRE Technical Brochure: WG C6/B4.37," (Reference: 875), *CIGRE Science & Engineering*, Jul. 2022.

[162] K. Strunz et al., "Benchmark Systems for Network Integration of Renewable and Distributed Energy Resources: CIGRE Task Force C6.04," *CIGRE Science & Engineering*, Apr. 2014, Art. no. 978-285-873-270-8.

[163] D. Jovcic et al., "DC-DC converters in HVDC grids and for connections to HVDC systems: CIGRE B4 Technical Brochure: 827," *CIGRE Science & Engineering*, Mar. 2021.

[164] N. Soltau, H. A. B. Siddique, and R. W. de Doncker, "Comprehensive modeling and control strategies for a three-phase dual-active bridge," in *2012 International Conference on Renewable Energy Research and Applications (ICRERA)*, Nagasaki, Japan, Nov. 2012 - Nov. 2012, pp. 1–6, doi: 10.1109/ICRERA.2012.6477408.

[165] S. P. Engel, M. Stieneker, N. Soltau, S. Rabiee, H. Stagge, and R. W. de Doncker, "Comparison of the Modular Multilevel DC Converter and the Dual-Active Bridge Converter for Power Conversion in HVDC and MVDC Grids," *IEEE Trans. Power Electron.*, vol. 30, no. 1, pp. 124–137, 2015, doi: 10.1109/TPEL.2014.2310656.

[166] M. Berger, I. Kocar, H. Fortin-Blanchette, and C. Lavertu, "Hybrid Average Modeling of Three-Phase Dual Active Bridge Converters for Stability Analysis," *IEEE Trans. Power Delivery*, vol. 33, no. 4, pp. 2020–2029, 2018, doi: 10.1109/TPWRD.2018.2817878.

[167] LG Energy Solution, *ESS Battery Division: ADVANCED BATTERIES FOR ENERGY STORAGE*, 2021. [Online]. Available: www.lgessbattery.com

[168] M. Chen and G. A. Rincon-Mora, "Accurate electrical battery model capable of predicting runtime and I-V performance," *IEEE Trans. Energy Convers.*, vol. 21, no. 2, pp. 504–511, 2006, doi: 10.1109/TEC.2006.874229.

[169] V. H. Nguyen *et al., Eds. European Guide to Power System Testing: The ERIGrid Holistic Approach for Evaluating Complex Smart Grid Configurations* (T. Strasser, E. de Jong, and M. Sosnina, Eds). Switzerland: Springer, 2020. [Online]. Available: https://link.springer.com/chapter/10.1007/978-3-030-42274-5_4#citeas

[170] R. Musca, A. Vasile, and G. Zizzo, "Grid-forming converters. A critical review of pilot projects and demonstrators," *Renewable and Sustainable Energy Reviews*, vol. 165, no. 16, p. 112551, 2022, doi: 10.1016/j.rser.2022.112551.

[171] North American Electric Reliability Corporation (NERC), "Integrating Inverter-Based Resources into Low Short Circuit Strength Systems: Reliability Guideline," NERC, Dec. 2017. [Online]. Available: https://www.nerc.com/comm/RSTC_Reliability_Guidelines/Item_4a._Integrating%20_Inverter-Based_Resources_into_Low_Short_Circuit_Strength_Systems_-_2017-11-08-FINAL.pdf

[172] Australian Energy Market Operator (AEMO), "System strength: System strength in the NEM explained," AEMO, Mar. 2020. [Online]. Available: https://aemo.com.au/-/media/files/electricity/nem/system-strength-explained.pdf

[173] S. Haykin and B. van Veen, *Signals and Systems,* 2nd ed. John Wiley & Sons Inc, 2003.

[174] R. W. Kenyon, A. Sajadi, A. Hoke and B. -M. Hodge, Ed., *Open-Source PSCAD Grid-Following and Grid-Forming Inverters and A Benchmark for Zero-Inertia Power System Simulations*. 2021 IEEE Kansas Power and Energy Conference (KPEC), 2021, doi: 10.1109/KPEC51835.2021.9446243.

[175] Manitoba Hydro International Ltd, "PSCAD TM- IEEE 9 Bus System," May. 2018. [Online]. Available: https://www.pscad.com/knowledge-base/article/25

[176] Siemens Energy. "Key technical parameters of SVC PLUS FS®." [Online]. Available: https://www.siemens-energy.com/global/en/offerings/power-transmission/portfolio/flexible-ac-transmission-systems/svcplus-frequency-stabilizer.html

Appendix

A1. System strength and Short Circuit Ratio

System strength (NERC 2017): '*System strength refers to the sensitivity of the terminal voltage of the inverter-based resource to variations of current injections*' [171].

System strength (AEMO 2020): '*System strength as the ability of the power system to maintain and control the voltage waveform at any given location in the power system, both during steady-state operation and following a disturbance'* [172] .

Short Circuit Ratio (SCR): From control theory perspective SCR is understood as impedance ratio between nominal converter and grid equivalent. It is represented by (A 1.1.)

$$\mathrm{SCR} = \frac{Z_{\mathrm{CON\ nominal}}}{Z_{\mathrm{THV}}} \qquad \text{(A 1.1)}$$

where,

$Z_{\mathrm{CON\ nominal}}$ is the nominal converter impedance,

Z_{THV} is the equivalent of the grid.

A2. Dynamics of continuous system's interaction with discrete system

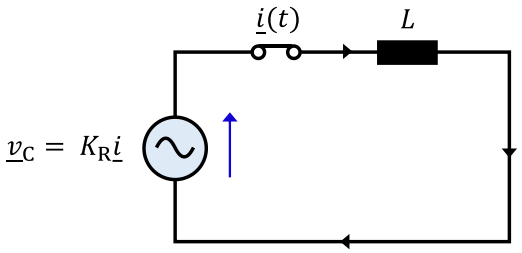

Figure A 1: Simple first order circuit in space vector representation.

Solving the system with hold of the input current and hence output voltage is calculated as follows. Considering initial conditions for $\underline{i}_0 = \underline{i}_t = 0$, where $\underline{i}_0$ is an arbitrary voltage input value and is determined by load flow calculation in case of discreet simulation. The general voltage solution of the network in time-domain is given by the following:

$$\underline{i}(t) = \frac{\underline{v}_C}{L} t - C \qquad \text{(A 2.1)}$$

where 'C' is a constant and is determined by initial conditions.
Now, we apply first interval $t = 0\ to\ T_S$,considering Figure A 1 as reference, the following (A 2.2) and (A 2.3) are derived for intervals $t = 0$ and $t = T_S$ respectively.

$$t = 0 \qquad \underline{i}(t) = \underline{i}_{01} = -C \qquad \text{(A 2.2)}$$

$$t = T_S \qquad \underline{i}(T_S) = \underline{i}_{01} \left(1 - \frac{K_R T_S}{L}\right)^1 \qquad \text{(A 2.3)}$$

Similarly, for the second interval $T_S \leq t \leq 2T_S$, considering Figure 2.15 as reference the following equation is obtained:

$$t = 2T_S \qquad \underline{i}(T_S) = \underline{i}_{01} \left(1 - \frac{K_R T_S}{L}\right)^2 \qquad \text{(A 2.4)}$$

From (A 2.3 and (A 2.4) the generalized equation is written as (A 2.5), where $\underline{i}_0$ is the initial value of current from load flow and T_S is the sampling time period and n is the number of samples.

$$\underline{i}(nT_S) = \underline{i}_0 \left(1 - \frac{K_R T_S}{L}\right)^n \qquad \text{(A 2.5)}$$

Equation (A 2.5) is the final solution and equivalent to Equation (2.38) described in Chapter 2, Section 2.5.2.

A3. Space vector representation of voltage

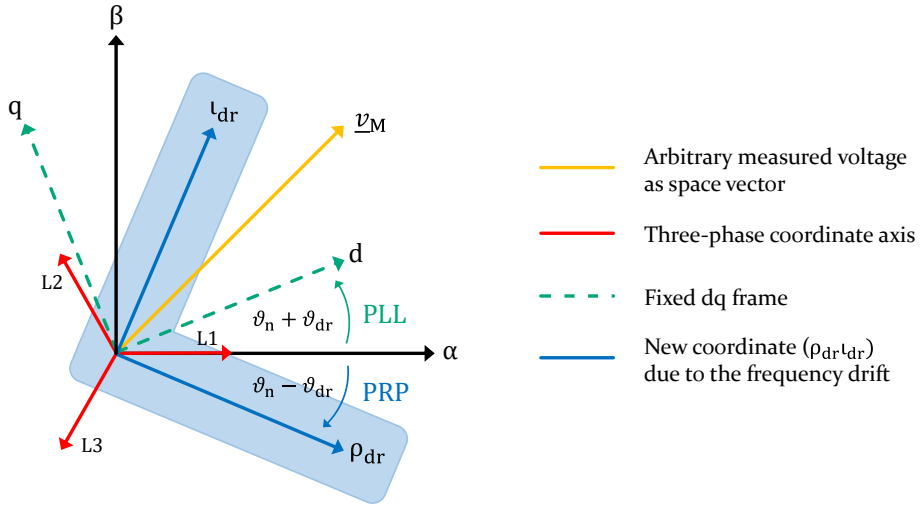

Figure A 2: Various coordinate systems in space vector theory.

There are several options of a coordinate system to represent an arbitrary space vector $\underline{v}_M$ as depicted in Figure A 2. Since dq designates a rotating coordinate system, the coordinates of space vector $\underline{v}_M$ are constant values at steady-state. Whereas in αβ coordinate system at rest, the coordinates of space vector $\underline{v}_M$ are given by trigonometric functions.

Now, to recover three phase quantities from αβ coordinate system the projections onto $L1$, $L2$ and $L3$ coordinate axis have to be performed (right-handed).

A coordinate transformation is bijective – Two real signals ≡ one complex signal as described below:

$$v_\alpha = {(2v_{1M} - v_{2M} - v_{3M})}/{3} \qquad \text{(A 3.1)}$$

$$v_\beta = {(v_{2M} - v_{3M})}/{\sqrt{3}} \qquad \text{(A 3.2)}$$

For control purpose, $\underline{v}_M = v_\alpha + \mathrm{j} \cdot v_\beta$ is transformed into $\rho_{dr}\iota_{dr}$ coordinate system for PRP The space vector components are transformed as:

$$\begin{bmatrix} v_\rho \\ v_\iota \end{bmatrix} = \begin{bmatrix} cos\,(\vartheta_n - \vartheta_{dr}) & sin\,(\vartheta_n - \vartheta_{dr}) \\ -sin\,(\vartheta_n - \vartheta_{dr}) & cos\,(\vartheta_n - \vartheta_{dr}) \end{bmatrix} \begin{bmatrix} v_\alpha \\ v_\beta \end{bmatrix} \qquad \text{(A 3.3)}$$

A4. Nomenclature for voltage

In RMS simulation domain, the per-unit values are based on RMS values and in EMT simulation domain they are based on EMT base value (peak).

In EMT domain for a mono-frequent positive sequence signal, the based quantity matches the corresponding based RMS domain quantity.

$\hat{V}_{\mathrm{LG}} = \frac{\sqrt{2}\cdot V_{\mathrm{n}}}{\sqrt{3}} \triangleq 1$ pu, is the EMT base value,

$V_{\mathrm{LG}} = \frac{V_{\mathrm{n}}}{\sqrt{3}} \triangleq 1$ pu,is the RMS base value,

where, $V_{\mathrm{n}} = 0.69$ kV (line-line or Root Mean Square value).

For example, a positive sequence signal at fundamental frequency, space vector with magnitude of nominal value ($\hat{V}_{\mathrm{LG}}$) is represented by:

$$\underline{v} = \hat{V}_{\mathrm{LG}} \cdot e^{\mathrm{j}(2\cdot\pi\cdot f_{\mathrm{n}}\cdot t+\theta)} = \hat{V}_{\mathrm{LG}} \cdot e^{\mathrm{j}\theta} \cdot e^{\mathrm{j}(2\cdot\pi\cdot f_{\mathrm{n}}\cdot t)} = \underline{\hat{V}} \cdot e^{\mathrm{j}(2\cdot\pi\cdot f_{\mathrm{n}}\cdot t)} \qquad \text{(A 4.1)}$$

In cartesian coordinate system the space vector is given by:

$$\underline{v} = v_{\alpha} + \mathrm{j} \cdot v_{\beta} \qquad \text{(A 4.2)}$$

In the EMT domain plots, the based voltage magnitude are given by $\frac{|\underline{v}|}{\hat{V}_{\mathrm{LG}}}$.

While, in RMS domain simulation plots the based voltage magnitude are displayed as $\frac{V}{\left(\frac{V_{\mathrm{n}}}{\sqrt{3}}\right)}$, considering line-to-ground voltage ($V_{\mathrm{LG}} = \frac{V_{\mathrm{n}}}{\sqrt{3}}$).

A5. Solution of stable operating point

The voltage at the measurement node is given by:

$$\underline{V}_{\mathrm{M}} = \underline{V}_{\mathrm{C}} - \mathrm{j}X_{\mathrm{C}}\underline{I}_{\mathrm{C}} \tag{A 5.1}$$

As $\underline{V}_{\mathrm{M}}$ is a real quantity, since $\mathrm{Im}\{\underline{V}_{\mathrm{M}}\} = 0$. Hence, the following is considered. $\underline{V}_{\mathrm{M}} = \left|\underline{V}_{\mathrm{M}}\right|\mathrm{e}^{\mathrm{j}0}$. On solving (A 5.1) for φ in terms of $\underline{V}_{\mathrm{M}}$, and substituting the value for $\underline{I}_{\mathrm{C}}$, (A 5.2) to obtained with $\underline{V}_{\mathrm{C}} = 1\mathrm{e}^{\mathrm{j}\varphi}$. Equation (A 5.3) describes the denominator value in (A 5.2) as described below:

$$\underline{V}_{\mathrm{M}} = \mathrm{e}^{\mathrm{j}\varphi} - \mathrm{j}X_{\mathrm{C}}\left(\frac{-R + \underline{V}_{\mathrm{C}}R + \mathrm{j}X_{\mathrm{C}}\underline{V}_{\mathrm{C}}}{X_{\mathrm{N}}(X_{\mathrm{T}} + X_{\mathrm{C}}) - \mathrm{j}R(X_{\mathrm{N}} + X_{\mathrm{C}} + X_{\mathrm{T}})}\right) \tag{A 5.2}$$

$$D = X_{\mathrm{N}}(X_{\mathrm{T}} + X_{\mathrm{C}}) - \mathrm{j}R(X_{\mathrm{N}} + X_{\mathrm{C}} + X_{\mathrm{T}}) \tag{A 5.3}$$

On further simplification the final solution is given by:

$$\underline{V}_{\mathrm{M}} = \mathrm{e}^{\mathrm{j}\varphi}\underbrace{\left(1 - \frac{1}{D}(\mathrm{j}RX_{\mathrm{C}} - X_{\mathrm{C}}X_{\mathrm{N}})\right)}_{c1} + \underbrace{\frac{\mathrm{j}RX_{\mathrm{C}}}{D}}_{c2} \tag{A 5.4}$$

The equation (A 5.4) is general solution. Equation (A 5.4) is utilized to plot the network solutions and is a circle. Here, $c1$ and $c2$ are network impedances. Equation (3.6) is obtained by imposing the condition $\mathrm{Im}\{\underline{V}_{\mathrm{M}}\} = 0$ to (A 5.4) in the Appendix.

The complete solution of (3.6) in terms of the network impedances is given in (A 5.5).

$$\varphi = -\sin^{-1}\left(\frac{\left(RX_{C}{}^{2}X_{\mathrm{N}} + RX_{\mathrm{C}}X_{\mathrm{N}}X_{\mathrm{T}}\right)}{\sqrt{\left((X_{\mathrm{N}}X_{\mathrm{T}})^{2} + \left(X_{\mathrm{N}}{}^{2}X_{\mathrm{C}}X_{\mathrm{T}}\right) + (RX_{\mathrm{N}})^{2} + (RX_{\mathrm{T}})^{2} + (R^{2}X_{\mathrm{C}}X_{\mathrm{N}}) + (2R^{2}X_{\mathrm{N}}X_{\mathrm{T}}) + (R^{2}X_{\mathrm{C}}X_{\mathrm{T}})\right)^{2} + (RX_{\mathrm{C}}X_{\mathrm{N}})^{2}}}\right) - \tan^{-1}\left(\frac{\left(-RX_{\mathrm{C}}X_{\mathrm{N}}{}^{2}\right)}{\left((X_{\mathrm{N}}X_{\mathrm{T}})^{2} + \left(X_{\mathrm{N}}{}^{2}X_{\mathrm{C}}X_{\mathrm{T}}\right) + (RX_{\mathrm{N}})^{2} + (RX_{\mathrm{T}})^{2} + (R^{2}X_{\mathrm{C}}X_{\mathrm{N}}) + (2R^{2}X_{\mathrm{N}}X_{\mathrm{T}}) + (R^{2}X_{\mathrm{C}}X_{\mathrm{T}})\right)}\right) \tag{A 5.5}$$

A6. Frequency shifting property of Laplace transform

In systems theory, expressions based on the Laplace s-domain in complex frequency domain are represented by the following:.

$$s = \mathrm{j}\omega \tag{A 6.1}$$

where, jω is the angular frequency on the imaginary axis.

In the context of dq-transformation, a signal corresponds to a multiplication by $\mathrm{e}^{-\mathrm{j}\omega t}$. i.e., $x(t) \cdot \mathrm{e}^{-\mathrm{j}\omega t}$, in time domain.

The application of frequency shifting property defined in (A 6.2) results in (A 6.3), where LT stands for Laplace transform. [173]

$$\mathrm{e}^{-at} \cdot x(t) \overset{LT}{\leftrightarrow} X(s + a) \tag{A 6.2}$$

$$x(t) \cdot \mathrm{e}^{-\mathrm{j}\omega t} \overset{LT}{\leftrightarrow} X(s + \mathrm{j}\omega) \tag{A 6.3}$$

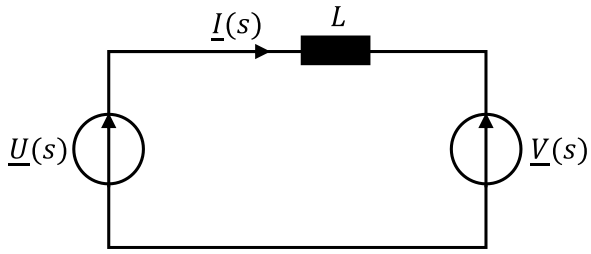

Figure A 3: Circuit diagram.

Space vector equation (A 6.4) is an example for the application of frequency shifting property. It is applied to the circuit in Figure A 3, using the passive sign convention with English voltage source orientation (conventional flow) [111, 133]. The circuit is equivalent to Figure 3.5. Here $\underline{v}(t)$ and $\underline{u}(t)$ are voltages in αβ domain.

$$\underline{v}(t) = \underline{u}(t) - L\frac{\mathrm{d}}{\mathrm{d}t}\underline{i}(t) \overset{LT}{\leftrightarrow} V(s) = U(s) - sLI(s) \tag{A 6.4}$$

Evaluating (A 6.4) at steady-state conditions with $s = \mathrm{j}\omega$, the following equation is attained:

$$\begin{bmatrix} V_\alpha(\mathrm{j}\omega) \\ V_\beta(\mathrm{j}\omega) \end{bmatrix} = \begin{bmatrix} 0 & \omega L \\ -\omega L & 0 \end{bmatrix} \begin{bmatrix} I_\alpha(\mathrm{j}\omega) \\ I_\beta(\mathrm{j}\omega) \end{bmatrix} + \begin{bmatrix} U_\alpha(\mathrm{j}\omega) \\ U_\beta(\mathrm{j}\omega) \end{bmatrix} \tag{A 6.5}$$

Applying transformation from αβ to dq domain to equation (A 6.4), (A 6.6) is obtained. Simplifying (A 6.6), (A 6.7) and finally obtains (A 6.8) with $\underline{V}$, $\underline{U}$ and $\underline{I}$ in time domain as follows:

$$\underline{v}(t) = \underline{u}(t) - L\frac{\mathrm{d}}{\mathrm{dt}}\underline{I}(\mathrm{t})\mathrm{e}^{\mathrm{j}\omega t} \tag{A 6.6}$$

$$\underline{V}(t)e^{\mathrm{j}\omega t} = \underline{U}(\mathrm{t})\mathrm{e}^{\mathrm{j}\omega t} - \mathrm{j}\omega L\underline{I}(t)\mathrm{e}^{\mathrm{j}\omega t} - L\mathrm{e}^{\mathrm{j}\omega t}\frac{\mathrm{d}}{\mathrm{dt}}\underline{I}(t) \tag{A 6.7}$$

$$\underline{V}(t) = \underline{U}(t) - \mathrm{j}\omega L\underline{I}(t) - L\frac{\mathrm{d}}{\mathrm{dt}}\underline{I}(t) \tag{A 6.8}$$

Now, applying LT to (A 6.8, the expression below is obtained:

$$\underline{V}(s) = \underline{U}(s) - \mathrm{j}\omega L\underline{I}(s) - s\underline{I}(s)L \tag{A 6.9}$$

Decomposing (A 6.9) into d and q componenet, and evaluating at steady-state with $s = \mathrm{j}\omega$, the following is obtained:

$$\begin{bmatrix} V_{\mathrm{d}}(\mathrm{j}\omega) \\ V_{\mathrm{q}}(\mathrm{j}\omega) \end{bmatrix} = \begin{bmatrix} -sL & \omega L \\ -\omega L & -sL \end{bmatrix}\begin{bmatrix} I_{\mathrm{d}}(\mathrm{j}\omega) \\ I_{\mathrm{q}}(\mathrm{j}\omega) \end{bmatrix} + \begin{bmatrix} U_{\mathrm{d}}(\mathrm{j}\omega) \\ U_{\mathrm{q}}(\mathrm{j}\omega) \end{bmatrix} \tag{A 6.10}$$

Now, applying frequency shifting property in (A 6.3) to LT part of (A 6.4), and considering the space vector definition $\underline{x} = x(t) \cdot \mathrm{e}^{\mathrm{j}\omega t}$, equation below is obtained:

$$\underline{V}(s - \mathrm{j}\omega) = \underline{U}(s - \mathrm{j}\omega) - sL\underline{I}(s - \mathrm{j}\omega) \tag{A 6.11}$$

Now setting $s' = s - \mathrm{j}\omega$ in (A 6.11), (A 6.12) results. On decomposing (A 6.12) into d and q componenet, (A 6.13) and (A 6.14) is gained as below:

$$\underline{V}(s') = \underline{U}(s') - (s' + \mathrm{j}\omega)L\underline{I}(s') \tag{A 6.12}$$

$$\big(V_d + \mathrm{j}V_q\big)(s') = \big(U_d + \mathrm{j}U_q\big)(s') - (s' + \mathrm{j}\omega)L\big(I_d + \mathrm{j}I_q\big)(s') \tag{A 6.13}$$

$$\begin{bmatrix} V_{\mathrm{d}}(s') \\ V_{\mathrm{q}}(s') \end{bmatrix} = \begin{bmatrix} -s'L & \omega L \\ -\omega L & -s'L \end{bmatrix}\begin{bmatrix} I_{\mathrm{d}}(s') \\ I_{\mathrm{q}}(s') \end{bmatrix} + \begin{bmatrix} U_{\mathrm{d}}(s') \\ U_{\mathrm{q}}(s') \end{bmatrix} \tag{A 6.14}$$

Evaluating at steady.-state condition s = jω, hence $s' = 0$, the following is obtained:

$$\begin{bmatrix} V_{\mathrm{d}}(0) \\ V_{\mathrm{q}}(0) \end{bmatrix} = \begin{bmatrix} 0 & \omega L \\ -\omega L & 0 \end{bmatrix}\begin{bmatrix} I_{\mathrm{d}}(0) \\ I_{\mathrm{q}}(0) \end{bmatrix} + \begin{bmatrix} U_{\mathrm{d}}(0) \\ U_{\mathrm{q}}(0) \end{bmatrix} \tag{A 6.15}$$

Equations (*A 6.5*) and (A 6.15) display steady-state with the same dependencies as regards to AC or DC quantities, respectively. However, they are not equivalent.

Here, s' is the steady-state condition in dq domain and is zero value. For uniformity, it is referred to as s in dq domain in this work.

A7. Phase and frequency interpretation

Voltage space vector in dq domain and corresponding phase are described below:

$$\underline{v}(t) = \hat{\underline{V}} \cdot \mathrm{e}^{(\mathrm{j}2\pi F_\mathrm{n} t))} = \sqrt{2} \cdot \underline{V} \cdot \mathrm{e}^{(\mathrm{j}2\pi F_\mathrm{n} t))} \quad \text{(A 7.1)}$$

$$\arg\left(\underline{V}(t)\right) = \operatorname{atan}\left(\frac{\mathrm{Im}\{\underline{V}(t)\}}{\mathrm{Re}\{\underline{V}(t)\}}\right) \quad \text{(A 7.2)}$$

where, on sampling

$$\mathbf{arg}\left(\underline{\boldsymbol{V}}(\boldsymbol{k} \cdot \boldsymbol{T_\mathrm{s}})\right),\ \boldsymbol{k} = \mathbf{1} \ldots \boldsymbol{n}\ \ (\mathbf{set\ of\ natural\ numbers})$$

$$\Delta \arg = \arg\left(\underline{V}(k \cdot T_\mathrm{s})\right) - \arg\left(\underline{V}((k-1) \cdot T_\mathrm{s})\right) \quad \text{(A 7.3)}$$

$$\Delta F = f(\Delta \arg) \quad \text{(A 7.4)}$$

$$\Delta F = F - F_\mathrm{n} \quad \text{(A 7.5)}$$

where, F is frequency, F_n is the nominal values and ΔF is the difference in frequency as given in (A 7.4)and (A 7.5).

Argument or arg has the full mathematical information (A 7.3) and frequency is extracted from the filter (e.g., a discrete 1st order filter system). Equation (A 7.1) is the RMS representation of voltage space vector consistent with simulation results and the phase or argument displayed (A 7.2) is the phase of $\underline{V}$.

A8. Scenario description of self-stabilizing droop and current limitation control

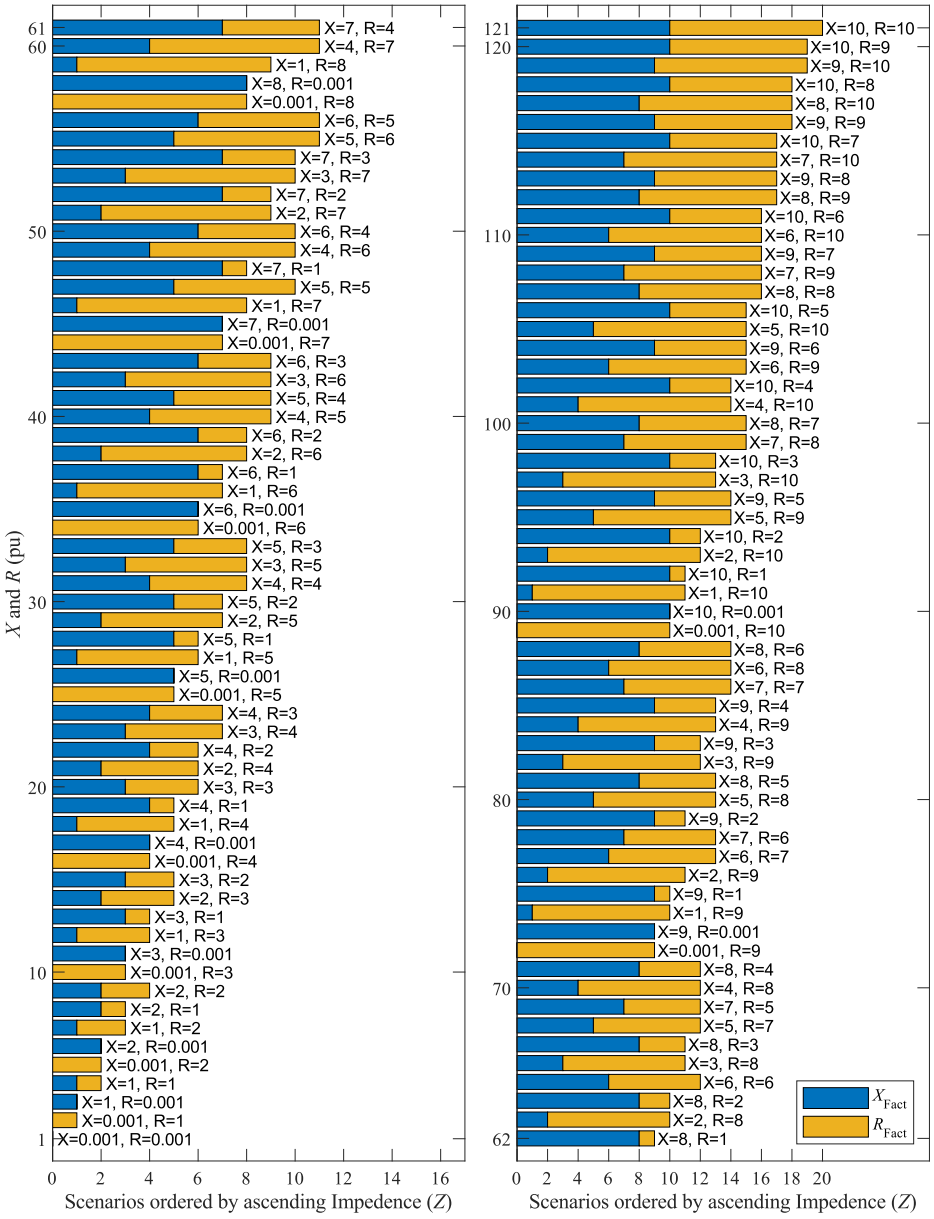

Figure A 4: Scenarios ordered in ascending Z value with its explicit R_{Fact} and X_{Fact}.

A9. Responses of self-stabilizing droop (K_2)

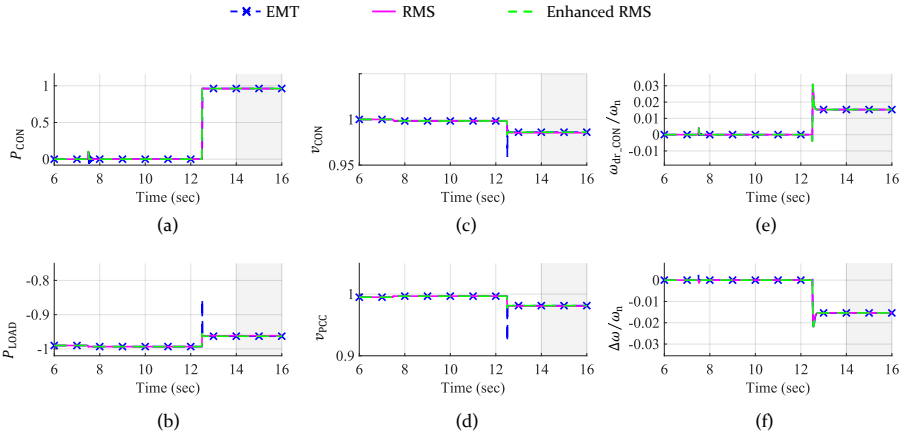

Figure A 5: Case 2: (a) Active power flow with no reference change; (b) Load active power flow; (c) and (d) Voltage magnitude; (e) Frequency drift in converter control; (f) Frequency deviation in network.

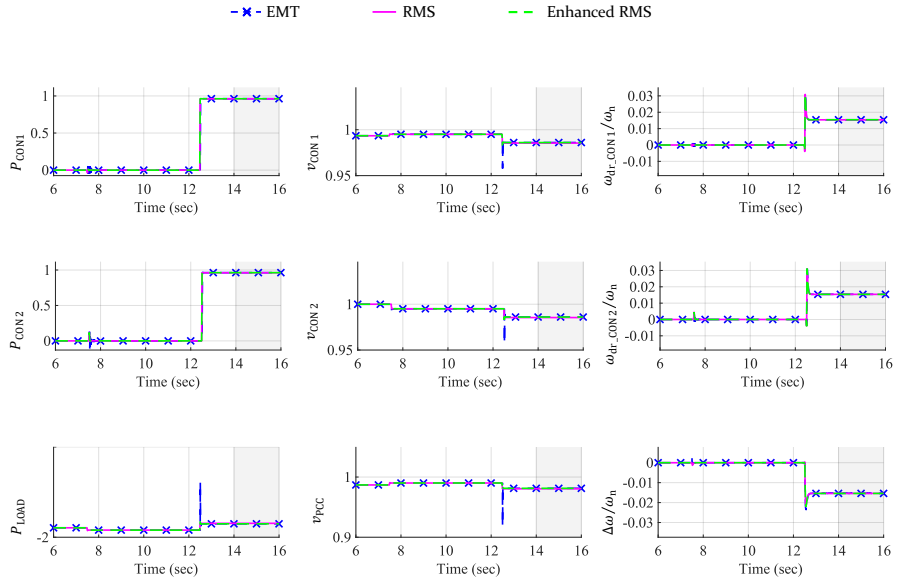

Figure A 6: Case 3: (a) and (b) CON1 and CON2 active power flow no reference change; (c) Load active power flow; (d), (e) and (f) Voltage magnitude; (g) and (h) Frequency drift in converter control; (i) Frequency deviation in network.

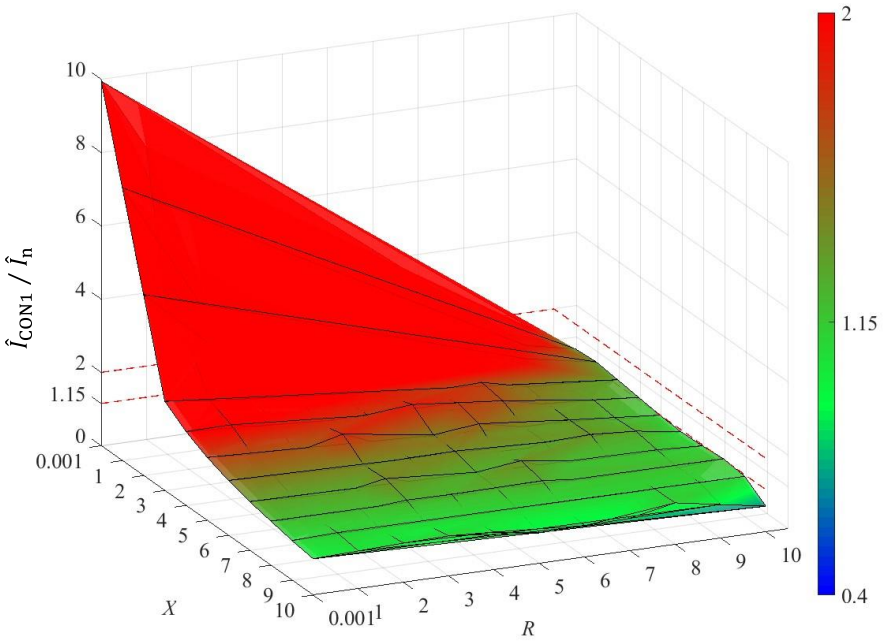

Figure A 7: Maximum $\hat{I}$ of CON1 for each 121 cases without current limitations.

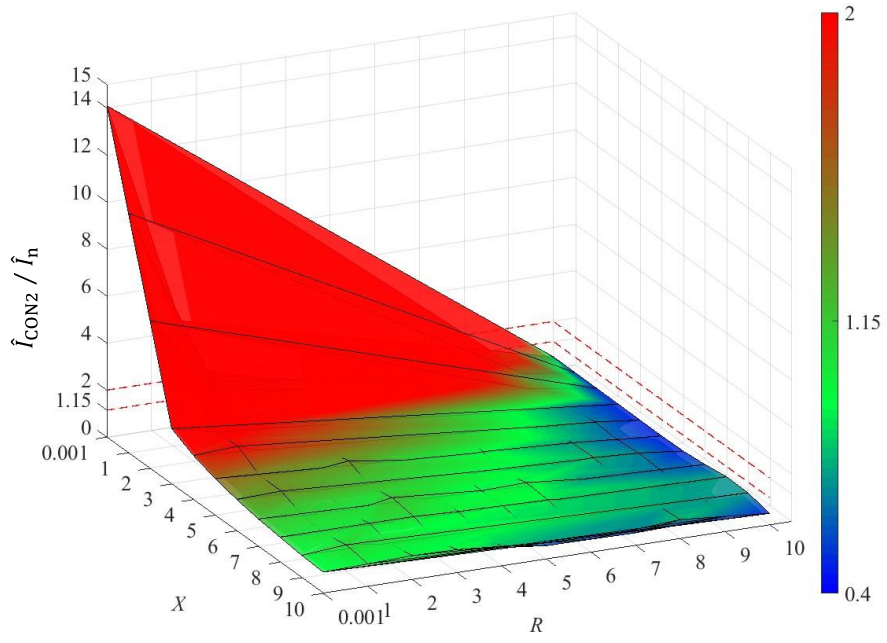

Figure A 8: Maximum $\hat{I}$ of CON2 for each 121 cases without current limitations.

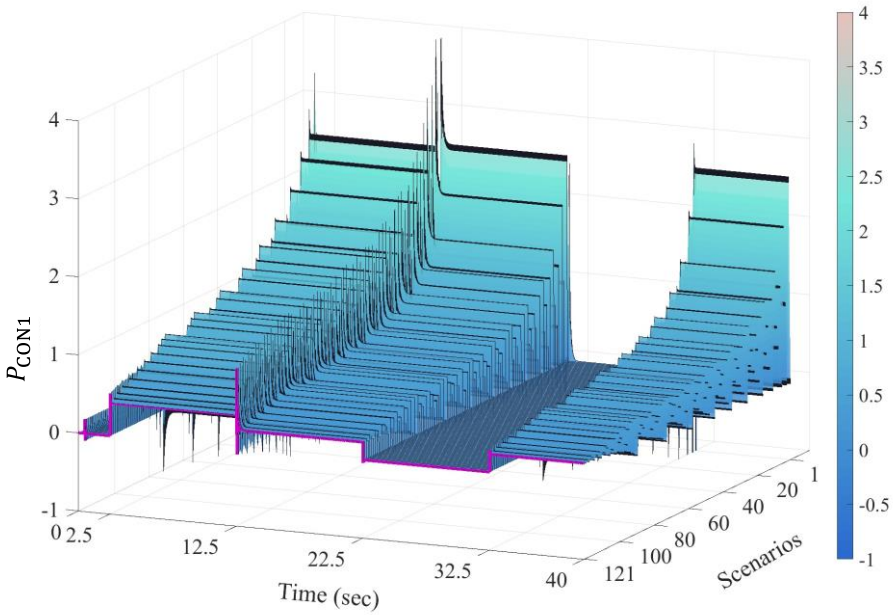

Figure A 9: CON1 active power flows for 121 shunt impedance variation with no reference change.

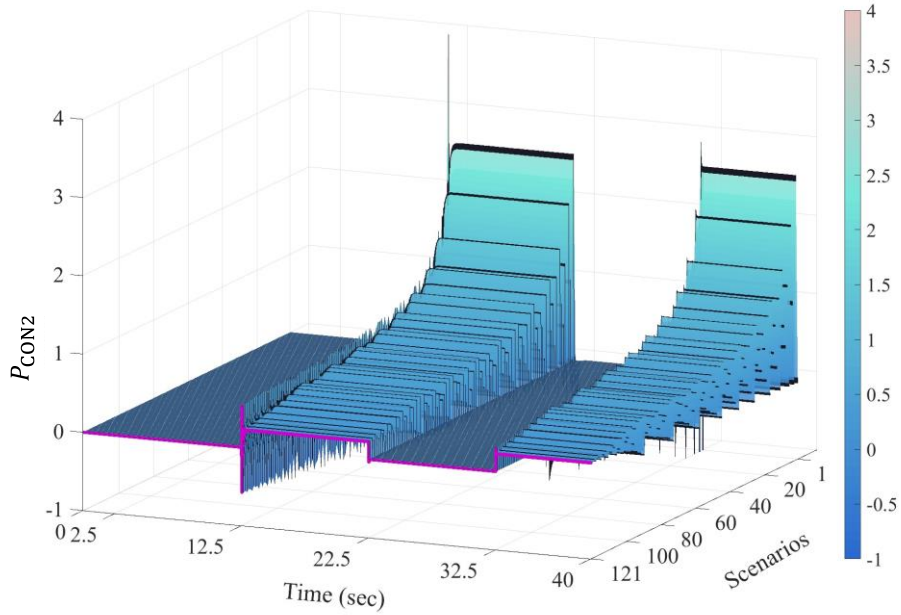

Figure A 10: CON2 active power flows for 121 shunt impedance variation with no reference change.

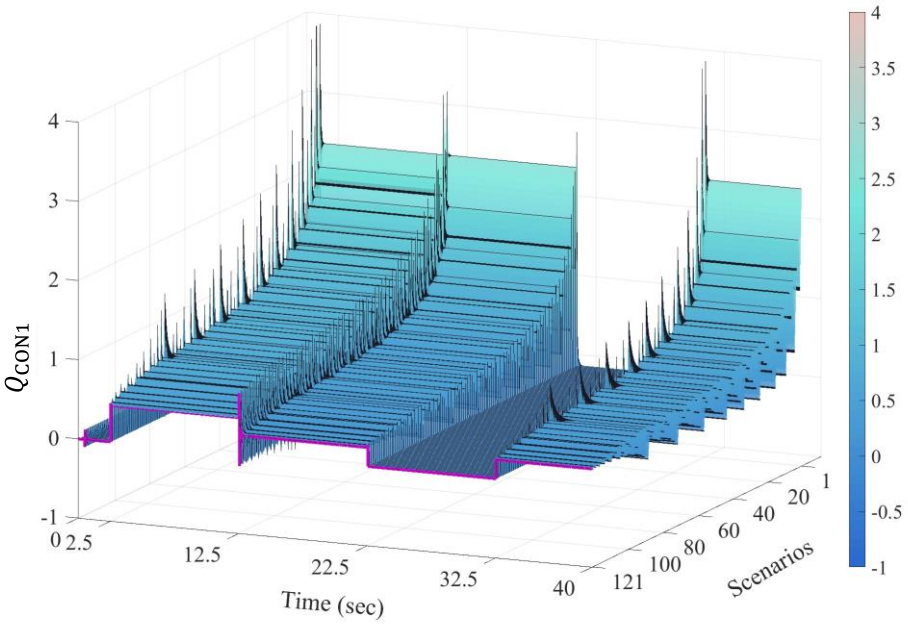

Figure A 11: CON1 reactive power flows responses for 121 cases of shunt impedance variation with no reference change.

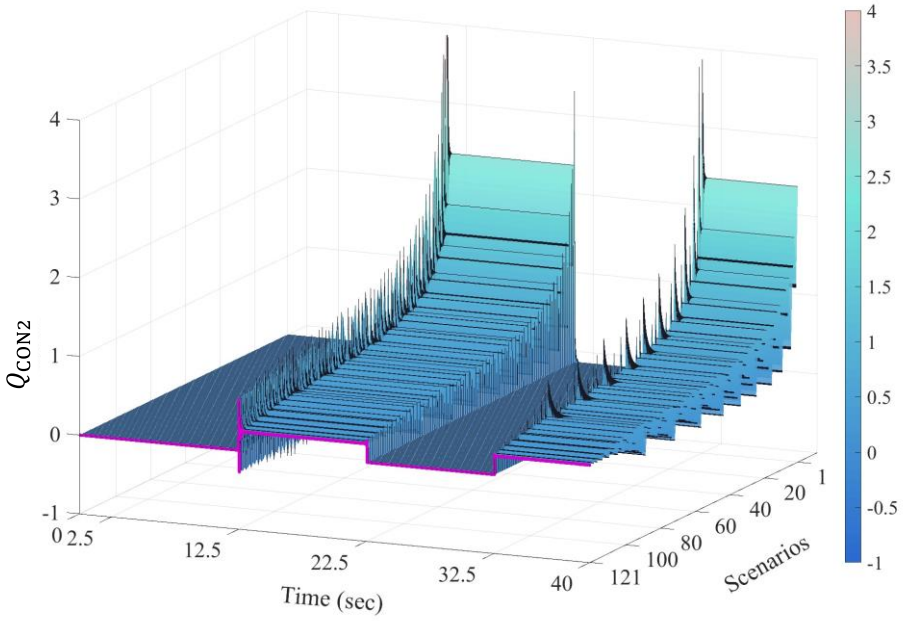

Figure A 12: CON2 reactive power flows responses for 121 cases of shunt impedance variation with no reference change.

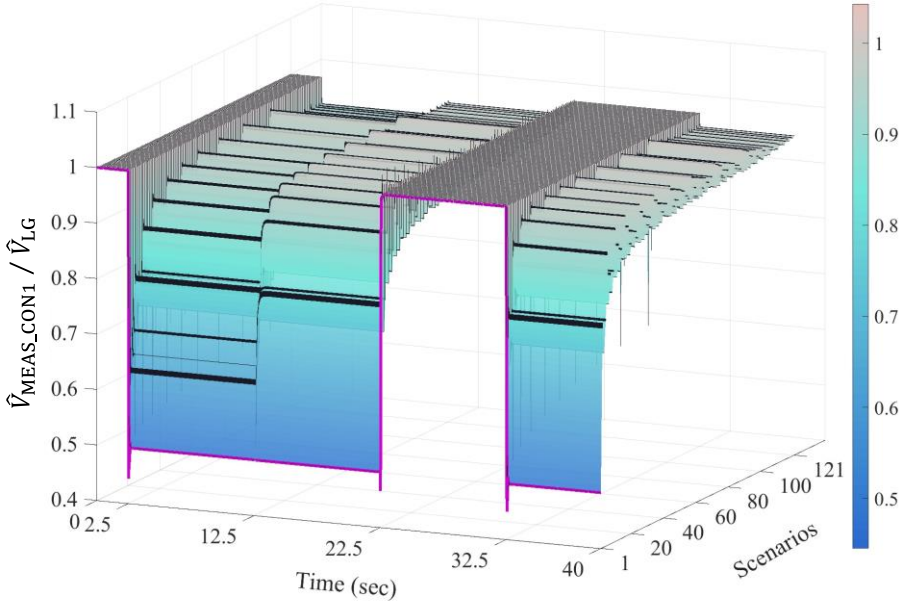

Figure A 13: CON1 voltage space vector magnitude ($\hat{V}$) at MEAS1 node for 121 shunt impedance variation.

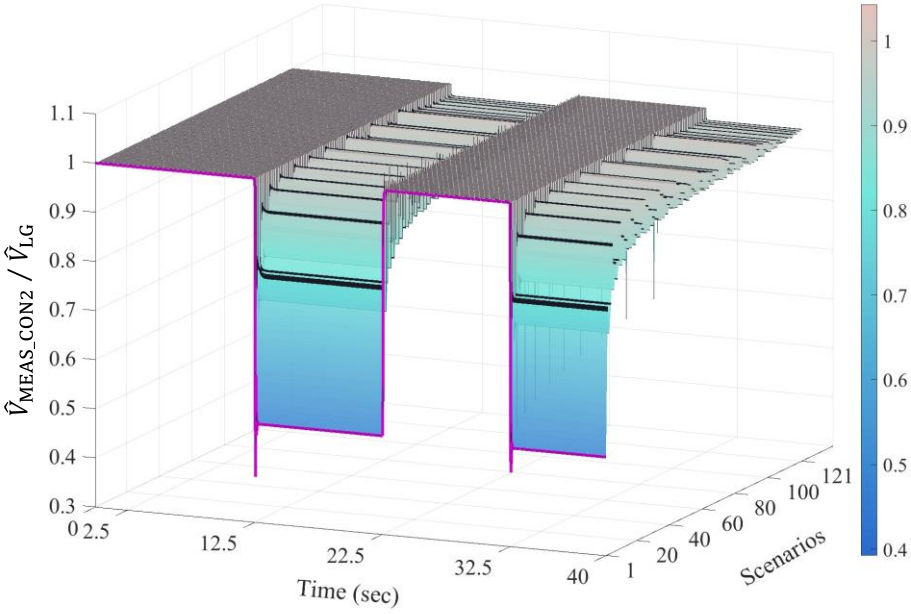

Figure A 14: CON2 voltage space vector magnitude ($\hat{V}$) at MEAS2 node for 121 shunt impedance variation.

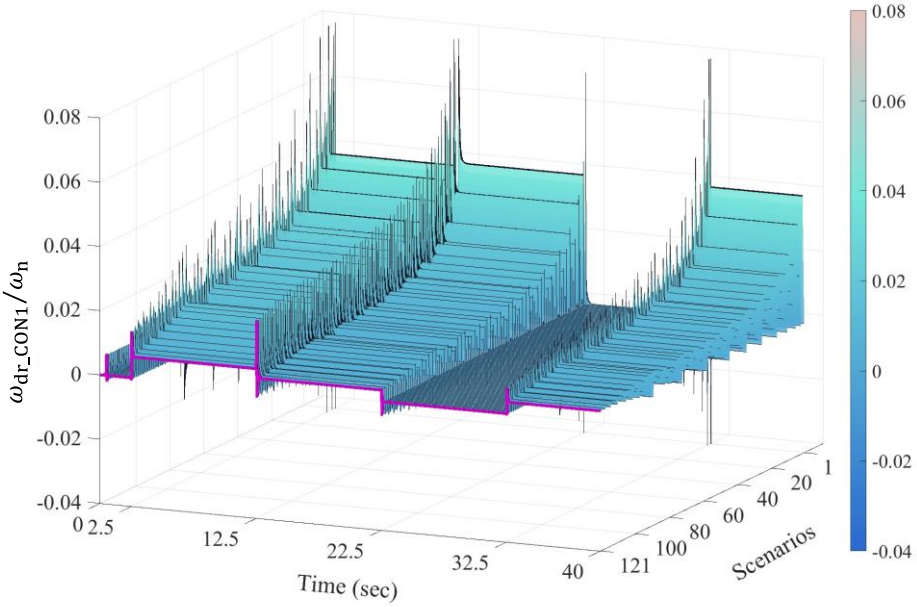

Figure A 15: Frequency drift in converter control CON1 (ω_{dr}) for 121 shunt impedance variation.

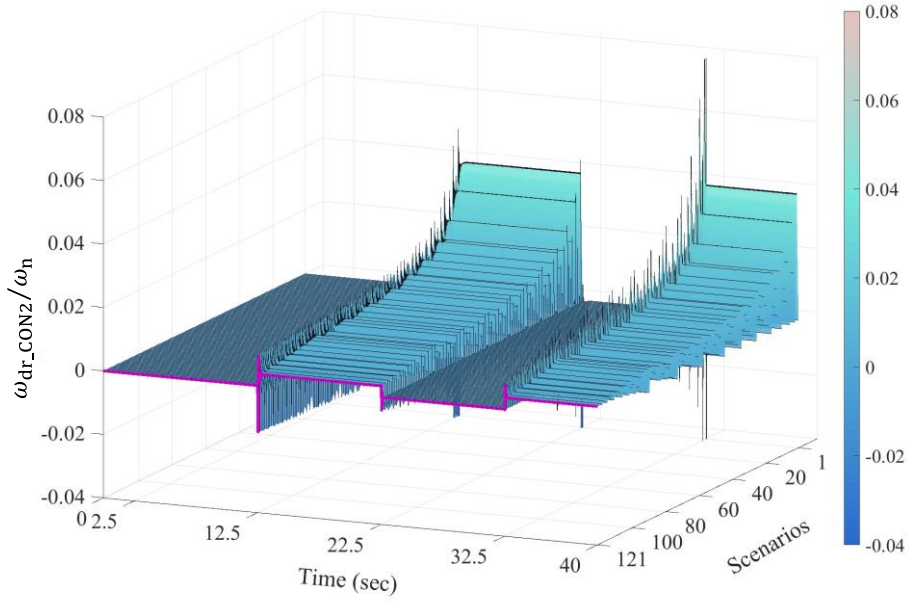

Figure A 16: Frequency drift in converter control CON2 (ω_{dr}) for 121 shunt impedance variation.

A10. Response of current limiting control

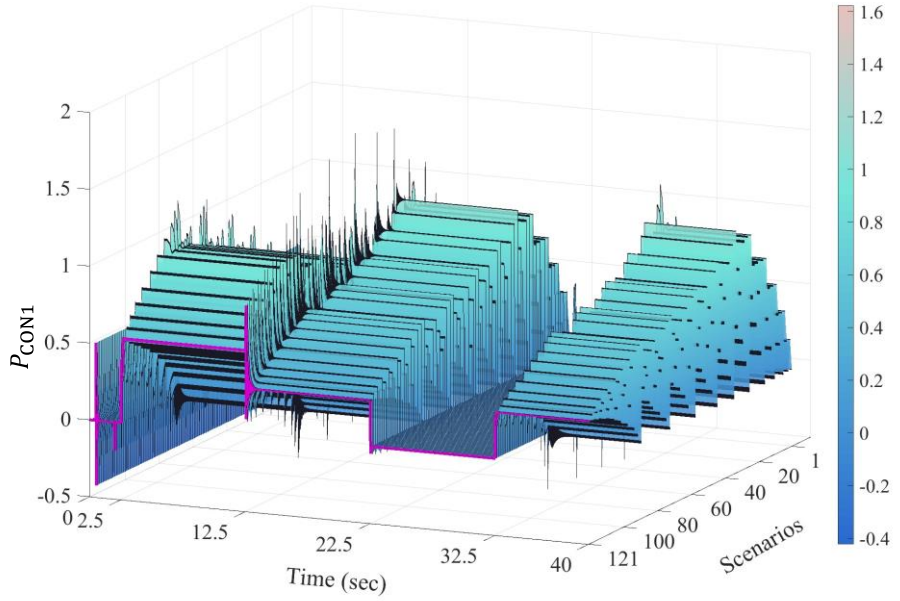

Figure A 17: CON1 active power flows responses with current limiter for various shunt impedance values (121 cases) and no reference change.

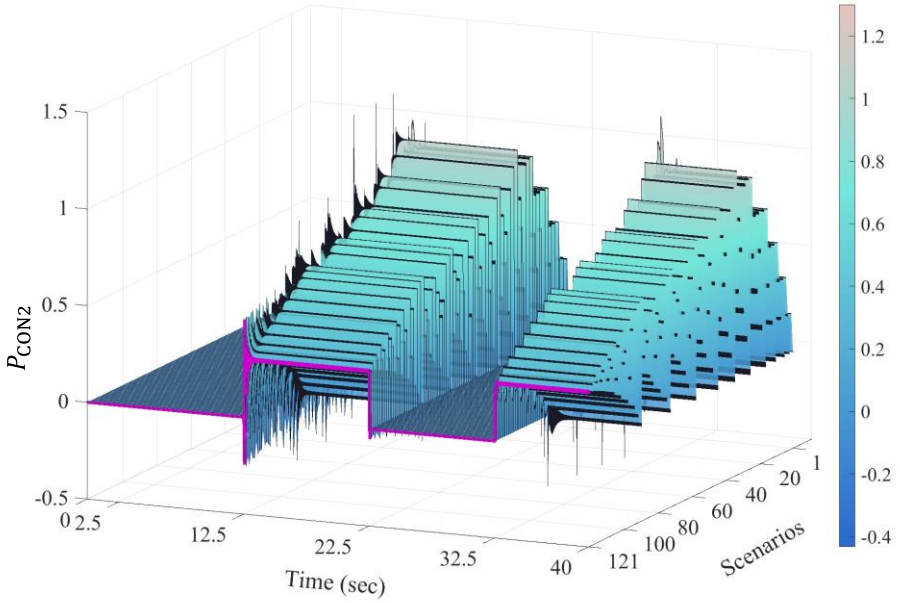

Figure A 18: CON2 active power flows responses with current limiter for various shunt impedance values (121 cases) and no reference change.

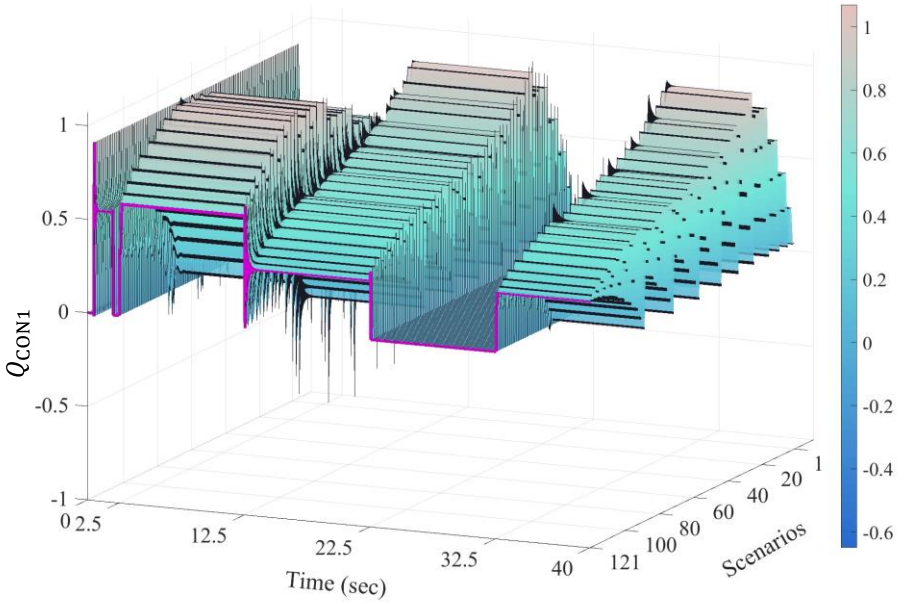

Figure A 19: CON1 reactive power flows responses with current limiter for various shunt impedance values (121 cases) and no reference change.

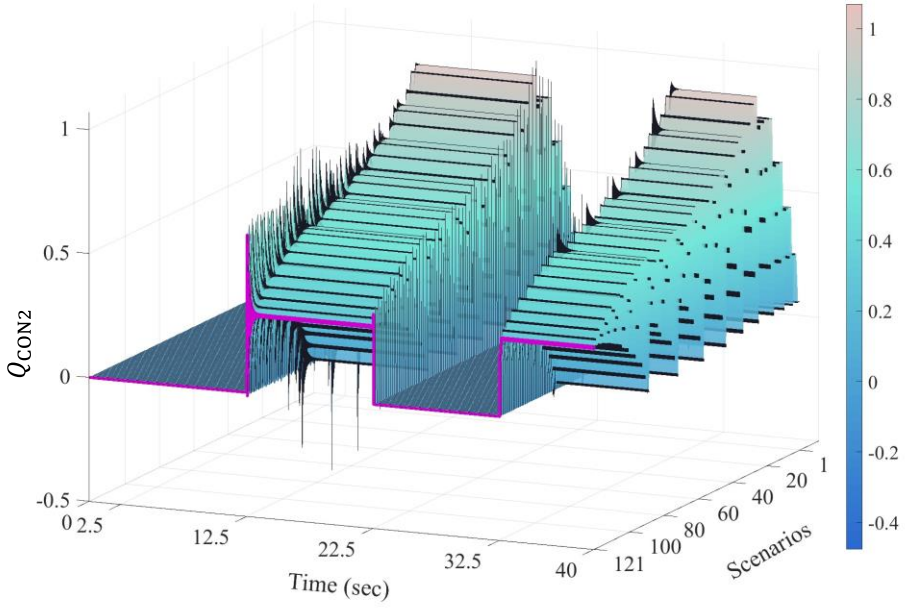

Figure A 20: CON2 reactive power flows responses with current limiter for various shunt impedance values (121 cases) and no reference change.

A11. Test bench and scenario description: IEEE 9 Bus System

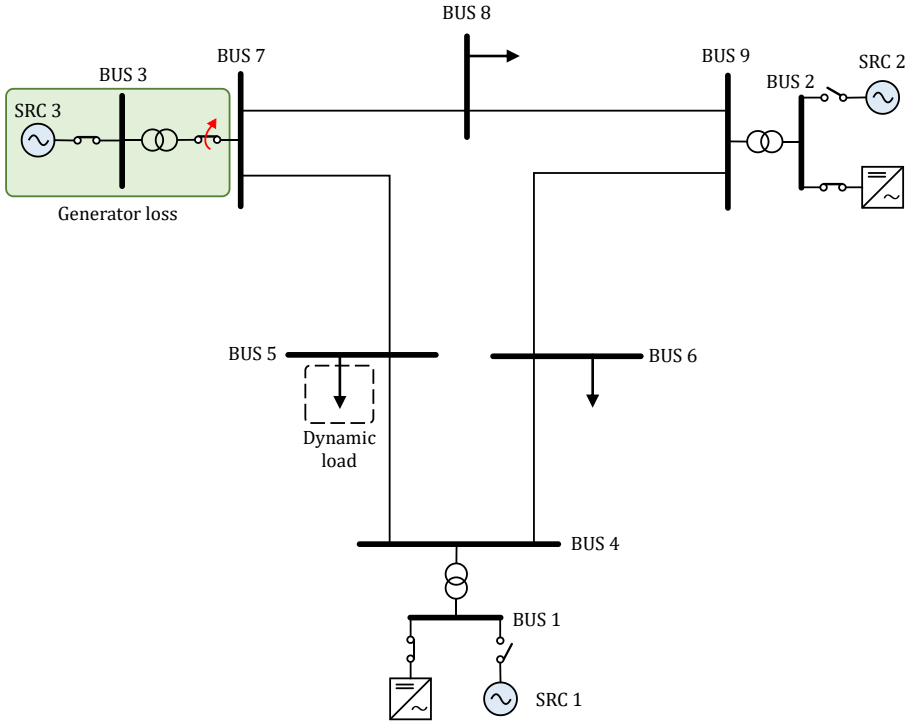

Figure A 21: IEEE 9-Bus System with disturbances marked in figure.

The IEEE 9-Bus system is the considered test bench for comparing the different GFM schemes as it commonly used for assessing the dynamic behavior of new elements and concepts in power system operations. The network parameters are selected according to [174, 175]. Each source (SRC) has sufficient capacity to provide additional active and reactive power support. Figure A 21 displays the IEEE 9-Bus System with the necessary modifications to the original case comprising of only machines. The following three test cases are considered:

- Case 1: SRC 1 and 2 are replaced with Droop-based GFM.
- Case 2: SRC 1 and 2 are replaced with VSM GFM.
- Case 3: SRC 1 and 2 replaced with PRP GFM.

Table A 1 presents each source's active and reactive power flow values on a 100 MVA system base. A minor power dispatch deviation in the GFM

schemes is noticeable compared to the base case due to differences in Q(V) control in each control scheme caused by the converter controls' simplicity. The network comprises of three loads modelled as constant power, except at Bus 5, modelled as a dynamic load (frequency dependent with impedance characteristic). The event occurs at 0.6 sec and is simulated in each test case subjected to one loss of generation disturbance scenario. The scenario is a significant disturbance that involves the disconnection of Bus 7, causing dynamic loss of a generation unit – SRC 3 modelled as a synchronous machine. This scenario also represents dynamic islanding, demonstrating each control scheme stabilizing and forming capabilities when the grid is fully converter-operated. Additionally, due to loads being frequency dependent, the self-regulating effect is visible in the plot Figure 5.4. Section 5.2 analyses and compares the response to the event for each scheme. Further details are available in [32].

Table A 1: Initial operating point of the sources in the test cases.

Case		**Bus 1**	**Bus 2**	**Bus 3**
Base	p (pu)	1.481	1.518	0.187
	q (pu)	0.189	0.087	-0.113
Droop	p (pu)	1.481	1.518	0.173
	q (pu)	0.131	0.063	0.060
VSM	p (pu)	1.481	1.518	0.157
	q (pu)	0.174	0.025	0.078
PRP	p (pu)	1.481	1.518	0.513
	q (pu)	0.199	0.084	-0.149

Droop, VSM, and PRP control are compared in the above test bench with respective parameters in Table A 2, Table A 3 and Table A 4.

Table A 2: Droop control parameters.

Parameters	**Unit**	**Values**
k_{p}	pu	0.05
k_{q}	pu	0.20
T_{f}	sec	0.05

Table A 3: VSM control parameters.

Parameters	**Unit**	**Values**
T_{a}	sec	10.0
k_{q}	pu	0.10
k_{f}	pu	1.00
T_{f}	sec	1.00
k_{d}	pu	25.00

Table A 4: PRP control parameters.

Parameters	**Unit**	**Values**
K_1	pu	1.00
T_1	sec	$\frac{1}{50 \times 2\pi}$
T_2	sec	0.01

A12. Load flow solution of a single source

Based on the network described in Figure 5.1, the load flow solution is described as follows:

$$P + \mathrm{j}Q = \frac{\left|\underline{V}\right|^2}{R - \mathrm{j}X} \tag{A 12.1}$$

$$P = \frac{R \cdot \left|\underline{V}\right|^2}{R^2 + X^2} \tag{A 12.2}$$

$$Q = \frac{X \cdot \left|\underline{V}\right|^2}{R^2 + X^2} \tag{A 12.3}$$

The active power equates to (A 12.2), while the reactive power is (A 12.3).

The solution (A 12.2) or (A 12.3) has no dependency on phase.

Therefore, a GFM scheme should not incorporate control of absolute phase but reflect frequency dependency on X as ($X = \omega L$).

A13. Application of Phase Restoring Principle as super-capacitors

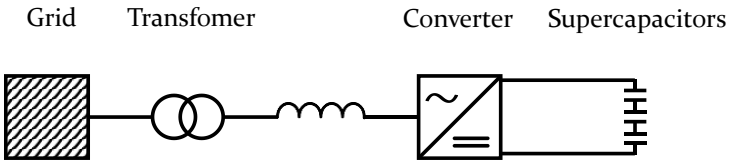

Figure A 22: Capacitor solution as SVC PLUS Frequency Stabilizer®, a Siemens Energy Solution (adapted from Siemens Energy AG [176]).

A14. Laboratory set up of the MVDC-HVDC test system

Figure A 23:
(a) Real time simulators: RTDS NovaCor 1.0 (©2024 RTDS Technologies Inc. AMETEK);
(b) System setup as PHiL in microgrid ENGiNe laboratory with simulation running on RSCAD®FX of RTDS and the CHiL linear amplifiers (SPS);
(c) Three-phase fan-heater of up to 7 kW rating used as switchable loads;
(d) MMC converter with integrated Li-ion batteries.

Table A 5: Parameters of HVDC-MVDC Converter (640 kV/110 kV) [163].

Parameters	Unit	Value
S_{DCDC}	MW	200
$U_{\mathrm{DC,HV}}$	kV	640
$U_{\mathrm{DC,MV}}$	kV	110
f_{AC}	Hz	150
$U_{\mathrm{AC,HV}}$	kV	377
$U_{\mathrm{AC,MV}}$	kV	56
$U_{\mathrm{SM,HV}}$	kV	2.0
$n_{\mathrm{SM,HV}}$	-	330
$n_{\mathrm{SM,MV}}$	-	51

Table A 6: Parameters of battery integrated via DC/DC converter (110 kV/1 kV) [165, 167].

Parameters	Unit	Value
$S_{\mathrm{DCDC,tot}}$	MW	55
P_{DAB3}	kW	250
$U_{\mathrm{pri,DC}}$	kV	110
$U_{\mathrm{sec,DC}}$	kV	1
f_{sw}	kHz	1
$n_{\mathrm{SM,seriesperstack}}$	-	22
$n_{\mathrm{SM,parallelperstack}}$	-	22

*__Note__: sw- switching frequency, SM-sub modules

Abbreviations & Symbols

Abbreviations

3Ph-DAB	Three-Phase Dual-Active Bridge (3Ph-DAB)
AC	Alternate Current
AEMO	Australian Energy Market Operator
APC	Active Power Control
BPS	Bulk Power System
CHiL	Control-Hardware-in-the-Loop
CL	Current Limiter Logic in Phase Restoring Principle
COPS	Converter Operated Power System
DAB	Dual-Active Bridge
DC	Direct Current
DG	Distributed Generation
DI	Discrete integrator
EMT	Electromagnetic Transient
ENTSO-E	European Network of Transmission System Operators
FFR	Fast Frequency Response
FLL	Frequency-Locked Loop
GFL	Grid-Following
GFM	Grid-Forming
GW	Gigawatts
HECO	Hawaiian Electric Company
HiL	Hardware-in-the-Loop

HMI	Human-Machine Interface
HVDC	High Voltage Direct Current
IBR	Inverter-Based Resource
LT	Laplace Transform
Li-ion	Lithium-ion battery
MEAS	Measurement node for PRP
MPPT	Maximum Power Point Tracking
MV	Medium Voltage
MVDC	Medium Voltage Direct-Current
MVA	Mega voltampere
Mvar	Mega voltampere
MW	Mega watt
NEM	Australian National Electricity Market
NGA	New Grid Access
NGESO	National Grid Electricity System Operator
OEM	Original Equipment Manufacturer
PCC	Point of Common Coupling
PD-I	Proportional–derivative-integral controller
PDT	Phasor Domain Transients
PE	Power Electronic
PF	Power Factor
PHiL	Power-Hardware-in-the-loop
PD	Proportional-derivative controller
PI	Proportional-Integral controller

PID	Proportional–integral–derivative controller
PLL	Phase-Locked Loop
PRP	Phase Restoring Principle
pu	per-unit
PWM	Pulse Width Modulation
RMS	Root Mean Square
RoCoF	Rate of Change of Frequency
RTS	Real-time simulator
S&H	Sample and Hold
SCR	Short Circuit Ratio
SLK	Slack or grid equivalent
SM	Synchronous Machine
SO	System Operator
SSA	State-Space-Averaging (SSA)
SSCI	Sub-Synchronous Controller Interaction
STATCOM	Static Synchronous Compensator
TSO	Transmission System Operator
VS	Vector Shift
VSC	Voltage Source Converter
VSM	Virtual Synchronous Machine
WG	Working Group

General Symbols

$\|x\|$	Absolute value
$\cong$	Approximately equal to
$\underline{z} = Re\{\underline{z}\} + Im\{\underline{z}\} = \|\underline{z}\|e^{\mathrm{j}arg\{\underline{z}\}}$	Arbitrary complex number
$arg\{z\} = \tan^{-1}\left(\frac{Im\{z\}}{Re\{z\}}\right)$	Argument of the complex function
$X(s)$	Frequency domain value
$Im\{z\}$	Imaginary part of complex number
j	Imaginary unit
s	Laplace operator
$\approx$	Linear approximate
X	Magnitude (real value)
$\hat{X}$	Peak value
x	Per-unit value
π	Pi
$\underline{X}$	Phasor in complex domain
$Re\{z\}$	Real part of complex number
$\mathbb{Z}$	Set of integers
Δ	Small deviation

$\underline{x}(t)$ or $\underline{x}$	Space vector
$f: A \rightarrow B$	Surjection
$x(t)$	Time domain value

Subscripts

CON	Converter source related
C	Coupling impedance node
DC	DC-link related
d	d-component
Fact	Impedance factor
LL	Line-to-line
LG	Line-to-ground
m	Measurement data
meas	Measurement node related
n	Nominal value
pcc	PCC related
MEAS	PRP measurement node related
N	Network impedance node
peak	Peak values

T	Transformer impedance node
THV	Thévenin-equivalent voltage or grid equivalent
q	q-component
0	Quantity at the operating point or initial conditions
ref	Reference value
1	Related to Converter 1
2	Related to Converter 2
SLACK	Slack source related

Special symbols

ϕ_0	Absolute load flow phase
P_m	Active power
αβ	Alpha-beta coordinate frame.
φ	Arbitrary converter phase
θ	Arbitrary measurement phase
S	Complex power
C	Constant
$\underline{I_C}$	Converter current
V_CON or $U(s)$	Converter source voltage
X_C	Coupling impedance
$I = \left\lvert \underline{i} \right\rvert$	Current magnitude
I_Ref	Current reference

i^*	Current setpoint of an ideal current source
I_d	Current's direct component
I_q	Current's quadrature component
$det(A)$	Determinant of a matrix A
$\delta(\mathrm{j}\omega)$	Dirac distribution
dq	dq coordinate frame.
$\Delta\omega$	Frequency deviation
X_GEN	Generator impedance inclusive of transformer impedance
i_h	homogeneous solution
$\underline{Z} = R + \mathrm{j}X$	Impedance load in complex domain
$Z = \sqrt{R^2 + X^2}$	Impedance load magnitude
L	Inductance
φ_0	Initial phase of the converter output voltage
$V_0 = \hat{V}_\mathrm{LG}$	Initial magnitude of the converter output voltage in pu
P^*	Inner active power setpoint generated in control
ω^*	Inner frequency setpoint generated in control
Q^*	Inner reactive power setpoint generated in control
V^*	Inner voltage amplitude setpoint generated in control
H	Machine inertia constant
xd''	Machine sub-transient impedance
$P_\mathrm{1m} \equiv P_1$	Measured power of converter 1
$P_\mathrm{2m} \equiv P_2$	Measured power of converter 2
X_N	Network impedance

φ	Network phase
ω_{n}	Nominal
$\hat{I}_{\mathrm{n}}$	Nominal continuous peak current
$\hat{V}_{\mathrm{n}}$	Nominal continuous peak voltage
F_{n}	Nominal frequency in Hertz
f_{n} or ω_{n}	Nominal frequency in pu
V_{n}	Nominal voltage
$\rho_{\mathrm{dr}}\iota_{\mathrm{dr}}$	Novel coordinate system
i_{p}	Particular solution
$\hat{V}_{\mathrm{LG}}$	Peak line-to-ground voltage
F_{p}	Perturbation frequency in Hz
θ	Phase angle
$\Delta\varphi$	Phase difference or phase change
$\phi(t)$	Phase of the voltage
$(\vartheta_{\mathrm{n}} - \vartheta_{\mathrm{dr}})$	Phase Restoring angle
$\underline{V}$	Phasor part of voltage
$\hat{I}$	Peak current (magnitude)
$\hat{V}$	Peak voltage (magnitude)
$c' = \frac{1}{c}$	Power frequency droop or weighted gain
P_{m}	PRP Control active power measurement
P_{ref}	PRP Control active power reference
P_{ref1}	PRP Control active power reference 1
P_{ref2}	PRP Control active power reference 2
F_{dr}	PRP internal control drift frequency in Hertz

$f_{\mathrm{dr}}\ or\ \omega_{\mathrm{dr}}$	PRP internal control drift frequency in pu
$\frac{X_{\mathrm{L}}}{R_{\mathrm{L}}} = \frac{\omega_{\mathrm{n}} L}{R_{\mathrm{L}}}$	Q factor
$^{q}/_{q}$	q/q controller transfer
S_{n}	Rating of the converter.
X_{Fact}	Reactance factor
e'	Reference voltage of PWM
R_{Fact}	Resistance factor
R	Resistive load
I_{RMS}	RMS current
$V_{\mathrm{RMS}} = \frac{V_{\mathrm{LL}}}{\sqrt{3}} \triangleq \frac{V_{\mathrm{n}}}{\sqrt{3}}$	RMS voltage
sec	Seconds
Ts	Simulation time step
Sk''	Short circuit power
$\underline{I_N}$	Slack or grid equivalent current
$\underline{v}$	Space vector representation of voltage
$\phi_1 = \frac{\mathrm{d}\phi}{\mathrm{dt}}$	Steady-state frequency
f or ω	System frequency
$\underline{v}_{\mathrm{t}}$	Terminal voltage
V_{t}	Terminal voltage magnitude
θ_t	Terminal voltage phase angle
t	Time
$\underline{V_{\mathrm{C}}}$	Three-phase converter voltages in phasor
$\underline{V_{\mathrm{M}}}$	Three-phase measurement voltages in phasor

X_{T}	Transformer impedance
V_{MEAS} or $V(s)$	Voltage at the measurement node
E	Voltage magnitude
V_{PCC}	Voltage PCC in pu
$\underline{V} = V^{\mathrm{j}\vartheta}$	Voltage phasor
v_{Ref}	Voltage reference
v^*	Voltage setpoint of an ideal voltage source
V_{d}	Voltage's direct component
V_{q}	Voltage's quadrature component

Scientific Activities

The list of all scientific publications and academic activities at the institute are listed below.

Publications in journals and technical brochure

J1. A. Kuri, R. Zurowski, G. Mehlmann, D. Audring and M. Luther, "A Novel Grid Forming Control Scheme Revealing a True Inertia Principle," in IEEE Transactions on Power Systems, vol. 36, no. 6, pp. 5369-5384, Nov. 2021, doi: 10.1109/TPWRS.2021.3071126.

J2. A. Kuri, R. Zurowski, G. Mehlmann and M. Luther, "Power Dispatch Capacity of a Grid-Forming Control Based on Phase Restoring Principle," in IEEE Systems Journal, doi: 10.1109/JSYST.2022.3229103.

J3. CIGRE TECHNICAL BROCHURE – CIGRE WG C4.56: "Electromagnetic transient simulation models for large-scale system impact studies in power systems having a high penetration of inverter-connected generation," Reference: 881, 2022

J4. G. Mehlmann *et al.*, "The Kopernikus ENSURE Co-Demonstration Platform," in IEEE Open Journal of Power Electronics, vol. 4, pp. 987-1002, 2023, doi: 10.1109/OJPEL.2023.3332515.

J5. M. Richter, A. Kuri, J. Richter, T. Wagner, S. Henninger, G. Mehlmann, "Demonstration of Grid-Forming Controls in Hybrid AC/DC Grid in a Real-Time PHiL Environment," in *Electronics* 2025, *14 , no 4*, 730. https://doi.org/10.3390/electronics14040730

Publications in conference proceedings

C1. A. Kuri, G. Mehlmann, M. Luther, D. Audring and R. Zurowski, "Phase Restoring Principle: Concept of a novel grid-forming converter scheme," Power Supply Transformation - Grid Regulation and System Stability; 14. ETG/GMA-Symposium, Leipzig, Germany, 2022, pp. 1-6.

C2. A. Kuri, R. Zurowski, G. Mehlmann and M. Luther, "Converter Modelling Aspects at the Boundary between EMT and RMS Domain," 2022 International Conference on Smart Energy Systems and Technologies (SEST), Eindhoven, Netherlands, 2022, pp. 1-6, doi: 10.1109/SEST53650.2022.9898501.

C3. R. Höse, A. Kuri, G. Mehlmann, R. Zurowski, D. Audring and M. Luther, "Performance of synchronizing units under reduced system strength," 2021 IEEE PES Innovative Smart Grid Technologies Europe (ISGT Europe), Espoo, Finland, 2021, pp. 01-06, doi: 10.1109/ISGTEurope52324.2021.9640080.

C4. D. Audring and A. Kuri, "Modelling and challenges of integration of large renewable power plants," 2021 56th International Universities Power Engineering Conference (UPEC), Middlesbrough, United Kingdom, 2021, pp. 1-6, doi: 10.1109/UPEC50034.2021.9548197.

C5. A. Kuri and E. Brackenhammer, "Challenges for Integration of Renewable Energy in Public Grid," Wind and Solar Integration workshop 2022, Oct 2022, The Hague, Netherlands.

C6. A. Raab, D. Frauenknecht, M. Luther, A. Kuri and A. Wellhoefer, "Hybrid EMT and Phasor based MMC-HVDC Model for Advanced Power System Simulation," 2022 IEEE Power & Energy Society General Meeting (PESGM), Denver, CO, USA, 2022, pp. 1-5, doi: 10.1109/PESGM48719.2022.9917109.

C7. C. Scheibe, A. Kuri, Y. Feng, L. Zhao, X. Xiong, P. La Seta, *et al.*, "Interfacing real-time and offline power system simulation tools using UDP or FPGA systems", Electr. Power Syst. Res., vol. 212, Nov. 2022, doi: 10.1016/j.epsr.2022.108490

C8. C. Scheibe, A. Kuri, L. Graf, R. Venugopal and G. Mehlmann, "Real Time Co-Simulation of Electromechanical and Electromagnetic Power System Models," 2022 International Conference on Smart Energy Systems and Technologies (SEST), Eindhoven, Netherlands, 2022, pp. 1-6, doi: 10.1109/SEST53650.2022.9898468.

C9. A. Kuri, X. Zhou, G. Mehlmann, M. Luther, A. Kuri and P. La Seta, "Dynamic model reduction based on coherency and genetic optimization methodology," ETG Congress 2021, Online, 2021, pp. 1-6.

C10. M. Sukumaran, A. Kuri, G. Mehlmann and M. Luther, "Modular Controller Design applied to Network Reduction Suited for Offline and Online Simulation," 2021 56th International Universities Power Engineering Conference (UPEC), Middlesbrough, United Kingdom, 2021, pp. 1-6, doi: 10.1109/UPEC50034.2021.9548267.

C11. A. Kuri, S. Gäbel, I. Burlakin, T. Wagner, G. Mehlmann and M. Luther "A Novel Concept for Dynamic Network Reduction Dedicated to Real-Time Application, " CIGRE 2022 Kyoto Symposium, Japan

C12. I. Burlakin, J. Porst, E. Scheiner, A. Kuri, G. Mehlmann, U. Kühnapfel and M. Luther, "Dynamic Modelling of Transmission Systems Based on Primary Energy Sources," NEIS 2022; Conference on Sustainable Energy Supply and Energy Storage Systems, Hamburg, Germany, 2022, pp. 1-6.

C13. A. Kuri, A. Raab, A. Takhtaganov, G. Mehlmann and M. Luther, "Comparison of Phase Restoring Principle with other Grid-Forming Methodologies," 2023 IEEE Power & Energy Society General Meeting (PESGM), Orlando, Florida, USA, 2023.

C14. G. Mehlmann, C. Scheibe, S. Resch, G. Kordowich, J. Richter, T. Wagner, A. Kuri, M. Richter, J. Jäger, M. Luther, "Concept and Operation of a distributed multi-domain Power System Laboratory with HiL-capabilities," ETG Congress 2023.

Publications related to the thesis

The publications related to this thesis are reported above and are assigned to the different chapters as follows (Table A 7).

Table A 7: Mapping of chapters to publications.

Chapter	Journal(s)	Conference Paper(s)
2	J3	C1, C2, C3, C4,C5, C13
3	J1, J2	C1
4	J1, J2	C1
5	-	C1, C13
6	J4, J5	C14

Supervised master theses

1. Miao Zheng, M215: Hybridsimulation (RMS und EMT) in PSS®NETOMAC mit generischem RMS-Modell eines VSC-basierten HGÜ -Systems, 17.05.2020.
2. Stefan Frauenknecht, M217: Entwicklung eines Algorithmus zur Anwendung eines Reduktionsverfahrens für dynamische Netzmodelle, 04.05.2020.
3. Xiaoyu Zhou, M237: Multi-Objective Genetic Algorithm-NSGA- II based optimization technique applied to model reduction, 12.03.2021.
4. Richard Höse, M231: Interaction between synchronizing units and weak grids, 12.03.2021.

5. Moraish Sukumaran, M236: Controller Aggregation Methodologies and Optimization applied to Dynamic Network Reduction, 30.04.2021.
6. Sebastian Gäbel, M245: Anwendung von Optimierungstechniken auf die Netzreduktion und dessen Integration in ein Echtzeitsimulationssystem, 07.01.2022.
7. Xuechun Wang, M261: Network Reduction Techniques for Converter Technologies, 03.06.2022.

Supervised bachelor theses

8. Sebastian Schöler, B262: Entwicklung und Analyse eines zukunftsweisenden Netzwerks auf der Grundlage des Nordic Testsystems, 03.05.2021.
9. Artur Takhtaganov, B283: Implementation and Analysis of Different Grid-Forming Converter Control Strategies, 15.07.2022.

Supervised scientific internship reports

10. Xiaoyu Zhou, F77: Dynamic Network Reduction in Power Factory, 02.08.2020.
11. Yujun Liu, F78: Excitation system aggregation: Methodology and optimization for aggregation of models and validation, 16.08.2020.
12. Richard Höse, F83: Mathematical and simulative investigation of Sample and Hold, 23.07.2020.
13. Xuechun Wang, F88: Network Reduction Tool Development and Methodologies, 03.12.2021.
14. Baihui Chen, F100: Bewertung der Stabilität in einem Umrichter - dominierten Netz, 12.09.2021.

Supervised seminar reports

15. Julian Martin, Methods and simulation tools for Dynamic Network Reduction in Stability studies (Methoden und Werkzeuge zur dynamischen Netzreduktion für Stabilitätsuntersuchungen), 22.07.2019.
16. Sanja Milović, Modeling Requirements for Power Electronic Converters for Performing Grid Integration Studies, 09.02.2020.
17. Thomas Kräh, Vergleich von Zeitbereichs- und Frequenzbereichsanalysemethoden in EMT-Modellen, 23.12.2020.
18. Jincheng Wang, Insights into converter integrated power system and its modeling, 29.01.2021.

19. Sebastian Gäbel, Introduction to multi-objective genetic algorithm: NSGA-II Sorting criteria for optimization challenges in power engineering, 30.04.2021.
20. Artur Takhtaganov, Grid Forming Converters Shaping the New Grid, 04.06.2021.
21. Patricia Hartmann, Auswirkungen des hohen Umrichteranteils in einem zukünftigen Netz mit 100 % erneuerbarer Energien, 02.07.2021.
22. Han, Mengjun, Overview on hybrid EMT and dynamic-phasor simulation applied to Real Time Simulators, 10.09.2021.
23. Jiating Ye, Black start capability and power balancing concepts of full-converter wind turbines, 12.01.2022.

The increasing deployment of inverter-based resources (IBRs) in power systems has fundamentally shifted their roles, requiring them to deliver many grid services traditionally provided by synchronous machines. While most existing IBRs are grid-following, tracking the system frequency, the vision of a 100 % converter-operated grid requires these resources to establish grid voltage and frequency actively. This transformation necessitates grid stability, adequate response to disturbances, and reliable ancillary services, thereby leading to the emergence of advanced Grid-Forming (GFM) control strategies. These approaches leverage the speed and flexibility of power electronic converters alongside the stabilizing characteristics of synchronous machines, enabling effective support for microgrids and bulk power systems. This thesis introduces a novel GFM converter control strategy from a power system perspective that attains global stability. The approach is developed in three phases. In Phase 1, the ‚Phase Restoring Principle' (PRP) is introduced, which utilizes an innovative angular transformation to generate a nominal grid frequency without an additional master control. Hence, emulating an ideal source with infinite inertia and the response is free of undesirable swing dynamics. Building on this foundation, Phase 2 incorporates an enhanced active power control to achieve steady-state active power limitation and facilitates cooperation with other sources through arbitrary setpoint dispatches. Phase 3 addresses current limitations based on the voltage magnitude limiter concept with innovative usage of anti-windup methods. Thus, protecting semiconductor devices during severe faults while preserving GFM characteristics. Comprehensive validation is provided through analytical derivations, numerical simulations in various simulation domains, and a laboratory environment by adopting Power-Hardware-in-the-Loop tests. The results confirm global stability and robust performance across various network configurations, demonstrating that the developed control scheme is mature and viable for practical GFM field applications.

ISBN 978-3-96147-822-4

9 783961 478224

FAU UNIVERSITY PRESS 2025